The Influence of Hull Boundary Layers on Waterjet Intake Performance

by

J. L. Roberts, B.E. (Hons.)

Department of Civil and Mechanical Engineering

Submitted in fulfilment of the requirements
for the degree of
Doctor of Philosophy

University of Tasmania

February 1998

Statement of Originality

This thesis contains no material which has been accepted for the award of any other degree or diploma in any tertiary institution. To the best of my knowledge and belief, this thesis contains no material previously published or written by another person, except when due reference is made in the text.

This thesis may be made available for loan and limited copying in accordance with the *Copyright Act 1968.*

J. Roberts 2/2/1998

Jason L. Roberts

Abstract

The influence of hull boundary layers on typical waterjet propulsion system intakes used in the fast catamaran ferry industry has been experimentally and computationally studied. Particular attention was paid to the effect of boundary layer thickness on flow quality at the pump impeller face.

A scale waterjet intake model mounted on the side wall of a wind tunnel enabled performance to be determined experimentally. Surface mini-tufts, ingestion streamtube determination, skin friction measurements and velocity and thermal anemometry traverses were used to detail the flow. The most significant observation was the presence of a separation zone on the intake roof. Two complete sets of results were obtained: one with the wind tunnel's naturally thin boundary layer and another with an artificially thickened boundary layer. The latter showed more extensive flow separation.

Computational work was conducted using the commercial finite element package FIDAP. Grid independence required a surprisingly large number of nodes (approximately 300,000). However, good agreement with experimental results was obtained with about 120,000 nodes.

Waterjet intakes installed on fast catamaran ferries ingest thick hull boundary layers (hull boundary layer thickness is comparable with the intake diameter). Both experimental and computational results show that a thick hull boundary layer adversely effects the performance of such intakes. Therefore, inclusion of thick hull boundary layers in the modelling/designing of waterjet systems is essential for realistic performance predictions.

The intake performance under manoeuvring conditions (zero vessel speed) was also studied both experimentally and computationally. It was found that cut-water flow separation choked the inlet and severely limited the available manoeuvring thrust. Computational results for an increased cut-water radius indicated that substantial improvement is possible with no detrimental effect on cruise performance.

Acknowledgements

I would like to thank Dr G. J. Walker for his friendship, supervision and editorial input, above and beyond the call of duty, throughout this project. The assistance of the technical staff of the University of Tasmania's Civil and Mechanical Engineering Department was also invaluable.

I am indebted to A/Prof K. Cavell for the supply of (and safety guidance on the use of) the carbon monoxide used in parts of the experimental program. Dr R. Coleman and H. Clement optically surveyed the pressure tapping in the experimental model. Dr Ron Cresswell supplied frequent advice on the computational model used herein.

Financial support for this project was provided through an Australian Postgraduate Award scholarship with supplementary support through the Australia Maritime Engineering Cooperative Research Center.

The friendship and brainstorming sessions with other postgraduate students (especially Bill Solomon, Jeremy Hughes and Damien Holloway) is also gratefully acknowledged.

I would like to thank my wife (Dr) Donna for her love, support and significant editorial input.

Finally, I would like to thank my family and friends for their support and tolerance.

Contents

List Of Figures

List Of Tables

Nomenclature

a_T	hot-wire overheat ratio
h	convective heat transfer coefficient
k	thermal conductivity
p	static pressure
q	dynamic pressure
u	time mean velocity
u'	instantaneous fluctuation from u
u^*	wall friction velocity $= \sqrt{\frac{\tau_w}{\rho}}$
u^+	dimensionless velocity $= \frac{u}{u^*}$
u_{ref}	reference velocity, typically u_∞ but $\overline{u_{duct}}$ for manoeuvring conditions
x	streamwise distance with origin at start of intake ramp
y	normal distance from hull plane
y^+	dimensionless wall distance $= \frac{yu^*}{\nu}$
z	spanwise distance from model centre-line
C_f	skin friction coefficient $= \frac{\tau_w}{1/2\rho u_{ref}^2}$
C_p	pitch coefficient $F(q_1, q_2, q_3)$
C_y	yaw coefficient $F(q_1, q_2, q_3, q_4, q_5)$
D	intake duct diameter
I	turbulence intensity $= \frac{u'}{u_\infty}$
L	characteristic length (for hot-wire probes this is the wire diameter)
N_u	Nusselt number $= \frac{hL}{k_f}$
P	total pressure
Q	flow rate
R_e	Reynolds number based on intake diameter $= \frac{Du_\infty}{\nu}$
T	temperature ($^\circ C$)
α	yaw angle (in degrees)
β	pitch angle (in degrees)
ϵ	turbulent dissipation
ϵ^+	dimensionless turbulent dissipation $= \epsilon\frac{\delta}{u_\infty}$
κ	von Kármán constant $= 0.41$
μ	kinematic viscosity
ν	dynamic viscosity
ρ	density
τ_w	wall shear stress

Superscript

$\bar{}$ averaged conditions

Subscript

∞ wind tunnel inlet conditions

f at film conditions

Prologue

This study investigates the flow in marine intakes for waterjet propulsion systems, and in particular flush intakes as typically installed in fast catamaran ferries.

Research into intakes for propulsion is extensive in the aero-space sector. However, there is relatively little research into marine intakes in comparison. Both types of intakes are similar as they are both designed to deliver fluid at high pressure and high uniformity to the engine/pump. Both intakes inevitably work near, or even beyond, boundary layer separation (due to adverse pressure gradients and offset geometries). While much information on intakes can be "read across" from the aero-space sector to the marine sector there are unique problems in both fields. The layout of aircraft intakes are governed by structural and equipment arrangement considerations, while the mass of entrained water is a major concern in marine applications. Therefore, aircraft intakes are situated near the front of aircraft where fuselage boundary layers are thin and easily "dealt with". This is not feasible for marine intakes (as the mass of entrained water would be a significant percentage of the potential payload) so these intakes are frequently placed well aft where a hull boundary layer of thickness comparable to the intake diameter exists (especially in fast catamaran ferry applications). Cavitation is another potential problem in marine intakes that is obviously not an issue for aero-space intakes. The possibility of cavitation not only directly effects the intake design (requiring that the static pressure does not fall below the water vapour pressure) but also may limit the application of devices (such as vortex generators) used in aircraft intakes to control flow non-uniformity at the engine/pump face.

This thesis therefore aims to address the current lack of research into the influence of hull boundary layers on marine intakes.

Limitations

A balanced approach consisting of both experimental and numerical modelling of the flow through a waterjet intake has been undertaken. However, this study has been limited by several factors, including:

- experimental testing with a wind tunnel model only. Cavitation tunnel testing would have allowed the study of cavitation performance and provided information on Reynolds number sensitivity. However, logistical considerations precluded this;
- experimental testing of an intake only. Ideally a full system including impeller shaft, impeller, stator and nozzle should be tested as interactions (such as pre-swirl introduced by the impeller) may be important;

- limited computer resources. Approximately 300,000 nodes were required for grid independent solutions, but these jobs required massive amounts of computer resources. Each run involved a special one-off job needing sole access to a multi-institution super-computer for several days. The majority of the computer simulations were therefore carried out on smaller workstations with a coarser grid (approximately 120,000 nodes); and
- a model Reynolds number about 100 times smaller than full scale. Cavitation tunnel testing would have allowed operation at higher Reynolds numbers (around twelve times larger) and given some indication of the magnitude of scale effects.

Thesis Outline

Waterjet propulsion systems are introduced in Chapter 1. A background survey of literature relevant to this study is presented in Chapter 2. Chapters 3 and 4 detail the research methods used for the experimental and computational program respectively (including information on the artificially thickened hull boundary layer used to investigate the influence of hull boundary layer thickness).

The results have been presented in three separate sections. Chapter 5 contains the experimental and computational results for the thin hull boundary layer study (using the wind tunnel's natural wall boundary layer). Chapter 6 reproduces these results using an artificially thickened hull boundary layer. Chapter 7 contains results for manoeuvring operation including a section with an increased cut-water lip radius. (Throughout this thesis the use of the word manoeuvring refers to zero boat speed operation of the waterjet.)

The results are analysed and discussed in Chapter 8. Conclusions are drawn and recommendations for future studies are suggested in Chapter 9.

Chapter 1

Introduction

1.1 General Introduction To Waterjets

Waterjet propulsion systems are a means of propelling high speed marine vessels. They overcome the cavitation problems associated with conventional screw propellers at high speeds by decelerating the propulsive fluid before the impeller/propeller by using a duct to deliver the propulsive fluid to the impeller. The other significant advantage of waterjet propulsion systems is the high manoeuvring forces available at low/zero boat speed. Roy [115] also lists shallow draft, safety, reduced noise radiation (around 10 dBA according to Svensson [128]) and reduced magnetic signature as advantages of waterjet propulsion systems. Other cited advantages of waterjet propulsion systems include reduced vibration (Hale and Vorrie [59]) and reduced engine wear (Svensson [128]).

1.2 High Speed Marine Propulsion

The most common problem with high vessel speeds is the resulting low static pressure on the surface of a conventional unducted propeller. This frequently leads to cavitation and its associated problems of physical damage to the propeller, loss of thrust and noise production. There are three common approaches to overcoming cavitation, namely designing a propeller blade section for cavitating operation (e.g., super cavitating propellers), increasing the static pressure through venting (e.g., surface piercing propellers) and increasing the static pressure through diffusion (e.g., waterjets).

Super cavitating propellers are, broadly speaking, conventional marine propellers with specially designed blade sections for high speed applications (consisting in part of a thin leading edge). The blade normally has a thick, truncated rear edge with the cavitation sheet formed during high speed operation completing the blade profile (Thurston and Amsler [133]). This results in efficient high speed operation. However, as the blade shape relies on the presence of cavitation, low speed and manoeuvring condition performance may be seriously compromised. Furthermore, at low/medium speed operation the propeller is only partly cavitating with the possibility for resulting cavitation damage (Kruppa [78]). Finally, the extreme stress at the thin leading edge has caused several operational failures (Barr [14]) and to overcome this more exotic (and expensive) materials such as titanium alloys are frequently used.

Surface piercing propellers rely on venting from the atmosphere to control cavitation problems (Kruppa [78]). The do not suffer the cavitation limitations of conventional screw propellers but have poor low speed manoeuvrability (Alexander [4]). Another consideration with this type of propulsion is the extremely large cyclic variation in blade loading and stressing (Barr [14]).

Waterjets overcome the cavitation problem by diffusing the flow before it reaches the impeller thereby increasing the static pressure at the impeller face above vapour pressure. This diffusion is achieved by ducting the propulsive fluid to an inboard pump. For fast catamaran ferry applications the most common configuration of ducting used is a flush offset intake. The duct delivers the fluid to the propulsor which is essentially an axial or mixed flow pump with an associated stator to recover the energy contained in the swirl motion of the fluid leaving the impeller. The pressure energy added by the impeller is converted into kinetic energy by the nozzle. This is shown diagrammatically in Figure 1.1.

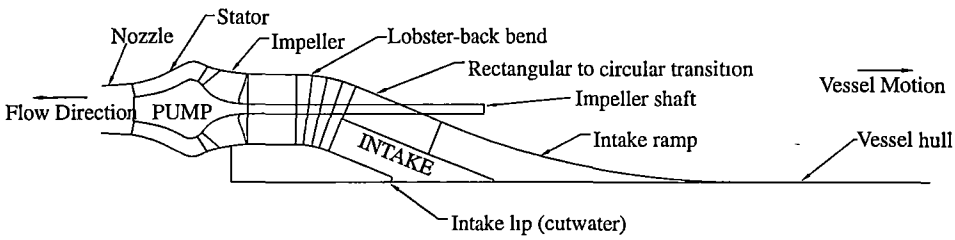

Figure 1.1: Schematic representation of a typical fast catamaran ferry waterjet propulsion system

Manoeuvring thrust is obtained by deflecting the nozzle flow using steering buckets. Therefore, waterjets offer good manoeuvring thrust as the thrust is only dependent on the mass flux of propulsive fluid and is virtually independent of vessel speed. Shallow water operation and low noise radiation are also benefits of using waterjets according to Allison and Goubault [9].

Another key difference between waterjet propulsion systems and conventional screw propellers is that while conventional screw propellers are usually custom designed waterjet units tend to be "off the shelf" units (Szantyr and Bugalski [131]) with Allison and Goubault [9] suggesting that this has limited the potential of waterjet systems.

However, waterjets like all propulsion systems have potential liabilities. The most obvious one is a relatively complex integrated design. For example, the duct must deliver high quality fluid to the propulsor for efficient operation (Davison [32]). Offset diffusion ducts have well documented flow distortion problems (Tindell [134]) and these are compounded by the ingestion of a relatively thick hull boundary layer. An investigation into the effects of boundary layer ingestion on the performance of waterjet intakes is presented herein.

Chapter 2

Literature Review

2.1 Introduction

Allison [6] provides a comprehensive introduction to waterjets, including historical developments from the granting of the first patent in 1631 to the establishment of waterjets as an accepted and reliable method of marine propulsion in the 1950's; and beyond to current developments (see also Pike [102] and Roy [115]). Allison [6] also introduces the two types of waterjet inlets, namely ram (also known as pod or strut) and flush inlets. Ram inlets are used on hydrofoil craft and a large percentage of the waterjet literature in the mid to late 1960's concentrated on this type of installation (Brandau [19]) (e.g., Hatte and Davis [62], Levy [83] and Johnson Jr. [72]). Hull boundary layer ingestion is not an issue for these installations (as the intake lies outside the hull boundary layer, Arcand and Comolli [12]). Surface effect ships (SES) may use a semi-pod inlet (see Kashiwadani [74]) which shares features of both pod and flush intakes. Air ingestion is a potential problem for semi-pod installation on SES's (ITTC [69]). See also Sasajima and Mishima [119] for a more in-depth discussion. Flush intakes are used on monohulls (see Svensson [127] and Frith [45]), planing craft (see Griffith-Jones and Bowen [55], Griffith-Jones [56] and Fujisawa and Ogawa [46]) and catamarans (see Haglund et al. [58], Nereng et al. [95] and the current study). A large body of proprietary information about flush intake performance exists but public domain knowledge on this topic is scarce (Allison [6]). The current study aims to address this shortcoming.

2.2 Hull-Waterjet Interaction

The hull and waterjet influence each other in a complex manner that can only be resolved by model testing (Haglund et al. [58]). This interaction between the hull and waterjet has been extensively studied (e.g., van Terwisga [141], Alexander et al. [5], van Terwisga [142], van Terwisga [143] and van Terwisga [144]) with the performance of the overall system, in general, not equalling the sum of the individual free-component performances. Svensson [128] lists possible sources for the interaction(s) including alteration of vessel trim, alteration of the pressure distributions on the hull and alteration of the wave pattern and hence resistance. The effects of the hull on waterjet performance is typically accounted for by the introduction of energy and momentum corrections (e.g., van Terwisga [143]). Detailed intake measurements (either experimentally or

computationally) with the more realistic hull boundary layer at inflow are not undertaken in this case. The other typical mechanism for calculating interaction effects is via experimental testing of entire systems (see for example van Terwisga [141] and Coop et al. [28]) where the measurements focus on the entire system. Again, the details of the intake flow with thick boundary layers is not resolved. The present study investigates the influence of hull boundary layers on intake performance.

2.3 Hull Boundary Layer Ingestion

It has been known since the late 1960's that the inflow conditions to waterjet intakes "... may be of great importance for energy conversion in the jet propulsion and must not be overlooked" Kruppa et al. [77]. For large displacement ships hull boundary layer ingestion will appreciably effect the waterjet performance (Arcand and Comolli [12]). As a result, many researchers (e.g., Dyne and Lindell [35], Steen and Minsaas [123], Svensson [128] and Haglund et al. [58]) have considered hull boundary layer ingestion.

Dyne and Lindell [35] considered the effect of the hull boundary layer for the correct scaling of test results to full scale (see also Steen and Minsaas [123]) but say nothing about the effect boundary layers have on intake performance.

Steen and Minsaas [123] discuss boundary layer ingestion in terms of inflow momentum and concluded that assuming a rectangular ingestion cross section with a width of 1.3 times the physical width (e.g., Dyne and Lindell [35] and Iannone and Rocchi [66]) may seriously underestimate full scale thrust as the ingestion streamtube width is approximately twice the physical width of the intake. (The current study measures the ingestion streamtube width around 1.7 and 2 times the physical width for thin and thick boundary layer cases respectively.) Assuming an ingestion streamtube with of 1.3 times the physical width will result in an underestimation of the amount of propulsive fluid originating in the hull boundary layer and therefore an overestimation of the inflow momentum. Assuming an ingestion streamtube width equal to the physical width (e.g., Kruppa et al. [77] and Manins [84]) will further underestimate full scale thrust.

It has been stated, either explicitly or implicitly (e.g., Kruppa et al. [77], Svensson [128], Hoshino and Baba [65] and Haglund et al. [58]), that it is generally beneficial to ingest the hull boundary layer. For example, Haglund et al. [58] states "To achieve a high hull efficiency the inlet should be designed to ingest as much of the hull boundary layer as possible". Ingestion of boundary layer fluid can improve propulsive efficiency (Goldsmith and Seddon [50] and Smith Jr. [121]) as the same thrust can be achieved for less energy expenditure (Arcand [11] and Roberts and Walker [110]) due to the quadratic and cubic dependence on fluid velocity for momentum and energy respectively. Smith Jr. [121] gives a detailed discussion on the benefits of wake ingestion. However, Roberts et al. [112] have shown that these potential benefits will only be fully realised if ingestion of the boundary layer fluid does not impair the efficiency of the impeller in transferring energy to the fluid.

English [37] discusses the issue of hull boundary layer ingestion, concluding that there is little information on the effect of hull boundary layer ingestion on intake losses. He suggests that designing intakes for minimal distortion rather than encouraging boundary layer ingestion (for increased thrust for the same energy expenditure) may be prudent. This is in agreement with Kim [75], who discusses the effect of boundary

layer ingestion on overall efficiency and concludes that effective wake utilisation is not possible with waterjets. Roberts and Walker [110] also introduce the possibility that boundary layer ingestion may not be beneficial. By considering the increased frictional drag associated with growing a new boundary layer downstream of the intake they showed that in some scenarios the increase in thrust due to boundary layer ingestion is more than offset, with more power being required to propel the vessel.

Griffith-Jones [56] investigated the influence of hull boundary layer ingestion on intake performance using computational fluid dynamics. The results of this study were inconclusive. While their results showed no significant difference with thin boundary layer results, they bring into question their grid coarseness and ability to resolve boundary layer features accurately.

McCreath and Smith [87] investigated the influence of boundary layer thickness on aircraft-type (NACA) intakes and concluded that boundary layer thickening adversely influenced performance. However it should be remembered that these type intakes are designed to "sweep" away the boundary layer using shed vortices unlike typical waterjet intakes which "suck in" the boundary layer.

On the issue of boundary layer ingestion English [37] concludes that "It is doubtful if a reliable assessment of this on propulsive efficiency can be made without experiment,...". The current study is based on a balanced experimental and computational investigation of boundary layer ingestion effects.

2.4 Impeller Face Distortion

Waterjet intakes should deliver high quality flow to the pump (good pressure recovery and low distortion (Allison [6])) as pump efficiency will be adversely influenced by high distortion (ITTC [69] and Kruppa [79]). Kruppa [79] investigated the influence of inflow disturbances on pump efficiency and notes that high specific speed pumps (such as axial flow pumps) are more sensitive to inflow disturbances than lower specific speed pumps. Svensson [130] discusses the influence of distortion due to the inlet (compared to uniform inflow) on pump performance but there is no mention of hull boundary layers.

The offset and diffusing nature of the intake will inevitably produce flow non-uniformity. The flow in offset ducts in the aero-space industry have well documented secondary flow (e.g., Rowe [114], Bannsod and Bradshaw [13] and Jenkins and Loeffler Jr. [70]) and distortion (e.g., Tindell [134] and Tindell [135]) problems. Furthermore, diffusion of the flow will amplify any flow non-uniformities at the start of the intake (Betz [15]), just as contracting sections are used in wind tunnel facilities to improve flow uniformity. Roberts et al. [112] consider the performance of a straight centre-line two-dimensional diffuser for a typical fast catamaran ferry case, including a thick inflow boundary layer, and show that stalling of the diffuser is likely. This will reduce the diffuser's efficiency (Morgado and Gato [90]). Nereng et al. [95] also note that high intake angles and boundary layer ingestion "makes it difficult to avoid separation". Furthermore, centre-line curvature will effect the diffuser performance due to turbulent shear stress modifications (Parsons and Hill [99]).

Flush intakes give a very non-uniform flow at the impeller face with associated potential cavitation and efficiency loss problems (Nereng et al. [95]). Using conven-

tional, fast running, highly loaded waterjet pumps that are smaller than desirable can be expected to cause problems with cavitation erosion, vibration excitation and pump efficiency when operated in severely distorted inflows (English [37]). English [37] points out that the flow distortion at a pump face is a critical factor with such heavily loaded propulsors and attempts to improve flow uniformity should be made.

Distortion will result in cyclically varying impeller blade loadings with resulting vibration, noise and potential fatigue problems (Roberts et al. [112]). Operational experience of this is reported in Nereng et al. [95]. Vibrational problems with conventional screw propellers are known to be associated with a non-uniform inflow velocity field (Matherson [86] and Nereng et al. [95]). Roberts et al. [112] point out that another significant result of distortion is a lateral force on the impeller due to unbalanced loading. Coupled with relatively soft bearings and a long flexible shaft, this can lead to the reduction or even elimination of impeller tip running clearances. Distortion is also the most important destabilising influence on aero-engine performance (Campbell and Ellis [23]) with circumferential variations having significant effect while radial variations are relatively insignificant (Saravanamuttoo [118]).

Bruce et al. [20] discuss the design of pumpjets with boundary layer ingestion for axi-symmetric bodies and state that circumferential distortions are undesirable and that an impeller operating in such a flow field may suffer from periodic cavitation, vibration and loss of efficiency.

"Published records of detailed flow explorations at pump entry are sparse,..." (English [37]). Again, the current study addresses this deficiency.

2.5 Experimental Testing

There are two basic approaches to modelling the flow in waterjet intakes, namely experimental testing and numerical modelling. While numerical modelling offers the ability to undertake optimisation studies at less cost than conventional experimental testing (see Allison [7] for a case study involving a waterjet intake), experimental data for validation is required. Experimental testing may also reveal flow phenomena present in the actual flow which the numerical model has no mechanism for predicting. In the current study secondary flows in a streamwise corner was experimentally observed, but the numerical model was unable to predict this due to limitations in the approximations to the governing equations.

Griffith-Jones [56] details experimental testing of a wind tunnel model (using the tunnel's naturally thin wall boundary layer) and full scale measurements on a planing hull test boat. Aartojärvi [1] discusses testing techniques for waterjet inlets; like Fujisawa and Ogawa [46], he measures the inlet boundary layer but makes no mention of artificially thickening what is a relatively thin boundary layer compared to the intake diameter. Turnock et al. [139] used wind tunnel testing on a model with a straight intake roof and slope discontinuity at intake/hull intersection. This shape was chosen for compatibility with a previous study. Again, they only used the wind tunnel's naturally thin boundary layer, with which they noted intake roof separation (as did Pingzhong and Lixiang [103]).

Haglund et al. [58] undertook full scale and cavitation model testing on a catamaran ferry waterjet installation. They measured the full scale hull boundary layer thickness

at inlet and concluded that the cavitation tunnel's naturally thin boundary layer was a satisfactory approximation. Intake roof separation was also noted by Haglund et al. [58] during model testing. This was eliminated in the full size unit by smoothing the curvature distribution for the ramp. Note that the model in the current study is designed to have continuous curvature all the way along the intake until the lobster back bend.

Steen and Minsaas [123] have undertaken both cavitation modelling of intakes and towing tank based self propulsion testing of entire models. Nereng et al. [95] describe wind tunnel testing of intakes as well as cavitation testing, with the latter including a "simulated hull", although they do not appear to test at varying boundary layer thickness. They cite the principle parameters varied, and do not include boundary layer thickness.

To the best of the author's knowledge only one very recent (1997) paper (van de Vorst et al. [140]) discusses experimental testing (in a wind tunnel) with varying inflow boundary layer thickness. They however give no information on their results (which are probably proprietary), do not discuss the mechanism for artificial thickening (other than to say "varying thickness could be created by inserting different disturbances ahead of the test section") and fail to mention turbulence when describing their boundary layer measurements. As free stream turbulence effects skin friction (Bradshaw [17]) and there is potential for a subtle flow separation (separation from a smoothly curved surface) in waterjet intakes, knowledge of the inflow turbulence profiles is essential. There is no indication of how realistic the artificial boundary layer of van de Vorst et al. [140] is, although this aspect is only one part of a very comprehensive and systematic test (and CFD validation) program.

The current study uses wind-tunnel based experimentation using both the wind tunnel's naturally thin boundary layer and an artificially thickened boundary layer which is more realistic for typical fast catamaran ferry waterjet intakes.

2.6 Computational Fluid Dynamics

There is extensive literature on computational fluid dynamic (CFD) studies of waterjets (including Griffith-Jones [56], Førde et al. [43], Szantyr and Bugalski [131], Kashiwadani [74] Turnock et al. [139], Seil et al. [120], van Terwisga [144] and the current study). Several approaches have been used, including purely potential flow studies (van Terwisga [144] and Dai et al. [30]), coupled potential flow and boundary layer codes (Førde et al. [43] and Szantyr and Bugalski [131]) and fully viscous and turbulent solvers (Griffith-Jones [56], Seil et al. [120], Turnock et al. [139], Dai et al. [30] and the current study).

Førde et al. [43] used Euler and thin layer Navier-Stokes codes. Their calculated losses for the flush type intakes are unrealistically low. Their largest loss is 2.1% of impeller face dynamic head, which they attribute to mesh coarseness (around 30,000 points employed).

Szantyr and Bugalski [131] used a potential flow panel method code to study the flow in waterjet intakes including stator and rotor modelling. Boundary layer blockage effects were taken into account using "short cut" methods. Their agreement with experimental results was good. However, there is no mention of the inflow boundary

layer which is probably very thin compared to the inlet diameter. The experimental testing schematic shows no mechanism for boundary layer thickening. Furthermore, the intakes appear to have straight intake ramps with a slope discontinuity at intake/hull intersection which is quite a different scenario to the intake of the present study.

Griffith-Jones [56] also used CFD to study intakes, using a commercial package FLUENT (a finite volume code with $k-\epsilon$, RNG and Reynolds Stress Model turbulence modelling options). A maximum of 150,000 cells was used due to hardware and software limitations. Computational analysis of the effect of hull boundary layer on intake performance by Griffith-Jones [56] indicated that "... the large change in boundary layer thickness does not significantly alter the intake flow." However, he points out that his boundary layer modelling is questionable and cell skew caused large discontinuities in boundary layer thickness, both at the hull/intake intersection and in the intake itself (where mapping the structured Cartesian grid to a circle resulted in high cell skew). Griffith-Jones' [56] prediction of roof separation did not agree well with experimental measurements, which he again attributes to insufficient grid resolution. This further calls into question his conclusions on the influence of hull boundary layer thickness. Overall, Griffith-Jones' agreement between CFD and experimental results were fair, although grid limitations and the more severe geometry than the present study (steeper ramp angle and large ramp slope discontinuity) hindered the CFD analysis.

Turnock et al. [139] used a Reynolds averaged Navier-Stokes code and a $k-\epsilon$ turbulence model and obtained fairly good agreement with experimental measurements. Pylkkänen [107] used FLOW-3D with $k-\epsilon$ turbulence modelling on flush intakes. A grid sensitivity analysis was undertaken but the results of it are not clearly given. The latter author states that "calculated minimum and maximum pressures, maximum velocity and the velocity distribution at the impeller face were quite insensitive to minor changes in the grid size". However there is no quantitative indication as to what "minor changes" represent. He states further that "in order to get a suitable viscous sublayer thickness, as dense a grid as the pre-processing module allows has to be used".

Førde et al. [43], Griffith-Jones [56] and Turnock et al. [139] discuss the limitation of their results in terms of grid coarseness, but none have undertaken a grid sensitivity analysis (although Turnock et al. [139] suggests that their 120,000 nodes may require a factor of five increase to accurately model the flow). A grid sensitivity analysis should be standard practice in all CFD analyses, as it is no longer sufficient to publish results performed on a single fixed grid (Wilcox [150]). The importance of grid convergence is essential for turbulence computations because of the need to distinguish between numerical error and turbulence-model error (Wilcox [150]). On the subject of grid convergence, Rumsey and Vatsa [116] state that "mesh refinement ... can sometimes lead to dramatically different results, particularly for 3-D separated flows" (the type of flows under consideration herein). Other CFD studies of waterjet intakes (such as Seil et al. [120] and Szantyr and Bugalski [131]) do not mention grid sensitivity at all. Lack of grid sensitivity analysis is not confined to this field of research. Freitas [44] summarises benchmarking cases for commercial CFD codes and states that "some vendors were satisfied with solutions generated at a single grid resolution, never attempting to demonstrate a grid convergent solution".

Van Terwisga [144] undertakes both grid sensitivity analysis and experimental validation of his potential flow modelling. While he has shown grid independence there appears to be a problem with conservation of mass for the lower IVR case, which he

attributes to problems with proximity to the flow singularities used to model the flow. This is in agreement with the current author's experience with potential flow codes used for internal flow applications. The experimental validation shows fair agreement (considering the neglection of viscous terms) for static pressure distributions, although van Terwisga states that potential flow methods do not satisfactorily predict the flow inside the intake.

To the best of the authors knowledge no papers on CFD analysis of waterjet propulsion systems discuss the grading of elements towards the wall (although some such as Griffith-Jones [56] and Pylkkänen [107] clearly have graded meshes). With some of the codes used this may not be an option. The current study found that grading the available elements towards the wall is at least as important as the total number of elements.

Turnock et al. [139] also note that grid improvements are required to accurately model the surface shear stress. Pylkkänen [107] is the only other paper to the author's knowledge that discusses calculated/measured skin friction, although he only gives shear stress for a few points of unspecified location. The current study obtains excellent agreement between calculated skin friction and experimentally measured values.

Another failing of some CFD studies is the lack of experimental validation (e.g., Seil et al. [120] and Førde et al. [43]). However, Førde et al. [43] did recommend experimental validation for their CFD study. van de Vorst et al. [140] discuss CFD applied to waterjet intakes and state that "before relying on these tools thorough validation is required".

Allison [7] details a case study of the design of a US Marine Corps amphibious vehicle and cites the financial advantage of using computational fluid dynamics (CFD) compared with conventional experimental testing in the design of a waterjet intake. Rivoire and Vigneron [109] discuss the use of CFD in the aerospace industry for initial optimisation and more targeted experimental testing. (Note that this is in an industry with over 30 years experience in the use of, and more importantly validation of, CFD in the types of flows of interest to the aerospace sector). Strazisar [126] states that in his opinion using a multi-disciplinary approach (experimental, flow physics and computation) is the most advantageous approach to modelling. "The comparison of numerical results to experimental data is also needed to be confident in the use of these CFD methods during the design process" (Joubert and Goutines [73]).

Boundary conditions are also not clearly defined for many of the studies, especially boundary conditions for turbulent parameters. This is apparently a problem in the field of CFD in general, with Fisher and Rhodes [39] noting the inadequate definition of boundary conditions (especially at inflow) as one of the key difficulties in applying CFD to real engineering problems. Seil et al. [120], Griffith-Jones [56], Turnock et al. [139] and Pylkkänen [107] do not give any information on turbulent boundary conditions so we can only assume that they have used isotropic dissipation relations. However, as most of the validation for CFD results is from cavitation tunnel or wind-tunnel experimentation this assumption of isotropy may not be valid as the turbulence at the start of the tunnel working section will be anisotropic. Goldstein [51] states "most modern wind tunnels are of the return flow type with a large contraction ratio, and the transverse turbulent velocity components are in this case certainly not equal to the longitudinal one". Furthermore, for any general boundary layer turbulent non-isotropy becomes significant near the wall (Rotta [113]) and the available data on near

wall dissipation is limited and variable (Patel et al. [100]). The current study uses experimentally derived dissipation (and turbulent kinetic energy) boundary conditions for the flow actually studied as per the recommendation of Larock and Schamber [80].

2.7 Cutwater Lip

Manins [84] states that the intake lip should have a good radius, while Førde et al. [43] states that "This lip is one of the key issues for a good design" of flush type intakes (see also Allison [7]).

The requirement of a sufficient intake lip radius for adequate static operation has also been noted in the aerospace literature, with the developmental programs for both the F-14 (see Tindell et al. [136]) and Kestrel/Harrier fighter aircraft (see Goldsmith and Seddon [50]) and the engine intakes for the Boeing 747 airliner (see Viall [145]).

Haglund et al. [58] experimentally studied the effect of cut-water lip geometry on intake performance, concluding that this lip is the most cavitation prone part of the intake and that small changes in lip angle had a noticeable impact on cavitation and inlet efficiency. Brandau [19] also notes lip cavitation susceptibility at cruise operation.

The current study computationally investigates the lip radius in terms of obtaining an acceptable compromise between manoeuvring and cruise performance.

2.8 Manoeuvring Performance

Low speed and/or manoeuvring performance has received relatively little attention in the published literature. Törneman [137] discusses the operational importance of good manoeuvrability with a case study for a small (60 passenger) vessel, with the reduction in manoeuvring time achieved via waterjet propulsion systems saving around US$60,000 per annum.

Delao [34] studied the pump design for a flush intake hydrofoil craft and found choking of the intake at higher pump speeds. Allison and Dai [8] note that manoeuvring thrust is only a small fraction of ahead thrust due to limited deflection angles. Furthermore, the off-design operation of the intake may lead to intake cavitation (see also Brandau [19]) as well as pump cavitation.

Aartojärvi [1] shows results at "high intake load" corresponding to low speed operation and these show cutwater separation as found in the current study. However, it appears that these results are at a non-zero forward boat speed as distinct from the current study.

Svensson [129] says that waterjet units optimised for high speed operation may not be able to absorb full power at zero speed and that bollard pull ahead figures of 0.095 kN/kW for low speed optimised units may fall below 0.07 kN/kW for high speed optimised units. Additionally intake cavitation/separation blockage may reduce the maximum allowable engine speed (and hence power) further limiting manoeuvring thrust Roberts et al. [112]. Haglund et al. [58] notes operational experience of cavitation damage to inlets but does not attempt to apportion this to cruise or manoeuvring operation. Allison and Goubault [9] also notes the possibility of both pump and inlet cavitation during low boat speed operation.

Separation of the flow at the cut-water will produce a large pressure loss limiting engine speed due due to cavitation susceptibility (Roberts et al. [112]). This separation (which has also been noted by Dai et al. [30]) will also result in a very non-uniform flow at the impeller face, with a large velocity at the top of the intake. The same flow behaviour is noted in the intakes for unmanned aircraft, e.g., Abdel-Fattah and Fisher [2].

This thesis both experimentally and computationally studies the zero boat speed intake flow, as well as computationally studying the effect of increasing the cutwater lip radius to control flow separation.

Chapter 3

Experimental Research Methods

3.1 Overview

The experimental program is based on an acrylic scale model of a waterjet intake. This was tested using a wind tunnel, and data acquired using an IBM PC compatible computer. Testing for ingestion streamtube cross section, surface flow visualisation, velocity and turbulence traverses, and surface shear stress measurements comprised the experimental component of this study. This chapter details the equipment and techniques used for this experimental program.

The upstream wind tunnel wall boundary layer was artificially thickened for one series of testing and the mechanism for thickening is discussed in some detail.

The scope of the experimental program was to: provide an insight into the physical flow processes in waterjet intakes; provide quantitative flow measurements for a "typical" intake; and provide validation data for the computational section of this study.

3.2 Instrumentation

3.2.1 Data Acquisition

All experimental data was acquired via the commercial software package LABVIEW (versions 3.1.1 and 4.1) running on an IBM compatible 486DX2-66 computer interfaced with a National Instruments Lab PC+ 12 bit data acquisition (DAQ) card.

3.2.2 Temperature Measurement

A Temptrol PT100 TX 0-50 platinum resistance thermometer (range 0–50°) was used to measure the wind-tunnel air temperature. This instrument was calibrated against a JOFRA D55SE temperature bath and calibrator (uncertainty less that ±0.1°C, Calibration Certificate T06727). The calibration obtained was $T = -12.3129 + 15.3752V - 0.01988V^2$ where T is the temperature in °C and V is the measured voltage. Figures 3.1 and 3.2 summarise the calibration curve and associated error.

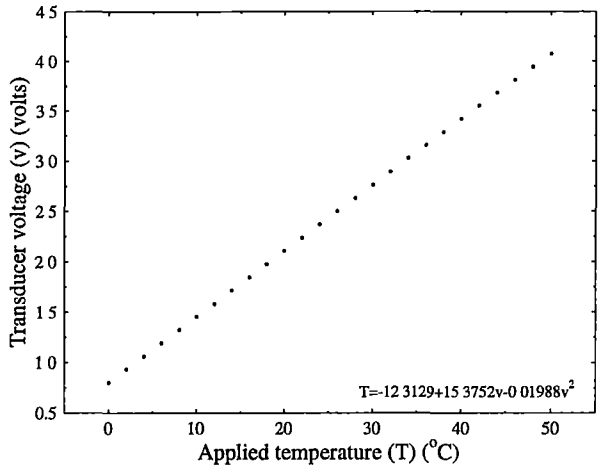

Figure 3.1: Temperature transducer (Temptrol PT100 TX 0-50) calibration curve.

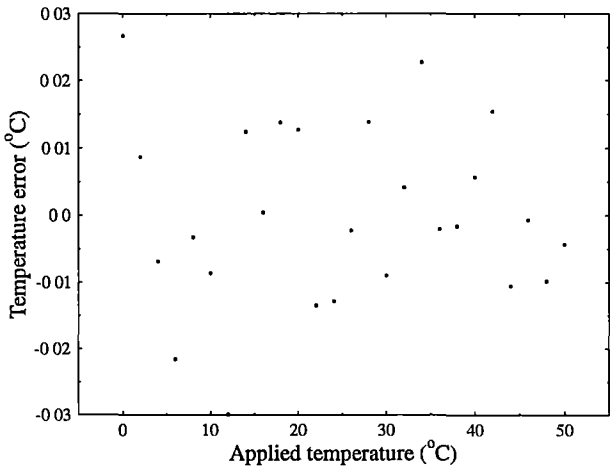

Figure 3.2: Error residual in Temptrol PT100 TX 0-50 calibration curve

3.2.3 Ambient Pressure Measurement

A Vaisala PA 11A digital barometer, interfaced to the data acquisition computer via a RS232 link, measured the ambient atmospheric pressure. The specified accuracy of this unit is ± 0.18 hPa.

3.2.4 Ambient Relative Humidity Measurement

A Vaisala HMI 33 temperature and humidity unit measured ambient relative humidity. The specified accuracy of this unit is $\pm 1\%$ of relative humidity.

3.2.5 Pressure Measurement

A 48J9 Scanivalve and an internally mounted Druck PDCR23D strain gauge type differential pressure transducer (range ± 1.0 psi) measured wind tunnel differential pressures. The pressure signal was externally amplified via a battery powered AD620 instrumentation amplifier with gain ≈ 10 to increase the pressure resolution, as only part of the pressure range was required. Pressures were typically acquired for 2000 samples at 1 kHz and five replicates taken. The pressure transducer was calibrated against a Betz projection micro-manometer (readability ± 0.01 mm water). To minimise errors due to thermal drift in the electronics, zero pressure differentials were measured as the first and last pressures of each scan (the first and last pressure ports of the scani-valve were directly connected to the reference pressure line). These zeros were subtracted from each reading which were then expressed as a pressure coefficient (referenced to tunnel inlet conditions), so that any drift in range would also be compensated for. As the zero error is automatically corrected for only the calibration curve slope (137.283 Pa/V) is required with the calibration curve and associated errors given in Figures 3.3 and 3.4 respectively. This slope was only used in determining velocity values to determine the test Reynolds number, intake flow rate and velocities for the hot-wire calibration.

3.3 Water Jet Model

The experimental testing was based around a scale model intake (see Figure 3.5 for full scale primary dimensions) mounted vertically (as a side wall panel) of a recirculating wind tunnel. A secondary flow circuit extracted air through the intake via a secondary pump which expelled to atmosphere. Make-up air was introduced by natural suction upstream to the low-speed return working section through a cover plate (of area 0.363 m^2) which was removed for this purpose.

3.3.1 Wind Tunnel Specifications

The wind tunnel used for this study has a working section of 0.61x0.61x1.22 m. Corner chamfering of the working section reduce the effect of corner vortices and reduces the working cross section to 0.34 m^2. Flow uniformity (within $\pm$ 0.5%) and low turbulence (less than 0.2% free stream turbulence) are achieved by a 6.2:1 contraction and upstream honeycomb with wire gauze screens.

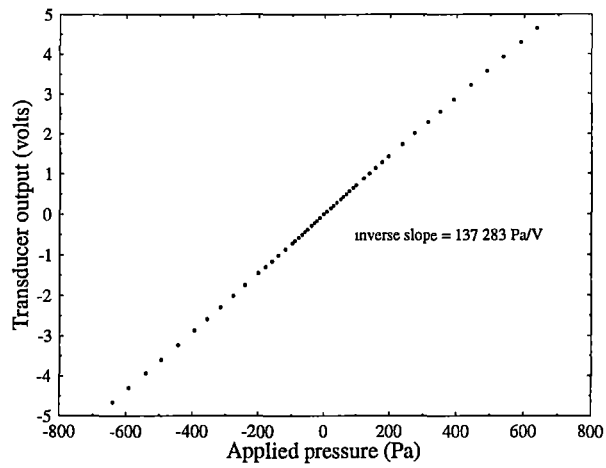

Figure 3.3: Pressure transducer (Druck PDCR23D) calibration curve.

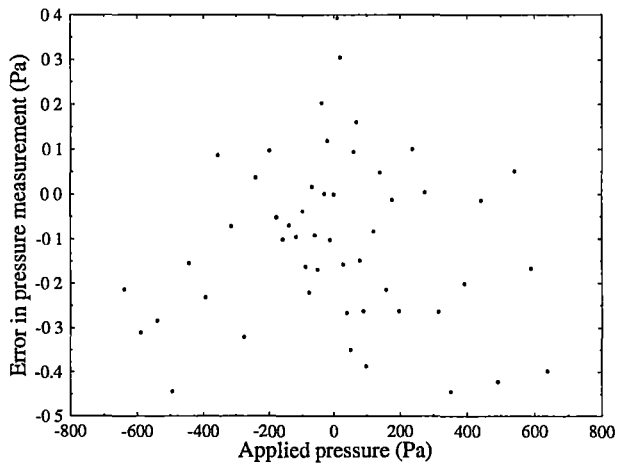

Figure 3.4: Error residual in Druck PDCR23D transducer calibration.

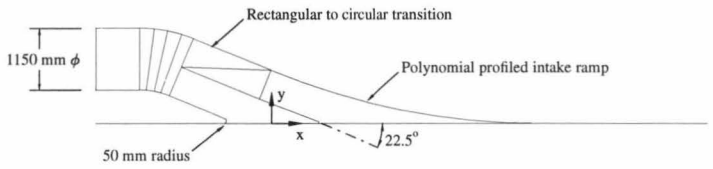

Figure 3.5: Centre-line cross-section of full-scale waterjet geometry showing principal dimensions and coordinate system used for the definition of the ramp profile (equation 3.1).

3.3.2 Model Specifications

The wind-tunnel model used herein is shown in Figure 3.6. Figure 3.5 shows the centre-line cross section for the full size waterjet. The model was hand constructed in acrylic with an intake diameter was 150 mm (or 1:7.67 scale) by Plastic Fabrications Pty Ltd.

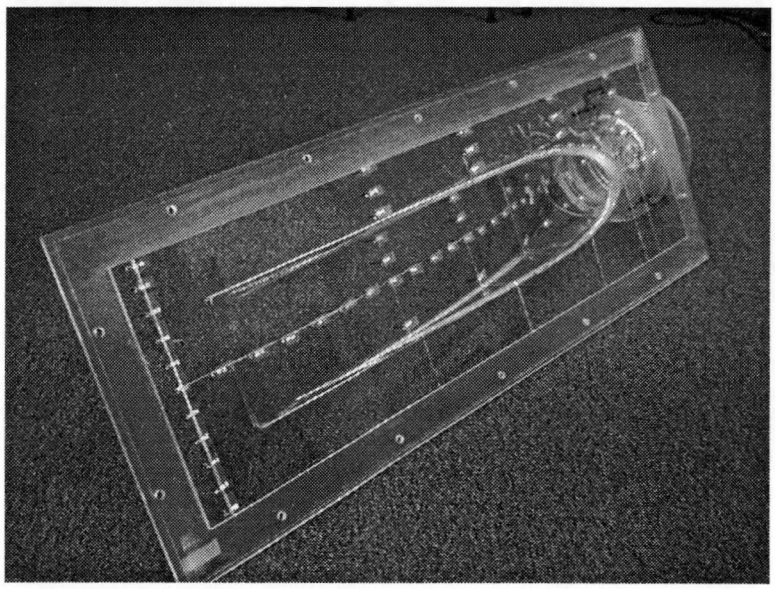

Figure 3.6: Waterjet model used in wind-tunnel testing

Typically the intake roof of a waterjet is a circular arc. However, this results in curvature discontinuities at both ends of the arc which produce pressure spikes (the benefits of continuous curvature for turbomachinery blades is discussed in Walraevens and Cumpsty [148]). This is detrimental to overall performance. The circular arc was replaced by a fifth order polynomial

$$y = ax^5 + bx^4 + cx^3 + dx^2 + ex + f \tag{3.1}$$

with prescribed values of

$$\begin{array}{ll} y = 0 & \text{at } x = 4.975 \\ y = 0.990 & \text{at } x = 0 \\ \frac{dy}{dx} = 0 & \text{at } x = 4.975 \\ \frac{dy}{dx} = -tan(22.5°) & \text{at } x = 0 \\ \frac{d^2y}{dx^2} = 0 & \text{at } x = 4.975 \\ \frac{d^2y}{dx^2} = 0 & \text{at } x = 0 \end{array} \tag{3.2}$$

The last two conditions enforce continuous curvature with the joining straight line segments. Note dimensions are in metres and represent the full size unit. Solution of Equations 3.1 and 3.2 requires

$$\begin{aligned} a &= 8.026178 * 10^{-5} \\ b &= -2.680307 * 10^{-3} \\ c &= 2.0047 * 10^{-2} \\ d &= 0 \\ e &= -0.4142135 \\ f &= 0.989566 \end{aligned}$$

Figure 3.7 shows the polynomial profile overlayed with the more traditional circular arc profile. The fuller shape of the polynomial curve results from the gradual increase in curvature, compared to the step change for the circular arc.

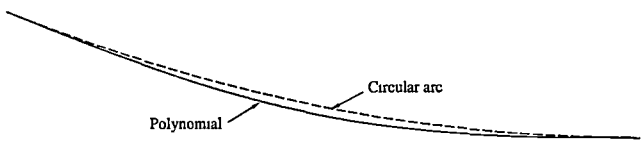

Figure 3.7: Comparison of intake ramp profiles showing the polynomial curve and the more common circular arc profile.

The model has 118 static pressure tappings distributed as shown in Figure 3.8, which also shows the location of the cross-sections used for hot-wire and 5 hole pressure probe traverses.

3.3.3 Wind Tunnel Blockage

Ideally the waterjet model should be tested in a wind tunnel large enough to approximate the operation in deep water, ie a semi-infinite medium. However, the wind tunnel used here has a working section area of 0.34 m^2 compared to the model intake area of 0.0177 m^2. Clearly this model removes fluid from the working section and produces an adverse pressure gradient on the wind tunnel walls which does not correctly represent the true operating conditions with an infinite unconfined stream. To overcome this, a plate to vary the working section area as a function of streamwise distance can be introduced into the tunnel to compensate for the flow removal from the tunnel. The

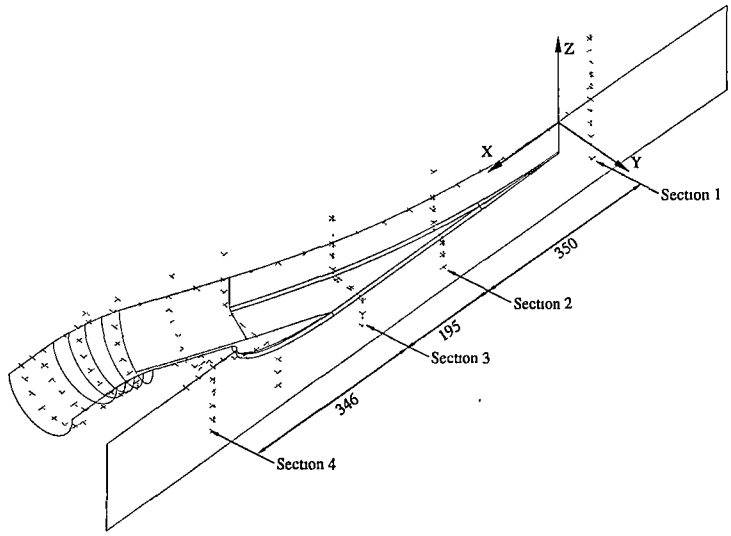

Figure 3.8: Location of pressure tappings and measurement cross-sections, half model shown for reference. All dimensions in millimetres.

natural growth in the wind tunnel boundary layer partly serves as this area varying plate.

The net flow acceleration due to the combined effects of wall boundary layer growth in the empty tunnel and intake flow extraction was measured experimentally via four static pressure tappings in the working section. These pressure tappings were located in pairs (top and bottom of the working section), one pair was 75 mm downstream of the start of the working section, the second pair was 75 mm upstream of the end of the working section. The working section inlet velocity was measured via the pressure differential across the tunnel contraction ($v_{\text{tunnel}} = 1.321\sqrt{\Delta p}$). All pressures were measured relative to atmospheric pressure and taken in triplicate.

Table 3.1 shows the dimensionless velocity at the four pressure tappings and the inferred blockage between the start and end of the working section. The blockage on the bottom of the tunnel is consistently larger than that for the top of the tunnel. Furthermore, the blockage is not a simple function of speed. These facts are possibly due to the non-uniform nature of the flow upstream of the contraction due to the upstream bend and natural convection of thermal boundary layer fluid. Overall the average blockage is 2.5%.

The "anti-blockage" created by the withdrawal of fluid from the waterjet model has a value of 2.60% at an inlet velocity ratio of 0.5. For IVR's around this value the natural growth in the wind tunnel boundary layer compensates for the flow removal by the waterjet. Therefore, the wind-tunnel flow is a fair approximation to a semi-infinite medium.

Table 3.1: Measured velocity blockage coefficients for the wind tunnel working section as a function of tunnel velocity, measured at the four static pressure tappings and the overall blockage, for an empty working section with solid walls.

Tunnel R_e (based on 610 mm section width)	Dimensionless velocities				
	Upstream Bottom	Upstream Top	Downstream Bottom	Downstream Top	Tunnel Blockage
$151*10^3$	1.003	0.988	1.025	1.017	1.025
$243*10^3$	1.004	1.001	1.030	1.017	1.021
$347*10^3$	1.001	0.997	1.030	1.016	1.024
$484*10^3$	1.003	1.001	1.033	1.021	1.025
$607*10^3$	1.003	1.001	1.035	1.022	1.027
$737*10^3$	1.003	0.996	1.033	1.019	1.026
$841*10^3$	1.005	0.997	1.034	1.020	1.026
$970*10^3$	1.005	0.999	1.035	1.022	1.027
$1102*10^3$	1.009	1.002	1.035	1.021	1.022

3.4 Experimental Techniques

3.4.1 Flow Visualisation

Flow visualisation was conducted using a fluorescent mini-tuft technique (e.g., Crowder [29]). The tuft material was a fluorescent dye impregnated spun polyester sewing thread of diameter 0.1 mm (manufactured by Birch). This material was chosen as it had good visibility under the lighting provided by four Sylvania 20 W black-lights (which produce light both in the ultra-violet and visible spectrum). The fluorescent dye in the cotton absorbs the u-v light and re-radiates visible light, while the visible light is beneficial in showing the model geometry.

Two products were investigated for attaching the tufts to the model surface, Loctite 401 and CIBA Araldite gel. The Loctite product was easier to use because of its superior wetting of the polyester thread but was difficult to remove cleanly from the model when no longer required. The Araldite gel was chosen because tufts could be removed from the model surface when finished with without leaving a residue. The removal was achieved by physically pulling the tuft off and then removing any remaining adhesive with isopropyl alcohol wipes.

The glued portion of the tuft may be at a different orientation to the free length of the tuft (because the former is not free to rotate) and this may confuse interpretation of the visualisation results. Following the suggestion in Yang [153], a small amount of vegetable black was added to the Araldite making it opaque, thereby obscuring the length of tuft attached to the surface. This did not affect the adhesive properties of the gel, although it did have two effects on the attachment procedure. The gel was easier to see with the vegetable black added, simplifying the attachment. However, the addition of a dry powder to the Araldite mix also made the gel become "tacky" more quickly, so small batches of the gel were mixed more frequently.

Yang [153, Chapter 9, Table 1] relates the minimum tuft length to the tuft diam-

eter and following these guidelines a tuft length of 25 mm was used. To minimise entanglement the tufts were placed on a grid at 30 mm spacing in both directions.

A Canon EOS 1000FN 35 mm SLR camera with a 35-80 mm zoom lens recorded the flow visualisation results. ASA 100 film was used with an aperture setting of f4.0 and an exposure of 1 second. This relatively long exposure results in blurring of tuft images in separation regions while images of tufts in areas of attached flow are sharp.

The original photographs were digitally scanned and enhanced for reproduction (see Section 5.1.2 Figures 5.2 and 7.1).

3.4.2 5 Hole Probe Calibration

A United Sensors DA125 probe (Figure 3.9) was used to measure flow velocity and three dimensional direction. The five hole probe was calibrated in a free jet (nozzle diameter 80 mm), with the probe rotated in yaw and pitch relative to the fixed jet of variable speed. The calibration was carried out over a range of yaw and pitch of $\pm 30°$ in $5°$ increments and four different speeds (7–27 m/s). Five replicate readings were taken for each combination of yaw, pitch and speed. Jet speed and yaw were automatically set via the data acquisition computer while pitch was manually set.

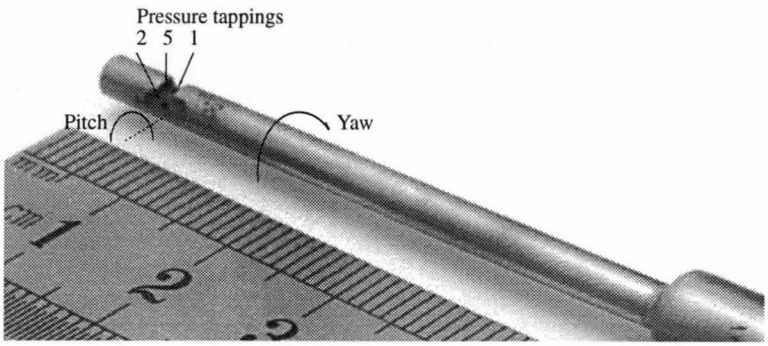

Figure 3.9: United Sensors DA125 5 hole probe used to determine flow velocity and direction. Pressure tapping 3 is mirror of tapping 2 about the probe axis while tapping 4 is mirror of tapping 5 about the line joining tappings 2-1-3.

3.4.2.1 Determination of Angle Origins

The angle origins are not directly known but calculated below.

For yaw (α) the angle origin was taken to be when the yaw coefficient ($C_y = \frac{q_1 - q_3}{q_1 - q_2}$) was unity, fitted for the entire range of pitch. However, the denominator is small for values of α around $25°$ leading to very large values of the yaw coefficient. To overcome this problem the yaw coefficient was fitted in two halves (one for $\alpha < 10°$ and the other for $\alpha > -15°$ the latter using the reciprocal of the yaw coefficient).

A cubic was fitted to the resulting data using a least squares technique for raw values on yaw less than $10°$ This polynomial was

$$\frac{q_1 - q_3}{q_1 - q_2} = 1.13861 - 8.0885044 * 10^{-2}\alpha + 3.1428 * 10^{-3}\alpha^2 + 4.77627 * 10^{-5}\alpha^3 \quad (3.3)$$

where α is measured in degrees and this coefficient has a value of unity at $\alpha = -1.66°$.

For raw yaw values greater than $-15°$ the reciprocal of the yaw coefficient was used giving

$$\frac{q_1 - q_2}{q_1 - q_3} = 0.897506 + 6.779 * 10^{-2}\alpha + 2.06654 * 10^{-3}\alpha^2 - 3.34014 * 10^{-5}\alpha^3 \quad (3.4)$$

and this cubic has a value on unity at $\alpha = -1.45°$.

The resulting average value for yaw origin is therefore $-1.55°$.

For pitch (β) the angle origin was taken to be when the function $\frac{q_1 - q_5}{q_1 - q_4}$ was unity. Only data at a yaw within 10° of zero was included and a rational function fitted to the resulting data using a least squares technique for raw pitch values greater than $-30°$. This rational function was

$$\frac{q_1 - q_5}{q_1 - q_4} = \frac{13.3071 - 0.290352 * \beta}{70.6427 + 4.47587 * \beta + 7.70173 * 10^{-2}\beta^2} \quad (3.5)$$

where β is measured in degrees and this function has a value of unity at $\beta = -16.35°$.

For raw pitch values less than $-5°$ the reciprocal of the pitch coefficient was used giving

$$\frac{q_1 - q_4}{q_1 - q_5} = \frac{149.675 + 1.85174 * \beta}{62.3442 + 6.426 * \beta + 0.649767\beta^2} \quad (3.6)$$

with unity at $\beta = -15.64°$.

The resulting average value of pitch was therefore $-16.00°$.

3.4.2.2 Curve Fitting

When calculating any of the pressure coefficients, all replicates were averaged and any outlier points excluded from this averaging. Points were deemed to be outliers if the difference between the point value and the replicates average (including the potential outlier) was more than 1.71 standard deviations (of the entire replicate including the potential outlier). Davies and Goldsmith [31] suggests this method for selecting outliers and the factor of 1.71 (which is a function of the sample size (see Grubbs [57] for details), in this case 5) is for a 5% significance level that the point is an outlier.

The resulting yaw and pitch coefficients were fitted as functions of pitch, yaw and jet pitot pressure. This data fit was via a least squares method in four dimensional space. The basis of this method is explained below based on the single parameter ($F(x)$) description given in Conte and de Boor [26].

The N data points $f(x, y, z)$ are to be represented by a function $F(x, y, z)$ where $F(x, y, z)$ can be defined as

$$F(x, y, z) = c_1\phi_1(x, y, z) + c_2\phi_2(x, y, z) + \cdots + c_j\phi_j(x, y, z) \quad (3.7)$$

for some series of predefined functions ϕ.

From which a variation in data points for this sum of functions can be defined as

$$E(c_1, c_2, \ldots, c_j) = \sum_{i=1}^{N} (f_i - F_i(c_1, c_2, \ldots, c_j)). \tag{3.8}$$

To minimise this variation in a least squares sense we want to select the c_k's so that E is a minimum. This minimum occurs when $\frac{\partial E}{\partial c_k} = 0$. These j partial derivatives result in j equations in the j unknown c_k's, where the k^{th} equation has the form

$$\sum_{i=1}^{N} c_1\phi_1\phi_k + \sum_{i=1}^{N} c_2\phi_2\phi_k + \cdots + \sum_{i=1}^{N} c_j\phi_j\phi_k = \sum_{i=1}^{N} f_i\phi_k. \tag{3.9}$$

The resultant series of simultaneous equations is well behaved in general and easily solved.

The polynomial terms were selected for inclusion in the least squares fit via a forward selection procedure outlined in Davies and Goldsmith [31] (this reference discusses this technique for including different variables, but the technique is equally valid for different polynomial terms) where terms are added to the model one by one. The term that reduces the average absolute error by the largest amount is included until no further improvement is possible. In this case the terms are polynomial in the three variables α, β and p_1 up to fifth order including cross terms.

3.4.2.3 Yaw Calibration

It was necessary to consider two half ranges for the yaw calibration as for the yaw origin determination. The yaw coefficients used were $C_y = \frac{q_2 - q_1}{q_3 - q_1}$ for $\alpha > -5°$ and $C_y = \frac{q_3 - q_1}{q_2 - q_1}$ for $\alpha < 0°$. The actual curves used are

$$\begin{aligned} C_y = &- 7.9683483 * 10^{-2}\alpha + 1.016535 + 2.3649950 * 10^{-3}\alpha^2 - 2.5246999 * 10^{-7}\alpha^4 \\ &+ 2.0548892 * 10^{-5}\alpha\beta^2 - 1.3071087 * 10^{-6}\alpha^2\beta^2 + 2.4199498 * 10^{-8}\alpha^3\beta^2 \\ &- 1.5416271 * 10^{-8}\alpha^4\beta + 7.6383083 * 10^{-7}\alpha^3\beta - 2.6113408 * 10^{-5}\alpha^3 \\ &+ 3.1362182 * 10^{-9}\alpha^2\beta^3 - 1.0493847 * 10^{-5}\alpha^2\beta + 4.2725037 * 10^{-10}\alpha\beta^4 \\ &- 7.1861066 * 10^{-8}\alpha\beta^3 - 5.0995845 * 10^{-7}\beta^3 - 3.4739467 * 10^{-5}\beta^2 \\ &+ 9.5933495 * 10^{-4}\beta + 3.4718123 * 10^{-10}\beta^5 + 3.1142830 * 10^{-10}\alpha^4 * q_1 \\ &- 9.1198959 * 10^{-9}\alpha^3 q_1 + 2.3314759 * 10^{-9}\beta^4 + 3.4667341 * 10^{-12}\beta^4 q_1 \end{aligned} \tag{3.10}$$

for $C_y = \frac{q_2 - q_1}{q_3 - q_1}$

and

$$\begin{aligned} C_y =& 7.4846081 * 10^{-2}\alpha + 0.9821897 + 3.5306364 * 10^{-9}\alpha^5 + 2.4790543 * 10^{-3}\alpha^2 \\ &+ 2.3273551 * 10^{-5}\beta^2 - 2.8547674 * 10^{-4}\alpha\beta + 5.4315833 * 10^{-6}\alpha q_1 \\ &- 3.4010378 * 10^{-7}\beta q_1 + 3.4363184 * 10^{-5}\alpha^3 - 2.1717611 * 10^{-8}\alpha^4\beta \\ &+ 5.6713549 * 10^{-8}\alpha^2 q_1 - 1.2709163 * 10^{-6}\alpha^3\beta + 3.9788288 * 10^{-9}\alpha^2\beta^3 \\ &+ 1.2221356 * 10^{-7}\alpha\beta^3 - 3.0863905 * 10^{-8}\alpha^3\beta^2 - 1.5294755 * 10^{-6}\alpha^2\beta^2 \\ &- 1.9926450 * 10^{-5}\alpha\beta^2 + 5.4003557 * 10^{-10}\beta^5 - 9.2504185 * 10^{-4}\beta \\ &- 2.6686701 * 10^{-5}\alpha^2\beta - 6.0591856 * 10^{-9}\beta^4 + 2.3238117 * 10^{-7}\beta^3 \\ &+ 6.1493269 * 10^{-11}\alpha^4 q_1 + 2.2462822 * 10^{-5} q_1 - 1.2338461 * 10^{-9}\beta^3 q_1 \end{aligned} \tag{3.11}$$

for $C_y = \frac{q_3 - q_1}{q_2 - q_1}$ overall giving α to within a maximum error of 0.91°. Figures 3.10 and 3.11 summarise the yaw calibration.

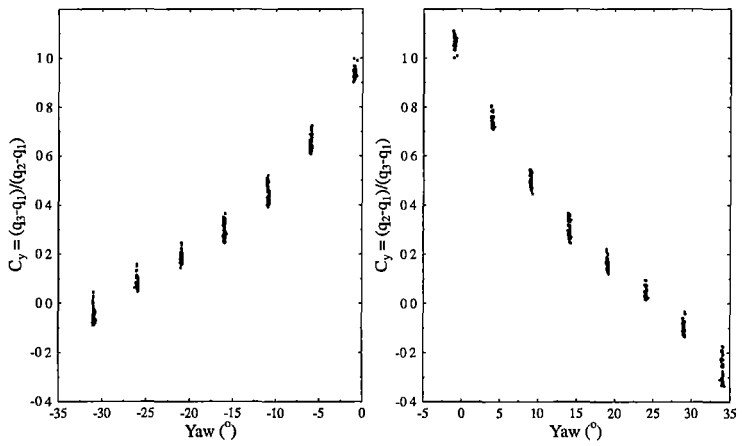

Figure 3.10: Measured 5 hole pressure probe yaw coefficients as a function of yaw angle, each band shows readings for the range of pitch and total pressures tested.

In retrospect the calibration should have included a probe based Reynolds number rather that the dynamic pressure q_1, as this would account for changes in fluid properties. However, the above calibration is only a relatively weak function in q_1 so this is not a major concern.

Yaw (α) is calculated iteratively from the above polynomials, but it is necessary to know β in advance. However, since C_y is a relatively weak function in β this can be overcome in an iterative manner, calculating α assuming $\beta = 0$, then using this value of α to find β and continuing this procedure until α has stabilised. As explained below it is not possible to accurately find β over the entire yaw range. However, an initial

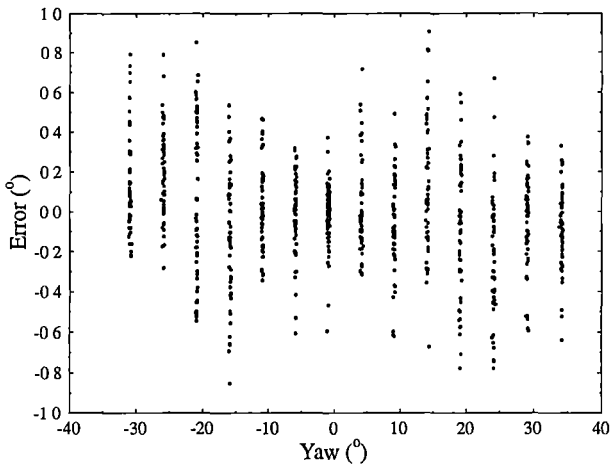

Figure 3.11: Error distribution for C_y as a function of yaw for Equations 3.10 and 3.11

estimate (within $\pm 3.5°$) of pitch for all yaw can be found using

$$\begin{aligned} C_p = & -3.2750525 * 10^{-2}\beta + 1.2637961 * 10^{-8}\alpha^2\beta^3 - 6.7970227 * 10^{-6}\alpha^3 \\ & - 1.2234263 * 10^{-7}\alpha^3\beta - 1.9551097 * 10^{-8}\alpha^4\beta - 1.7757749 * 10^{-7}\alpha^4 \\ & + 3.6734447 * 10^{-2} - 1.2298497 * 10^{-4}\alpha\beta - 2.4348416 * 10^{-3}\alpha \\ & + 2.0247637 * 10^{-6}\beta^2 - 2.2212816 * 10^{-9}\beta^5 - 7.9316742 * 10^{-6}\alpha^2\beta \\ & + 5.6594972 * 10^{-6}\beta q_1 + 3.9171839 * 10^{-9}\alpha\beta^4 - 3.2775836 * 10^{-6}\alpha\beta^2 \\ & + 2.6675312 * 10^{-7}\beta^2 q_1 - 7.8580080 * 10^{-5}q_1 - 9.2642512 * 10^{-11}\beta^4 q_1 \\ & - 1.4472568 * 10 * -10\alpha^4 q_1 - 8.9374508 * 10^{-9}\alpha^3 q_1 + 3.6756117 * 10^{-6}\alpha q_1 \\ & + 1.3916611 * 10^{-5}\alpha^2 \end{aligned} \tag{3.12}$$

for $C_p = \frac{q_4 - q_5}{q_1 - (q_2+q_3+q_4+q_5)/4}$.

3.4.2.4 Pitch Calibration

Due to the construction of the probe, the pitch pressures show a large degree of sensitivity to pitch, yaw and speed. Therefore, it was not possible to obtain an accurate fit for C_p over the entire range of all variables. Several methods of fitting were tried including least squares fitting, neural networks and genetic algorithms. However, none produced a fit that gave the pitch to better than $\pm 3°$. Based on this result it was decided to use the probe in a nominally nulled yaw mode. B Therefore, the probe was used in an iterative manner, requiring a minimum of two readings. The first reading will give an estimate of yaw based on the estimated pitch. The probe will then be rotated in yaw by this amount, and a second reading used to find both pitch and speed. This new pitch reading will be used to recalculate the yaw based on the original pressure readings and the probe further rotated in yaw if required.

Using quasi-nulled yaw data and the forward selection method described above to fit for $C_p = \frac{q_4 - q_5}{q_1}$ by a polynomial of up to fifth order terms (but only linear in dynamic pressure, ie. a polynomial up to terms like $\beta^i q_1^j$ where $i + j <= 5$ and $j <= 1$) gave the following polynomial.

$$\begin{aligned} C_p =& 1.9419385 * 10^{-2} - 1.7561866 * 10^{-2}\beta - 1.3134499 * 10^{-5}q_1 + 8.8015986 * 10^{-5}\beta^2 \\ &+ 5.3722888 * 10^{-6}\beta q_1 - 1.5329556 * 10^{-6}\beta^3 + 4.1516540 * 10^{-8}\beta^2 q_1 \\ &- 4.0243577 * 10^{-8}\beta^4 - 4.0009303 * 10^{-9}\beta^3 q_1 + 8.2417206 * 10^{-10}\beta^5 \\ &- 1.8950438 * 10^{-11}\beta^4 q_1 \end{aligned} \tag{3.13}$$

which gives β within 0.9° and Figures 3.12 and 3.13 summarise the pitch calibration.

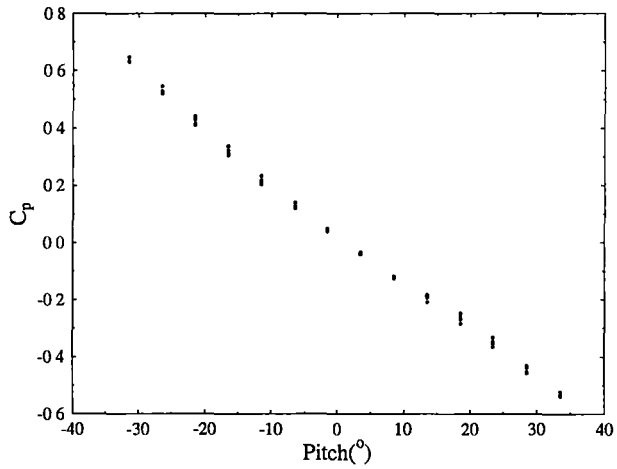

Figure 3.12: C_p distribution as a function of pitch, each band shows data over the range of total pressure tested.

3.4.2.5 Dynamic Pressure

q_1 is an accurate representation (to better than 0.5%) of the dynamic pressure when the probe is operated in a nulled yaw mode.

3.4.3 Ingestion Streamtube Determination

Ingestion streamtube cross sections are required for momentum balances and the calculation of wake fractions. Griffith-Jones [56] experimentally measured ingestion stream tubes using smoke photography, however the spatial resolution was limited and the probe size (9 mm diameter) was large compared to the inlet (215 mm diameter).

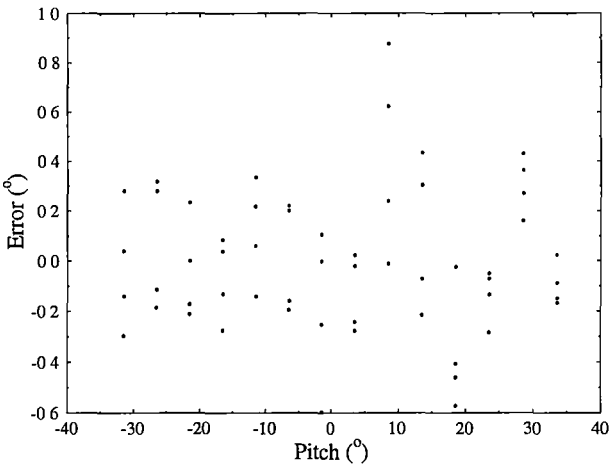

Figure 3.13: Error distribution for C_p as a function of pitch from Equation 3.13

Roberts and Walker [111] describes the tracer gas technique used herein, similar to work conducted on turbine cascades by Moore and Smith [89] and on axial flow compressors by Gallimore and Cumpsty [47] and Wisler et al. [152]. The latter two studies used ethylene as the tracer gas (molecular mass 28.05 kg/kmol) because buoyancy effects are virtually eliminated due to the molecular mass being only 3% lower than air. Flame ionisation detection was used to measure the ethylene gas concentrations.

Wagner et al. [146] used carbon dioxide (molecular mass 44.01 kg/kmol) as the tracer gas for studies on axial compressor rotors. Detection was via non-dispersive infrared (NDIR) detectors. However, the large difference in molecular mass may lead to unwanted buoyancy effects.

Carbon monoxide was used in this study as it had the desirable features of both techniques. First, buoyancy effects are not significant (molecular mass of CO is 28.01 kg/kmol) and second, the inexpensive and simple NDIR detection method can be applied. NDIR detection relies upon the infrared absorption spectrum characteristics of the gas under observation. A general hydrocarbon NDIR (as found in automotive exhaust gas analysers) uses the characteristic absorption peak of low molar mass alkanes (transmission of 5% at $\approx$ 3.4 μm, Sadtler Research Laboratories [117]) which is suppressed in ethylenes (where transmission at that wavelength is about 90% Sadtler Research Laboratories [117]). Consequently ethylene is not suitable for use with a general hydrocarbon NDIR.

A Horiba MEXA-321E automotive gas analyser was used to determine tracer gas concentrations, this unit and other automotive exhaust gas analysers have a general hydrocarbon NDIR and a carbon monoxide NDIR. As ethylene will not be efficiently detected by the general hydrocarbon NDIR, carbon monoxide is the obvious choice for the tracer gas.

Carbon monoxide was injected via a 1.2 mm internal diameter backwards facing pitot tube in a plane 270 mm upstream of the start of the intake ramp. The pitot

tube was traversed in this plane to provide 9 traverses in the top half-plane with 5mm spacing inside each traverse. A repeatable amount of carbon monoxide was injected approximately isokineticly by releasing a regulator full of carbon monoxide, while the flow rate was measured using a rotameter.

Gas sampling was done using a sampling probe placed on the duct centre-line 28 diameters downstream of the intake. This allows for complete mixing of the tracer gas, so that a one point sample should be accurate. The tracer gas concentration is in the order of 10 ppm while full scale deflection for the Horiba MEXA-321-E was 2%. Therefore, the signal was amplified by a battery powered AD620 instrumentation amplifier before being acquired on the computer. The acquired signal typically has a very low signal to noise ratio (typically of order 1) and the noise was primarily high frequency (Figure 3.14). The high frequency noise was remove by heavy low-pass filtering (a fifth order Butterworth filter with cut-off frequency of 0.35 Hz was used). Pulse characteristics of base-line level, pulse delay and duration were then determined (Figure 3.15). The signal was corrected for base-line level and integrated, with a pseudo carbon monoxide level given by the difference in integrated signal between the start and end of the pulse (as given by pulse delay and duration), see Figure 3.16.

A sigmoidal function of the form

$$\text{Pseudo CO Concentration} = a\left(1 - \frac{1}{1 + e^{-b(x-c)}}\right) \tag{3.14}$$

was fitted to the data for any traverse (Figure 3.17) where x is the normal distance of the injection point from the wind tunnel wall; a and b provide scaling while c indicates the offset from the origin of the 50% concentration point. In the absence of diffusion and turbulent mixing the measured concentration traverse would be a step function, with the bounding ingestion streamtube clearly determined. Diffusing and turbulent mixing "smear" out this step function into a sigmoidal function with the bounding ingestion streamtube being given by the 50% concentration point. Thus c is the position of the bounding ingestion streamtube for that traverse.

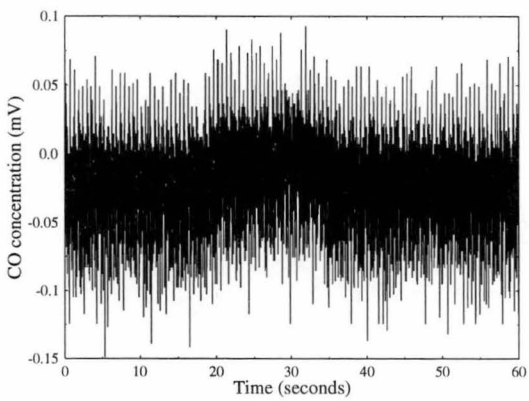

Figure 3.14: Typical raw carbon monoxide concentration in outlet duct.

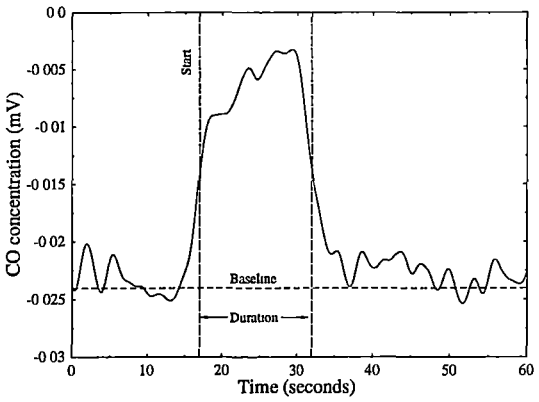

Figure 3.15: Typical low-pass filtered carbon monoxide concentration in outlet duct.

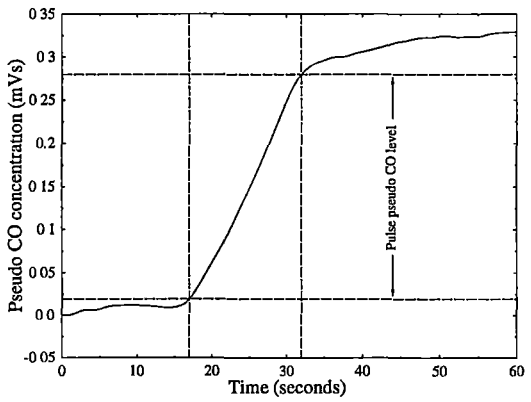

Figure 3.16: Typical integrated carbon monoxide concentration in outlet duct.

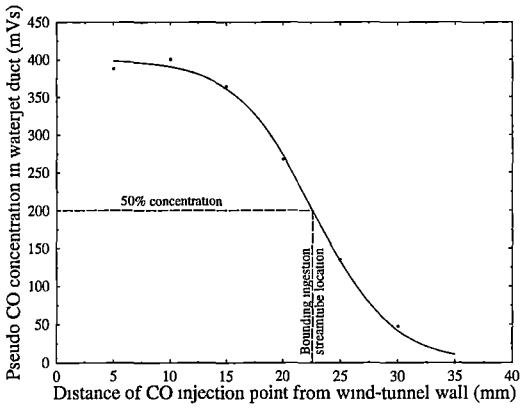

Figure 3.17: Typical carbon monoxide concentration traverses.

3.4.4 Hot-wire Anemometry

Hot wire work was conducted using a modified DISA 55M constant temperature anemometer and a DANTEC 55P15 miniature wire boundary layer probe. The modification involved separation of the signal and power electrical grounds reducing the zero-flow AC noise output due to ground loops. The output from the anemometer was acquired on the data acquisition computer for 1 second at a sampling frequency of 60kHz, and analysed for DC and AC voltages.

The hot-wire was calibrated against a pitot-static tube using the calibration procedure of Walker [147]. This calibration is a modification of Collis and Williams [25]'s calibration procedure for the heat loss from an infinitely long heated cylinder in cross flow to account for finite length effects. A non-dimensional data fit of the form

$$N_u \left(1 + \frac{a_T}{2}\right)^{-0.17} = A + B * R_e^{0.45} + C * R_e^{0.90} \tag{3.15}$$

was solved in a least squares sense for the unknown constants A, B and C. This type of data fit eliminates the effects of thermal drift in the wind-tunnel and atmospheric condition changes over long data collection runs (this method of calibration in non-dimensional terms appears to better compensate for thermal drift than the correction to anemometer output voltage method used by Griffith-Jones [56]) . A typical calibration is shown in Figure 3.18. Once the probe has been calibrated, it was periodically re-calibrated with no electrical contacts being broken (as this may change the contact resistance thus altering the calibration).

Electrically conducting tracks were painted onto the model surface (using a Circuit Works$_{TM}$ conductive pen to lay silver tracks) and used to find the probe displacement origin. The probe was moved toward the wall until there was electrical contact between the track and the probe. The repeatability of this technique was better that 0.05 mm. Care should be taken to ensure that the anemometer is not in operation when the probe is thus shorted to the model surface.

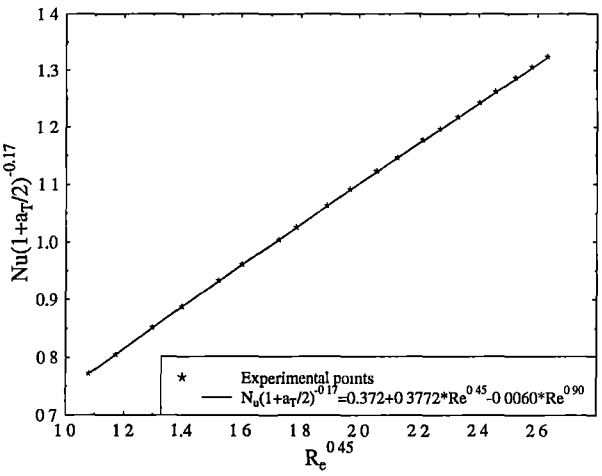

Figure 3.18: Typical hot-wire calibration curve.

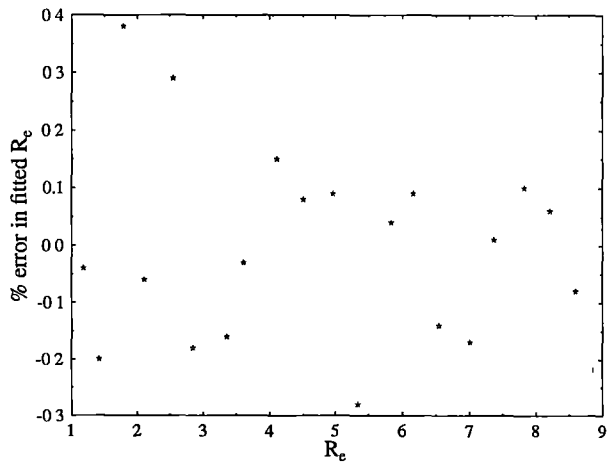

Figure 3.19: Typical hot-wire calibration curve residual.

3.4.5 Hot-wire Mounting

Vibrational problems were noticed when using the hot-wire probe with the traversing rig (based on a Mitutoyo 192-106 0.01–300 mm height gauge). Investigation of the vibrations using an accelerometer (attached to the Mitutoyo mounting block wound fully out) identified two low vibration speed ranges on the wind-tunnel, one near 400 rpm and the other near 550 rpm (Figure 3.20). However, at the 550 rpm speed the probe suffered severe vibrations when the traversing rig was wound in around 100 mm. This vibration was at a frequency of 29.4Hz. The natural frequency (ω_n) of the probe was calculated using Rayleigh's formula ([22])

$$\omega_n^2 = \frac{\int_0^l EI \left(d^2Y/dx^2\right)^2 dx}{\int_o^l \mu Y^2 dx} \tag{3.16}$$

where EI is the bending stiffness, Y is the deflection (calculated for a uniform load in this case), x is the axial position (to a maximum length l) and μ is the mass per unit length. The calculated natural frequency for the stepped cantilever probe is around 58 Hz.

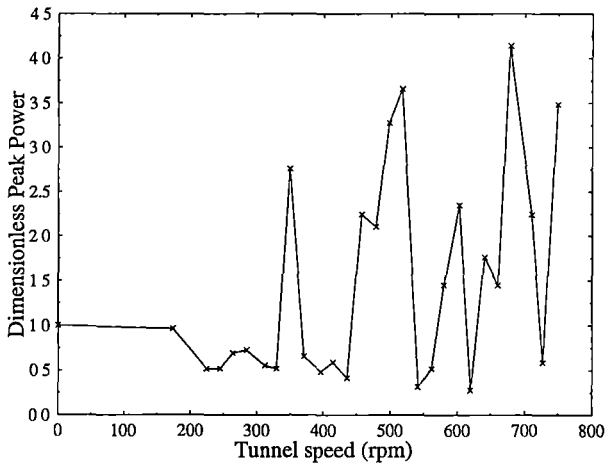

Figure 3.20: Wind tunnel vibrational response measured at mounting block of fully wound out Mitutoyo traversing rig. Spectral peak power was non-dimensionised with respect to spectral peak power at zero speed. This finite amplitude at zero speed is due to vibration of floor slab induced by electrical motor-generator set used in the Ward-Leonard speed control for the tunnel drive motor.

The Mitutoyo traversing rig has two natural frequencies (measured via a Brüel & Kjær accelerometer and ringing the system with a sharp blow) of 22.9 Hz and 30.8 Hz. The former is dominant when the rig is fully out and the latter dominant when the rig is wound in between 125 and 200 mm (Table 3.2). It appears that the large amplitude vibrations noted at 550 rpm with the rig wound in is due to coupling between the probe

Table 3.2: Mitutoyo traversing rig natural frequencies (measured via ringing).

Position (mm)	Natural frequency (Hz)
0 (fully out)	22.9
100	25.5
125	30.9
150	30.9
175	30.7
200	30.8

(with energy being supplied from the flow-excitation) and the traversing rig, with the excitation from the probe being at about half the natural frequency of the traversing rig.

The vibrational problems were overcome by re-tuning the probe support by changing the relative lengths of the two halves of the stepped cantilever.

3.4.6 Skin Friction

Skin friction was measured using the "razor blade" technique as described in Winter [151] and Pai and Whitelaw [97]. The basis of this technique is that a Stanton-type tube can be easily produced by attaching a razor-blade over a static pressure tapping Winter [151]. The pressure differential (Δp) introduced by the presence of the blade can be directly related to the skin friction.

Typically the blade is attached by either glue or held magnetically. However, the thickness of the model acrylic virtually eliminated the attractive force from available magnets while frequent movement of the blades made gluing impractical. Therefore, for the current study the blades (NT brand cutter, D100 blades, 0.381 mm thick and sharpened on both sides so that h the height of the leading edge from the surface is 0.191 mm) were taped to the surface (using 3M Scotch transparent tape 0.05 mm thick). The presence of the tape modifies the flow around the blade, influencing the pressure, however Pai and Whitelaw [97] give a calibration for taped blades:

$$y^* = -0.512 + 0.741x^* \tag{3.17}$$

where $x^* = \log_{10}\left(\frac{\Delta p h^2 \rho}{\mu^2}\right)$ and $y^* = \log_{10}\left(\frac{\tau_w h^2 \rho}{\mu^2}\right)$ from which it is easily shown that

$$C_f = \frac{\mu^2}{2\rho^2 v^2 h^2 10^{0.512}} \left(\frac{h^2\rho}{\mu^2}\right)^{0.741} \Delta p^{0.741} \tag{3.18}$$

When attaching the blades over the pressure tapping care should be taken to ensure that the blade leading edge completely covers the pressure tapping, otherwise erroneously low skin frictions values will result. Pai and Whitelaw [97, Figure 5] give results for pressure differential (Δp) against blade leading edge position ($\Delta x/D$) (see Figure 3.21) showing that Δx should never be positive.

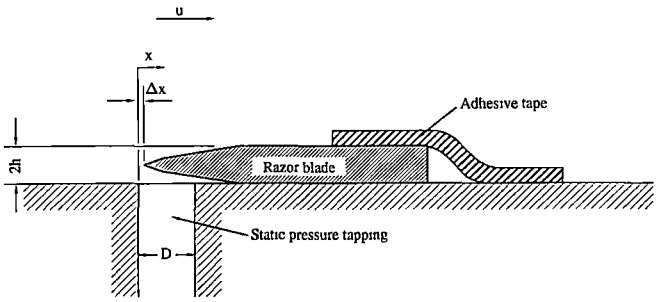

Figure 3.21: Razor-blade technique setup and nomenclature from Pai and Whitelaw [97].

To account for three-dimensional effects the razor blades were taped to the surface at 5 different orientations ($0°, \pm 15°$ and $\pm 30°$). Using the fact that the pressure varies approximately as $\cos^2$ with angle for angles up to 30° (Winter [151]), Equation 3.18 shows that the skin friction coefficient should vary as $\cos^{1.482}$ of the inclination of the blade from the local skin friction angle (angle of the limiting streamline referenced to the free stream direction). A least squares fit of this form was applied to the data to calculate the angle of the skin friction vector and its magnitude in this direction.

It was easy to obtain a consistent and repeatable angle zero of the skin friction vector for the pressure tappings on the hull and ramp sections. For the other pressure tappings (on the circular sections of the model) there was no consistency or repeatability in the angle zeros. Therefore, only the magnitude of the skin friction from the least squares fit for these latter section of the model are presented.

For the circular sections of the model it was necessary to make curved razor blades that fitted snugly to the model surface. This was done by heating the blades up to red hot and allowing them to air cool, making the blades more malleable. The blades were then bent around a 38 mm diameter template (the smaller diameter allows for "spring back") at inclinations of $0°, \pm 15°$ and $\pm 30°$ which produced blades of approximately the correct curvature.

Skin friction values were also inferred from hot-wire anemometry measurements using a Clauser plot method very similar to that of Ozarapoglu (Winter [151]). The relation

$$u^+ = \frac{ln(y^+)}{\kappa} + B \tag{3.19}$$

for

$$35 \leq y^+ \leq 350 \tag{3.20}$$

can be rewritten as

$$u\sqrt{\frac{\rho}{\tau_w}} = \frac{\ln\left(\frac{(y+y_0)\sqrt{\tau_w \rho}}{\mu}\right)}{\kappa} + B \tag{3.21}$$

where y_0 is a potential error in the y measurement origin and B is an empirical constant of 5.0. This equation can be solved in a least squares sense with the data points included in the fitting in an iterative manner to satisfy the constraints of Equation 3.20.

3.5 Boundary Layer Thickening

The natural boundary layer in the wind-tunnel working section is too thin by approximately a factor of five for correct kinematic similitude at testing scale. Therefore it was necessary to artificially thicken the wind-tunnel boundary layer for experimental testing. Note that one entire series of testing was performed using the naturally thin boundary layer for comparison purposes.

Several methods of artificial boundary layer thickening were trialled in a small recirculating wind tunnel, with the results summarised below. (Johnson [71] also contains information on boundary layer thickening for this application.) Note that during testing it was believed that a distance of approximately 750 mm upstream of the intake was available for the "normalisation" of the artificial thickened boundary layer. However, due to a design change in the model at a late stage this distance was reduced to 300 mm. This reduction in length will result in a more "distorted" inflow velocity profile but it is believed that the thickening mechanism that produced the best results at 750 mm would also produce the best results with the shortened length.

Only laterally distributed means of introducing the momentum deficit were considered. Isolated elements produce lateral non-uniformities which persist downstream (Cook [27])). Therefore, isolated elements (such as spires) which have been used in atmospheric wind tunnel work, were not investigated.

3.5.0.1 Thickening Requirements

Calculation of an approximate hull boundary layer thickness for a typical installation is based on the approximation of the hull upstream of the intake as a 65 metre long flat plate.

For a turbulent boundary layer we have (from White [149])

$$\frac{d\theta}{dx} = \frac{C_f}{2}. \tag{3.22}$$

This equation is used in conjunction with the Nash-Macdonald skin friction law (Nash and Macdonald [94])

$$\left(\frac{2}{C_f}\right)^{1/2} = 2.4711 \ln(Re_\theta) + 1.5G + \frac{1724}{G^2 + 200} - 12.12 \quad . \tag{3.23}$$

where $G = 6.1\sqrt{1.81} - 1.7 = 6.507$ when $\frac{dU}{dx} = 0$. Numerical integration of Equations 3.22 and 3.23 from the origin of the turbulent boundary layer gives a full scale boundary layer momentum thickness of 50.9 mm or a model scale thickness of 6.64 mm. The origin of the turbulent boundary layer was calculated to be 70 mm from the start of the plate (assuming instantaneous transition from laminar to turbulent flow at Re_x=1*10^6) at which point the momentum thickness is 0.05 mm.

3.5.0.2 Boundary Layer Fence

The drag results of Good and Joubert [53] as presented in Ranga Raju et al. [108] were used to determine the 16 mm height for a rectangular fence to provide the required momentum deficit to increase the boundary layer thickness by the required amount.

While the correct momentum thickness was obtained, the velocity distribution (Figure 3.22) indicates that a more distributed mechanism for introducing the momentum deficit was required. Bradshaw and Wong [18] studied re-attaching boundary layer flows and found that the size of the separated flow region (upstream of re-attachment) is a key factor in the boundary layer relaxation after re-attachment. Bradshaw and Wong [18] also discussed turbulence near a re-attachment. They concluded that the large turbulent eddies are torn in two at re-attachment, and that the downstream relaxation to an ordinary boundary layer is very slow. These findings suggested that a more distributed mechanism for introducing the momentum deficit was required.

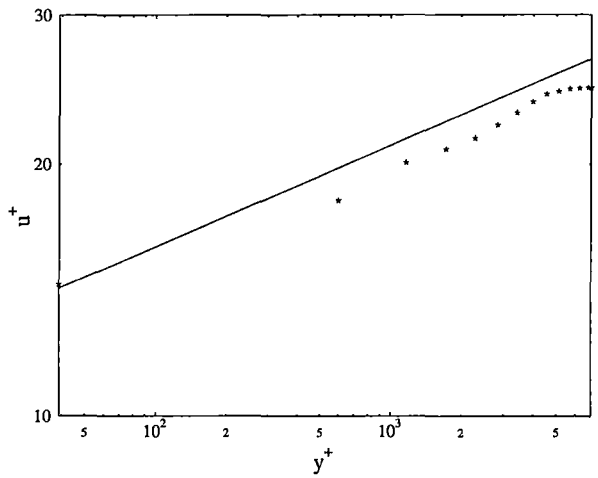

Figure 3.22: Non-dimensional velocity profile of flow 750 mm downstream of a 16 mm fence.

3.5.0.3 Cylindrical Rods

Cockrell and Lee [24] present a method for producing boundary layer velocity profiles, of arbitrary thickness, downstream of a cylindrical rod gauze. This method is based on a power law velocity distribution of the form $\frac{U}{U_\infty} = \left(\frac{y}{\delta}\right)^{1/n}$ and a drag coefficient for a cylindrical rod gauze of the form $K = K_0(1+s)$ (where s is the gauze resistance parameter and K_0 is a constant). Using this method (with $n = 7$ and $K_0 = 0.4$) the spacing of 3mm cylindrical rods to achieve the required velocity distribution was calculated to be (centre-line spacing) 6.3, 13.5, 21.1, 29.1, 37.4, 46.0 54.8 and 63.8 mm from the wall. However, as shown in Figure 3.23, there was still a shear layer present downstream of the outermost rod.

3.5.0.4 Gauze Screen

Gauze screens offer the a more distributed manipulation of the velocity profile. There the two possible approaches to velocity profile manipulation using gauzes: variable resistance gauzes and shaped gauzes. It was felt that the only practical method of

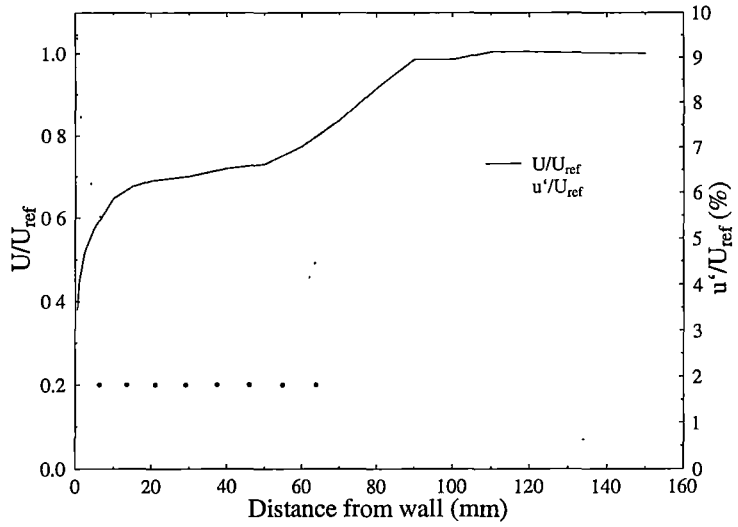

Figure 3.23: Velocity and turbulence profiles of flow 750 mm downstream of a series of rods (closed circles represent position of rods relative to the wall).

achieving variable resistance was to overlap several gauzes; this would have produced a shear layer at the edge of the overlap which might have persisted downstream. Therefore, of the two methods available only shaped gauzes were trialled.

Using theory presented in Laws and Livesey [81] a Fortran program was developed to generate the screen profile given upstream and downstream velocity profiles and screen characteristics. Screen characteristics were calculated from data in Laws and Livesey [81]. The program was validated against experimental data presented in de Vahl Davis [33].

The screen profile tested is shown in Figure 3.24 with a velocity traverse shown in Figure 3.25. The irregularities in the velocity profile are due to localised distortion of the gauze which are very difficult to avoid. Hence gauze screens were excluded from further consideration as boundary layer thickening devices.

3.5.0.5 Normal Blowing

Blowing through a perforated plate to produce a series of jets in cross-flow was the method finally selected for boundary layer thickening. The introduction of the momentum deficit is distributed, as required, and the intense mixing of the jet in cross-flow minimises the stream-wise distance required to achieve a "normal" boundary layer. Furthermore, the normal operation of the wind-tunnel results in the static pressure being below atmospheric (as the tunnel is vented in the low speed return working section to provide make-up air for the extraction through the intake) so the injection fluid is passively drawn through the plate from atmosphere. The amount of injection air (and associated boundary layer thickening) is easily varied by restricting the injection flow using a butterfly valve. Finally, the perforation distribution can be selected to give the correct mass flux (primarily a function of plate porosity) and turbulence profiles by manipulation of the diameter of the individual perforations. This method was successfully

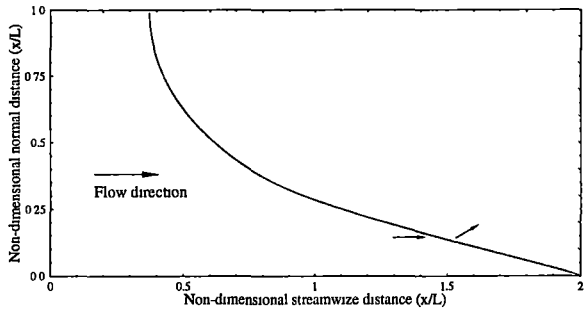

Figure 3.24: Dimensionless design screen shape (distances normalised by tunnel width L) for a gauze ($K = 0.9, B = 0.2$). As the screen will deflect flow towards the flow normal the boundary layer on the lower surface will be thickened.

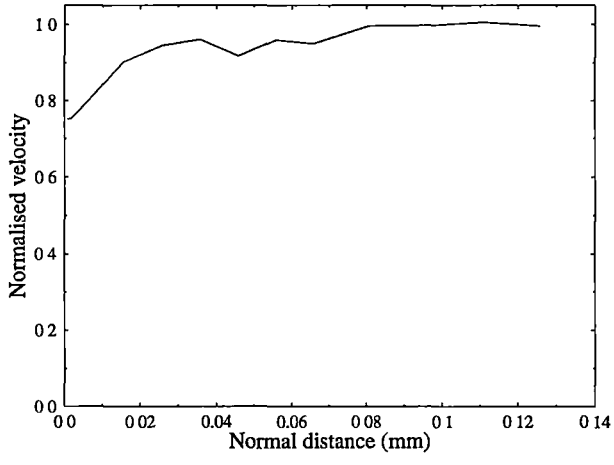

Figure 3.25: Velocity profile of flow 750 mm downstream of a gauze screen, irregularities are due to localised distortion of the gauze.

tested using a uniform perforated plate, with the results shown in Figure 3.26.

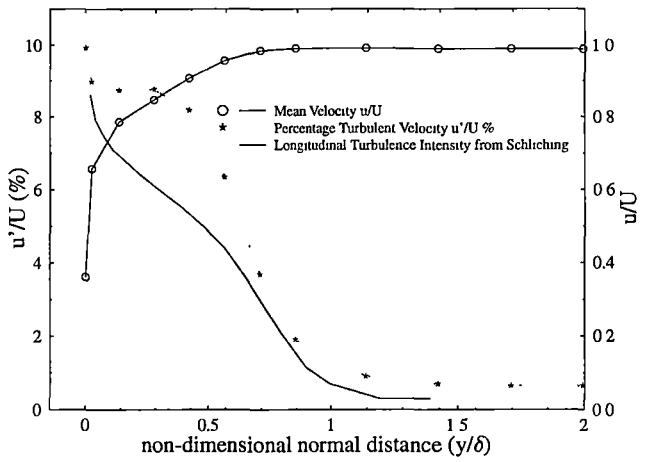

Figure 3.26: Velocity and turbulence profiles 750 mm downstream of injection through a uniform perforated plate (porosity=0.11, perforate diameter 2.5 mm arranged on a square grid).

As can be seen, the velocity and turbulence profiles are quite reasonable. The turbulence profile is high for the first half of the boundary layer (below $y/\delta = 0.5$). This is attributable to all the perforations being the same diameter and therefore all the resulting jets in cross-flow penetrating to the same depth. This results in the turbulence addition being concentrated in the inner boundary layer. To overcome this, a distributed perforation sizing was used for the actual boundary layer thickening. Data from Sterland and Hollingsworth [124] indicates that maximum turbulence for a jet in cross flow is at the near wall side of the core region. Correlations in Pratte and Baines [105] give the near wall side of the jet penetration profile as

$$\frac{x}{RD} = 1.35\left(\frac{z}{RD}\right)^{0.28} \tag{3.24}$$

where x is the distance from the wall, z is a streamwise distance, D is the jet diameter and R is the ratio of jet to free-stream velocity. Therefore, larger diameter jets penetrate further into the free-stream and produce turbulence further away from the wall. An approximation of the boundary layer turbulence intensity profile (triangular distribution with 8% turbulence intensity at the wall and 0% at the edge of the boundary layer) was used to calculate perforate (and therefore jet) diameter distributions. The overall plate porosity (0.0857) was selected based on the losses in the supply piping. A series of perforate diameters (1, 1.5, 2, 3.5, 5, 7 and 10 mm, selected for ease of manufacture) result in turbulence addition at corresponding normal distances from the wall of 7.2, 9.7, 11.9, 17.8, 23.0, 29.3 and 37.9 mm respectively. The total amount of turbulence is represented by the area under the turbulence intensity profile. Therefore, the fraction of area associated with each perforate diameter should equal the fraction of

perforate area each diameter corresponds to (assuming that the amount of turbulence introduced by a jet scales with jet area and possibly velocity). Figure 3.27 shows the perforated plate used and Table 3.3 summarises the perforate distribution. Note that unforeseen flow losses in the supply system required increasing of the plate porosity, this was achieved by over-drilling most of the holes by 0.5 mm on diameter and Table 3.3 reflects this hole sizing (note this increased the plate porosity to 0.1202). The velocity and turbulence profiles produced by this plate are shown in Figure 3.28.

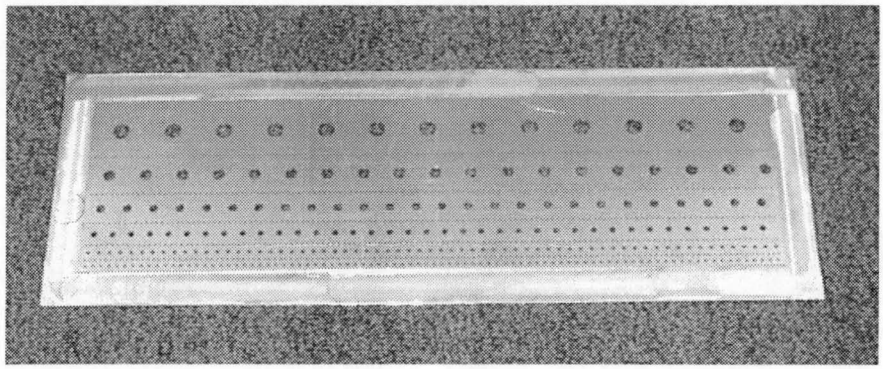

Figure 3.27: Perforated plate used for artificial thickening of the wind-tunnel boundary layer.

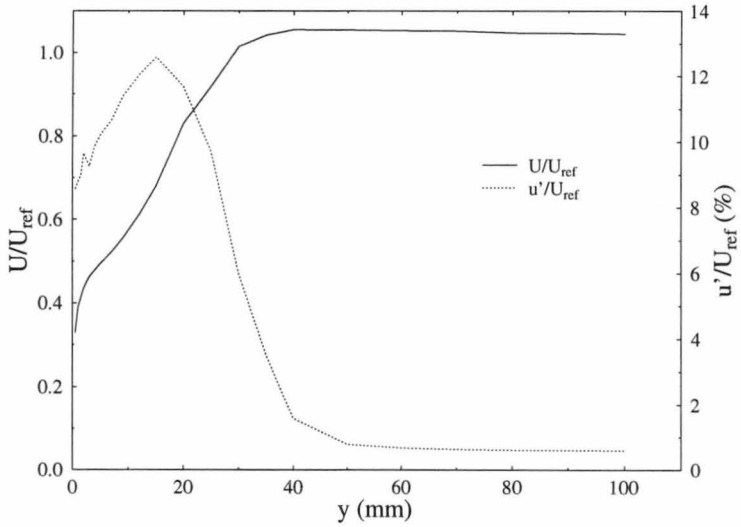

Figure 3.28: Velocity and turbulence profiles of flow 300 mm downstream (ie. start of intake) of the actual perforated plate during intake testing with an artificially thickened boundary layer.

Table 3.3: Perforate distribution for boundary layer thickening.

Hole diameter (mm)	Total number of holes	Number of rows	Distance from leading edge (mm)	Lateral pitch (mm)
1.5	660	5	22.8,43.3,57.8,68.0,75.8	3.0
2.0	88	1	78.8	4.5
3.0	66	1	72.0	7.6
4.0	37	1	62.8	10.6
5.5	26	1	51.0	15.2
7.5	18	1	34.0	21.2
10.0	13	1	7.5	30.3

Chapter 4

Computational Fluid Dynamics Research Methods

4.1 Overview

Details of the computational modelling of a waterjet intake (including a description of the commercial finite element code and details of the actual flow modelled) are presented in this chapter. Issues involved in both the selection of the finite element formulation used (e.g., types of elements, 8 node versus 27 node, etc) and the meshing of the physical geometry (including a grid sensitivity analysis) are discussed in detail. The identification of appropriate boundary conditions, especially for the turbulent flow quantities, are also considered.

4.2 Code Description

FIDAP v7.6 [42] was used for the CFD simulations. FIDAP uses a Galerkin weighted residual method for the finite element discretisation (Haroutunian and Engelman [60]) with departures from the Galerkin formulation permitted via the optional inclusion of steamline upwinding and pressure stabilisation terms (Haroutunian and Engelman [61]). The majority of the simulations used 8 node isoparameteric bricks with trilinear velocity and continuous trilinear pressure distributions. Solution of the resulting equations was via the pressure projection version of the segregated solver, with a conjugate residual method used to solve the symmetric coefficient matrix system associated with the pressure degree of freedom and a conjugate gradient squared method used for the non-symmetric coefficient matrix system for all other degrees of freedom. Petrov-Galerkin pressure stabilisation and streamline upwinding terms are also present to reduce spurious oscillations in the solution field.

Turbulence closure is via $k-\epsilon$ type models (standard, extended and RNG) or more specialised anisotropic models. Near-wall elements utilising specialised shape functions (based on Reichardt's law and van Driest's low Reynolds number mixing length model, Haroutunian and Engelman [61]) are used to model the flow near walls. The standard Boussinesq eddy viscosity model is supplemented by the Speziale and Launder models.

4.3 Meshing

Significant problems were encountered during the meshing phase of the CFD simulation (others such as Turnock et al. [139] have also commented on the difficulty of meshing such intakes). These problems were due both to the complex geometry and conditions imposed by the wall elements used by FIDAP as part of its $k-\epsilon$ turbulence modelling.

The compound curves in the region of the cutwater and associated filleting of the waterjet-hull intersection produce a geometry that is difficult to mesh. Many of the meshing strategies trialled for meshing this region of the flow became problematic where the ramp intersected the hull at a very acute angle. Furthermore, the wall elements used by FIDAP as part of the $k-\epsilon$ turbulence modelling fail to work correctly if more than one side of the element is in contact with a wall, ie. corners are required to be bisected. A meshing strategy was developed using the FIMESH module of FIDAP (rather than the more frequently used graphical FI-GEN module) and a parameterised input file. Figure 4.1 shows the complexity of the meshing strategy for the region surrounding the cut-water.

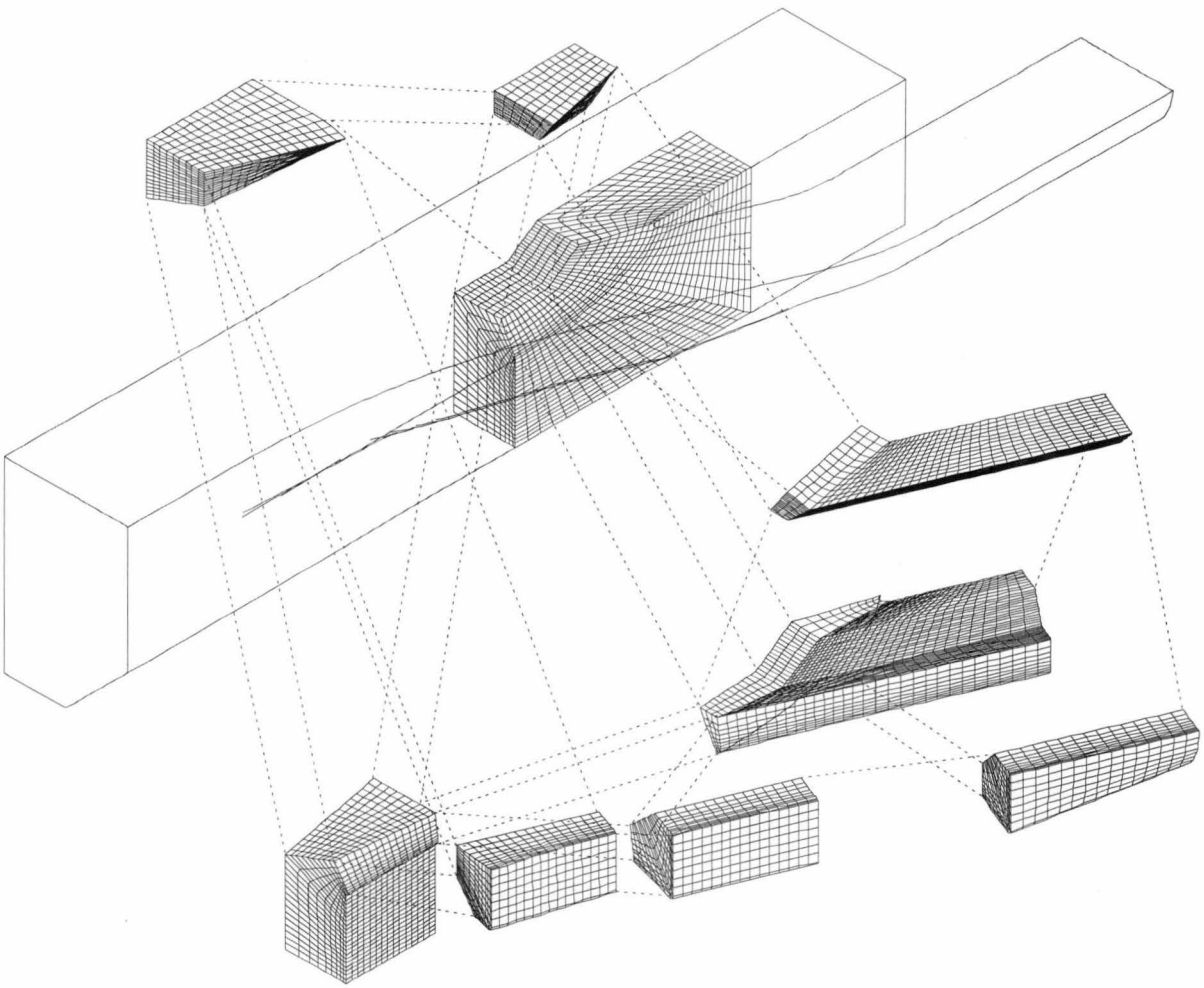

Figure 4.1: Exploded view of element groups that comprise the region near the cutwater. (Grid shown is part of the f5r048 simulation.)

The parameterisation of the FIMESH input file (see Appendix C) allowed for changes in grid grading toward the walls, changing of the overall grid density and using either 8 node or 27 node elements on the same nodal meshes. Grid densities of 1, 1.5 and 2 were tested to determine grid sensitivity (in general, densities in the arithmetic series 1, 1.5, 2, 2.5,... are possible. Computer resources limited the choice to the first three terms in this series, requiring 104, 360 and 880 megabytes of computer memory for the 1, 1.5 and 2 grid densities respectively). The grid densities are linear densities so that the number of nodes for the 1.5 density grid is $1.5^3 = 3.375$ times more that the 1 density grid. The 1, 1.5 and 2 density grids correspond to 41869, 136237 and 317025 nodes respectively. Note that grid densities of 1.83333 and 2.166667 were also used with slight modification (to account for different rounding to integers) to show grid independence which required the 2.0 times mesh (see Figure 4.2) with the flow parameters of minimum ramp centre-line skin friction, area averaged total pressure and distortion all showing grid independence at this point.

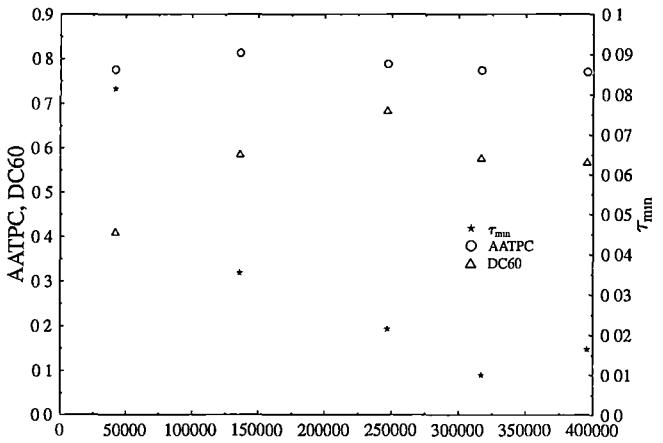

Figure 4.2: Variation of key intake flow parameters with grid density

Originally 27 node elements were used as the curved element sides possible with these elements should better resolve the physical geometry of the model. However, initial trials of both the 8 node and 27 node elements of the same nodal meshes (ie. each 27 node element is replaced by 8 8-node elements) gave better results for the 8 node elements. The reason for this is the wall elements employed by FIDAP as part of the turbulence modelling. Flow variables in these elements are given by shape family functions with the value of the turbulence variables k and ϵ at the "top" of the element being one of the primary influences. As these variables are evaluated at the "top" of the element rather that at the nearest off-wall node of the 27 node bricks the wall elements for 27 node bricks are approximately twice as thick as for 8 node bricks (see Figure 4.3). To correctly resolve the wall shear stress (vitally important in this study because of the possibility of flow separation on a subtly curved surface) relatively thin wall elements were required (see Figure 4.4) and therefore 8 node elements were used

for the majority of the FIDAP simulations.

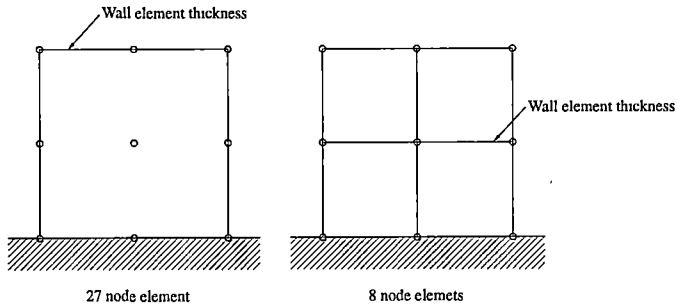

Figure 4.3: Side view of 27 and 8 node bricks fitted to the same nodal meshes. Note the comparative thickness of the wall elements for 27 node elements.

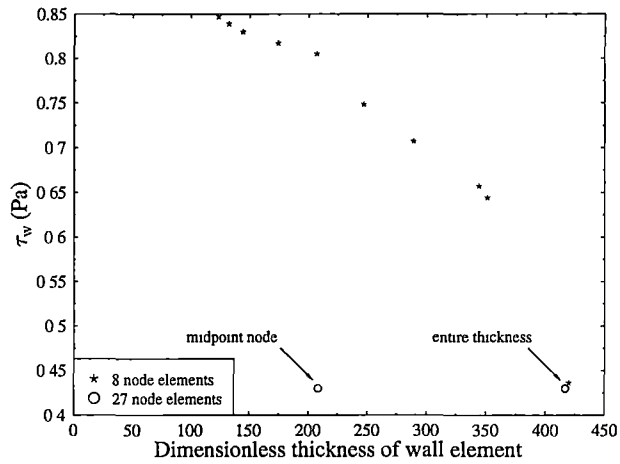

Figure 4.4: Wall shear stress at inflow as a function of wall element thickness. The 27 node result is for a single simulation showing the thickness of the entire element (10.83 mm) and the thickness to the midpoint node (5.42 mm).

The model geometry was input into the FIMESH input file in millimetres. As FIDAP requires a consistent set of units (in this case the SI set of units were used) the physical dimensions needed to be converted to metres. However, a bug in the FIDAP routine that calculates element Jacobians complicated this procedure. This bug results in element Jacobians being incorrectly calculated if the element size is more than a few orders of magnitude from 1. As this is the case for dimensions in both millimetres and metres, pre-scaling (via a parameterisation factor in the FIMESH input file) was used to produce element size of appropriate order. Table 4.1 summarises the effect of this pre-scaling factor on element distortion. (Note that the distortion values shown in this table are for identically shaped elements, so ideally distortion should be independent

of pre-scaling.) The pre-scaling factor used for the CFD simulations was 1/10. The conversion of the physical dimensions from millimetres to metres (using the FIDAP SCALE command) took the existing conversion from millimetres to centimetres (via the pre-scaling) into account.

Table 4.1: Effect of pre-scaling on FIDAP element Jacobians (for one of the early developmental grids). Figures represent number of elements with distortion metric in this sub-interval. Distortion metrics of 0.0 and 1.0 represents a badly distorted and undistorted element respectively.

Pre-scaling factor	Distortion Metric									
	0–0.1	0.1–0.2	0.2–0.3	0.3–0.4	0.4–0.5	0.5–0.6	0.6–0.7	0.7–0.8	0.8–0.9	0.9–1.0
1	21	69	279	354	119	117	160	209	563	337
1/1.25	0	21	39	39	136	200	233	372	484	704
1/1.5	0	0	4	49	18	45	117	315	583	1097
1/2	0	0	1	8	3	30	106	294	516	1207
1/10	0	0	1	8	3	30	103	279	498	1306
1/20	0	0	1	8	3	30	103	279	498	1306
1/50	0	0	1	8	3	30	103	279	498	1306

4.4 Flow Domain

Due to symmetry considerations only one half of the flow domain was modelled. Initially both the waterjet inlet and whole wind-tunnel working section were modelled (with the far wind tunnel chamfer being removed and the distance to the far wall decreased to compensate). However, this resulted in a large number (approximately half) of the elements being outside the waterjet intake duct. Reduction in the number of wind tunnel nodes was achieved by only modelling the wind tunnel to a plane parallel to the hull and 200 mm distant from it. The 200 mm distance (representing 1.33 intake diameters) was chosen to be sufficiently far from the intake as to have no major effect on it. This plane acted as an entrainment plane with boundary conditions taken from a corresponding plane in a previous FIDAP simulation with the entire wind tunnel modelled. Figure 4.5 shows this truncated wind tunnel domain and defines the various planes used to assign boundary conditions (the impeller face plane is also included for reference).

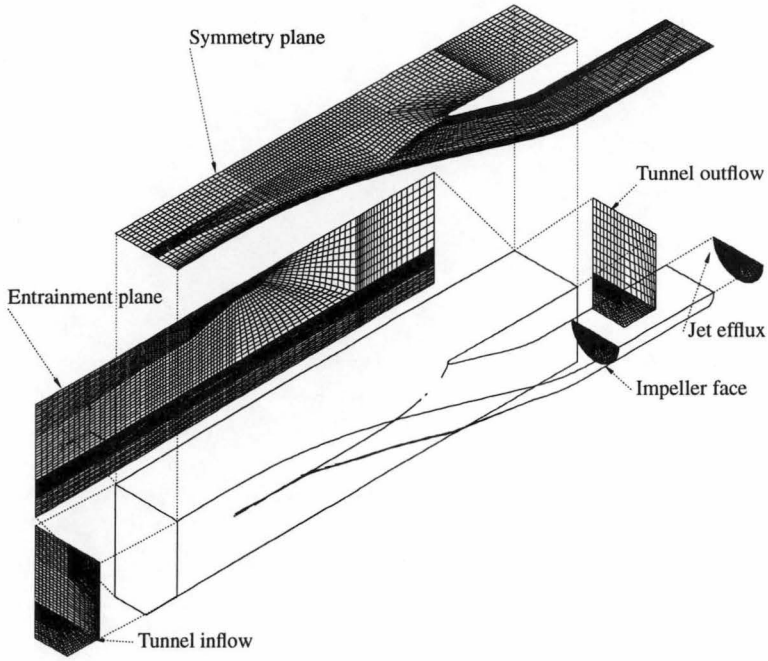

Figure 4.5: Location of planes used to assign boundary conditions for CFD analysis.

4.4.1 Boundary Conditions

4.4.1.1 Inflow Plane

Velocity The lateral and transverse (y and z) velocity components were set as zero and the streamwise (x) component was assigned a theoretical profile given by

$$u = \begin{cases} u^* \left[\frac{\ln(1+\kappa y^+)}{\kappa} + 7.8 \left(1 - e^{-y^+/11} - \frac{y^+}{11} e^{-0.33 y^+} \right) \right] & \text{if } y^+ \leq 30 \\ u^* \left[\frac{\ln(y^+)}{\kappa} + 5.3 \right] & \text{if } 30 < y^+ \leq 350 \\ u_\infty \left(\frac{y}{\delta} \right)^{1/n} & \text{if } y^+ > 350 \end{cases} \tag{4.1}$$

with the constants 5.3 and $1/n$ chosen for a smooth interface between the various equations. These equations were used as they offered a good representation of the experimentally measured velocity profile.

Turbulent Kinetic Energy The turbulent kinetic energy (k) was easily calculated using the experimentally measured turbulence intensity (I) via the relationship $k = 1.5(IU_\infty)^2$ [41]. Table 4.2 summarises the experimental data points used for linear interpolation of turbulent flow variable boundary conditions used in the thin boundary layer simulation.

Turbulent Dissipation The near wall modelling in FIDAP is strongly dependent on the turbulence conditions at the edge of the wall element. However, the large variation in published data for turbulent dissipation (ϵ) (see Table 4.4) required the experimental

determination of dissipation rates. Patel et al. [100] also found that published data on near wall dissipation rates were quite limited and subject to large variation.

The dissipation rates were calculated from the turbulence spectrum derived from hot-wire measurements. The one-dimensional energy spectrum was calculated from the measured hot-wire turbulent velocity fluctuations (u'). The turbulent energy spectrum ($\phi(k_1)$) is then calculated via a Fast Fourier Transform (FFT) and the corresponding discrete frequencies (f) converted to one-dimensional wave numbers via the relation $k_1 = 2\pi f/u_\infty$. The FFT amplitudes were summed over 5 consecutive wave numbers to reduce the variance in the data (note the amplitudes are summed rather that averaged to preserve the normalisation of the energy spectrum [106] ie. $\int_0^\infty \phi(k_1)dk_1 = \overline{u'^2}$). The dissipation rate (ϵ) is found from the equation

$$\phi(k_1) = C\epsilon^{2/3}k_1^{-5/3} \tag{4.2}$$

which is valid for wave numbers in the inertial subrange. Lines of best fit of the form $\phi = ak_1^{-5/3}$ were fitted to the experimental data, giving

$$\epsilon = \left(\frac{a}{C}\right)^{1.5} \tag{4.3}$$

The lack of specific numerical bounds on what wave numbers constitute the inertial sub-range complicated the determination of a. A line segment which minimised the root mean square of the residue was used to calculate a. This line segment was selected by sweeping both the starting position and length through wavenumber based ranges (1–500 for starting position and 400-600 for length) and selecting the line segment which minimised the root mean square of the residue.

The constant C was obtained from the literature (0.53 Ames [10], 0.51 Leslie [82], 0.50 Townsend [138], with the former value being used in this study). Table 4.2 summarises the dissipation values used as boundary conditions at inflow for the thin boundary layer simulation. Table 4.3 reproduces this data for the thick boundary layer simulation. A typical spectrum is shown in Figure 4.6. Note regions with $\phi \propto k_1^{-4}$ as per Townsend [138, Figure 3.18] and Perry et al. [101, Figure 13] in the viscous sub-range and $\phi \propto k_1^{-1}$ as per Klebanoff [76] and Perry et al. [101] in the production range. At high wave numbers the measured curve deviates from the expected k_1^{-4} proportionality. This is probably due to the limited resolution (12 bits) of the data acquisition card used to sample the anemometer output.

4.4.1.2 Symmetry Plane

The z velocity was set to zero on this plane, while the two other velocity components were left free.

4.4.1.3 Entrainment Plane

All flow variables were assigned values interpolated from data at the same plane in a full wind tunnel FIDAP simulation.

4.4.1.4 Tunnel Outflow

No boundary conditions were applied to the wind tunnel outflow.

Table 4.2: Turbulence boundary conditions at inflow for the thin boundary layer CFD simulation

y/δ	y^+	I (%)	ϵ^+*1000
0.035	27.66	8.55	5.057
0.070	55.30	8.61	5.148
0.105	82.94	8.34	4.964
0.139	110.59	7.90	3.679
0.209	165.88	7.50	2.654
0.279	221.16	7.25	2.434
0.349	276.44	6.49	1.820
0.488	387.03	5.78	0.991
0.628	497.56	4.86	0.449
0.837	663.41	2.28	0.106
1.046	829.22	1.02	1.23e-2
1.395	1105.18	0.64	2.02e-3
1.743	1381.40	0.55	1.38e-3
2.441	1933.75	0.31	5.55e-4
3.138	2486.11	0.16	1.29e-4

Table 4.3: Turbulence boundary conditions at inflow for the thick boundary layer CFD simulation

y/δ	y^+	I (%)	ϵ^+*1000
0.006	16.28	9.30	6.260
0.012	32.56	8.99	5.868
0.018	48.84	9.06	8.009
0.024	65.13	9.83	7.657
0.036	97.69	9.98	8.092
0.048	130.25	9.85	9.065
0.060	162.82	10.67	9.401
0.084	227.94	10.93	12.85
0.108	293.07	11.58	15.77
0.144	390.76	12.03	20.48
0.180	488.45	11.35	23.43
0.240	651.26	10.19	22.60
0.300	814.08	8.42	16.67
0.420	1139.71	2.10	0.706
0.540	1465.34	0.93	0.021
0.719	1953.79	0.66	1.64e-3
0.959	2605.05	0.30	9.46e-4
1.199	3256.31	0.15	9.46e-4

Table 4.4: Published correlations for dissipation rates.

Equation	$\epsilon_{10}(m^2/s^3)$	Notes
$\epsilon = \frac{15}{2}\nu\left(\frac{\partial u}{\partial y}\right)^2$	4.9	Isotropic relation
$\epsilon = \frac{u^{*3}}{\kappa y}$	143	Bradshaw [17, page 37]
$\epsilon = W_2\frac{U_\infty^3}{\delta}$	23.4	Klebanoff [76, Figure 24]
$\frac{\epsilon\delta}{u^{*3}} = 1.2$	49	Hinze [64, Figure 7-27]
$\frac{\epsilon\delta}{u^{*3}} = 1.5$	61	Hinze [64, Figure 7-27] with intermittency correction
$\epsilon = \frac{\left(\frac{\tau}{\rho}\right)}{L_e}$	88	Bradshaw [16] , $\frac{\tau}{\tau_w}$ from Figure 2 , L_e from Figure 15
$\epsilon = \frac{\left(\overline{u^2}\right)^{3/2}}{L_e}$	116	Bradshaw [17, page 24]
ϵ of order $O(u^3/L)$	O(70)	Townsend [138, page 42]
-	80	Mansour et al. [85, Figure 5] (very rough)
FIDAP		
$\epsilon = \frac{\left(c_\mu^{1/2}k_{top}\right)^{1.5}}{\kappa y}$	24.0	[40], k_{top} evaluated from experimental data
Experimental		
$\phi_1(k_1) = 0.51\epsilon^{2/3}k_1^{-5/3}$	137.1	Leslie [82] with $\phi_1(k_1) = ak_1^{-5.3}$ from experimental data
$\phi_1(k_1) = 0.53\epsilon^{2/3}k_1^{-5/3}$	129.4	Ames [10] with $\phi_1(k_1) = ak_1^{-5.3}$ from experimental data

ϵ_{10} evaluated at 10 mm from the wall for a boundary layer with $\tau_w = 0.825$ Pa, $\delta = 14.34$ mm, $\rho = 1.177$ kg/m^3, $U_\infty = 17.75$ m/s and $\mu = 1.846e-5$ kg/m s.

4.4.1.5 Jet Efflux

No velocity conditions were set at this plane, as it was believed that prescribing velocity distributions here may adversely impact on the quality of the solutions.

The simulation inlet velocity ratio (IVR) was controlled by applying a pressure boundary condition to the outflow.

Uniform flow at jet efflux was applied for one particular solution for direct comparison with a pressure boundary condition solution (Figures 4.7 and 4.8) and there is negligible difference between the two solutions except within several element lengths of the outflow. Therefore, uniform velocity at outflow is an acceptable method of prescribing IVR, although the pressure condition was used throughout this thesis as the method had already been developed and more realistically represents the flow.

4.5 Post-processing

The majority of the post-processing was carried out using FIDAP. However, total pressure plots, area averaged total pressure coefficients and distortion coefficients (all evaluated at the impeller face plane) were evaluated using custom written Fortran programs.

Elemental connectivities and nodal values of the velocity and pressure degrees of freedom were written to file. The Unix scripting language Nawk was used to extract the relevant sections of these files to reduce the IO requirements of the Fortran programs.

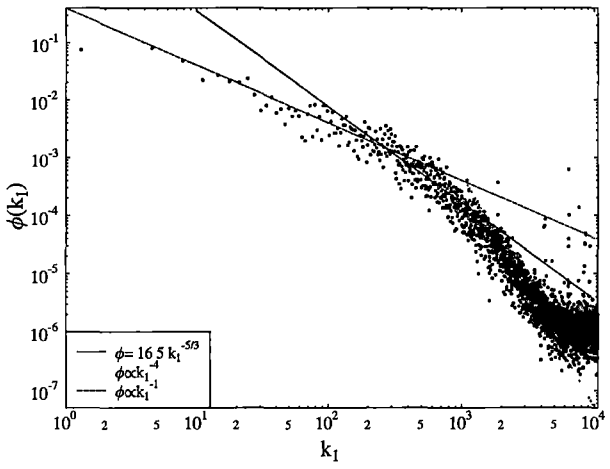

Figure 4.6: Typical energy spectrum at 9mm from the wall at inflow for the thin boundary layer measurements. Dissipation rate calculated from slope of line $\phi \propto k_1^{-5/3}$. Note regions with $\phi \propto k_1^{-4}$ in the viscous sub-range as per Townsend [138] and Perry et al. [101] and $\phi \propto k_1^{-1}$ in the production range as per Klebanoff [76].

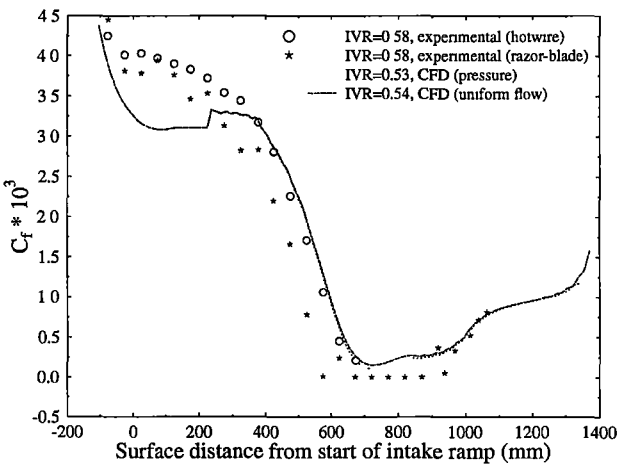

Figure 4.7: Ramp centre-line skin friction coefficient for pressure and uniform velocity boundary conditions at jet exit. Note the agreement between the two CFD results except in the immediate vicinity of the outflow.

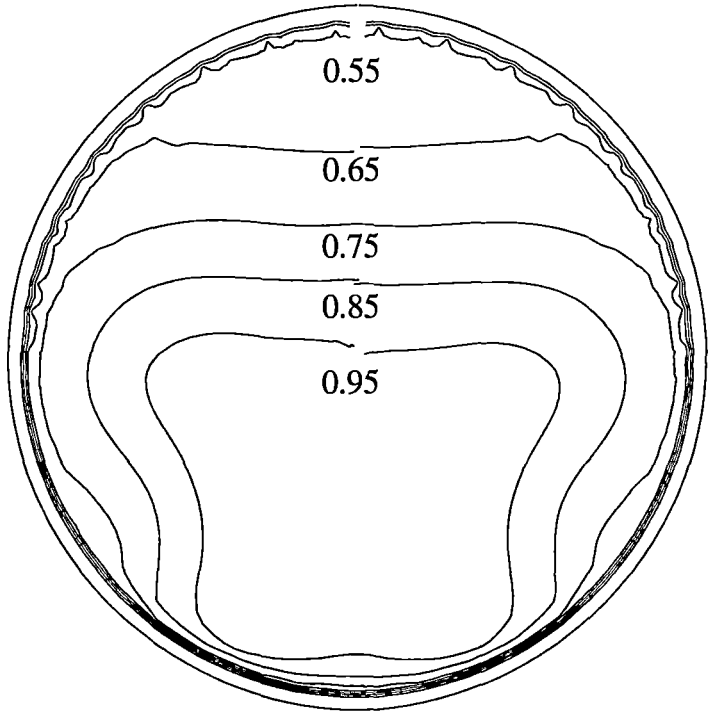

Figure 4.8: Impeller face total pressure coefficient contour plots for uniform velocity (left) and pressure (right) jet exit boundary conditions.

The element connectivity file contained data specifying which nodes connect to form elements at the impeller face. The solution variables were then calculated for each element by simple averaging of the appropriate nodal values. Physical coordinates of the nodes also allowed for the calculation of elemental areas and centroids. The centroids were calculated as the intersection of the element diagonals. While this is not necessarily accurate for general quadrilaterals, the low degree of element skew and their general small size should make this approximation acceptable.

The elemental total pressure coefficient was calculated via

$$C_{P_{elemental}} = \frac{p + \rho v^2/2}{\rho v_\infty^2/2} \tag{4.4}$$

as the static pressure at inflow was assigned as 0 Pa.

The area averaged total pressure coefficient (AATPC) was calculated by area weighted averaging of the elemental total pressure coefficients.

The distortion coefficient (DC_{60}) can be defined as

$$\mathrm{DC}_{60} = \frac{\mathrm{AATPC} - \mathrm{AATPC}_{60}}{\mathrm{IVR}^2} \tag{4.5}$$

where AATPC_{60} is the "worst" AATPC for any 60 degree sector. Symmetry conditions were assumed when calculating the pressure conditions for any 60 degree sector. This is the definition of distortion coefficient typically used in the United Kingdom for aero-engine research. It is difficult to explicitly state numerical limits for "good" and/or "bad" distortion coefficients. However, aeronautical intakes typically have a DC_{60} below 0.3 (e.g., Farr and Schumacher [38] and Bannsod and Bradshaw [13]) compared with values above 0.6 (at cruise operation) in the current study.

The total pressure coefficient data had to be interpolated onto a regular polar coordinate grid for contour plotting. This interpolation was done using the commercially available package Surfer (version 3.00) [49] using a regional variable theory technique known as Kriging and an octant search method. The slight waviness in the contour plots is due to the interpolation routine having difficulties in regions of lower input data densities. Figure 4.9 shows a typical total pressure coefficient plot at the impeller face plane obtained from the FIDAP CFD simulation.

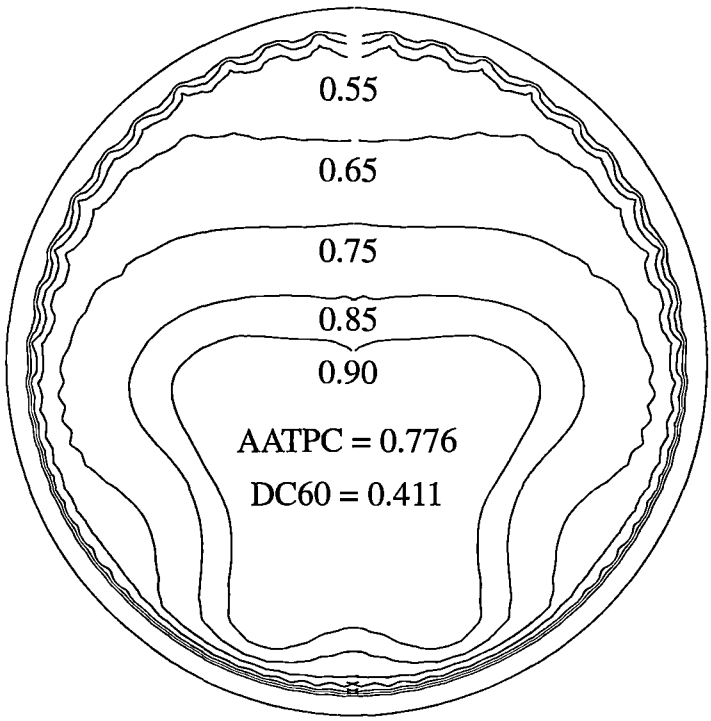

Figure 4.9: Typical total pressure coefficient at the impeller face for FIDAP thin boundary layer simulations.

Chapter 5

Thin Boundary Layer Results

Experimental and computational results are presented in turn for cruise operation with a thin inlet boundary layer (this chapter) cruise operation with a thickened intake boundary layer (Chapter 6) and manoeuvring operation (Chapter 7). Discussion of all of these results is, in general, postponed until Chapter 8.

Cruise operation (as used in this thesis) is for an inlet velocity ratio (IVR) of around 0.6. Typical free stream velocity for the experimental program and FIDAP simulations was around 18 m/s.

The naturally developed wind tunnel boundary layer was used for the thin boundary layer program. This boundary layer has a momentum thickness of around 1.2 mm (see Figures 5.27–5.29 for more information). In comparison, a realistic hull boundary layer thickness for this type of waterjet installation is around 6.6 mm scale size (see Section 3.5.0.1 for details).

5.1 Experimental

5.1.1 Bounding Ingestion Stream-tubes

Bounding ingestion stream-tubes were experimentally determined using a carbon monoxide gas tracer technique (see Section 3.4.3 for more details) for four different inlet velocity ratios (IVR's). The results are summarised in Figure 5.1. The intake flow rate can be found through integration of velocity over this area and compared to the flow rate determined from orifice plate measurements in the ducting downstream of the intake (Table 5.1). The measurement plane was 270 mm (or 1.8 intake diameters) upstream of the start of the intake ramp.

5.1.2 Flow Visualisation

The fluorescent mini-tuft visualisation was conducted for various inlet velocity ratios and free stream velocities with cruise results shown in Figure 5.2. Separation is evident (due to tuft image blurring, see Section 3.4.1 for further information on this technique) at low IVR's with Table 5.2 giving the position of this flow separation.

Table 5.1: Comparison of ingestion stream-tube cross sectional areas as directly measured (via the CO gas tracer technique) and calculated (assuming uniform velocity distributions).

IVR	Cross sectional area$^+$ (mm^2)	Difference in flow rate* (%)
0.25	2189	-1.4
0.39	3277	-6.4
0.51	4223	-7.1
0.71	5707	-8.5

$^+$ Estimated by extrapolating the stream-tube boundaries to the wall
* Percentage difference between flow through intake cross section and orifice plate reading normalised by orifice plate reading

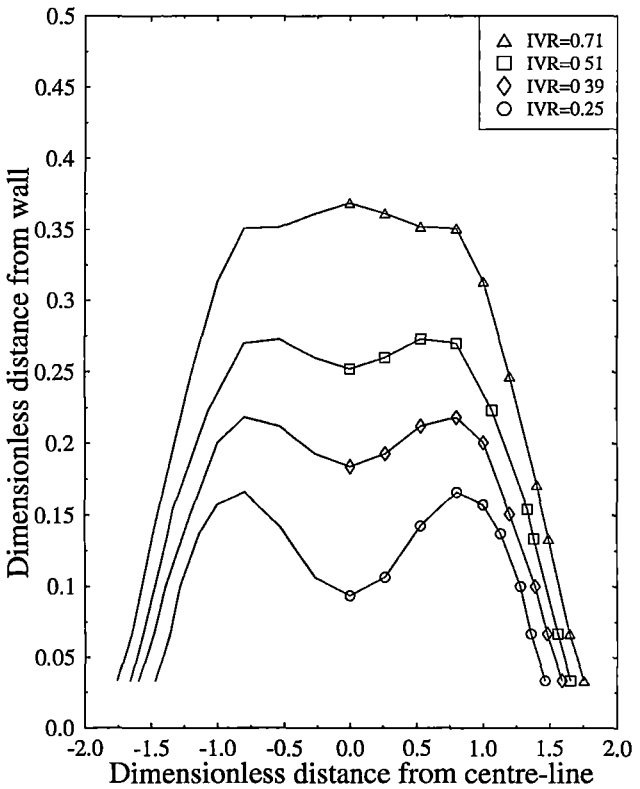

Figure 5.1: Bounding ingestion stream-tube cross sections, distances non-dimensionalised by the intake diameter.

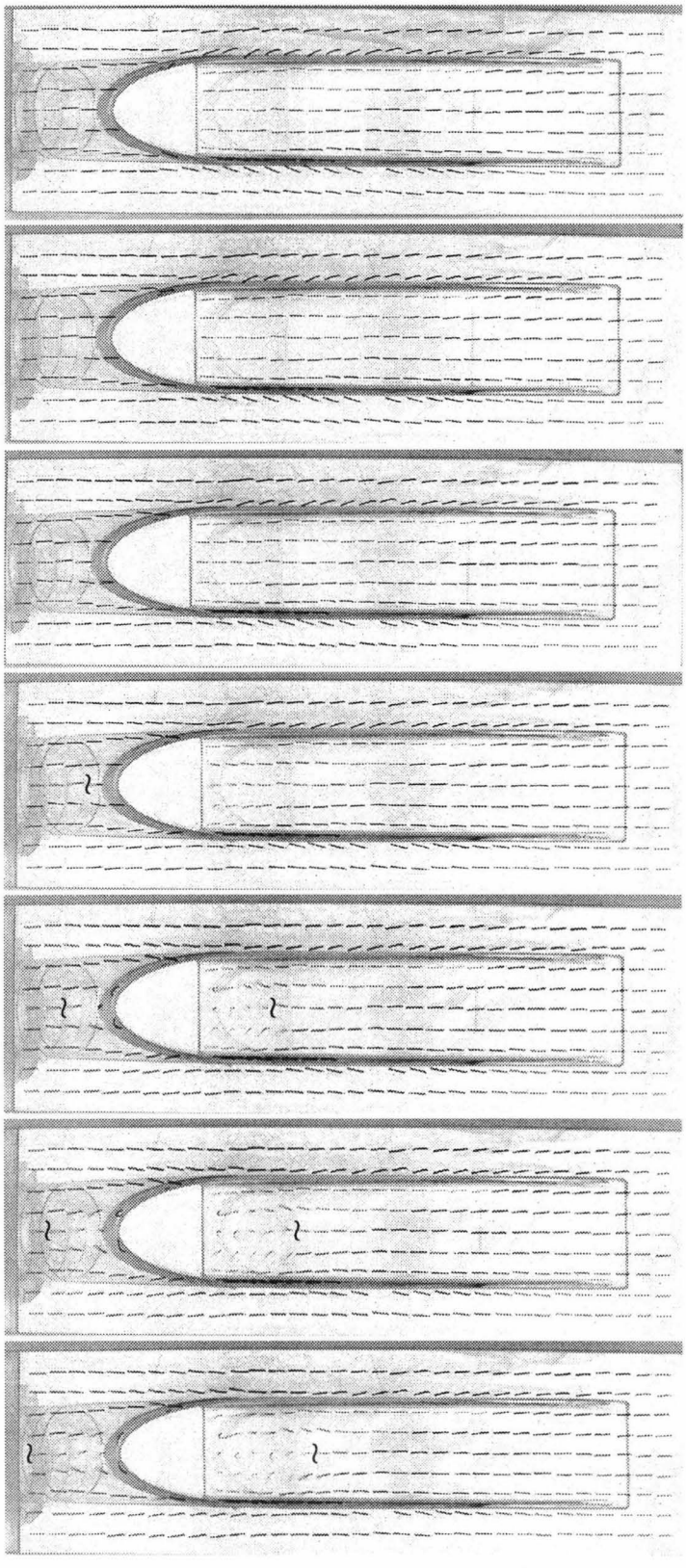

Figure 5.2: Fluorescent mini-tuft visualisation results for $Re_d = 218 * 10^3 \pm 5\%$. Intake ramp separation and re-attachment downstream of cut-water separation are indicated ($\wr$) where appropriate.

Table 5.2: Ramp and cutwater separation as observed using fluorescent mini-tuft visualisation.

IVR	Ramp separation point (mm from start of intake)	Cutwater separation length (mm)
0.19	480	145
0.35	510	115
0.46	525	85
0.66	–	55
No separation evident for higher IVR's		

5.1.3 Static Pressure Distributions

Static pressure distributions are shown in Figure 5.3 for the ramp centre-line and Figure 5.4 for the bottom half-circumference at the impeller face. The static pressure coefficient is defined by

$$C_p = \frac{p - p_\infty}{1/2\rho u_\infty^2} \tag{5.1}$$

where the wind tunnel work section inflow velocity (u_∞) is typically in the range 17–18 m/s.

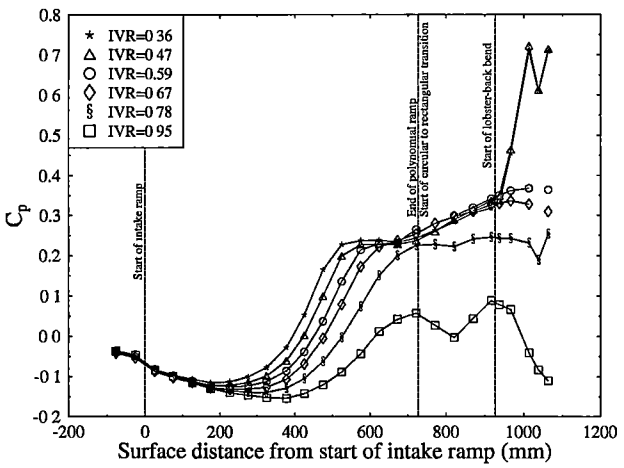

Figure 5.3: Ramp centre-line static pressure coefficient distribution.

5.1.4 Skin Friction

Figures 5.6 and 5.5 show skin friction coefficient ($C_f = \frac{\tau_{\text{wall}}}{1/2\rho u_\infty^2}$) vectors measured by the razor blade technique (see Section 3.4.6). Secondary flows in the intake corners

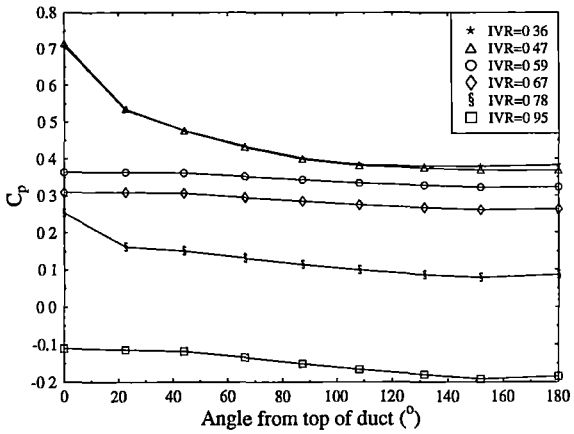

Figure 5.4: Impeller face half-circumference static pressure coefficient distribution.

are clearly visible. The effect of intake velocity ratio on ramp centre-line skin friction magnitude is shown in Figure 5.7. Ramp centre-line skin friction coefficient magnitude measured by both the razor blade technique and hot wire measurements using the Clauser technique (Equation 3.21) is given in Figure 5.8.

5.1.5 5 Hole Pressure Probe Traverses

The total pressure coefficient is defined as

$$C_P = \frac{P - p_\infty}{1/2\rho u_\infty^2}. \tag{5.2}$$

The area averaged total pressure coefficient ($AATPC$) can then be calculated as well as a distortion coefficient, defined as

$$\mathrm{DC}_{60} = \frac{P_f - P_\theta}{q_f} \tag{5.3}$$

where P is the area averaged total pressure and q is the dynamic pressure. The subscripts f and θ refer to the entire impeller face and the 60° sector with the "worst" total pressure respectively. It can easily be shown that these coefficients are related by

$$\mathrm{DC}_{60} = \frac{\mathrm{AATPC} - \mathrm{AATPC}_{60}}{\mathrm{IVR}^2} \tag{5.4}$$

where AATPC_{60} is the area averaged total pressure coefficient over the "worst" 60° sector.

5.1.5.1 Free-stream/model cross-sections

Secondary flow velocity vectors and total pressure coefficient contour plots for various cross sections (see Figure 5.9 for their location) are shown in Figures 5.10–5.13. The secondary flows shown here are in a plane normal to the undisturbed free stream velocity.

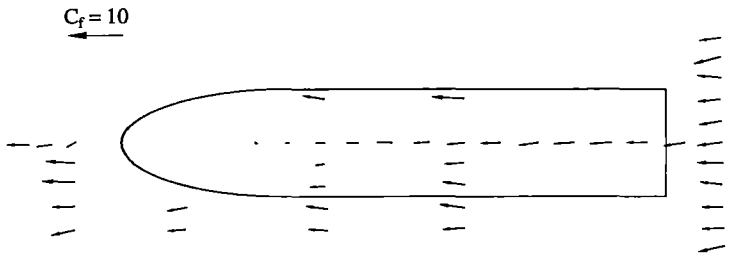

Figure 5.5: Vector plot of skin friction coefficient for IVR=0.58.

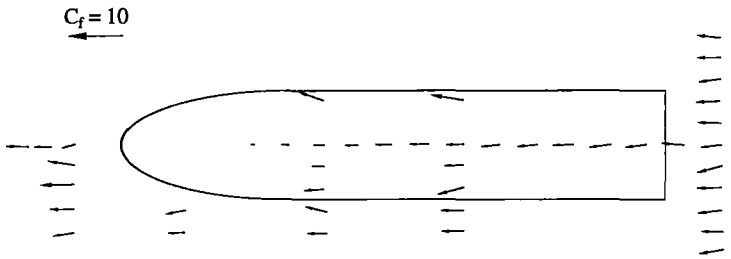

Figure 5.6: Vector plot of skin friction coefficient for IVR=0.69.

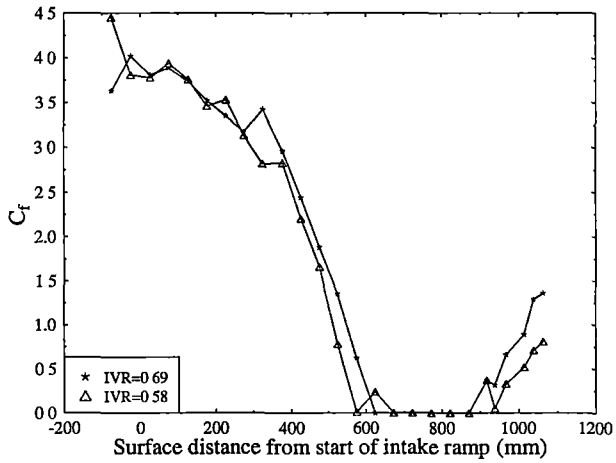

Figure 5.7: Intake ramp centre-line skin friction coefficient via razor blade method.

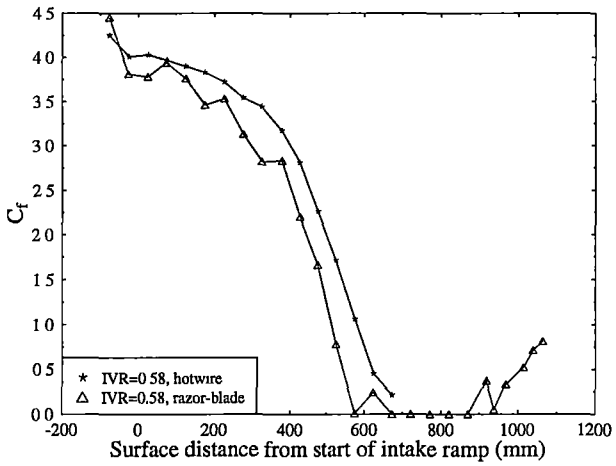

Figure 5.8: Comparison of skin friction coefficients along the ramp centre-line measured via hot-wire traverses and the razor blade technique.

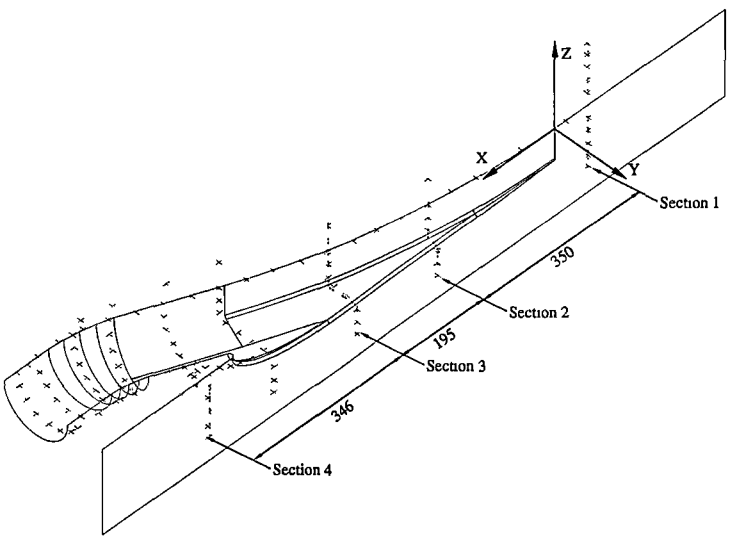

Figure 5.9: Location of pressure tappings and measurement cross-sections, half model shown for reference. All dimensions in millimetres.

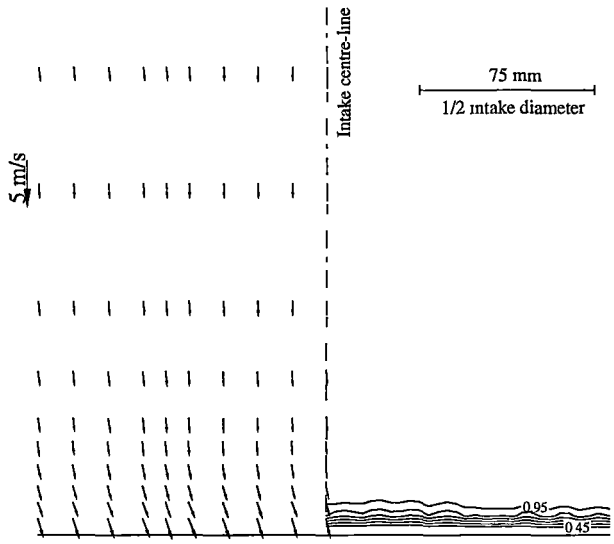

Figure 5.10: Secondary flow velocity vectors (left) and total pressure coefficient contours (right) at cross section 1, IVR 0.60 and U_∞=17.04 m/s.

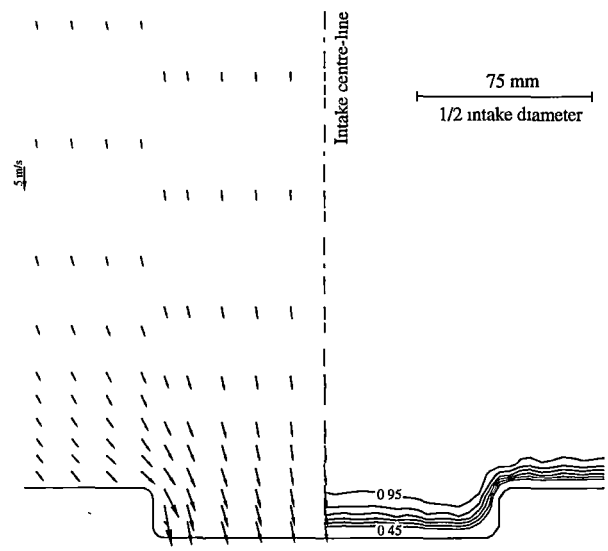

Figure 5.11: Secondary flow velocity vectors (left) and total pressure coefficient contours (right) at cross section 2, IVR 0.60 and U_∞=16.84 m/s.

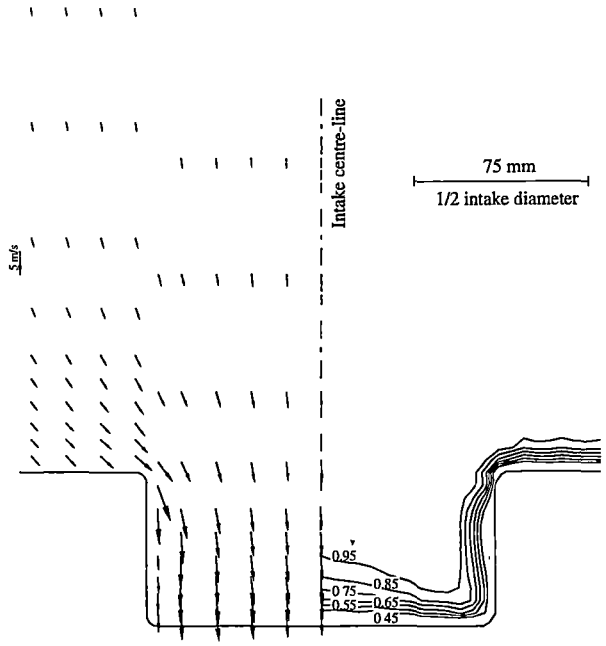

Figure 5.12: Secondary flow velocity vectors (left) and total pressure coefficient contours (right) at cross section 3, IVR 0.60 and U_∞=16.82 m/s.

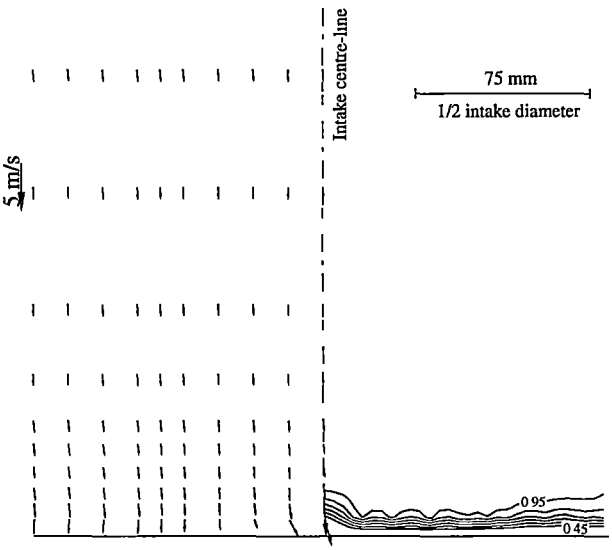

Figure 5.13: Secondary flow velocity vectors (left) and total pressure coefficient contours (right) at cross section 4 (outside the duct, downstream of the intake), IVR 0.61 and U_∞=16.38 m/s.

5.1.5.2 Impeller face

Results at the impeller face are based on 9 (20° increments) full diameter traverses of 20 points of equal radial increment, totalling 180 point readings. This is well in excess of the 48 points used in Farr and Schumacher [38] on the F-15 inlet developmental program. However, blockage (due to their eight leg rake), the need for dedicated transducers at each sensing point (they were considering dynamic distortion and so needed high frequency response) and effects on the installed turbo fan engine (this testing included test flight testing), were not a limiting factor in the current study.

Results at the impeller face are summarised in Table 5.3 and Figures 5.14 – 5.20. Static pressure coefficients at the wall were linearly interpolated from results in Figure 5.4 to allow for inclusion of the annular space near the wall.

Table 5.3: Comparison of experimental and empirical total pressure and experimental distortion coefficients at impeller face.

IVR	C_p	AATPC	TPC^*	DC60
0.59	0.343	0.757	0.72	0.674
0.72	0.214	0.782	0.80	0.477
0.83	0.047	0.785	0.83	0.320

* from Idel'chik [67]

Estimates for the total pressure coefficient can be obtained using the data of Idel'chik [67, Diagram 7-18] for a diverging wye:

$$\frac{\Delta P}{0.5\rho U_\infty^2} = A' \left[1 + \mathrm{IVR}^2 - 2\mathrm{IVR}\cos(\theta)\right] \tag{5.5}$$

where θ is the ramp angle (22.5° in this study) and $A' = 1.1 - 0.7Q_{\mathrm{duct}}/Q_{\mathrm{tunnel}}$ and Q is the flow rate. The total pressure coefficient is then

$$C_P = 1 - \frac{\Delta P}{1/2\rho u_\infty^2}. \tag{5.6}$$

Table 5.4: Comparison of AATPC (or equivalent) at impeller face from other sources.

AATPC	Source
0.75	Dyne and Lindell [35]
0.6–0.9	Gongwer [52]
0.6–0.8	Parker [98]
0.7	English [37]
0.8	Haglund et al. [58] and Fujisawa and Ogawa [46]

Secondary flow velocities were calculated using the probe calibrations given earlier (Section 3.4.2) and the yaw and pitch origins were calculated as described below.

The yaw and pitch at the duct centre were linearly interpolated for all nine traverses. The resulting flows in the x and y directions were then calculated and pitch and yaw offsets introduced to make the x and y velocities constant (for all traverses) in a least squares sense.

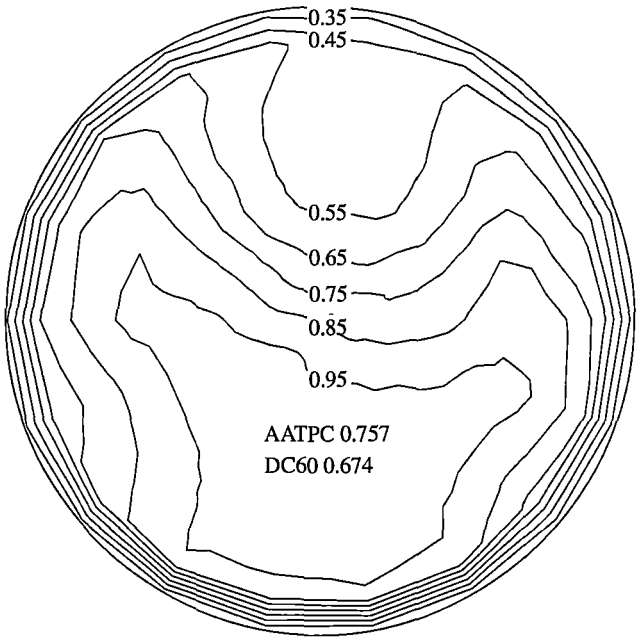

Figure 5.14: Total pressure coefficients at the impeller face for IVR=0.59.

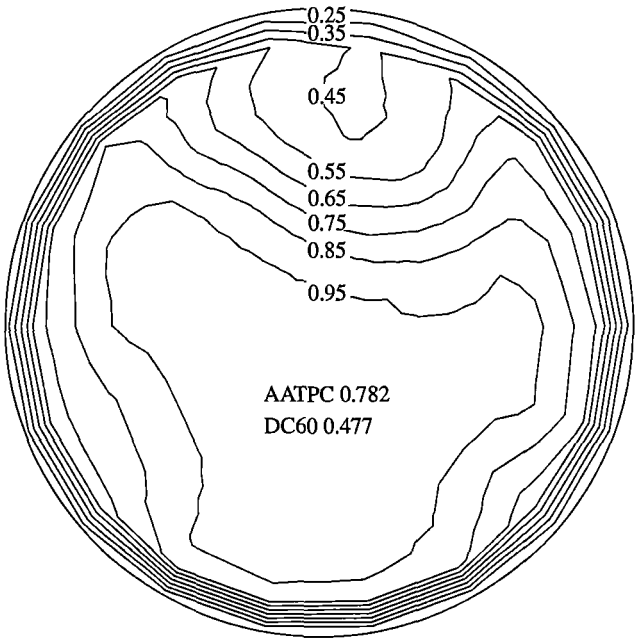

Figure 5.15: Total pressure coefficients at the impeller face for IVR=0.72.

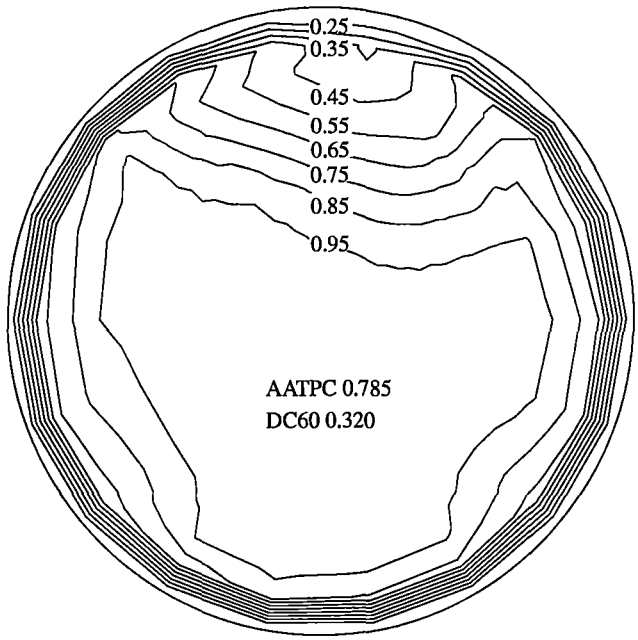

Figure 5.16: Total pressure coefficients at the impeller face for IVR=0.83.

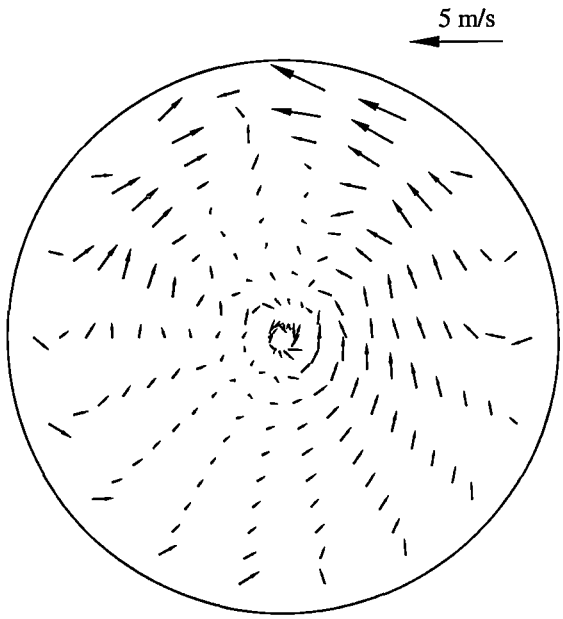

Figure 5.17: Secondary flow at the impeller face for IVR=0.59 and $\overline{U}_{\text{duct}}$=9.48 m/s.

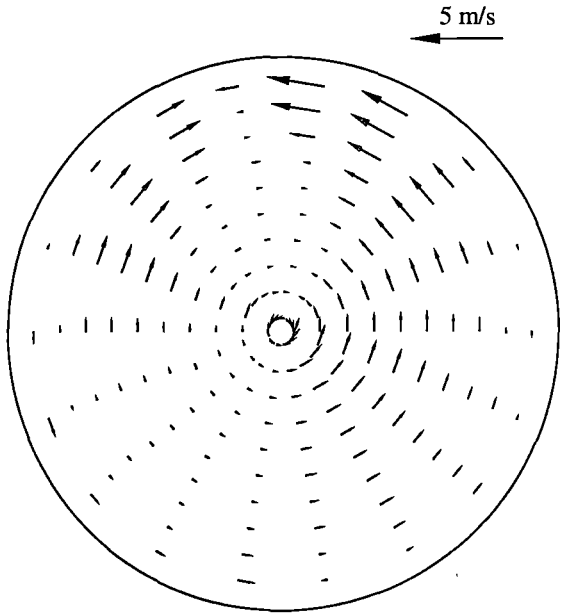

Figure 5.18: Circumferential component of secondary flow at the impeller face for IVR=0.59 and $\overline{U}_{\text{duct}}$=9.48 m/s.

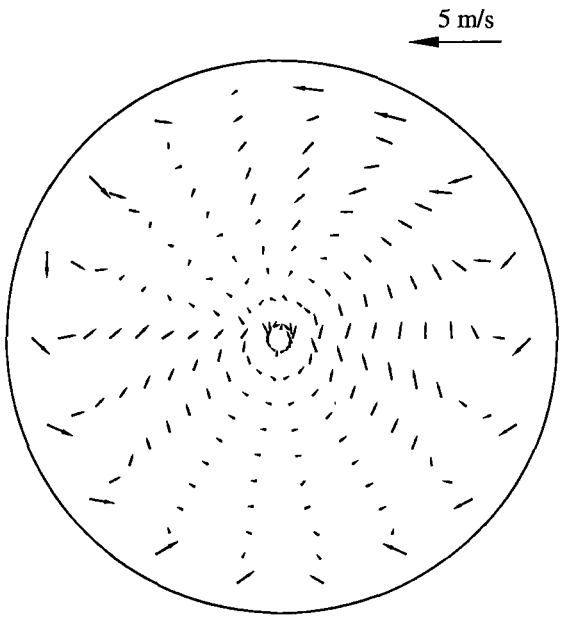

Figure 5.19: Secondary flow at the impeller face for IVR=0.83 and $\overline{U}_{\text{duct}}$=14.12 m/s.

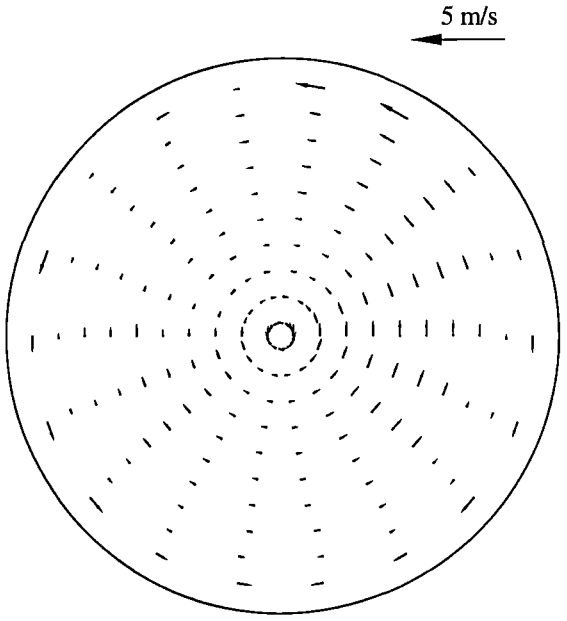

Figure 5.20: Circumferential component of secondary flow at the impeller face for IVR=0.83 and $\overline{U}_{\text{duct}}$=14.12 m/s.

5.1.6 Hot-wire Observations

Figures 5.21–5.24 gives contour plots of speed (perpendicular to sensor) normalised by free stream velocity and turbulence intensity ($=\frac{\sqrt{u'^2}}{U_\infty}$) at several cross-sections. Figures 5.25 and 5.26 provide the distribution of these quantities on the ramp centre-line. Boundary layer displacement thickness, momentum thickness and shape factor values derived from the hot-wire observations are given in Figures 5.27–5.30.

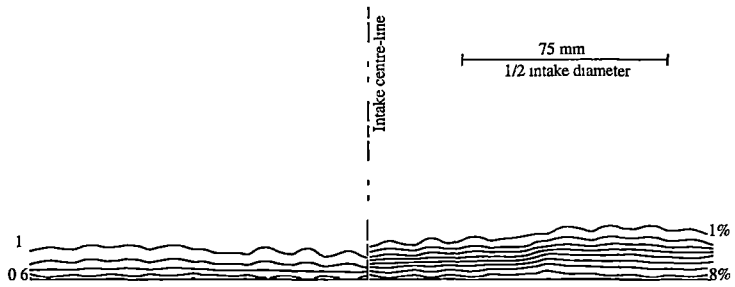

Figure 5.21: Mean velocity contours (left) and turbulence contours (right) at cross section 1, IVR 0.58 and U_∞=17.43 m/s.

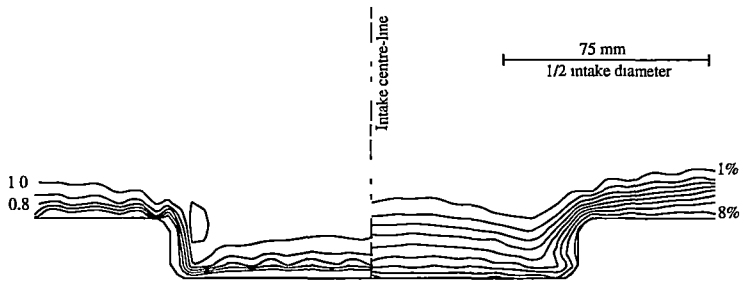

Figure 5.22: Mean velocity contours (left) and turbulence contours (right) at cross section 2, IVR 0.58 and U_∞=17.11 m/s.

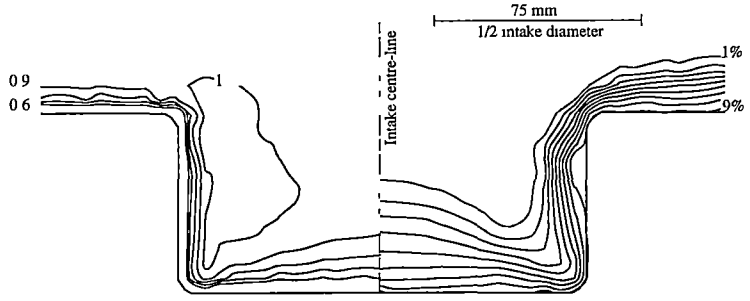

Figure 5.23: Mean velocity contours (left) and turbulence contours (right) at cross section 3, IVR 0.58 and U_∞=17.77 m/s.

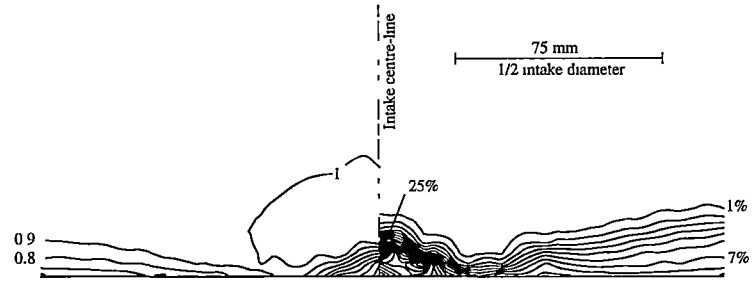

Figure 5.24: Mean velocity contours (left) and turbulence contours (right) at cross section 4a, IVR 0.58 and U_∞=17.01 m/s.

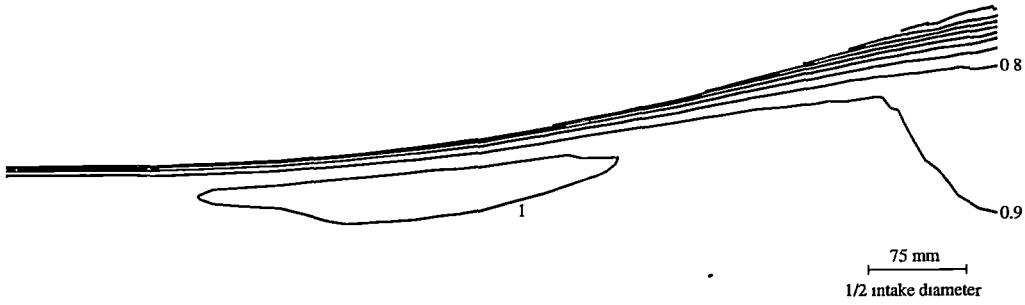

Figure 5.25: Mean velocity contours along the centre-line in the region of the ramp, IVR=0.58 and U_∞=17.02 m/s.

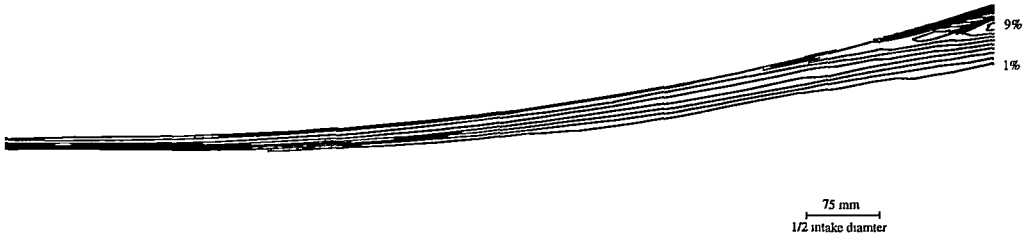

Figure 5.26: Turbulence contours along the centre-line in the region of the ramp, IVR=0.58 and U_∞=17.02 m/s.

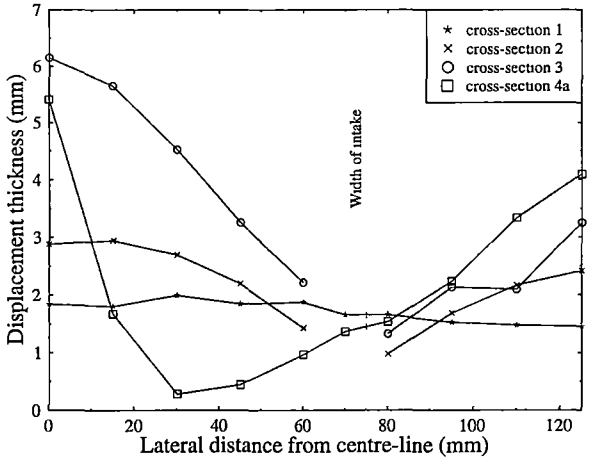

Figure 5.27: Boundary layer displacement thickness derived from hot-wire traverses (IVR=0.58). The discontinuities in the curves for sections 2 and 3 signify the uncertainty in these properties across the intake/hull intersection.

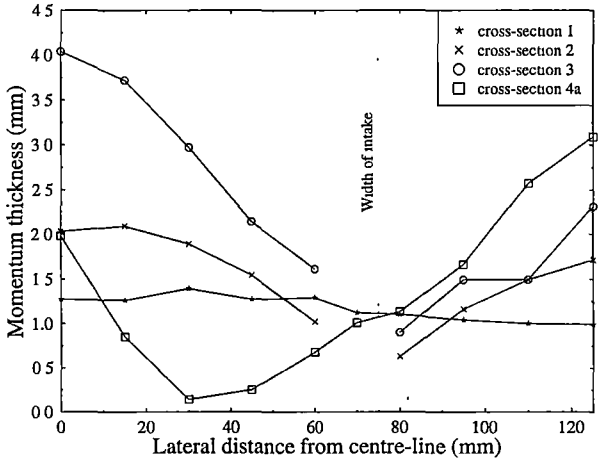

Figure 5.28: Boundary layer momentum thickness derived from hot-wire traverses (IVR=0.58). The discontinuities in the curves for sections 2 and 3 signify the uncertainty in these properties across the intake/hull intersection.

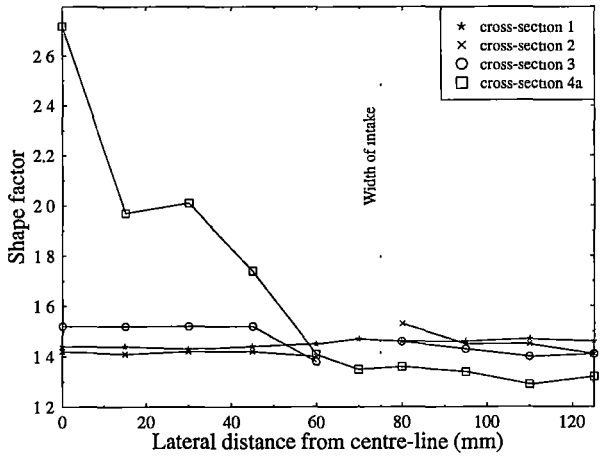

Figure 5.29: Boundary layer shape factors derived from hot-wire traverses (IVR=0.58). The discontinuities in the curves for sections 2 and 3 signify the uncertainty in these properties across the intake/hull intersection.

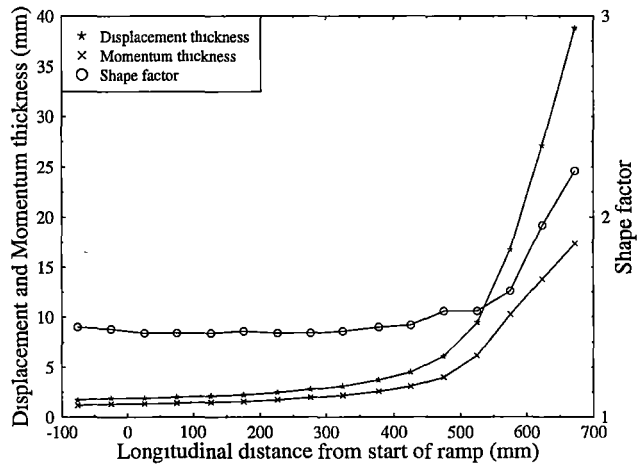

Figure 5.30: Displacement thickness, momentum thickness and shape factors along the centre-line, derived from hot-wire traverses (IVR =0.58).

5.2 Computational Fluid Dynamics

This section presents the FIDAP thin boundary layer simulations. Inflow boundary conditions are based on experimental measurements and are summarised in Section 4.4.1. All the simulations are for the truncated wind-tunnel domain with boundary conditions on this truncation plane supplied from an initial entire wind-tunnel working section and waterjet simulation. All models use and RNG turbulence model unless otherwise specified.

Table 5.5 summarises the principal features of the FIDAP simulations and gives significant single valued results.

Table 5.5: Summary of principal FIDAP parameters.

File	Description	# nodes	IVR	Y^+_{inflow}	AATPC	DC_{60}	$C^*_{f_{min}}$
f1r031	Base grid	41869	0.53	247	0.766	0.411	0.40
f5r031	1.5*density	136237	0.52	174	0.818	0.547	0.12
f5r043	graded closed to wall	136237	0.53	173	0.813	0.587	0.05
f5r044	Speziale turbulence model	136237	0.53	174	0.816	0.529	0.10
f5r045	Launder turbulence model	136237	0.53	174	0.811	0.469	0.13
f8r050	1.89*density	246987	0.52	144	0.788	0.585	-0.05
f2r050	2.0*density	317025	0.52	132	0.774	0.578	-0.14
f6r050	2.17*density	395598	0.52	123	0.770	0.569	-0.09
Experimental			0.59		0.757	0.674	–

* Minimum skin friction on ramp centre-line.

5.2.1 Ingestion Streamtube

Figure 5.31 shows the ingestion streamtube cross-section upstream of the intake with experimental results included for comparison. Note the good agreement in streamtube width.

5.2.2 Static Pressure Distributions

Figure 5.32 shows the ramp centre-line static pressure distribution for three different FIDAP grid densities.

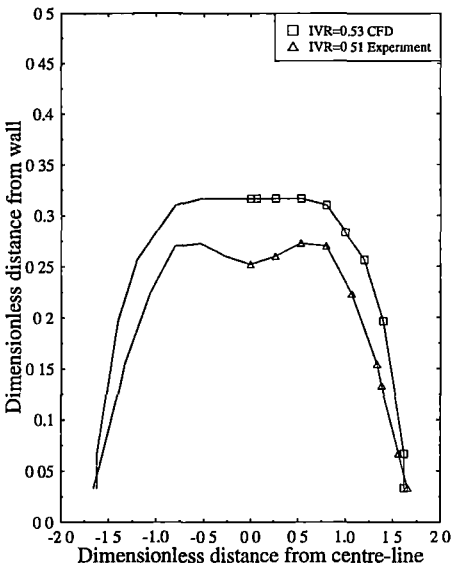

Figure 5.31: Ingestion streamtube cross section, FIDAP and experimental results.

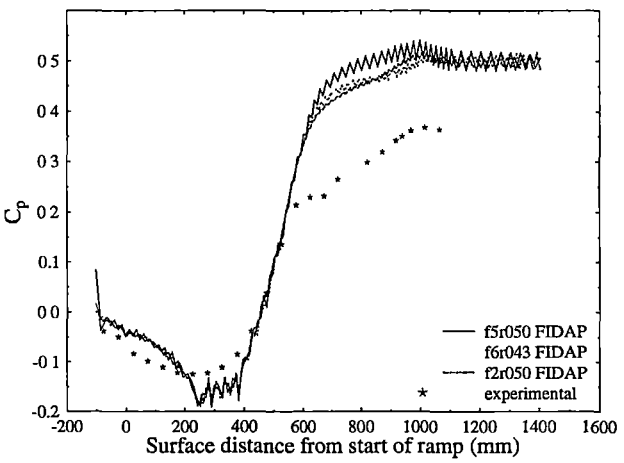

Figure 5.32: FIDAP ramp centre-line static pressure distributions, experimental results also shown for comparison.

5.2.3 Skin Friction

Ramp centre-line skin friction coefficients are shown in Figures 5.33 (for various FIDAP wall element thickness models) and 5.34 (for various FIDAP turbulence models). Figure 5.35 shows the skin friction magnitude distribution over the entire model surface.

5.2.4 Model Cross Sections

Comparison between FIDAP and experimental data for model sections 2 and 3 are presented in Figures 5.36 and 5.37.

5.2.5 Impeller Face Results

Figures 5.38 to 5.45 summarise the FIDAP results at the impeller face in terms of total pressure distributions, area averaged total pressure coefficients and distortion values.

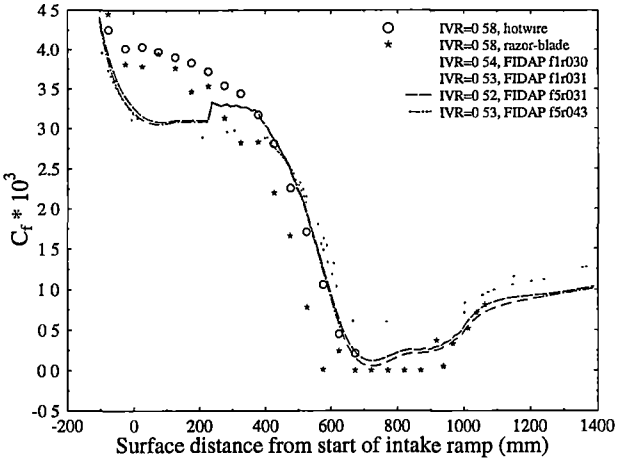

Figure 5.33: FIDAP skin friction coefficients along the ramp centre-line for various wall element thicknesses, also shown are experimental values.

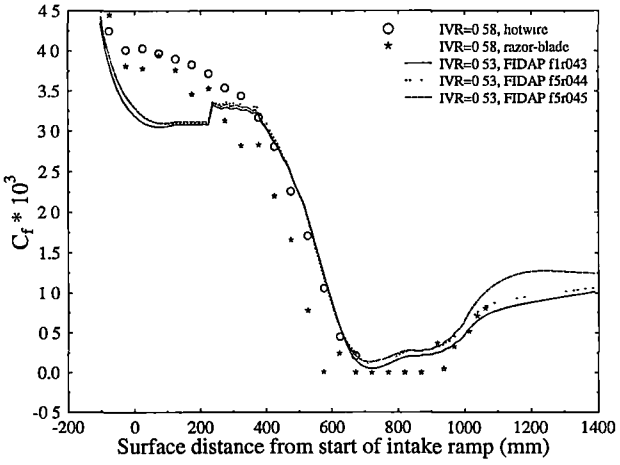

Figure 5.34: FIDAP skin friction coefficients along the ramp centre-line for various turbulence models, also shown are experimental values.

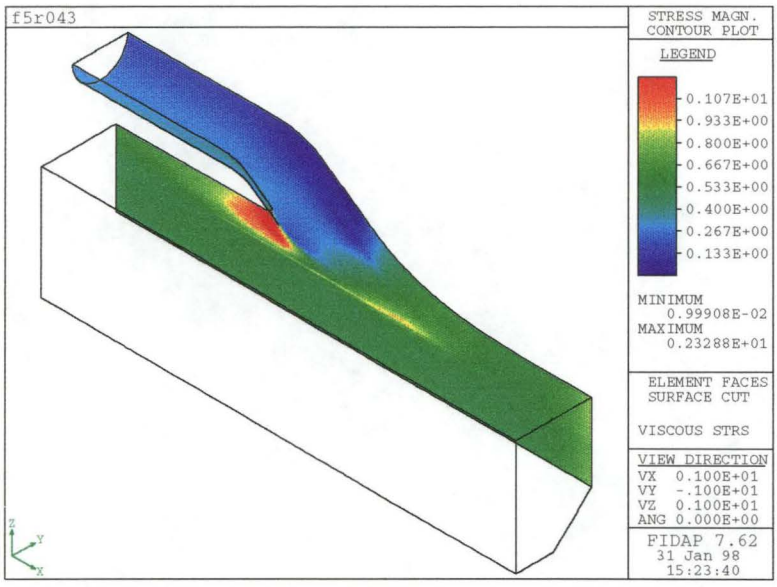

Figure 5.35: Skin friction distribution for FIDAP model f5r043.

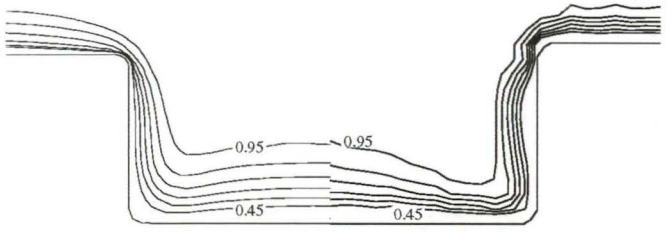

Figure 5.36: Total pressure contours at section 3 of the intake, shown on the left is the FIDAP simulation f2r050 while the experimental results are shown on the right.

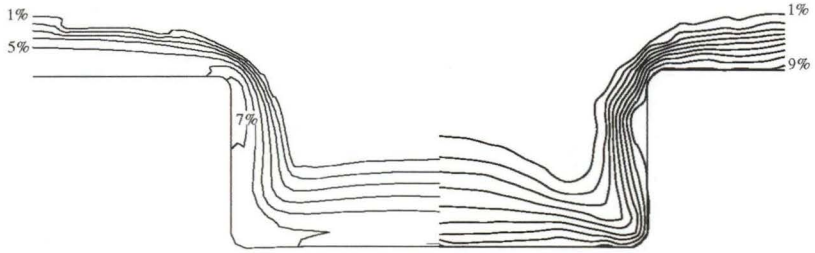

Figure 5.37: Turbulence intensity contours at section 3 of the intake, shown on the left is the FIDAP simulation f2r050 while the experimental results are shown on the right.

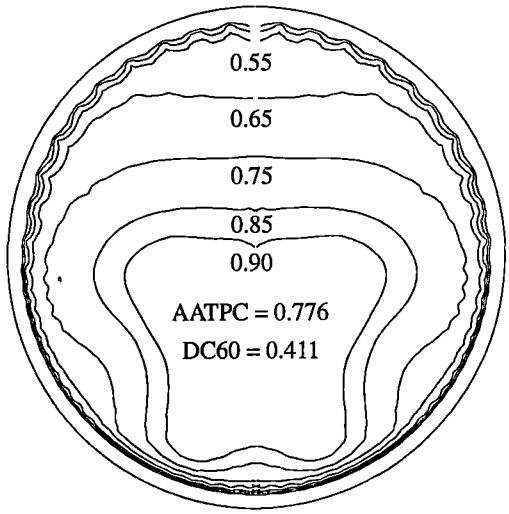

Figure 5.38: Total pressure coefficient contour plot at impeller face for FIDAP solution f1r031.

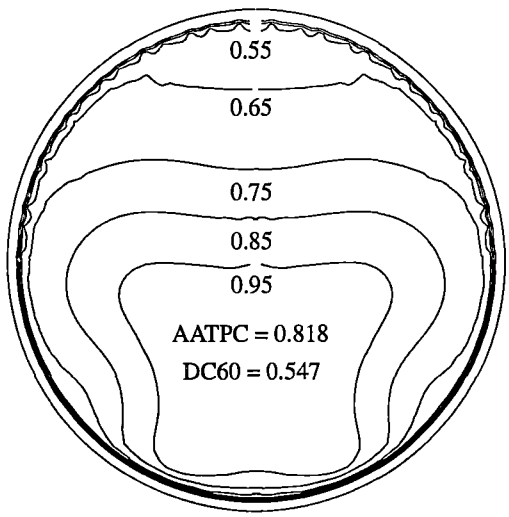

Figure 5.39: Total pressure coefficient contour plot at impeller face for FIDAP solution f5r031.

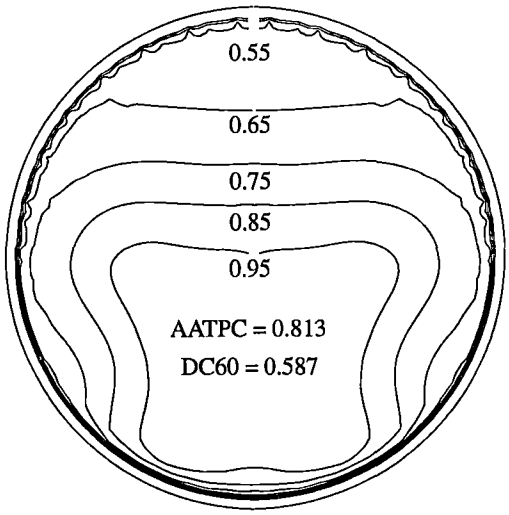

Figure 5.40: Total pressure coefficient contour plot at impeller face for FIDAP solution f5r043.

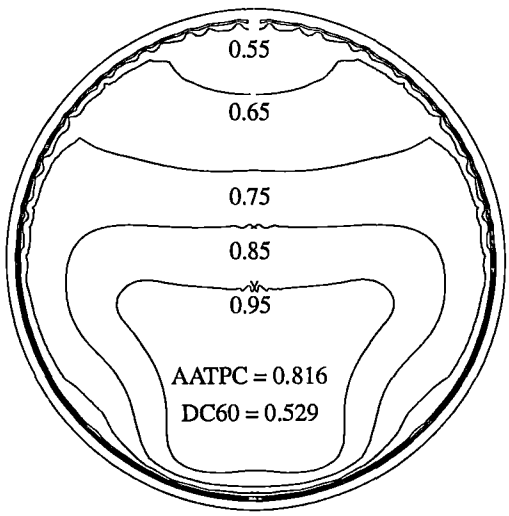

Figure 5.41: Total pressure coefficient contour plot at impeller face for FIDAP solution f5r044.

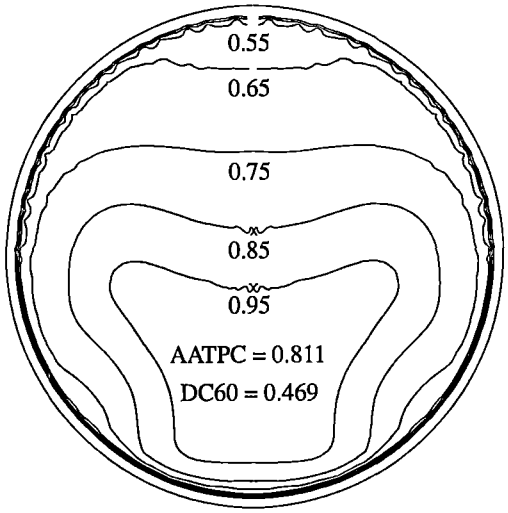

Figure 5.42: Total pressure coefficient contour plot at impeller face for FIDAP solution f5r045.

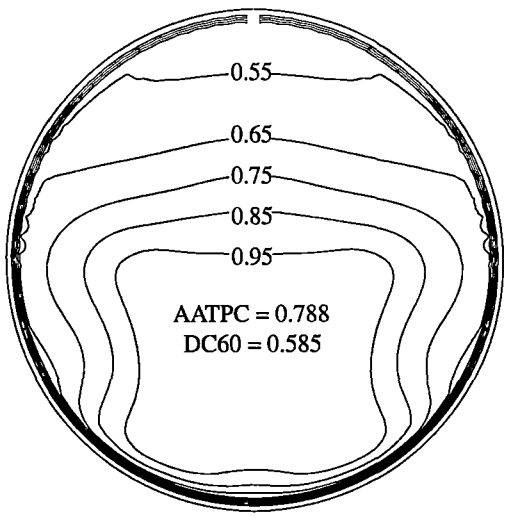

Figure 5.43: Total pressure coefficient contour plot at impeller face for FIDAP solution f8r050.

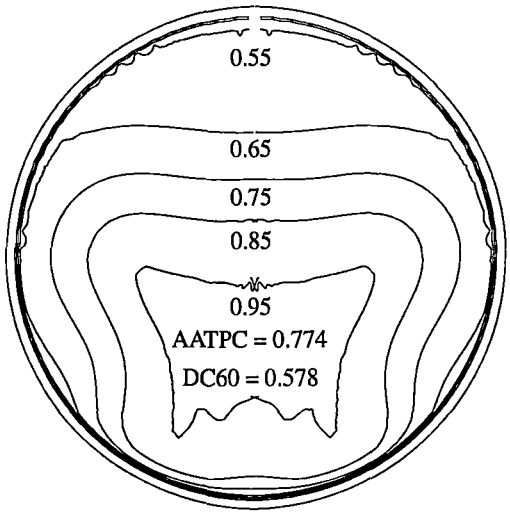

Figure 5.44: Total pressure coefficient contour plot at impeller face for FIDAP solution f2r050.

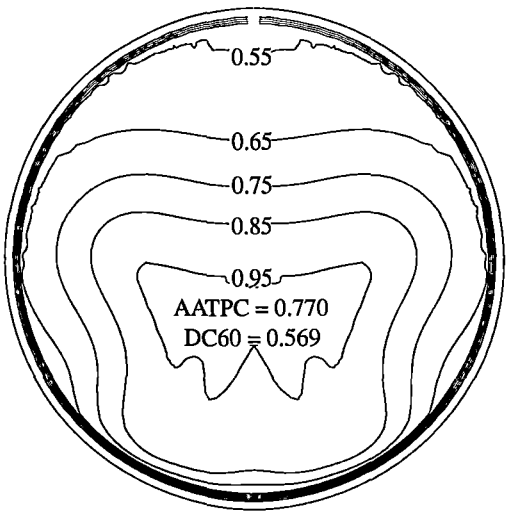

Figure 5.45: Total pressure coefficient contour plot at impeller face for FIDAP solution f6r050.

Chapter 6

Thick Boundary Layer Results

Experimental and computational results are presented in turn for cruise operation with a thickened intake boundary layer in this chapter. The naturally thin wind tunnel boundary layer (momentum thickness of 1.2 mm) was artificially thickened by normal blowing to produce a boundary layer with momentum thickness of between 5 and 6 mm (there is some spanwise variation). A calculation for a typical fast ferry installation gives a model scale boundary layer thickness of 6.6 mm (see Section 3.5.0.1), so this is a realistic boundary layer thickness for testing.

6.1 Experimental

6.1.1 Bounding Ingestion Stream-tubes

Figure 6.1 shows the carbon monoxide ingestion stream-tube results for the thick boundary layer study. Table 6.1 summarises the results and also gives interpolated thin boundary layer results. The measurement plane was at station 1, 75 mm upstream of the start of the intake ramp.

Table 6.1: Comparison of ingestion stream-tube cross sectional areas as directly measured (via the CO gas tracer technique) and calculated, also shown is an interpolated thin boundary layer result for the same IVR.

IVR	Cross sectional area^{+} (mm^2)	Difference in flow rate* (%)	Case
0.58	4707	-9.8	Thick boundary layer
0.58	4742	N/A	Thin boundary layer

$^{+}$ Estimated by extrapolating the stream-tube boundaries to the wall
* Percentage difference between flow through intake cross section and orifice plate reading normalised by orifice plate reading

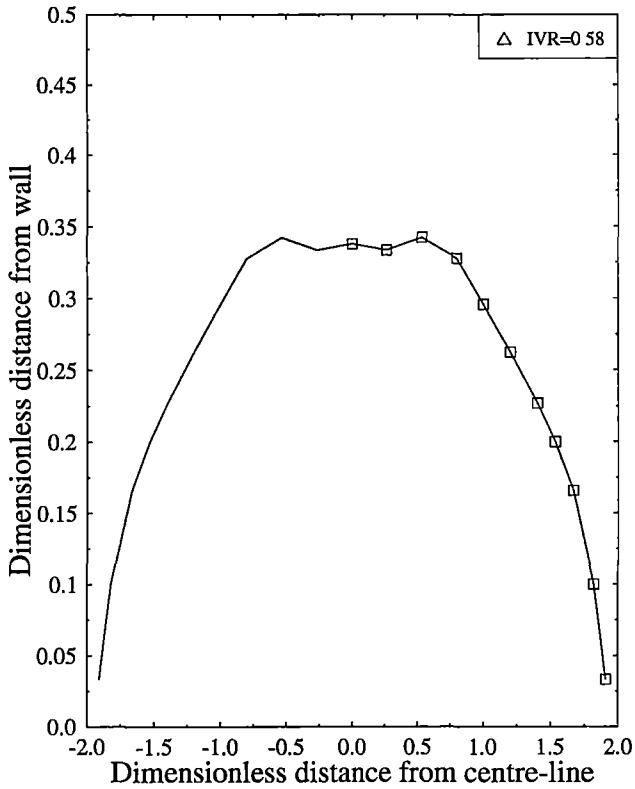

Figure 6.1: Boundary ingestion stream-tube cross section, distances non-dimensionalised by the intake diameter.

6.1.2 Flow Visualisation

The fluorescent mini-tuft visualisation was conducted for various inlet velocity ratios and free stream velocities with cruise results shown in Figure 6.2. Separation is evident at low IVR's with Table 6.2 giving the position of this flow separation.

6.1.3 Static Pressure Distributions

Static pressure coefficient distributions are shown in Figure 6.3 for the ramp centre-line and Figure 6.4 for the bottom half-circumference at the impeller face.

6.1.4 Skin Friction

Figure 6.5 shows skin friction coefficient vectors for the thick boundary layer case measured by the razor blade technique. Ramp centre-line skin friction coefficient magnitude

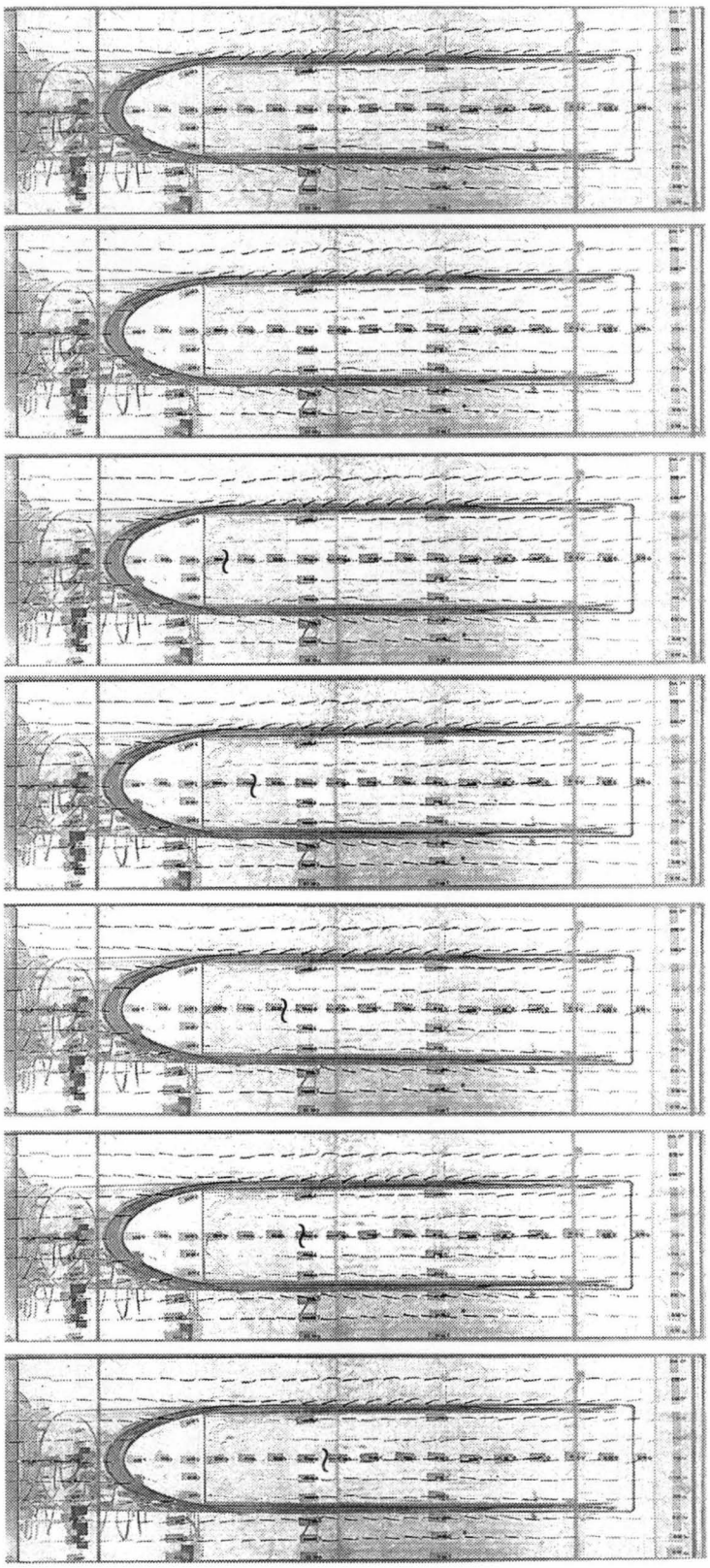

Figure 6.2: Fluorescent mini-tuft visualisation results for $Re_d = 199 * 10^3 \pm 5\%$. Intake ramp separation and re-attachment downstream of cut-water separation are indicated ($\wr$) where appropriate.

Table 6.2: Distance along intake ramp to separation as observed using fluorescent mini-tuft visualisation. Note no cutwater separation is evident as distinct from the thin boundary layer case.

IVR	Ramp separation point (mm from start of intake)
0.35	480
0.45	510
0.51	540
0.58	585
0.65	630
No separation evident for higher IVR's	

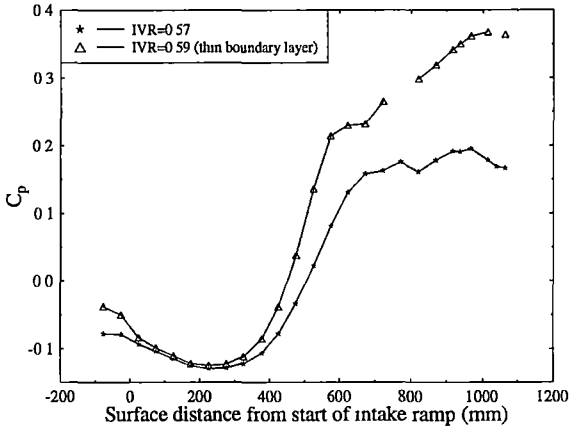

Figure 6.3: Ramp centre-line static pressure coefficient distribution.

measured using both the razor blade technique and hot wire measurements is given in Figure 6.6.

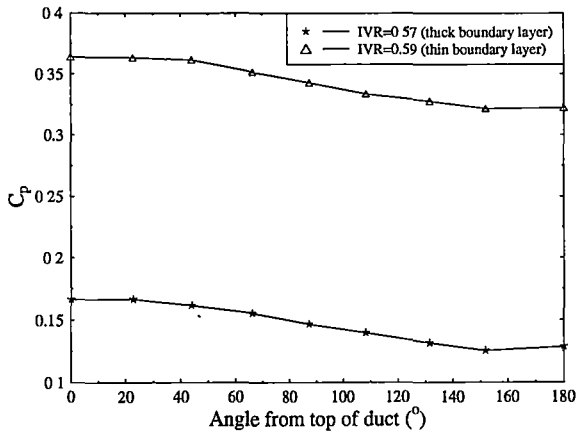

Figure 6.4: Impeller face half-circumference static pressure coefficient distribution.

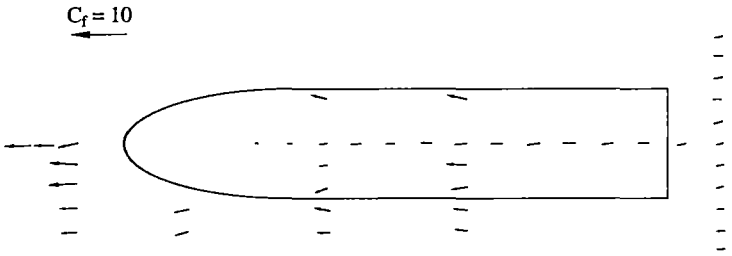

Figure 6.5: Vector plot of skin friction coefficient for IVR=0.57.

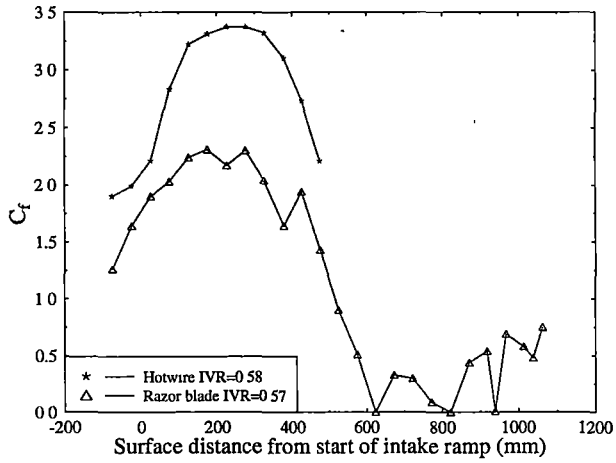

Figure 6.6: Comparison of skin friction coefficients along the ramp centre-line measured via hot-wire traverses and the razor blade technique.

6.1.5 5 Hole Pressure Probe Traverses

6.1.5.1 Free-stream/model cross-sections

Secondary flow velocity vectors and total pressure coefficient contour plots for the same cross sections as used in Chapter 5 are shown in Figures 6.7–6.10.

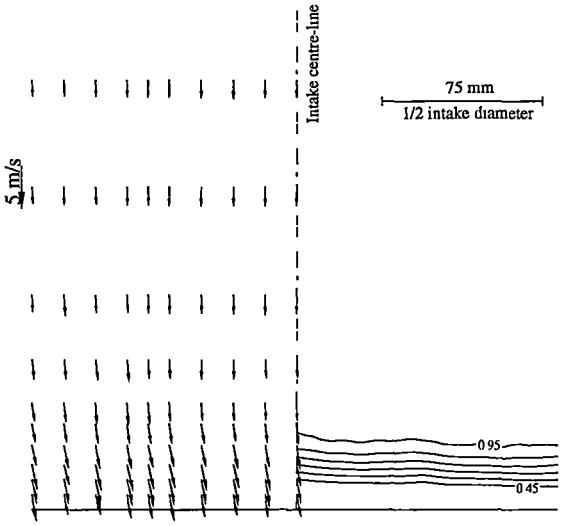

Figure 6.7: Secondary flow velocity vectors (left) and total pressure coefficient contours (right) at cross section 1, IVR 0.59 and U_∞=15.94 m/s.

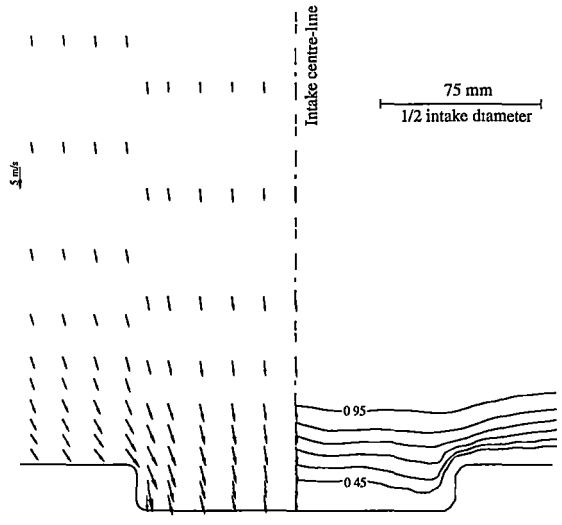

Figure 6.8: Secondary flow velocity vectors (left) and total pressure coefficient contours (right) at cross section 2, IVR 0.59 and U_∞=16.22 m/s.

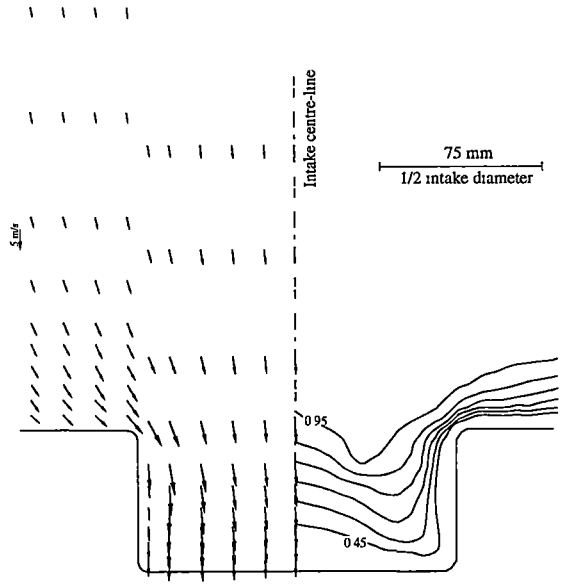

Figure 6.9: Secondary flow velocity vectors (left) and total pressure coefficient contours (right) at cross section 3, IVR 0.59 and U_∞=16.19 m/s.

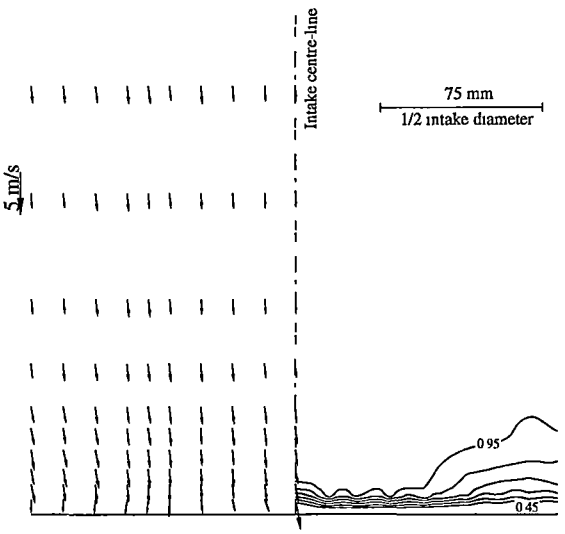

Figure 6.10: Secondary flow velocity vectors (left) and total pressure coefficient contours (right) at cross section 4, IVR 0.59 and U_∞=17.83 m/s.

6.1.5.2 Impeller Face

Figure 6.11 shows total pressure coefficient at the impeller face. Table 6.3 compares the experimental thick and thin boundary layer cases. Secondary flows at the impeller face are given in Figures 6.12– 6.13.

Table 6.3: Comparison of experimental thick and thin boundary layer cases giving total pressure and distortion coefficients at impeller face

Source	IVR	C_p	AATPC	TPC^*	DC60
Thin boundary layer	0.59	0.343	0.757	0.72	0.674
Thick boundary layer	0.59	0.147	0.558	0.508	0.639

* from Idel'chik [67] and Manins [84]

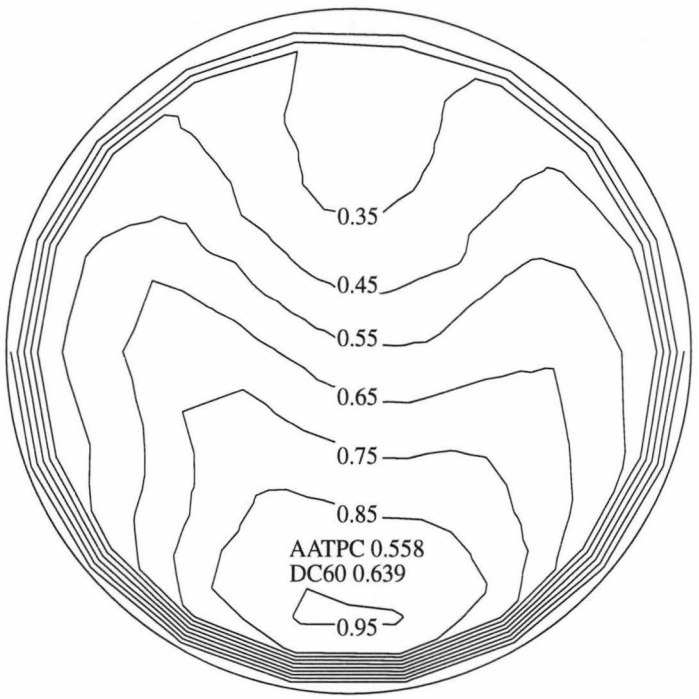

Figure 6.11: Total pressure coefficients at the impeller face for IVR=0.59.

6.1.6 Hot-wire Observations

Figures 6.14–6.17 give contour plots of speed (perpendicular to sensor) normalised by free stream velocity and turbulence intensity ($=\frac{\sqrt{u'^2}}{U_\infty}$) at several cross-sections. Figures 6.18 and 6.19 provide the distribution of these quantities on the ramp centre-line. Boundary layer displacement thickness, momentum thickness and shape factor values derived from the hot-wire observations are given in Figures 6.20–6.23.

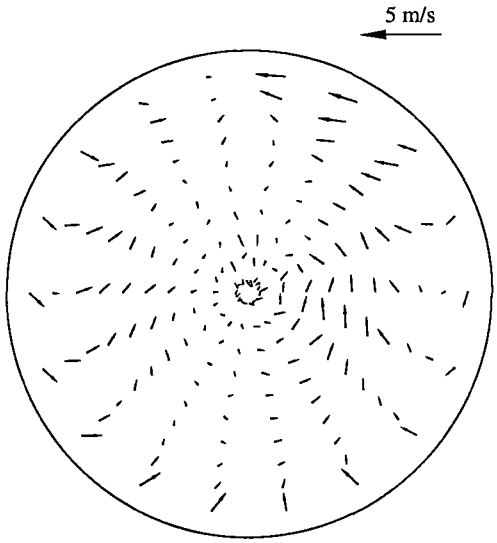

Figure 6.12: Secondary flow at the impeller face for IVR=0.59 and $\overline{U}_{\text{duct}}$=10.76 m/s.

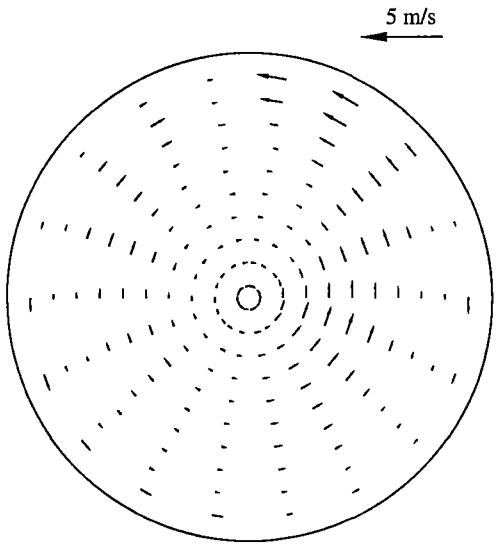

Figure 6.13: Circumferential component of secondary flow at the impeller face for IVR=0.59 and $\overline{U}_{\text{duct}}$=10.76 m/s.

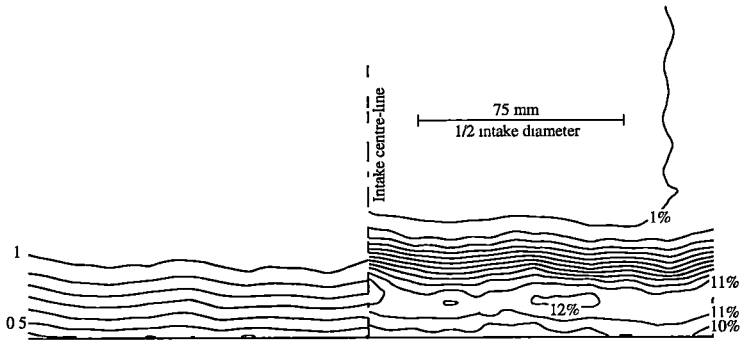

Figure 6.14: Mean velocity contours (left) and turbulence contours (right) at cross section 1, IVR 0.62 and U_∞=17.37 m/s.

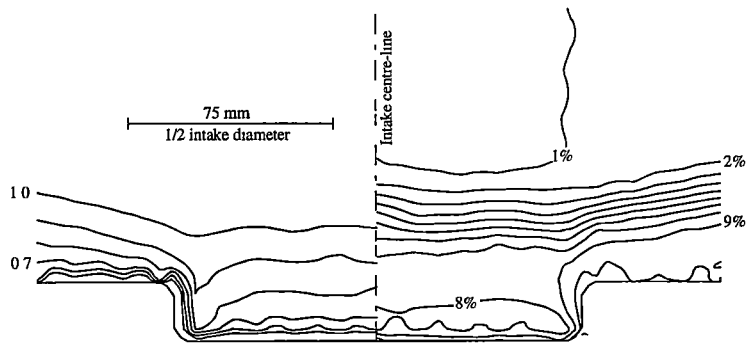

Figure 6.15: Mean velocity contours (left) and turbulence contours (right) at cross section 2, IVR 0.58 and U_∞=18.46 m/s.

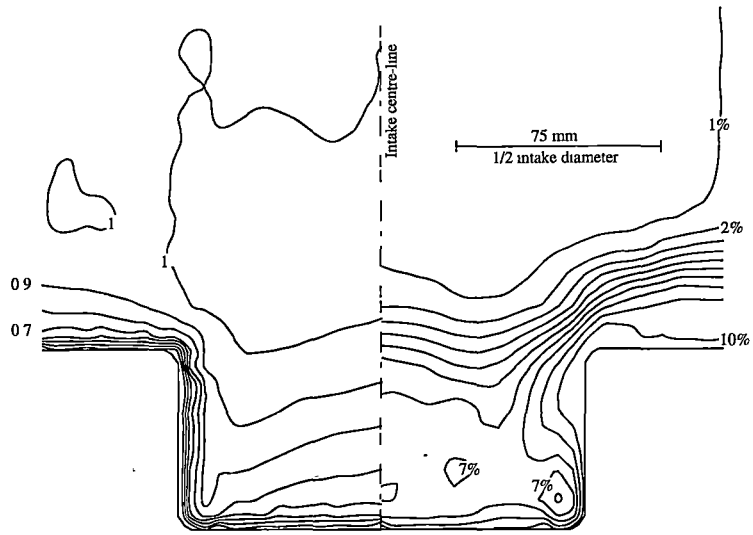

Figure 6.16: Mean velocity contours (left) and turbulence contours (right) at cross section 3, IVR 0.58 and U_∞=18.47 m/s.

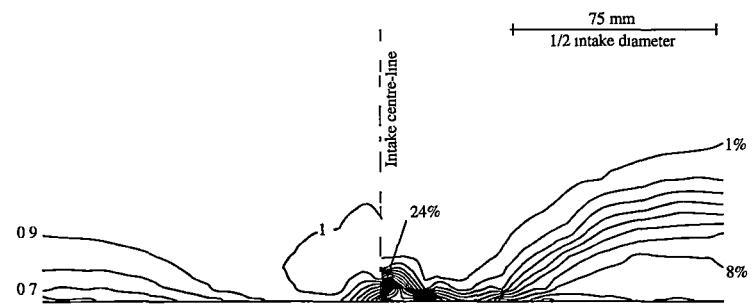

Figure 6.17: Mean velocity contours (left) and turbulence contours (right) at cross section 4a, IVR 0.60 and U_∞=17.74 m/s.

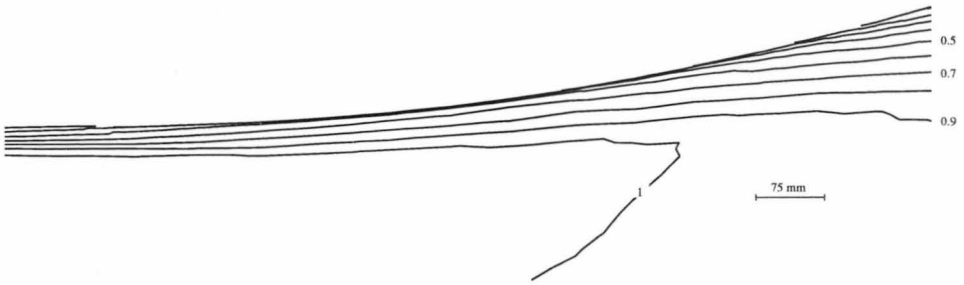

Figure 6.18: Mean velocity contours along the centre-line in the region of the ramp, IVR=0.58 and U_∞=18.40 m/s.

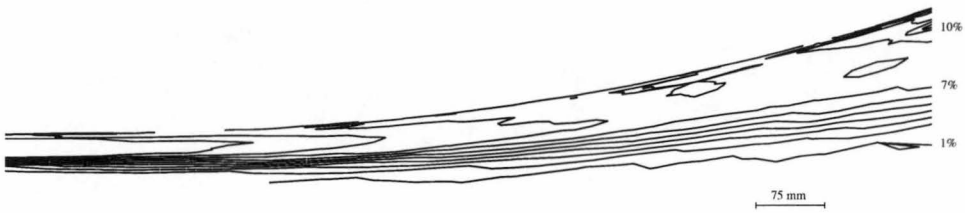

Figure 6.19: Turbulence contours along the centre-line in the region of the ramp, IVR=0.58 and U_∞=18.40 m/s.

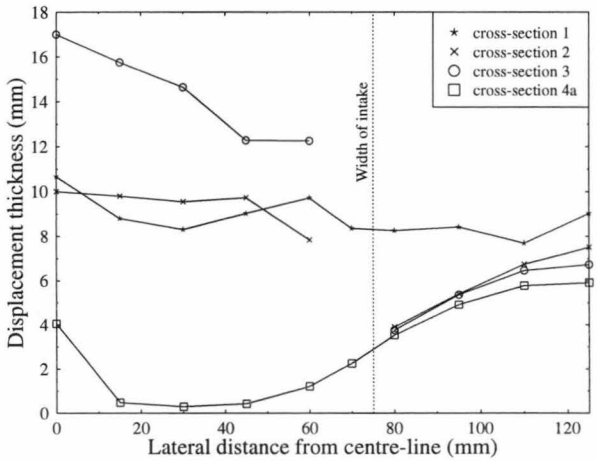

Figure 6.20: Boundary layer displacement thickness derived from hot-wire traverses (IVR =0.58). The discontinuities in the curves for sections 2 and 3 signify the uncertainty in these properties across the intake/hull intersection.

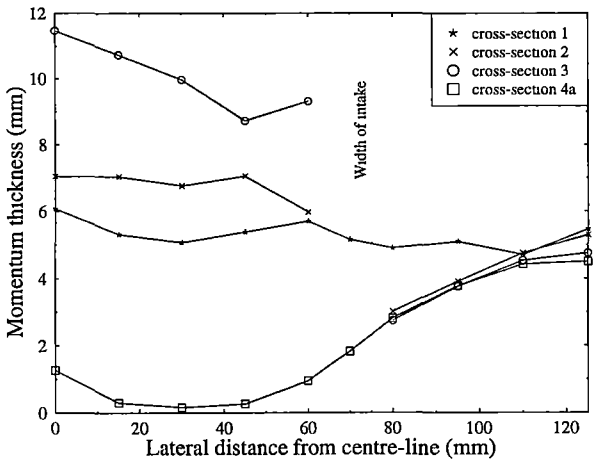

Figure 6.21: Boundary layer momentum thickness derived from hot-wire traverses (IVR =0.58). The discontinuities in the curves for sections 2 and 3 signify the uncertainty in these properties across the intake/hull intersection.

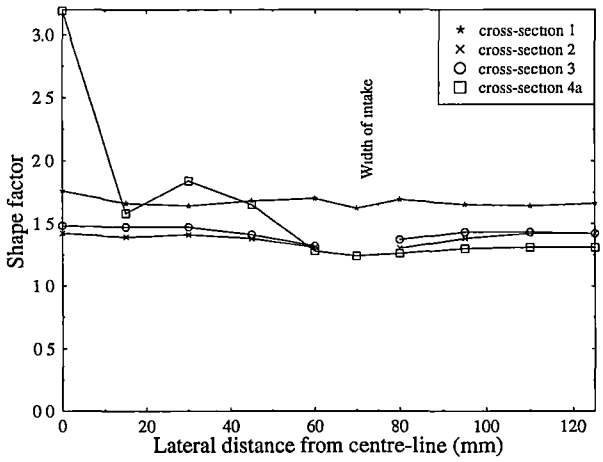

Figure 6.22: Boundary layer shape factors derived from hot-wire traverses (IVR =0.58). The discontinuities in the curves for sections 2 and 3 signify the uncertainty in these properties across the intake/hull intersection.

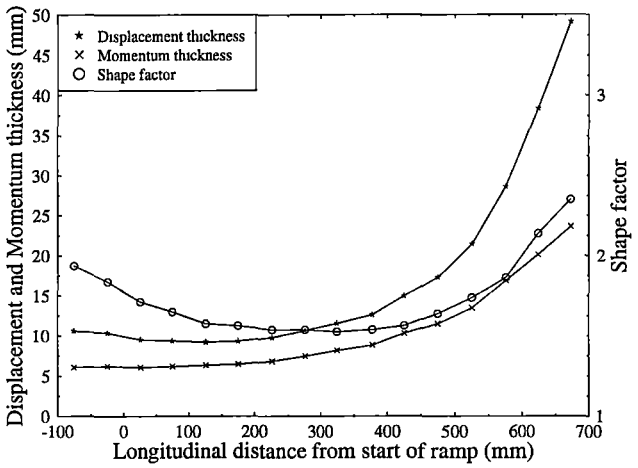

Figure 6.23: Displacement thickness, momentum thickness and shape factors along the centre-line, derived from hot-wire traverses (IVR =0.58).

6.2 Computational Fluid Dynamics

This section presents the FIDAP thick boundary layer simulation. Inflow boundary conditions are based on experimental measurements.

Table 6.4 summarises the principal features of the FIDAP simulation and gives significant single valued results.

Table 6.4: Summary of principal FIDAP parameters.

File	Description	# nodes	IVR	AATPC	DC_{60}	$C^*_{f_{min}}$
f5r945	Thick boundary layer	136237	0.60	0.561	0.592	0.47
Experimental			0.59	0.558	0.639	–

* Minimum skin friction on ramp centre-line.

6.2.1 Ingestion Streamtube

Figure 6.24 shows the ingestion streamtube cross-section upstream of the intake with experimental results included for comparison. Note the good agreement in streamtube width.

6.2.2 Static Pressure Distributions

Figure 6.25 shows the ramp centre-line static pressure distribution for the thick boundary layer simulation.

6.2.3 Skin Friction

Ramp centre-line skin friction coefficient distributions are shown in Figure 6.26, while the skin friction magnitude distribution over the entire model surface is given in Figure 6.27.

6.2.4 Impeller Face Results

Figure 6.28 summarises the FIDAP results at the impeller face in terms of total pressure distributions, area averaged total pressure coefficients and distortion values.

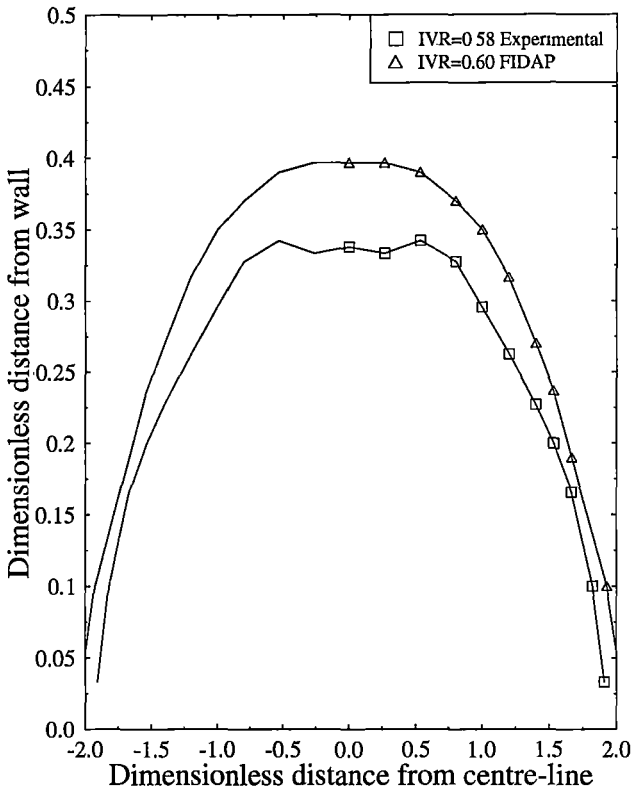

Figure 6.24: Ingestion streamtube cross section, FIDAP and experimental results.

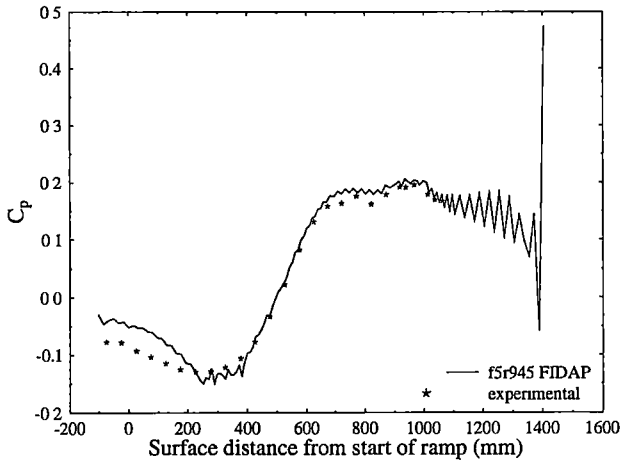

Figure 6.25: FIDAP ramp centre-line static pressure distribution, experimental results also shown for comparison.

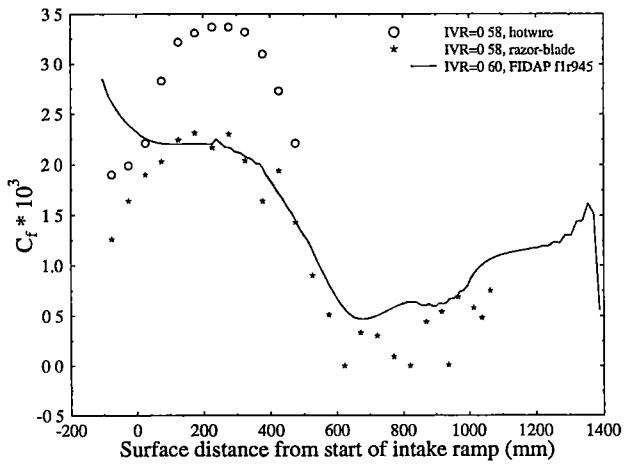

Figure 6.26: FIDAP skin friction coefficients along the ramp centre-line, also shown are experimental values.

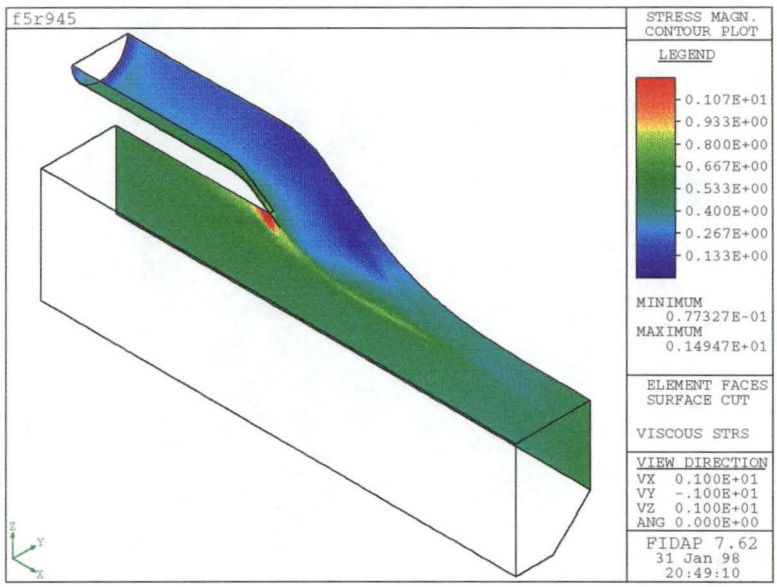

Figure 6.27: Skin friction distribution for FIDAP thick boundary layer simulation.

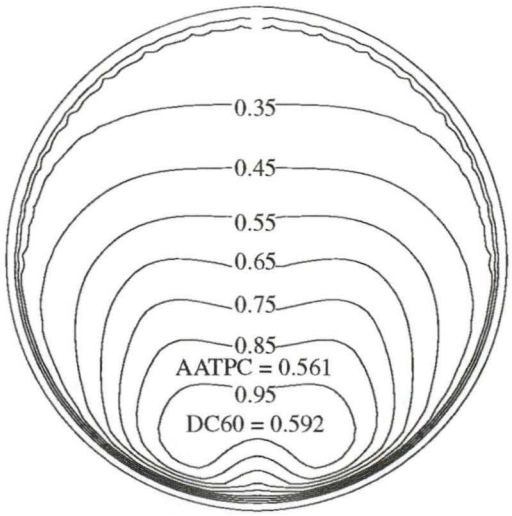

Figure 6.28: Total pressure coefficient contour plot at impeller face for FIDAP solution f5r945.

Chapter 7

Manoeuvring Results

This chapter presents experimental and computational results for manoeuvring operation (zero boat speed). Computational results showing the improvement in manoeuvring performance achieved by cutwater lip thickening are also presented. Finally, the cruise performance of this thickened cutwater lip intake is presented.

7.1 Experimental

7.1.1 Flow Visualisation

Fluorescent mini-tuft visualisation results for static operation are shown in Figure 7.1. At static operation a large percentage of the flow appears to be drawn from around the cutwater, with very little being drawn along the ramp.

7.1.2 Static Pressure Distributions

Static pressure distributions are shown for the bottom half-circumference at the impeller face in Figure 7.2. The static pressure coefficient for manoeuvring operation is defined as

$$C_p = \frac{p - p_\infty}{1/2\rho u_{\text{duct}}^2} \tag{7.1}$$

7.1.3 5 Hole Pressure Probe Traverses

Figure 7.3 shows total pressure coefficient contours at the impeller face. The irregular nature of the plot is indicative of the flow unsteadiness due to separation at the cutwater. This unsteadiness was further indicated by the difficulty in achieving null yaw for the probe. For steady flow (e.g., cruise operation) null yaw was typically achieved in one iteration and only occasionally required two iterations. For the manoeuvring case it typically required three, and frequently up to five, iterations to achieve null yaw.

For manoeuvring operation the total pressure coefficient is defined as

$$C_P = 1 + \frac{P - p_\infty}{1/2\rho u_{\text{duct}}^2}. \tag{7.2}$$

The constant 1 is introduced to allow for direct comparison with cruise operation.

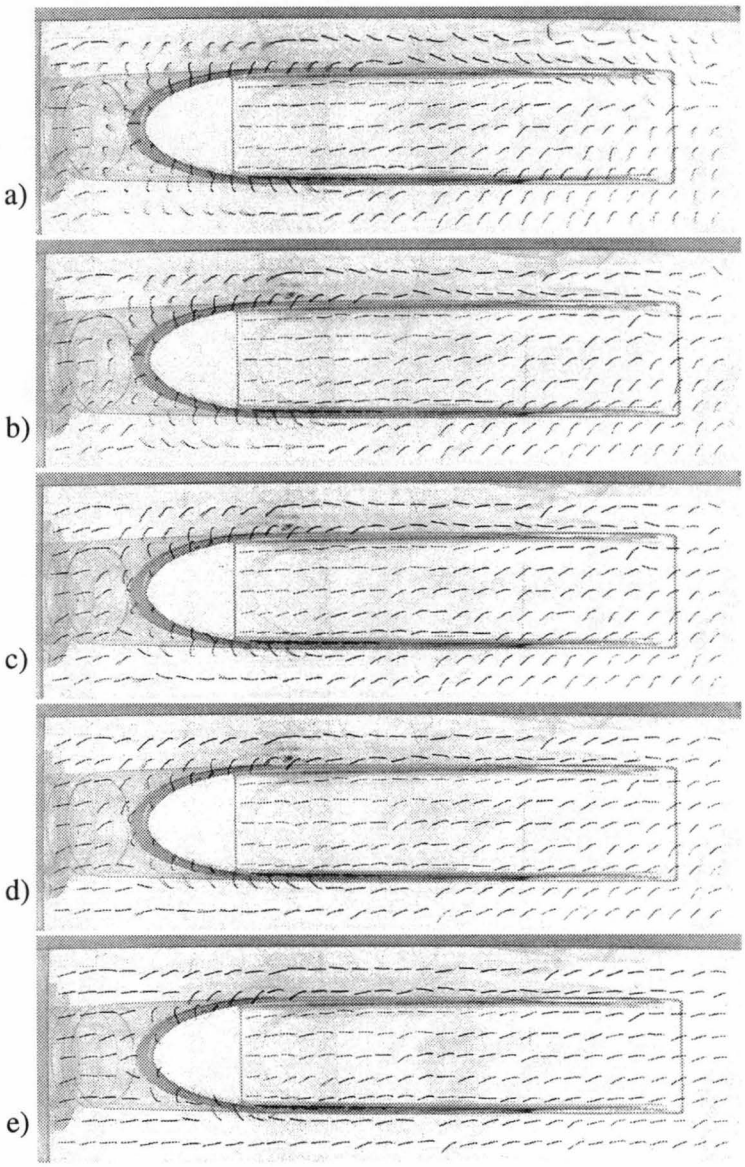

Figure 7.1: Fluorescent mini-tuft visualisation results for static operation.

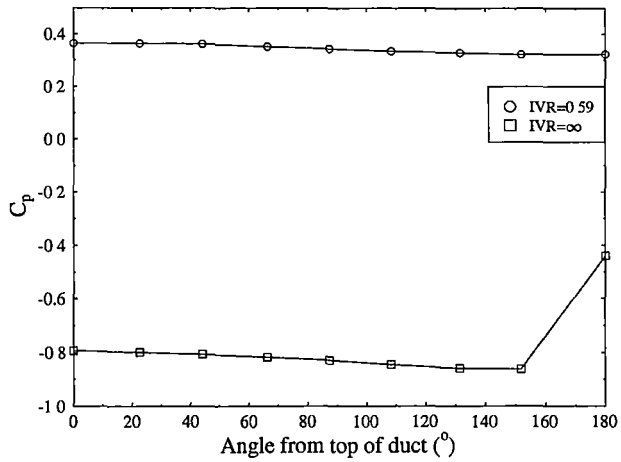

Figure 7.2: Impeller face half-circumference static pressure coefficient distribution. A typical cruise case (IVR=0.59) is shown for comparison purposes.

With the definition of total pressure coefficient used throughout this thesis a value of 1.0 represents lossless flow, while values below 1.0 represent flow losses.

Table 7.1 summarises these results.

Table 7.1: Comparison of experimental and empirical total pressure and experimental distortion coefficients at impeller face.

IVR	C_p	AATPC	TPC^*	DC60
∞	-0.826	0.244	0.05	0.676

* from Idel'chik [67]

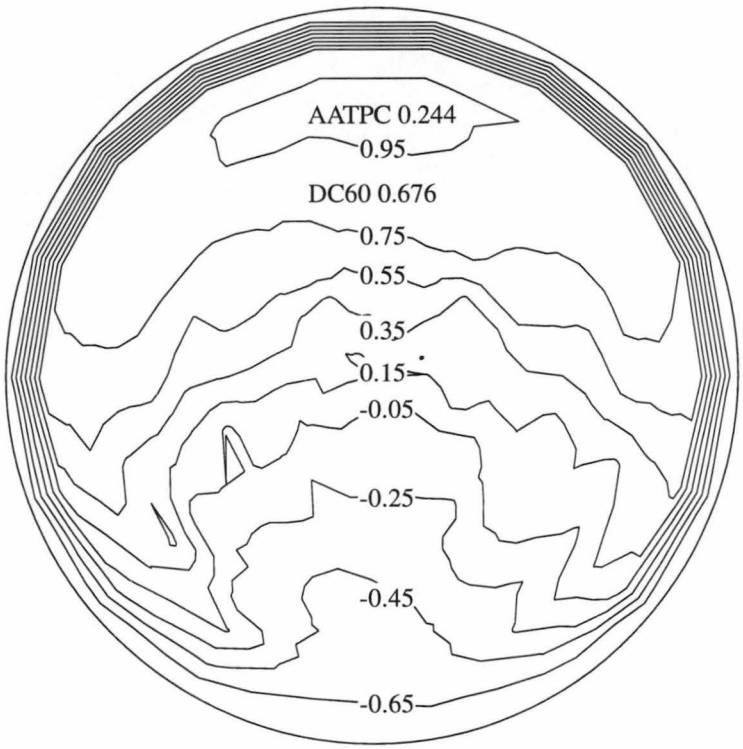

Figure 7.3: Total pressure coefficients at the impeller face for manoeuvring case.

7.2 Computational Fluid Dynamics

Three distinct FIDAP solutions sets are presented, namely thin and thick cutwater manoeuvring operation and thick cutwater cruise operation. Table 7.2 summarises the principal features of the FIDAP simulations and gives significant single valued results.

Table 7.2: Summary of principal FIDAP parameters.

File	Description	# nodes	U_{duct}	AATPC	DC_{60}
Manoeuvring operation					
f5r065	Thin cutwater	136237	5.01	0.170	0.767
Experimental	Thin cutwater		6.36	0.244	0.676
f5r067	Thick cutwater	136237	5.01	0.563	0.795
Thick cutwater cruise operation					
f5r992	1.5*density	136237	5.01	0.543	0.542

7.2.1 Thin Cutwater

Figures 7.4 and 7.5 show the FIDAP results for the thin cutwater (full scale cutwater radius of 50 mm) simulation. The boundary conditions for this simulation were a prescribed jet outflow velocity profile of average velocity 5 m/s and free inflow from all non-wall boundaries (except the symmetry boundary) with typical free stream kinetic turbulence energy and dissipation values.

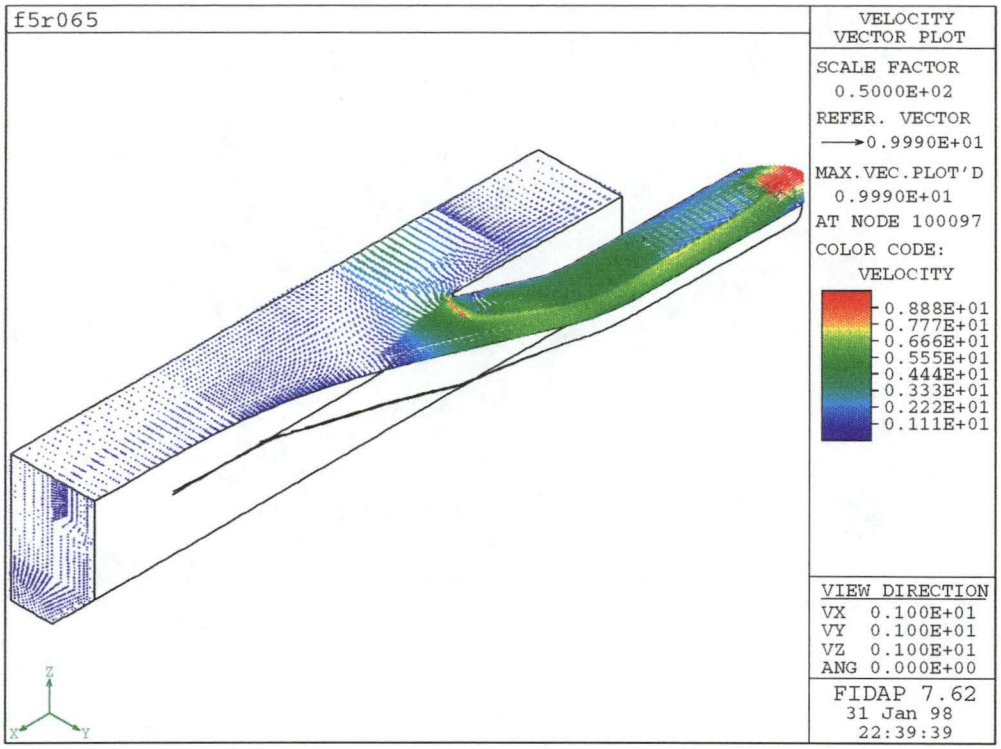

Figure 7.4: Velocity vector plot of manoeuvring operation for FIDAP thin cutwater model, $\overline{U}_{\text{duct}}$=5.01 m/s.

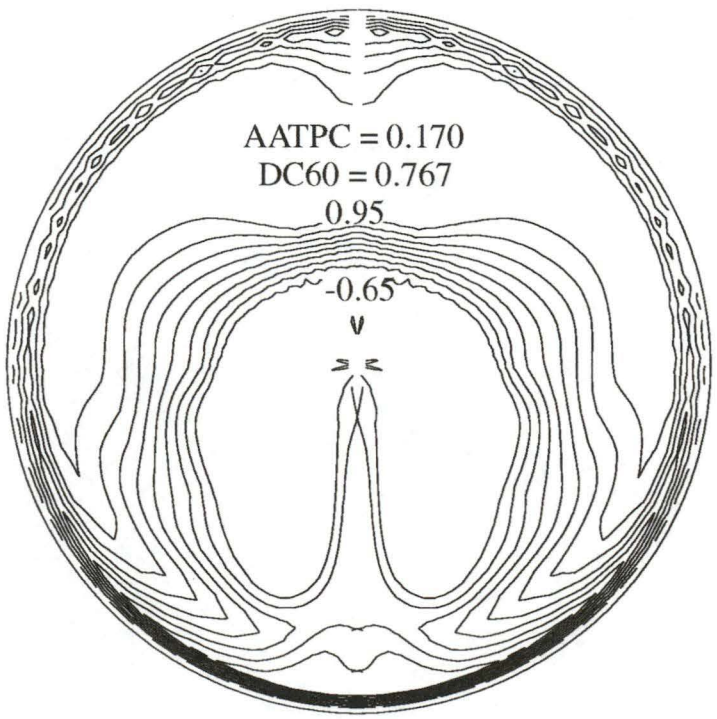

Figure 7.5: Impeller face total pressure coefficient contour plot for thin cutwater case.

7.2.2 Thick Cutwater

Figures 7.6 and 7.7 show the FIDAP results for the thick cutwater (full scale cutwater radius of 150 mm) simulation.

Table 7.3 compares the experimental results and FIDAP simulations in terms of area averages total pressure coefficient and distortion. Also included in this table is an empirical approximation for the total pressure coefficient. This empirical approximation was calculated from data in Idel'chik [67, Diagram 3-2] for the entrance loss of a flush mounted tube inclined at an angle θ (in this case θ=22.5°), ie.

$$\frac{\Delta P}{0.5\rho U_{\text{duct}}^2} = 0.5 + 0.3\cos\theta + 0.2\cos^2\theta. \tag{7.3}$$

Table 7.3: Comparison of experimental and FIDAP manoeuvring results including thick cutwater simulation.

Case	AATPC	DC_{60}
Experimental	0.244	0.676
CFD - Thin cutwater	0.170	0.767
CFD - Thick cutwater	0.563	0.795
Idel'chik [67]	0.05	–

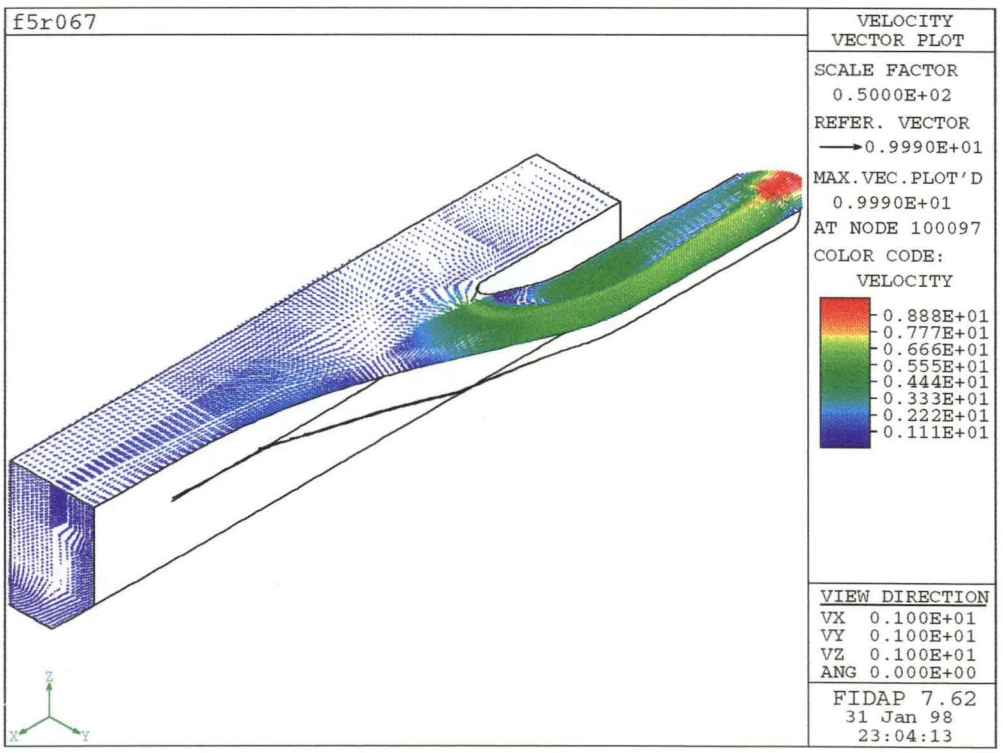

Figure 7.6: Velocity vector plot of manoeuvring operation for FIDAP thick cutwater model, $\overline{U}_{\text{duct}}$=5.01 m/s.

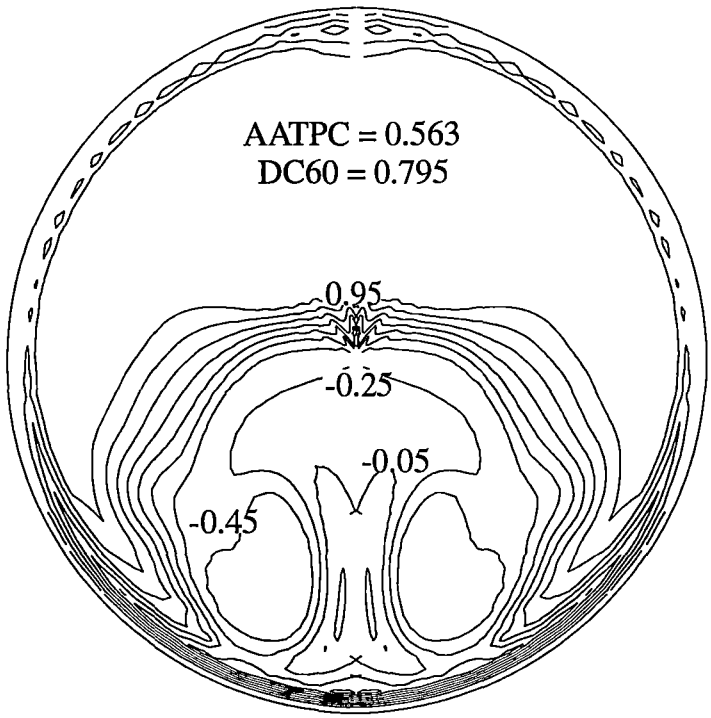

Figure 7.7: Impeller face total pressure coefficient contour plot for thick cutwater case.

7.2.3 Thick Cutwater Cruise Operation

Due to the large improvement in manoeuvring performance obtained with a thickened cutwater lip, cruise performance of this intake was also undertaken. Figures 7.8 and 7.9 show the FIDAP results for the thick cutwater (full scale cutwater radius of 150 mm) simulation.

A surface distribution of skin friction for this intake is shown in Figure 7.10.

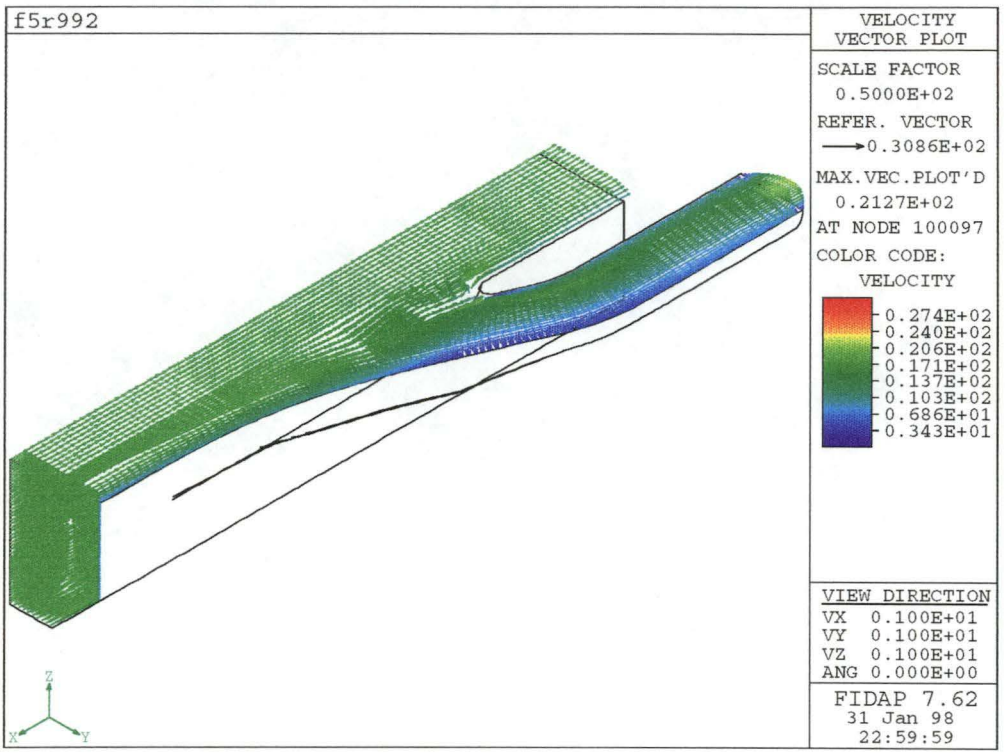

Figure 7.8: Velocity vector plot of cruise operation for FIDAP thick cutwater model.

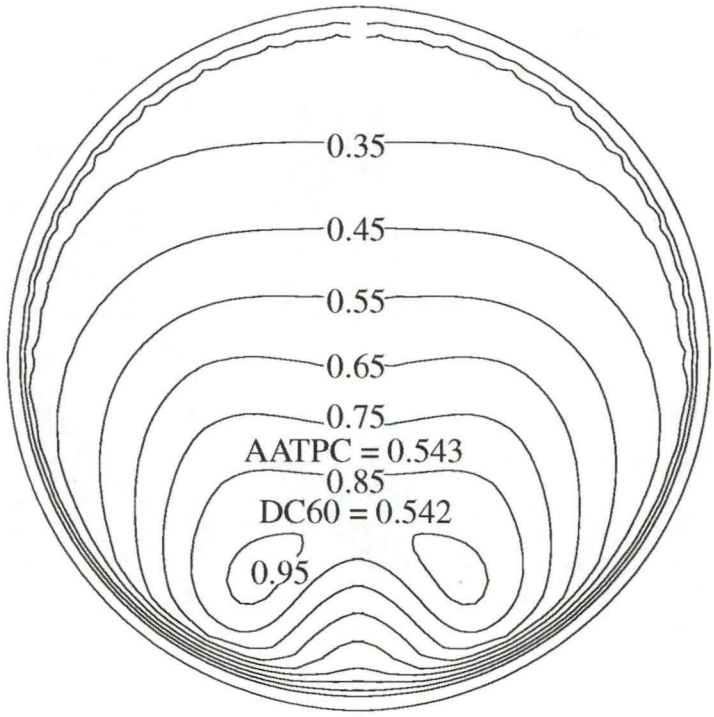

Figure 7.9: Impeller face total pressure coefficient contour plot for thick cutwater cruise operation.

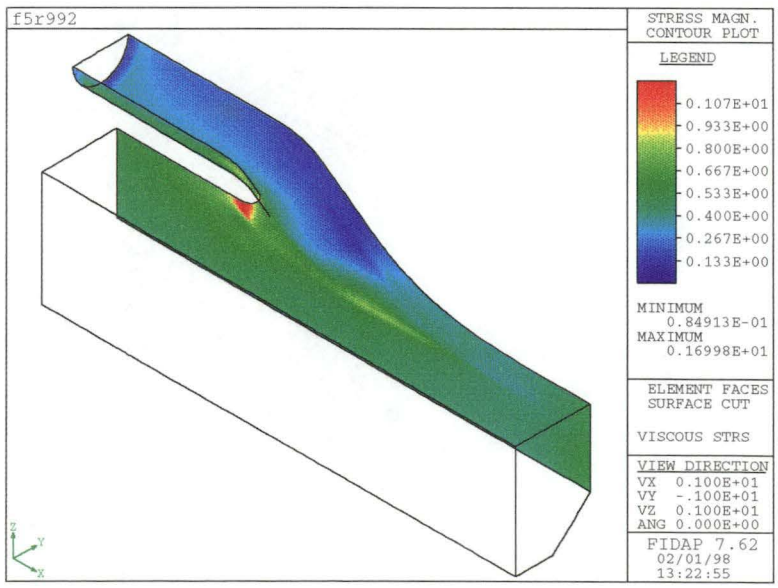

Figure 7.10: Skin friction distribution for FIDAP model f5r992.

Chapter 8

Discussion

The experimental and computational research carried out here has established that hull boundary layer thickness is a significant issue in waterjet intake performance. In particular, a thickening of the hull boundary layer will result in a corresponding decrease in the area averaged total pressure at the impeller face. The static pressure at impeller face is also lowered in thickened hull boundary layer operation. Specific issues arising from both the experimental and computational programs are discussed in turn in this chapter.

8.1 Experimental

8.1.1 Intake Ramp Separation

Separation from the intake ramp was directly observed via fluorescent mini-tuft visualisation and found to occur further forward at lower intake velocity ratios (IVR's). Static pressure measurements along the ramp centre-line also gave an approximate indication of separation.

Separation was predicted using Stratford's [125] criterion (Equation 8.1) for the turbulent boundary layer

$$\chi = A\left(R_e * 10^{-6}\right)^{0.1} - C_p\sqrt{s\left|\frac{dC_p}{ds}\right|} \tag{8.1}$$

where A is an empirical constant, s the distance along the surface and R_e is a surface distance based Reynolds number. The constant A has a value of 0.39 when $\frac{d^2p}{ds^2} \geq 0$ and $C_p \leq 4/7$, while if $\frac{d^2p}{ds^2} < 0$ the value of A is changed to 0.35. Separation is indicated by a negative value of χ. The modulus inside the square root in Equation 8.1 is introduced to simplify the analysis as in reality a negative argument represents accelerating flow and separation is unlikely. As Equation 8.1 involves the surface distance (s), a virtual origin of the turbulent boundary layer (and hence s) was calculated for the experimentally measured momentum thickness (θ) of 1.4 mm at inflow. Using the relation from White [149] for a continuously turbulent boundary layer in zero pressure gradient

$$\theta = 0.036s\left(\frac{U_\infty s}{\nu}\right)^{-1/5} \tag{8.2}$$

resulted in a virtual origin 574 mm upstream of the inflow measuring station.

A typical prediction using this method is given in Figure 8.1. In this particular example (IVR=0.36), separation is first predicted at 994 mm from the start of the intake ramp, with a point at 526 mm from the start getting close to separation. Stratford's criterion (Equation 8.1) is based on two dimensional flows and for the current application will tend to under-predict separation. Secondary flows in the intake will sweep low energy boundary layer fluid into the centre of the intake and this low energy fluid is more prone to separation. (Section 8.1.3 further discusses these secondary flows.) The near separation point at 526 mm is therefore likely to represent actual separation due to the secondary flow augmentation of low energy fluid accumulation on the duct centre-line. Therefore, the near separation at 526 mm is in good agreement with the flow visualisation results. Table 8.1 summarises the predictions of Stratford's criterion and shows favourable comparison with directly observed separation.

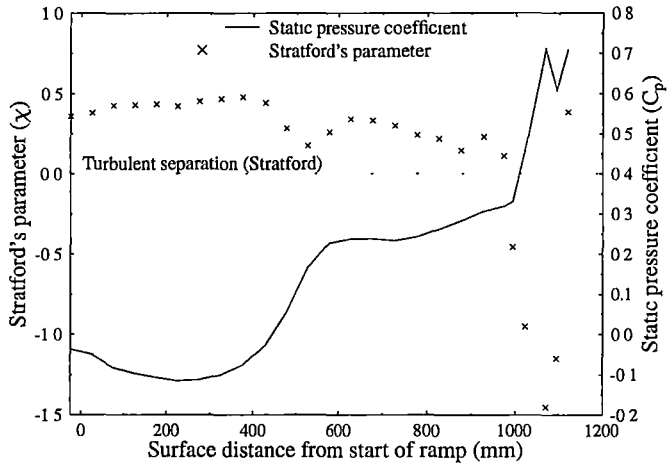

Figure 8.1: Ramp centre-line static pressure coefficient distribution and separation prediction via Equation 8.1 for an IVR of 0.36.

Table 8.1: Distance along intake ramp to separation: predictions and observations.

IVR	Predicted separation (mm from start of intake)	Observed separation‡ (mm from start of intake)
0.36	526	510
0.47	552	525
0.59	577	None
0.67	627	None

‡ Based on fluorescent mini-tuft visualisation.

Hot-wire anemometer voltage~time traces (Figure 8.2) also gave evidence of flow separation. The higher frequency fluctuations present in the attached boundary layer

case (Figure 8.2A) were not in evidence where other indicators suggested flow separation had occured(Figure 8.2B).

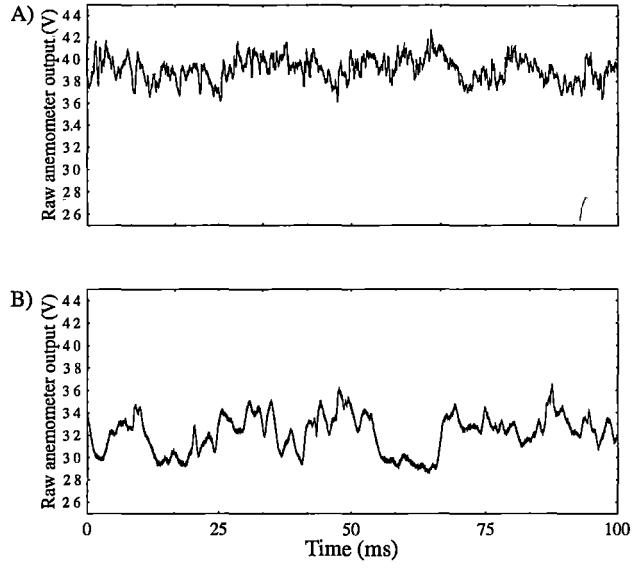

Figure 8.2: Raw hot-wire anemometer output voltage traces at 0.5mm from the wall for the thick boundary layer simulation. Longitudinal position A) at pressure tapping 15 and B) at pressure tapping 39.

The model was designed to have continuous curvature variation along the ramp (until the lobster-back bends). This is in contrast to designs currently used in the high speed ferry industry, where the intake ramp consists in part of a large radius circular arc. These have curvature discontinuities at both ends of the arc where it joins straight line segments. The pressure perturbations induced by these discontinuities may cause an already retarded boundary layer to separate, or increase the severity of a separation zone already present. Consequently, the extent of flow separation in current industrial intakes could well be greater than that observed in these model tests.

There appears to be a significant potential for improving industrial intake designs in this area. The advantages of continuous varying surface curvature are well known in the aeronautical industry. (See, for example, the work of Walraevens and Cumpsty [148] on leading edge shapes for turbomachinery blades.)

8.1.2 Ingestion Stream-tube

The width of the ingestion stream tube is approximately 1.7 intake diameters wide for the thin boundary layer work (Figure 5.1) increasing to approximately 2.0 in the thick boundary layer case (Figure 6.1). Steen and Minsaas [123] agree with these results citing an ingestion streamtube width around 2 times the physical width. This is substantially larger that the factor of 1.3 quoted in Dyne and Lindell [35]. Also, the cross section is rather elliptical and not rectangular as assumed in many papers on thrust prediction.

The thrust produced by waterjet propulsion systems results from the forced change in momentum of the propulsive fluid stream. An incorrect calculation for the momentum at inflow will therefore result in a mis-prediction of produced thrust. As the

measured ingestion streamtube width is substantially larger than the physical width of the intake a large proportion of the propulsive fluid originates in the hull boundary layer. This hull boundary layer fluid has a reduced momentum (compared to free stream fluid) and hence has the potential to produce more thrust for the same energy expenditure. However, if thrust calculations are based on a thinner ingestion streamtube width than reality, the thrust will be under predicted which may result in a waterjet propulsion system larger than optimum being selected at the vessel design stage.

Waterjet thrust calculations based on ingestion streamtube widths lower than the actual ingestion streamtube width will under predict thrust. The measured ingestion streamtube width in the present study is at the upper end of published values, but the high spatial resolution of the measuring technique and cross checking of flow rates provide firm evidence of the validity of these results.

The ingestion streamtube cross-section is roughly elliptical in shape for the highest IVR tested (0.71). This is in agreement with other published data (e.g., Griffith-Jones [56]). However, at lower IVR's (0.51 and below) the cross-section develops two peaks positioned at the physical width of the intake. These twin peaks are possibly indicative of vortical flow structures developing along the waterjet-hull intersection. At high IVR's the depth of the streamtube is sufficient to "bury" these vortical structures inside the ingested fluid.

8.1.3 Secondary Flows

The five hole pressure probe used to measure total pressure and flow direction (and therefore secondary flows) was calibrated in a uniform jet flow. When the probe is being used in a region with total pressure gradients the flow direction calibrations are likely to be in error (the total pressure measurement will not be influenced except possibly for streamline displacement effects). The flow angle in the plane of the maximum total pressure gradient will be most in error, with the orthogonal component only weakly affected.

There is noticeable non-uniformity in the rectangular cross-sections of the intake (Figures 5.11 and 5.12). There are three possible mechanisms contributing to this: turbulent flows in non-circular ducts; streamwise curvature; and ingesting fluid from beyond the spanwise extent of the intake.

Turbulent flow in rectangular ducts typically exhibits thickening of the boundary layer along the centre-line and thinning in the vicinity of the corners. (See, for example Brundrett and Baines [21] and Gessner and Jones [48]). Gosman and Rapley [54] point out that "A feature of turbulent flow in non-circular passages...is the 'secondary flows' that are generated in the cross-sectional plane in order to maintain equilibrium of the Reynolds stresses and pressure gradients... Although the secondary flow velocities are usually not more than 1% or 2% of the mean axial velocity,...they can influence local values of axial velocity and wall shear stress by as much as 30%."

Pressure gradients set up by the streamline curvature will induce secondary flows. These flows would tend to sweep boundary layer fluid from the corners towards the centre-line on surfaces with convex curvature (Pratap and Spalding [104]).

Finally, the ingestion of fluid from beyond the width of the intake would also establish secondary flows that would sweep boundary layer fluid towards the centre-line (as shown in Figure 8.3) although this will only effect fluid in the central region of the

intake).

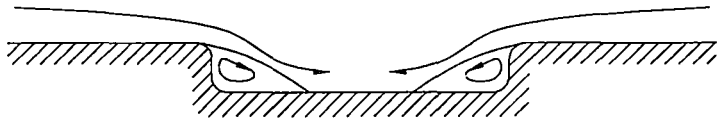

Figure 8.3: Secondary flow field due to the width of the ingestion streamtube.

Overall, the flow in the intake is very three dimensional in nature.

8.1.4 Flow Asymmetries

The experimental traverses at the impeller face show noticeable asymmetry (see, for example, Figure 5.14). These flow asymmetries are not present in the computational results (see, for example, Figure 5.40) because a plane of symmetry has explicitly been enforced.

It is believed that the experimental asymmetries are caused by secondary flows at inflow rather than any inherent flow mechanism in the intake. The model was mounted as a side wall of the tunnel and a secondary downward flow at entry would result in a bulk rotation of the flow at the impeller face in the sense observed in Figures 5.14–5.16. The origin of the secondary flow at inflow is believed to be primarily due to thermal convection (buoyancy effects). The air temperature inside the wind tunnel increases during testing and the core flow may be 10° C above ambient (which the tunnel walls will be close to). This temperature gradient through the thermal boundary layer will induce a density driven down-flow near the wall, which is experimentally observed (Figure 5.10). The magnitude of this down flow velocity is around 0.5 m/s 7 mm from the wall. The method of Ostrach [96] as presented in Incropera and DeWitt [68] was used to calculate the maximum velocity for a laminar boundary layer driven by free convection. This analysis gives a maximum velocity of around one quarter the measured velocity at around 5 mm from the surface. While the experimental flow is not purely free convection (there is a very large cross flow velocity) this analysis suggests that thermal effects do account for the observed secondary flow at entry. The large contraction immediately upstream of the wind tunnel working section was not taken into account in the above free convection analysis and may account, in part, for the discrepancy in maximum velocities.

Mounting the model on the other side of the wind tunnel would have indicated whether the flow asymmetry was due to inflow conditions or some mechanism inherent in the model (such as manufacturing imperfections). In the former case the bulk rotation would be in the opposite sense relative to the model, and in the latter case the same sense. It was not possible to mount the model on the other side of the wind tunnel, however, due to sizing differences in the wind tunnel working section windows. Modifications to the waterjet model to account for the different window sizing were considered impractical.

In summary, the experimentally observed rotation of the symmetry plane at the impeller face was probably due to thermally driven secondary flows at the working section inflow.

8.1.5 Boundary Layer Thickening

The streamwise length available (300 mm) for recovery of the boundary layer after thickening is very short (especially considering the extent of the boundary layer thickening, which increased the boundary layer displacement thickness from 1.8 mm to 10.7 mm). All the methods studied herein for boundary layer thickening were evaluated 750 mm downstream of the thickening device. This length was chosen as it was believed that this distance was available in the actual model to be tested. However, a redesign of the model reduced this distance to 300 mm. Therefore, the velocity and turbulence profiles at inflow were not expected to be as fully stabilised as in the boundary layer thickening trials. It was believed that normal blowing through a perforated plate (which produced the best results at 750 mm) was the best option as its distributed nature and ability to manipulate the turbulence profile (through changing perforate diameter) would produce the best results at 300 mm. Boundary layer measurements presented in Figures 3.28 and 6.23 indicate that the artificial boundary layer thickening was only partially successful. While the boundary layer has been significantly thickened, it is still relaxing to a equilibrium state at the start of the intake ramp, although this relaxation is not severe. The turbulence profile is only approximately correct, with noticeably higher turbulence levels than normal in the boundary layer. Even with these limitations the generated velocity profile was a good approximation to a thick hull boundary layer.

For the thin boundary layer case the agreement between the two measuring techniques used for skin friction determination (namely razor blade measurements and Clauser plot type fits to hot-wire data) was good, with the hot-wire based results being slightly higher and having less apparent scatter along the ramp centre-line.

In general, the hot-wire based measurements of skin friction are more repeatable and less prone to error, but they rely on the velocity profile having an inner similarity region where the velocity scale is the friction velocity (Winter [151]).

Measurement of skin friction was problematic for the thickened boundary layer case. There was a large discrepancy between the hot-wire and razor blade measurements. For the hot-wire based measurements separation is clearly a problem as there is no logarithmic law-of-the-wall region. Even in regions upstream of separation the boundary layer is still relaxing from the perturbation of boundary layer thickening, and the presence of a normal wall similarity region is doubtful.

The razor-blade technique should not have the same susceptibility to alterations in the velocity profile. "Since the device is located substantially within the sub-layer, the calibration is hopefully independent of the properties of the flow in the outer region" (Pai and Whitelaw [97]).

In general, the agreement between the two measuring techniques is fair for the thick boundary layer case. The essential features of the flow (relaxation of the boundary layer near the start of the ramp and a rapid decrease in skin friction downstream of this) are predicted by both techniques, although the actual levels differ significantly.

Given the short length available, it appears that a reasonable boundary layer profile (in terms of velocity and turbulence) has been produced.

8.1.6 Thickened Boundary Layer Operation

The total pressure loss in the intake appears to depend primarily on IVR and only very weakly (if at all) on inflow boundary layer thickness. Therefore, the area averaged total pressure at the impeller face is the sum of the inflow area averaged total pressure and the duct losses (ie. the reduction in inflow total pressure for thick boundary layer operation is accompanied by an equivalent reduction in total pressure at the impeller face).

Manins [84] gives an equation (based on a 1/9 power law velocity distribution, and a rectangular ingestion streamtube) for calculating the fraction (C_r) of mean dynamic pressure at the intake entrance (taking the reference static pressure as the static pressure at inflow results in the dynamic and total pressures being equal, so in this case it is also the fraction of total pressure at entrance)

$$C_r = \frac{9}{11}\left(\frac{h}{\delta}\right)^{2/9} \tag{8.3}$$

where h is the depth of the ingestion streamtube. Equation 8.3 is only valid when the boundary layer is thicker than the bounding ingestion streamtube. When this is not the case, it can easily be shown that

$$C_r = 1 - \frac{2}{11}\left(\frac{\delta}{h}\right). \tag{8.4}$$

Table 8.2 summarises the calculation of the energy available at inflow. There is good agreement between the calculated reduction in total pressure at inflow and the experimentally measured reduction in total pressure at the impeller face when operating conditions are changed from a thin boundary layer case to a thick boundary layer case.

Table 8.2: Change in available kinetic energy at the intake entrance (after Manins [84]).

Case	IVR	h (mm)	delta (mm)	C_r
Thin boundary layer	0.59	44*	13	0.946
Thick boundary layer	0.59	51	83	0.734
Difference	–	–	–	0.212

* interpolated from data at IVR's of 0.51 and 0.71.

A more detailed calculation of the area averaged total pressure at inflow (Section 1) derived from hot-wire traverses and the actual ingestion streamtube cross-section (from the CO ingestion work) gives a total pressure coefficient at inflow for the thin and thick boundary layer cases of 0.935 and 0.758 respectively. This decrease of 0.177 in the total pressure coefficient at inflow accounts for (within experimental uncertainty) the decrease of 0.199 in the total pressure coefficient at the impeller face. Therefore, it appears that the ingestion of a thickened hull boundary layer has little effect on the loss of the intake itself (except for a global reduction in total pressure). The reduction in static pressure with a thickened hull boundary layer (see Figure 6.4) may result cavitation on the impeller. This must be considered during the detailed design of the impeller.

Thickened boundary layer operation appears to result in a slight improvement in distortion (as measured by a DC_{60} distortion coefficient) with a DC_{60} of 0.674 and 0.639 for the thin and thick boundary layer cases respectively at an IVR of 0.59. and slightly earlier separation in the intake. However, both of these influences are small.

Thickened boundary layer operation of the intake can be successfully predicted with knowledge of the thin boundary layer performance of the intake, ingestion streamtube cross-sections and upstream boundary layer profiles.

The flow visualisation results shown in Figures 5.2 (thin boundary layer) and 6.2 (thick boundary layer) shown marked differences in separation downstream of the cutwater. In the thin boundary layer results cutwater separation is evident at an IVR of 0.66 and grows in extent with decreasing IVR. In contrast, no cutwater separation is evident in the thick boundary layer study, even at an IVR of 0.35. This indicates that spillage, which is a problem for thin boundary layer operation, is not a problem for thickened hull boundary layer operation. This is further confirmed by the FIDAP simulated skin friction distributions over the model surface. The large area of high friction on the hull downstream of the cutwater (outside the intake) in the thin boundary layer simulation (Figure 5.35) is dramatically reduced in size in the thick boundary layer simulation (Figure 6.27).

8.1.7 Manoeuvring Operation

The flow in a flush waterjet intake during manoeuvring operation (zero forward speed) is markedly different than for cruise operation. For cruise operation the governing feature is flow separation on the intake ramp and the flow at the impeller face is fairly uniform with a low energy region at the top of the intake. Manoeuvring operation is characterised by separation at the cutwater lip, with highly non-uniform flow at the impeller face. The low energy region at the impeller face has shifted to the bottom of the duct. Furthermore, the flow at the impeller face shows noticeable time unsteadiness.

This flow separation from the cutwater has several undesirable consequences, including:

- large spatial non-uniformity at the impeller face;
- reduction of static pressure at the impeller face (potentially causing cavitation problems on the impeller);
- restriction in the flow area in the intake (this will result in locally high velocities with the possibility of bulk cavitation in the intake); and
- less efficient impeller operation (caused by a combination of temporal unsteadiness and spatial non-uniformity).

The computational fluid dynamics package FIDAP was also used to investigate manoeuvring performance. Overall, the agreement between these results and experimental measurements at the impeller face was good, with area averaged total pressure coefficients of 0.170 and 0.244 respectively and distortion coefficients (DC_{60}) of 0.767 and 0.676 respectively. One flow feature not present in the computer simulation was the temporal unsteadiness, as the simulation was for steady state performance only.

Given the good prediction of manoeuvring performance by FIDAP, the effect of the cutwater lip radius on manoeuvring performance was also numerically studied. The cutwater lip radius was increased from a full scale equivalent of 50 mm to 150 mm. The improvement in total pressure coefficient at the impeller face was significant (increasing from 0.170 for thin thin cutwater lip to 0.563 for the thickened lip). This increased total pressure was accompanied by a slight increase in distortion (increasing from a DC_{60} of 0.767 to 0.795). The overall improvement in performance was seen to be worthwhile, so a thick hull boundary layer simulation of cruise operation was undertaken. This showed that the improvement in manoeuvring operation obtained by cutwater lip thickening had no significant influence on cruise performance (there was a slight decrease in both total pressure and distortion). These results suggest that further experimental and computational work on the influence of the cutwater profile be undertaken. An experimental model with interchangeable (and heavily pressure tapped) cutwater sections would be an ideal experimental platform to undertake such a study.

Throughout this thesis manoeuvring has referred to zero boat speed operation. These conditions are important for two reasons: intake operation is as far from design (or cruise) operation as possible; and manoeuvring operations are typically in close vicinity to wharves and other vessels. Therefore, docking operation may be problematic in areas subjected to strong winds (especially considering the large side area of the ferries exposed to such winds). Any limitations to manoeuvring thrust (such as engine speed limits due to intake cavitation) should be minimised in such situations.

8.2 FIDAP Analysis

The computational program carried out here both validates and complements the experimental research. Obviously, computational fluid dynamics (CFD) provides a mechanism for research than is often not possible (particularly when cost is taken into account) with an experimental program. The CFD results that follow have been experimentally validated and therefore provide a mechanism for further waterjet research.

8.2.1 Meshing

There are several issues concerned with the meshing of the intake. These include:

- the total number of elements in the computational domain;
- the distribution of these elements, especially grading of the available elements toward the surfaces; and
- the distortion of these elements.

The quality of the simulations was strongly influenced by both the total number of elements used for the simulation and the placement of these elements. Centreline skin friction distributions were used to evaluate grid performance. The distance of the first element from the wall was found to be the most important parameter for correct prediction of skin friction, regardless of how this distance was obtained. Therefore, grading of the available elements towards the walls is the optimal method

for correct skin friction prediction. The reduction in wall element thickness obtainable by element grading is achieved at no increase in computational cost. In contrast, increasing the overall number of elements to reduce the wall element thickness will result in an extremely large increase in computational cost. However, to maintain a reasonable looking grid, grading of the elements towards the wall can only be taken so far, and further reduction in wall element thickness is only obtainable by increasing the global number of elements.

The effect of wall element thickness also influenced the element type chosen for the FIDAP simulations. Originally it was planned to use 27 node elements because the curved element boundaries possible with these elements would better represent the physical geometry. However, these elements are approximately twice as thick as 8 node elements, and the skin friction distributions obtained with the 27 node elements reflect this doubling in wall element thickness. Therefore, the linear sided 8 node elements were used for the FIDAP simulations.

8.2.2 Grid Independence

Grid independence (as measured by minimum ramp centre-line skin friction, impeller face area averaged total pressure coefficient and impeller face distortion) was obtained using a grid with a linear density twice that of the default grid. However, the computer resources required for such a large grid (approximately 300,000 nodes, needing just under 1 gigabyte of computer memory and several CPU days on a Cray J916/12-2048 super computer time) was prohibitive, and only available for a one-off grid independence study. The grid used for the majority of the simulations had a linear density of 1.5 times the default grid. While true grid independence has not been achieved with this grid, the difference from the grid independent solution is slight. Furthermore, the agreement with experimental measurements (as discussed in Section 8.2.4) was excellent.

8.2.3 Boundary Conditions

The good agreement between experimental and computation results (see Section 8.2.4) is due to use of experimentally based boundary conditions. This is especially true for the turbulence boundary conditions. Not only are the wall elements sensitive to turbulence parameters at the top of these elements, but the experimentally derived dissipation rates are markedly different from the commonly used isotropic relation.

The two-step modelling procedure used for the experimental program consisted of an initial simulation of the intake and entire wind tunnel working section. Flow conditions were then extracted for a plane 200 mm (1.3 intake diameters) distant from the simulated hull, and these conditions assigned as boundary conditions for a simulation involving a truncated wind tunnel domain (with a corresponding increase in the number of elements situated inside the intake). This two-step procedure has been successful, as it satisfies the dual requirement of simulating the actual flow studied (the wind tunnel is not a semi-infinite flow domain) and having a sufficiently large number of elements in the intake to accurately model the flow. Care must be taken to re-simulate the entire wind tunnel and inlet whenever flow conditions are significantly altered (e.g., a change in IVR or boundary layer thickness).

The excellent agreement between the FIDAP simulations and experimental measurements is due in a large part to the use of experimentally determined boundary conditions. As the flow under investigation involves many hard to resolve features (such as separation of a subtly curved surface) and shows a strong dependence on flow conditions (such as IVR) a seemingly slight mis-match in inflow conditions between simulation and experiment could result in markedly different flow development. Therefore, it is recommended that future numerical modelling of waterjet intakes (in fact any intake) should be based on experimentally determined inflow boundary conditions.

8.2.4 Experimental Validation

Agreement between the experimental measurements and the FIDAP simulations was excellent. Various detailed comparisons between the experimental measurements and computer simulations are presented in this section.

8.2.4.1 Skin Friction Distributions

The correlation of ramp centre-line skin friction between experiment and simulation is noteworthy (see Figures 5.33 and 5.34). To the best of the author's knowledge this is the first published computational skin friction distribution in agreement with experimental measurement for waterjet intakes. Turnock et al. [139] discuss their computational grid in terms of predicting skin friction and conclude that the 120,000 nodes in their model is insufficient. The present study has excellent agreement with approximately 130,000 nodes. The discrepancy between the experimental and computational results at the start of the intake ramp is believed to be due to imperfections in the physical model. The model surface is slightly wavy near the start of the ramp and this may cause the experimental skin friction to be large than predicted.

Skin friction distributions also indicate separation when the wall shear stress falls to zero (although as Eichelbrenner [36] points out, this is not, in general, a sufficient condition to infer separation for three dimensional flows. However, as the flow near the ramp centre-line is fairly two-dimensional in nature the zero shear stress condition should be sufficient to infer separation in this case). Therefore, the good agreement in skin friction distribution also implies a good prediction of separation behaviour. Not only has the separation point been well predicted, but the re-attachment and subsequent development, well modelled. The accurate prediction of re-attachment is notoriously difficult, and the agreement obtained is surprisingly good.

The whole intake flow will be influenced to some degree by the separation from the curved ramp surface. Therefore, the accurate prediction of skin friction distributions (as achieved in this study) is essential for reliable numerical simulation.

8.2.4.2 Pressure Distributions

FIDAP ramp centre-line pressure distributions were also in good agreement with experimental measurements (as shown in Figure 8.4). The over-prediction of pressure beyond a surface distance of 525 mm is not as bad as this figure indicates as the vertical scale is exaggerated. Furthermore, the steepness of the pressure distribution in this region means that the pressure plateau is computationally predicted only slightly later than experimentally measured.

The other obvious feature shown in Figure 8.4 is the spurious oscillation in pressure in the FIDAP simulations. This type of oscillation can be controlled via a Petrov-Galerkin pressure stabilisation term in FIDAP. However, the overall good agreement between experimental and computational models did not warrant adjustment of this pressure stabilisation term from its default value.

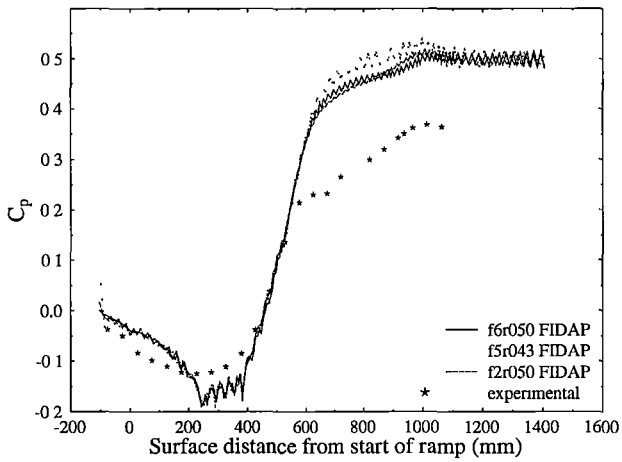

Figure 8.4: Ramp centre-line static pressure distributions for several thin boundary layer FIDAP simulations and experimental measurements, for an IVR of 0.59.

8.2.4.3 Impeller Face Parameters

Arguably the most informative single value parameters describing the performance of a waterjet intake are total pressure and distortion, both measured at the impeller face. Intake velocity ratio is the single biggest influence in intake performance, but does not in itself give a measure of the intake performance. The agreement between experimental and computational predictions of these values is good, with Table 8.3 showing this comparison. The only features of the flow experimentally observed at the impeller face that were not computationally predicted were the tongues of high energy fluid penetrating into the low energy region at the top of the duct during cruise operation. The failure to predict these tongues of high energy fluid is believed (based on work presented in Appendix B.3 on aircraft intakes) to be due to shortcomings in the turbulence model for predicting secondary flows. The Speziale anisotropic turbulence model did a better job of predicting these high energy intrusions than the RNG turbulence model. However, even these predictions were significantly weaker than the experimental observations. It appears that the Speziale turbulence model predicts some secondary flows due to the offset duct but does not predict the initial secondary flows in the rectangular section of the intake (see the next section for further discussion of these secondary flows).

Table 8.3: Comparison of experimental and computational total pressure and distortion at the impeller face.

Case	Experimental		FIDAP	
	AATPC	DC_{60}	AATPC	DC_{60}
Thin boundary layer*	0.757	0.674	0.774†	0.578†
Thick boundary layer*	0.558	0.639	0.561‡	0.592‡
Manoeuvring	0.244	0.676	0.170§	0.767§

* for an IVR of 0.59
† using solution f2r050
‡ using solution f5r945
§ using solution f5r065

8.2.4.4 Secondary Flows

The most notable discrepancy between experimental measurements and the FIDAP simulations was the failure of the latter in predicting the secondary flows in the intake. While this is not a major issue, as the overall agreement between experiment and simulation is good, it is still an important part of the physics of the flow that is not being correctly modelled. Furthermore, interactions between these secondary flows and other flow features (such as the subtle ramp separation) may conceivably result in mis-prediction of the intake performance.

The CFD modelling of the intake failed to capture the secondary flows in the intake as seen in Figures 8.5, 8.6 and 8.7. This is not surprising as in general wall functions for $k-\epsilon$ models do not predict streamwise corner flows well (Namia and Gessner [93]). To model streamwise corner flows requires some dependence on the lateral distance to the wall (as well as the normal distance) for the empirical constant (C_μ) in the Prandtl-Kolmogoroff expression for eddy viscosity ($\nu_t = C_\mu k^2/\epsilon$), while in FIDAP C_μ is strictly constant. Even the anisotropic turbulence models in FIDAP (based on the eddy-viscosity models of both Speziale and Launder) show no significant differences to the isotropic (RNG) turbulence model results shown in Figures 8.5 and 8.6.

In general, "...linear $k-\epsilon$ models of turbulence can give rise to highly inaccurate predictions of the normal Reynolds stresses which make it impossible to describe such effects as secondary flows in non-circular ducts." Speziale [122], with Myong and Kasagi [91] agreeing. Myong and Kobayashi [92] also question wall function accuracy for these types of flows.

8.3 Summary

- The agreement between experimental results and simulations using the finite element package FIDAP was excellent.
- The largest influence on intake performance is the intake velocity ratio.
- Hull boundary layer thickness appears to have little influence on the internal performance of the intake, with the only major effect being the global reduction

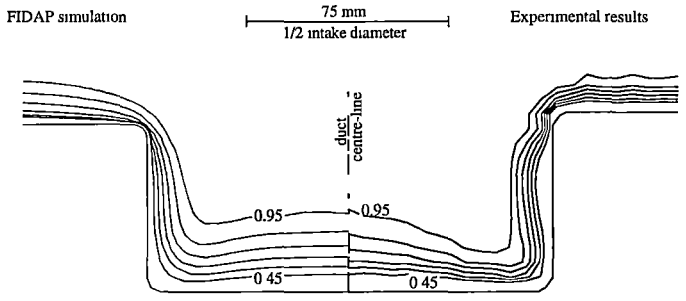

Figure 8.5: Total pressure contours at Section 3 of the intake. Comparison of FIDAP and experimental results.

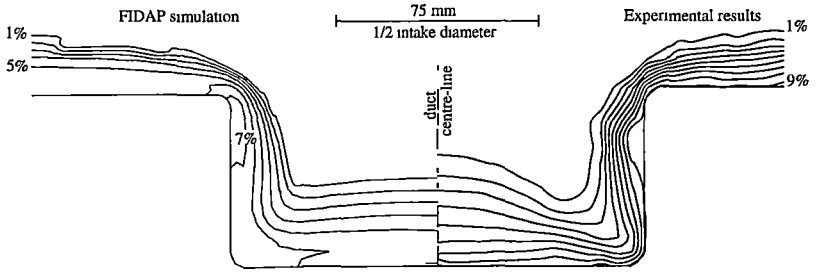

Figure 8.6: Turbulence intensity contours at Section 3 of the intake. Comparison of FIDAP and experimental results.

of total pressure corresponding the the thickening of the hull boundary layer at inflow. However, the reduction in static pressure at the impeller face may cause cavitation problems.

- The ingestion streamtube width is approximately 1.7–2 times the physical width of the intake, with the lower bound of this range being applicable for thin boundary layer operation (δ/d=0.096) and the upper bound for thick boundary layer operation (δ/d=0.556).
- Grid independence for the numerical solution was obtained (requiring 317,000 nodes), although computer resources required the use of a grid not quite at convergence for the majority of the simulations.
- Heavy grading of the available elements towards the walls improved the reliability of the numerical simulations.

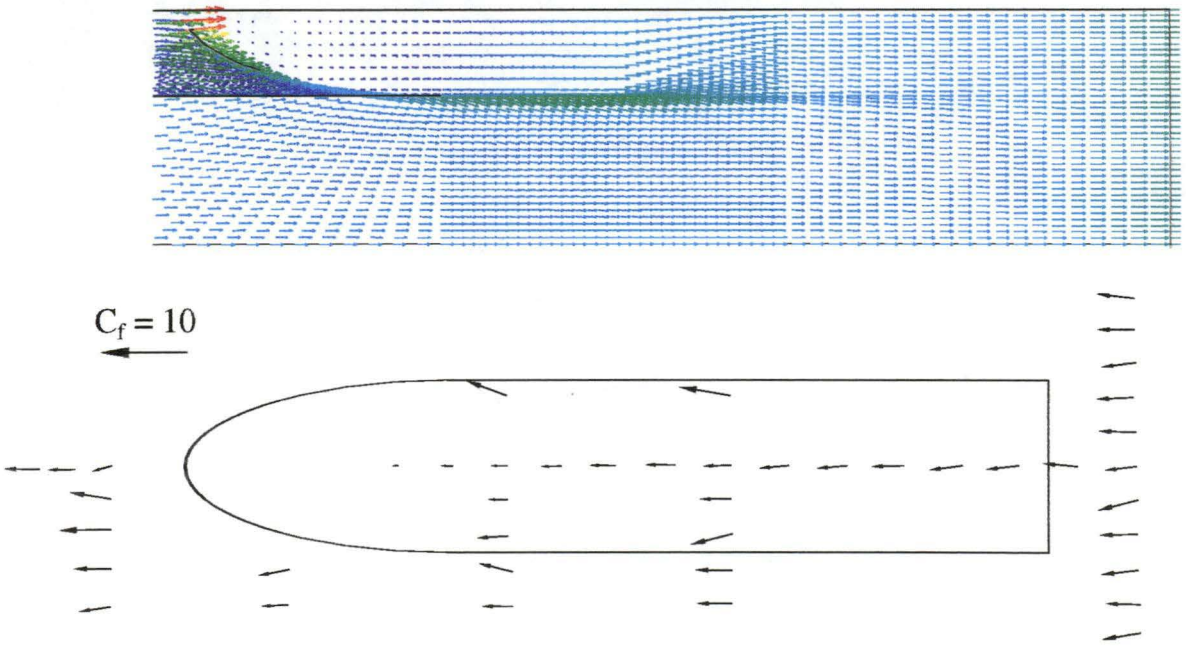

Figure 8.7: Skin friction vector plots, FIDAP simulation above and experimental measurements below.

Chapter 9

Conclusions

9.1 Summary

The specific objectives of this thesis were to:

- investigate the influence of hull boundary layer thickness on waterjet inlets;
- validate computational waterjet models using experimental data; and
- determine the influence of the cutwater lip radius on manoeuvring performance.

These objectives have, in turn, been investigated and it has been found that:

- thicker hull boundary layers adversely influence waterjet intake performance. Specifically, the area averaged total pressure at the impeller face decreases with increasing boundary layer thickness. However, distortion (as measured by a DC_{60} distortion coefficient) improves slightly with increased boundary layer thickness. The influence of the hull boundary layer on the intake performance can be accounted for by the reduction in inflow total pressure.
- the agreement between experimental and computational results is excellent, as exemplified by the ramp centre-line skin friction distribution. However, experimentally observed secondary flows in the streamwise corners of the intake were not predicted computationally (as the turbulence model has no mechanism for producing different normal Reynolds stresses). This did not significantly affect the quality of the results, however, with good agreement on impeller face area average total pressure and distortion levels. With such good validation of the computational code, optimisation studies using this code with similar meshing strategies and geometrically "similar" intakes could be undertaken with confidence.
- the improvement in manoeuvring operation achieved by thickening the cutwater lip indicates that further study in this area is warranted.

9.2 Implications Of Research

Fast catamarans ferries are an expanding segment of the transport industry. Any improvement (however slight) in either cruise performance or manoeuvrability is trans-

lated into a significant advantage to the ferry operator. The present study therefore has significant implications f for this industry.

The validation of a specific computational fluid dynamics package (FIDAP) allows for its use to further optimise inlet design (provided that inlet geometry remains generally similar to the validation geometry). This has obvious economic benefits for both designers and users of waterjet systems.

9.3 Recommendations For Future Study

- Due to the extreme combination of wall curvature, adverse pressure gradients and secondary flows in a streamwise corner, experimental measurement of all the Reynolds stresses would be valuable. This information would be especially useful for the selecting computational turbulence models to be used in future waterjet intake studies.

- A cavitation tunnel study of an internally identical model (strength considerations will require much thicker walls etc.) would be beneficial in determining the magnitude of scale effects. Furthermore, cavitation susceptibility studies including surface roughness (to account for hull fouling) would be informative.

- Currently the intake and hull are designed as two geometrically separate systems (with the possible inclusion of some performance interaction effects) joined together by a slight filleting of the intersection. These relatively harsh corners introduce secondary flows in cruise operation and restrict manoeuvring flow. Blending of these two systems (to produce a smoother, more sculptured intersection) may be beneficial. Computational fluid dynamics is an obvious mechanism to pursue this concept in the initial design phase. Experimental validation will still be required for any promising designs.

Appendix A

2-D Potential Flow Solution

A.1 Introduction

Potential flow solutions are only valid in regions of fluid flow where viscous forces are negligibly small. This excludes their application in regions where shear stress is significant, such as in boundary layers near solid surfaces. Many problems can be approximated by potential flow as the boundary layers may be thin. Even when the boundary layers are thick the region outside the boundary layer can be represented by potential flow, while some other technique is used for the boundary layer region.

The advantage of potential flow analysis is that numerical solution may be less time consuming than other methods of analysis. Furthermore, solutions can be combined by linear superposition, so that for example the potential flow around an aerofoil at any angle of attack is given by the linear combination of flows at two perpendicular directions. Another advantage of potential flow analysis is that analytical solutions exist for many flow field and these analytical solutions eliminate errors due to numerical approximation.

A.2 Applicability To The Current Study

This study is concerned with waterjet propulsion systems operating in the presence of a relatively thick hull boundary layer. This thick boundary layer makes it inappropriate to use potential flow analysis for the entire flow region of interest. The boundary layer is thin near the cut-water, since the hull boundary layer has been ingested by the waterjet, and potential flow modelling may give useful information in this region.

Potential flow analysis also provided a bench mark case used to validate FIDAP for the limiting case without any fluid viscosity (see Appendix B.2).

A theoretical solution for flow in the cut-water region of the intake was found using the Schwarz-Christoffel transform. This transform maps flow in a plane (normally the physical plane) onto an auxiliary plane where solution of the flow field is usually easier. This flow field can then be mapped back to the physical plane giving the solution. Such mapping techniques fall under the general classification of conformal mapping.

A.3 The Schwarz-Christoffel Transform

The Schwarz-Christoffel transform

$$\frac{dz}{d\zeta} = K(\zeta - a)^{\frac{\alpha}{\pi}-1}(\zeta - b)^{\frac{\beta}{\pi}-1}(\zeta - c)^{\frac{\gamma}{\pi}-1}\ldots \tag{A.1}$$

maps the real axis of the ζ plane into the boundary of a closed polygon in the z plane. The points $a, b, c\ldots$ are vertices of this polygon with corresponding interior angles $\alpha, \beta, \gamma\ldots$ The interior of this simple polygon is mapped to the upper half of the ζ plane. The constant K is complex giving scaling and orientation information. The interior angles sum to $(n-2)\pi$ where n is the number of vertices.

A.4 Theory

Flow in the region of the cut-water can be modelled as flow in the region of a branched canal. Solution to such a problem is given in Milne-Thomson [88, Section 10.8] and shall be expanded on below.

Consider the z (or physical) plane shown in Figure A.1.

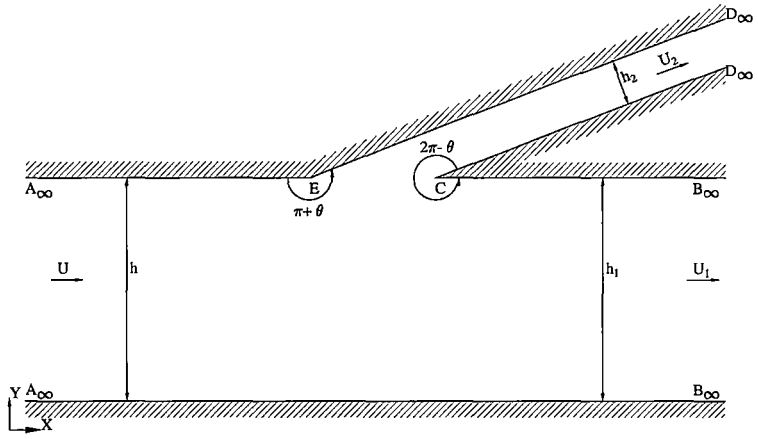

Figure A.1: Z-plane

If the intake is at an angle θ from the main flow then the interior angles at C and E are $2\pi - \theta$ and $\pi + \theta$ respectively (as shown in Figure A.1).

The number of vertices (A, B, C, D, E) is five $(n = 5)$ and the sum of the interior angles is $(2\pi - \theta) + (\pi + \theta) = 3\pi = (n-2)\pi$ as required.

This real plane can be mapped to the ζ plane (Figure A.2) via the Schwartz-Christoffel transform,

$$\frac{dz}{d\zeta} = K(\zeta + a)^{-1}(\zeta + b)^{-1}\zeta^{\frac{2\pi-\theta}{\pi}-1}(\zeta - c) \tag{A.2}$$

In this plane (as well as the real plane) we have inflow at A, outflow at B and D, a stagnation point at C and infinite velocity at E.

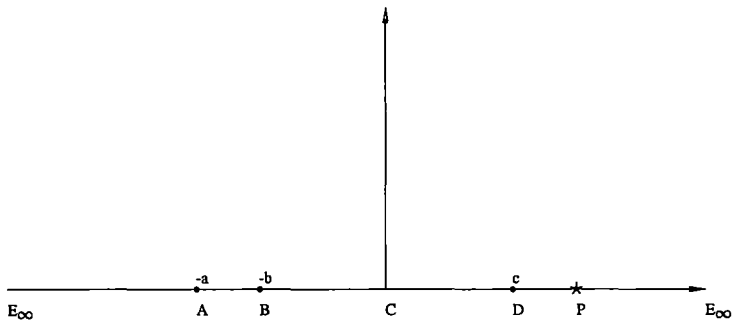

Figure A.2: ζ-plane

The constants K, a, b, c in equation A.2 are most easily found via further conformal mappings.

Consider the Q plane (Figure A.3) given by

$$Q = \ln(\frac{U}{\overline{q}}) = \ln(\frac{U}{q}) + i\alpha \tag{A.3}$$

where $\overline{q} = qe^{-i\alpha}$ is the local fluid velocity and U is the uniform velocity upstream of the branch.

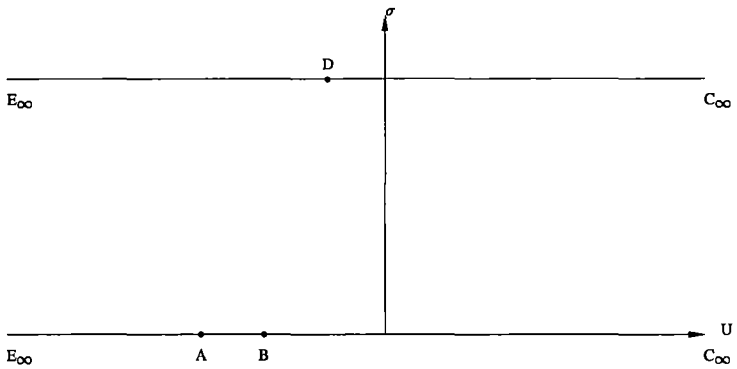

Figure A.3: Q-plane

The flow angle σ is zero for $E_\infty \to A \to B \to C_\infty$ and θ for $C_\infty \to D \to E_\infty$.
This Q-plane is related to the ζ by

$$\zeta = -e^{-\frac{\pi Q}{\theta}}. \tag{A.4}$$

Consider point A

$$\begin{aligned}
\zeta &= -a && \text{but from equation A.4} \\
\zeta &= -e^{-\frac{\pi}{\theta}\ln(\frac{U}{\overline{q}})} && \text{so that} \\
\zeta &= -\left(\frac{U}{\overline{q}}\right)^{-\frac{\pi}{\theta}} && \text{but at } A \\
\overline{q} &= Ue^{-0} = U && \text{giving} \\
\zeta &= -1 && \text{or} \\
a &= 1 && \text{(A.5)}
\end{aligned}$$

Consider point B

$$\begin{aligned}
\zeta &= -b && \text{and} \\
\overline{q} &= U_1 e^{-i0} = U_1 && \text{so that} \\
\zeta &= -\left(\frac{U}{U_1}\right)^{-\frac{\pi}{\theta}} && \text{or} \\
b &= \left(\frac{U}{U_1}\right)^{\frac{\pi}{\theta}} && \text{(A.6)}
\end{aligned}$$

Consider point D

$$\begin{aligned}
\zeta &= c && \text{and} \\
\overline{q} &= U_2 e^{-i\theta} && \text{so that} \\
\zeta &= \left(\frac{U}{U_2}\right)^{-\frac{\pi}{\theta}} && \text{using the result } e^{-i\pi} = -1 \\
c &= \left(\frac{U}{U_2}\right)^{\frac{\pi}{\theta}} && \text{(A.7)}
\end{aligned}$$

Now it is required to find K.
This is most easily done using the $\omega = \phi + i\psi$ plane (Figure A.4).
The ω plane is related to the ζ plane via a Schwarz-Christoffel transform

$$\frac{d\omega}{d\zeta} = R(\zeta + a)^{-1}(\zeta + b)^{-1}\zeta(\zeta - c)^{-1} \qquad \text{(A.8)}$$

where R is purely real, representing no change in orientation.
Now

$$\begin{aligned}
\omega &= \int \frac{d\omega}{d\zeta} d\zeta \\
&= R\left[\frac{ac\ln(\frac{a+\zeta}{c-\zeta}) - bc\ln(\frac{b+\zeta}{c-\zeta}) + ab\ln(\frac{a+\zeta}{b+\zeta})}{(b-a)(a+c)(b+c)}\right] + L \qquad \text{(A.9)}
\end{aligned}$$

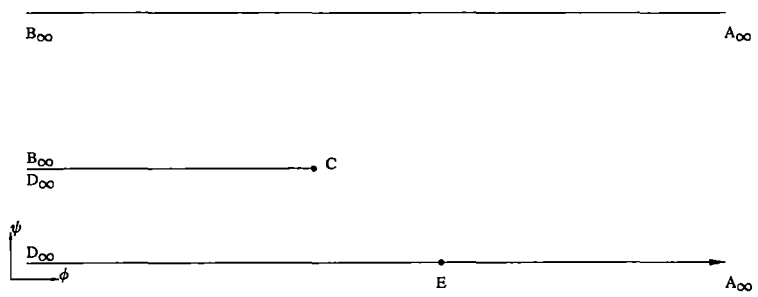

Figure A.4: ω-plane

and it is necessary to find the real constant R and the possibly complex constant of integration L.

Considering the point P such that $\zeta_p > C, \omega_p = t + 0i$, then

$$\omega = R\left[\frac{ac\ln(\frac{\zeta+a}{\zeta-c}) - bc\ln(\frac{\zeta+b}{\zeta-c}) + ab\ln(\frac{\zeta+a}{\zeta+b})}{(b-a)(a+c)(b+c)}\right] + \left(L - \frac{iR\pi c}{(a+c)(b+c)}\right) \tag{A.10}$$

since $\ln(-x) = \ln(x) + i\pi$.

Now define $L_1 = L - \frac{iR\pi c}{(a+c)(b+c)}$ and we have $a, b > 0$ and $\zeta > c > 0$ and ζ is real so that $\zeta - c, \zeta + a, \zeta + b$ are all positive. Hence all ln terms evaluate to real numbers giving

$$\omega = Rs + L_1 \tag{A.11}$$

where s is real.

Therefore $Rs + L_1 = t + 0i$ so that L_1 is real.

Consider Point C $\zeta = 0, w = \phi + iu_2h_2$ so that

$$\omega = R\left[\frac{ac\ln(\frac{a}{c}) - bc\ln(\frac{b}{c}) + ab\ln(\frac{a}{b})}{(b-a)(a+c)(b+c)}\right] + \left(L_1 + \frac{iR\pi c}{(a+c)(b+c)}\right) \tag{A.12}$$

$$= Ry + L_1 + \frac{iR\pi c}{(a+c)(b+c)} \tag{A.13}$$

$$= \phi + iu_2h_2 \tag{A.14}$$

where R, y, L_1 are all real.

Considering the imaginary part of equation A.14

$$R = \frac{u_2h_2(a+c)(b+c)}{\pi c}. \tag{A.15}$$

Considering the real part of equation A.14

$$\phi_c = R\left[\frac{ac\ln(\frac{a}{c}) - bc\ln(\frac{b}{c}) + ab\ln(\frac{a}{b})}{(b-a)(a+c)(b+c)}\right] + L_1. \tag{A.16}$$

As the potential at any point is only relative to the potential of other points in the flow, the potential at any point can arbitrarily be assigned and all others calculated relative to assigned potential.

Therefore choose $L_1 = 0$ so that

$$\phi_c = R\left[\frac{ac\ln(\frac{a}{c}) - bc\ln(\frac{b}{c}) + ab\ln(\frac{a}{b})}{(b-a)(a+c)(b+c)}\right] \tag{A.17}$$

Hence

$$\omega = \frac{u_2 h_2}{\pi(b-a)}\left[a\ln(\frac{\zeta+a}{\zeta-c}) - b\ln(\frac{\zeta+b}{\zeta-c}) + \frac{ab}{c}\ln(\frac{\zeta+a}{\zeta+b})\right] \tag{A.18}$$

$$\frac{dz}{d\zeta} = \frac{\frac{d\omega}{d\zeta}}{\frac{d\omega}{dz}} \tag{A.19}$$

$$= -\frac{R\zeta}{Ue^{-i\theta}(\zeta+a)(\zeta+b)(\zeta-c)\zeta^{\frac{\theta}{\pi}}} \tag{A.20}$$

Comparison with equation A.2 gives

$$K = \frac{-u_2 h_2(a+c)(b+c)e^{-i\theta}}{Uc\pi} \tag{A.21}$$

and

$$z = \int \frac{dz}{d\zeta} d\zeta \tag{A.22}$$

now

$$\frac{dz}{d\zeta} = \frac{K\zeta}{(\zeta+a)(\zeta+b)(\zeta-c)\zeta^{\frac{\theta}{\pi}}} \tag{A.23}$$

$$= \frac{K}{\zeta^{\frac{\theta}{\pi}}}\left(\frac{P_1}{\zeta+a} + \frac{P_2}{\zeta+b} + \frac{P_3}{\zeta-c}\right) \tag{A.24}$$

where

$$P_1 = \frac{a}{(a+c)(b-a)} \tag{A.25}$$

$$P_2 = \frac{b}{(b+c)(a-b)} \tag{A.26}$$

$$P_3 = \frac{c}{(a+c)(b+c)} \tag{A.27}$$

giving

$$z = KP_1\int \frac{d\zeta}{\zeta^{\frac{\theta}{\pi}}(\zeta+a)} + KP_2\int \frac{d\zeta}{\zeta^{\frac{\theta}{\pi}}(\zeta+b)} + KP_3\int \frac{d\zeta}{\zeta^{\frac{\theta}{\pi}}(\zeta-c)} \tag{A.28}$$

which gives

$$z = KP_1 \frac{\zeta^{1-\frac{\theta}{\pi}}}{(1-\frac{\theta}{\pi})a} {}_2F_1\left(1, 1-\frac{\theta}{\pi}; 2-\frac{\theta}{\pi}; -\frac{\zeta}{a}\right) + KP_2 \frac{\zeta^{1-\frac{\theta}{\pi}}}{(1-\frac{\theta}{\pi})b} {}_2F_1\left(1, 1-\frac{\theta}{\pi}; 2-\frac{\theta}{\pi}; -\frac{\zeta}{b}\right) + KP_3 \frac{\zeta^{1-\frac{\theta}{\pi}}}{(1-\frac{\theta}{\pi})c} {}_2F_1\left(1, 1-\frac{\theta}{\pi}; 2-\frac{\theta}{\pi}; \frac{\zeta}{c}\right) \tag{A.29}$$

where ${}_2F_1(a, b; c; z)$ is the Gauss Hypergeometric series.

A.5 Cutwater Rounding

Henrici [63, Section 5.14] details the alteration of the Schwarz-Christoffel transform to allow for the rounding of corners. In summary, if the concave corner (interior angle $\xi > \pi$) at m (between corners at l and n) is to be rounded then the factor

$$(\zeta - m)^{\frac{\xi}{\pi}-1}$$

in equation A.1 must be replaced by the factor

$$w_1(\zeta - m - \eta)^{\frac{\xi}{\pi}-1} + w_2(\zeta - m + \eta)^{\frac{\xi}{\pi}-1}$$

where w_1, w_2 are both positive numbers which sum to unity and η is selected so that $m + \eta$ and $m - \eta$ are both inside the sub-interval (l, n). The parameters w_1, w_2 and η control the shape and profile of the rounding in a complex manner.

Applying the above theory to the case of flow in the waterjet intake results in an identical theory with the exception of equation A.2 which is replaced by the following equation

$$\frac{dz}{d\zeta} = K(\zeta + a)^{-1}(\zeta + b)^{-1}\left(w_1(\zeta - \eta)^{\frac{2\pi-\theta}{\pi}-1} + w_2(\zeta + \eta)^{\frac{2\pi-\theta}{\pi}-1}\right)(\zeta - c). \tag{A.30}$$

As the values of a, b, c and K were calculated from flow in the ζ plane there values will be unaltered. It should be noted that equation A.30 gives identical results to equation A.2 for the case of zero radius of curvature ($\eta = 0$).

Solving for z gives

$$z = \frac{Kw_1(\zeta-\eta)^{2-\frac{\theta}{\pi}}}{2-\frac{\theta}{\pi}}\left[\frac{P_1}{\eta+a}{}_2F_1\left(1, 2-\frac{\theta}{\pi}; 3-\frac{\theta}{\pi}; -\frac{\zeta-\eta}{\eta+a}\right) + \frac{P_2}{\eta+b}{}_2F_1\left(1, 2-\frac{\theta}{\pi}; 3-\frac{\theta}{\pi}; -\frac{\zeta-\eta}{\eta+b}\right) + \frac{P_3}{\eta-c}{}_2F_1\left(1, 2-\frac{\theta}{\pi}; 3-\frac{\theta}{\pi}; -\frac{\zeta-\eta}{\eta-c}\right)\right] + \frac{Kw_2(\zeta+\eta)^{2-\frac{\theta}{\pi}}}{2-\frac{\theta}{\pi}}\left[\frac{P_1}{a-\eta}{}_2F_1\left(1, 2-\frac{\theta}{\pi}; 3-\frac{\theta}{\pi}; -\frac{\zeta+\eta}{a-\eta}\right) + \frac{P_2}{b-\eta}{}_2F_1\left(1, 2-\frac{\theta}{\pi}; 3-\frac{\theta}{\pi}; -\frac{\zeta+\eta}{b-\eta}\right) + \frac{P_3}{c+\eta}{}_2F_1\left(1, 2-\frac{\theta}{\pi}; 3-\frac{\theta}{\pi}; \frac{\zeta+\eta}{c+\eta}\right)\right] \tag{A.31}$$

where

$$P_1 = \frac{1}{(a+c)(a-b)} \tag{A.32}$$

$$P_2 = \frac{1}{(b+c)(b-a)} \tag{A.33}$$

$$P_3 = \frac{1}{(a+c)(b+c)}. \tag{A.34}$$

A.6 Calculation Considerations

A.6.1 Gauss Hypergeometric Series

The Gauss Hypergeometric series ${}_2F_1(a,b;c;z)$ is defined in terms of an infinite series ${}_2F_1(a,b;c;z) = \sum_{n=0}^{\infty} \frac{(a)_n (b)_n z^n}{(c)_n n!}$ where $(a)_n$ is Pochhammer's symbol $= \frac{\Gamma(a+n)}{\Gamma(a)}$ and $\Gamma(a)$ is the familiar gamma function.

The direct numerical evaluation of the Gauss Hypergeometric function is possible when $|z| < 1$ as then the series is monotonically decreasing and sufficient accuracy can be obtained with a finite number of terms. Abramowitz and Stegun [3, Chapter 15] contains a number of linear transforms for the Gauss Hypergeometric function. These transforms are useful because the magnitude of the argument z is altered.

$$\begin{aligned} {}_2F_1(a,b;c;z) &= (1-z)^{-a}\,{}_2F_1(a,c-b;c;\frac{z}{z-1}) && \text{(A.35)} \\ &= \frac{\Gamma(c)\Gamma(b-a)}{\Gamma(b)\Gamma(c-a)}(-z)^{-a}\,{}_2F_1\left(a,1-c+a;1-b+a;\frac{1}{z}\right) \\ &\quad + \frac{\Gamma(c)\Gamma(a-b)}{\Gamma(a)\Gamma(c-b)}(-z)^{-b}\,{}_2F_1\left(b,1-c+b;1-a+b;\frac{1}{z}\right) && \text{(A.36)} \end{aligned}$$

It is easy to evaluate $z_{min} = \min\left(z, \frac{1}{z}, \frac{z}{z-1}\right)$ which will result in the quickest convergence of the infinite series within some tolerance and apply the appropriate linear transform.

A.6.2 Streamline Tracing

The algorithm for producing streamlines simply traces a stream line in the ζ plane and maps the resulting coordinates back to the z plane. The tracing in the ζ plane is achieved by projection along the current velocity tangent in the ζ plane. Due to the source/sinks on the real axis of the ζ plane there are regions of high localised curvature. To accurately streamline trace in these regions and still maintain an acceptable speed of computation an adaptive step size was used for the projection. A base step size was multiplied by the square of the distance to the nearest flow singularity.

A.7 Results

The results presented in Figures A.5–A.8 were produced for the case with cut-water rounding produced by $\eta = 1 * 10^{-2}$, $w_1 = 0.5$ and $w_2 = 0.5$.

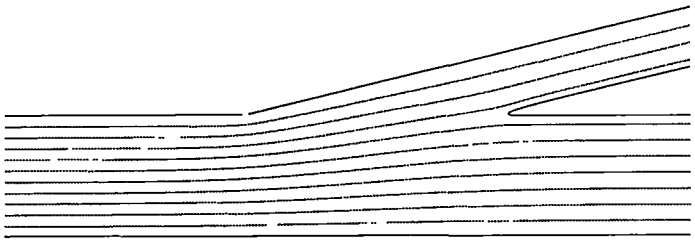

Figure A.5: Streamline tracing.

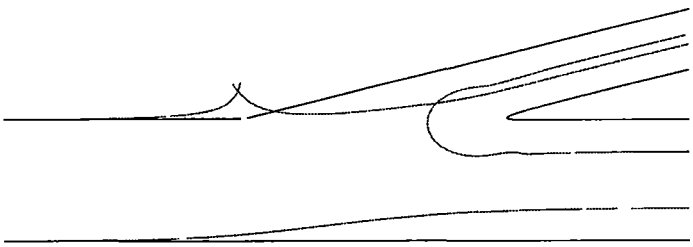

Figure A.6: Surface pressure distribution.

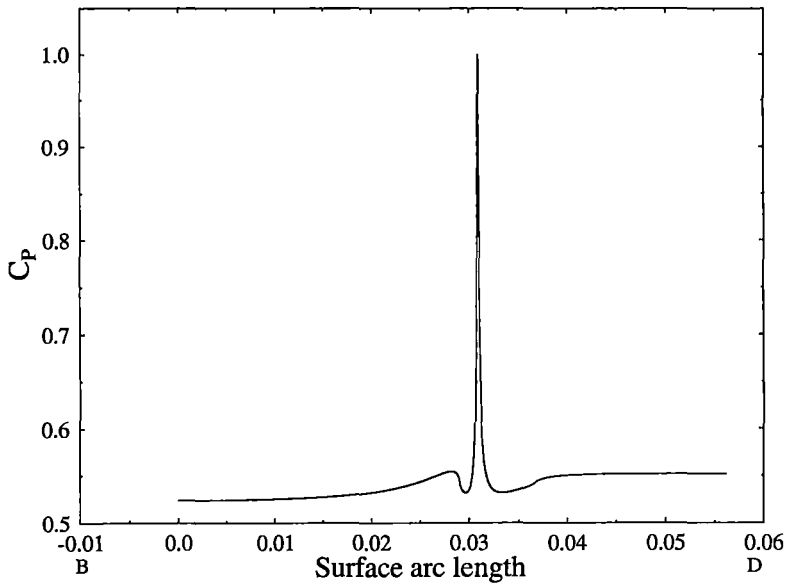

Figure A.7: Surface pressure distribution along BCD.

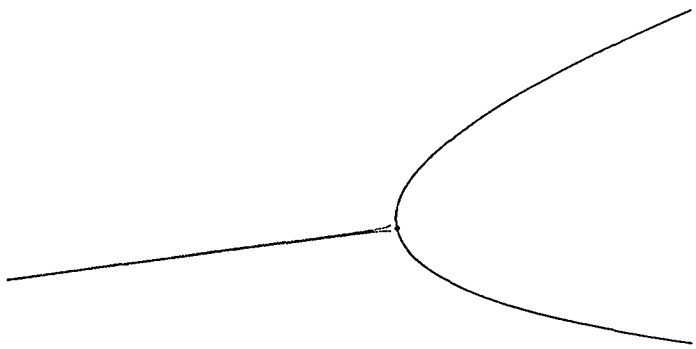

Figure A.8: Streamlines close to stagnation at the cutwater.

Appendix B

Benchmarking FIDAP

B.1 Introduction

For gaining familiarity and competency in the use of FIDAP and in verifying its accuracy in solving fluid flows similar to the one under consideration several bench-marking cases were solved. These included the solving of a two dimensional representation of a waterjet intake for potential flow and a three dimensional approximation to the dorsal intake of the Lockheed Tri-Star aircraft with turbulence modelling.

B.2 Two Dimensional Waterjet

The physical geometry of the flow is shown in Figure B.1.

This geometry is identical to the case considered for potential flow solution via a Schwarz Christoffel transform with the inclusion of cut-water rounding (Appendix A).

Stability requirements for FIDAP exclude the possibility of zero dynamic viscosity as this results in an infinite Reynolds number (both globally and based on element properties) which is not solvable in the standard Galerkin formulation. So to obtain an "inviscid" solution it was necessary to use as low a kinematic viscosity as possible while still maintaining acceptable convergence and stability. The reason for the inability to solve with zero dynamic viscosity is due to the ill-conditioning of the problem. This was seen with the solution of an identical problem using FIDAP running on two different hardware platforms: a Silicon Graphics (SGI) Iris Indigo and a Cray J90. The problem was unstable and failed to converge on the SGI while a stable solution was obtained on the Cray (with a longer word length).

Results obtained were consistent with findings reported in both Zienkiewicz and

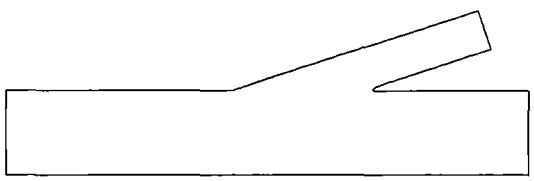

Figure B.1: Geometry of two dimensional waterjet bench-marking case

Taylor [154] and Taylor et al. [132] in that the solution becomes unstable as the Reynolds number increases and develops the characteristic zig-zag velocity vector as shown in Figure B.2. This can be overcome by introducing streamwise upwinding which is a viscosity tensor in the streamwise direction. However, this is additional viscosity in the streamwise direction so only as little as needed to obtain stability should be added. The effect of adding two much upwinding is to shift flow features downstream and to change the flow rates through the system.

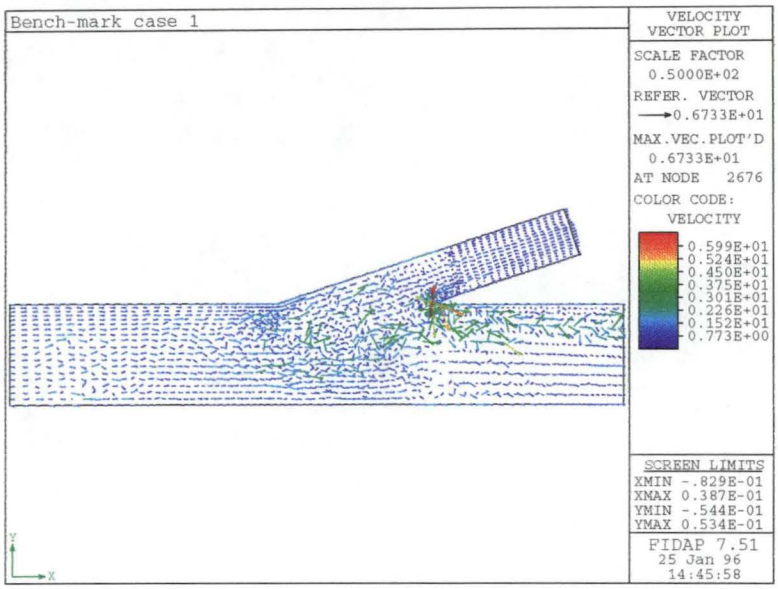

Figure B.2: Typical low viscosity instability problems.

To obtain reasonable solutions it was required to have a refined grid near the cutwater and change in slope/curvature discontinuity along the upper curve. Near the cutwater the increased grid density was required to allow for the correct location of the stagnation point. The increased grid density near the tangent point on the upper curve was required to keep the element based Reynolds number reasonably small. At this point the fluid velocities become large (infinite for invisicid flow) and a small element dimension is required to maintain a relatively small Reynolds number. A typical grid density distribution is shown in Figure B.3.

B.2.1 Sensitivity Analysis

To investigate the sensitivity of the solution to both grid density and dynamic viscosity a series of solutions were performed varying one parameter and keeping the other constant.

Firstly, the effect of grid density was considered. The same relative element distribution was used with different numbers of elements. The basic grid used had an element density as shown in Figures B.4 and B.5 with boundary element spacings as shown in Table B.1. The ratio columns in Table B.1 refer to the spacing of the elements along the boundary. If only one of the columns contains a number then the spacing is single sided, while if both contain a number the spacing is double sided. For single sided spacing the ratio is the ratio of first to last element length along the boundary,

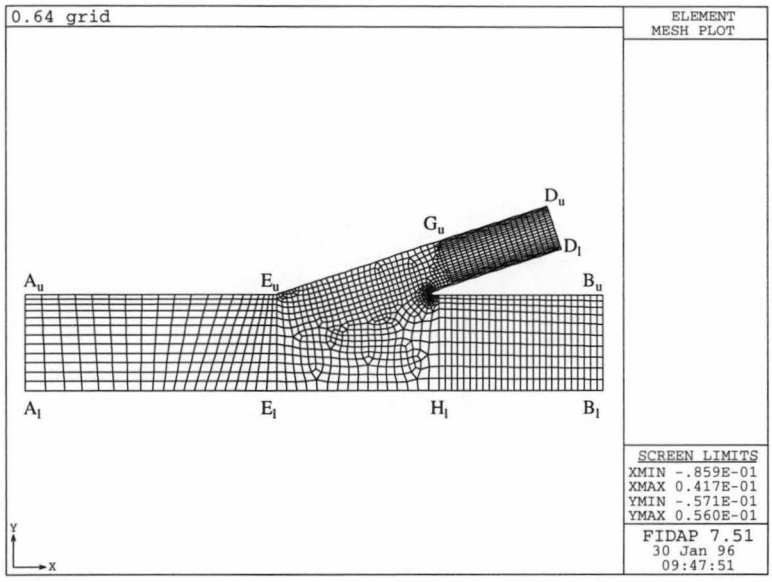

Figure B.3: FIDAP low density grid for sensitivity analysis (2-D), showing mesh definition points (for G_l and H_u see Figure B.5).

with "ratio 1" the first element is closest to the start of the segment and for "ratio 2" the end of the segment. The spacing between the first and last element is based on a geometric ratio factor calculated to fit the required number of points in the segment maintaining the correct ratio of first to last element length. For double sided grading the element spacing is two single sided spacings meeting at a dimensionless position along the segment of "Center" (default 0.5) such that the elements immediately either side of the center point have approximately the same length.

The regions $A_u - E_u - E_l - A_l$, $G_u - D_u - D_l - G_l$ and $H_u - B_u - B_l - H_l$ were all map meshed while the remaining region $E_u - G_u - G_l - H_u - H_l - E_l - E_u$ was pave meshed.

The two other grids used for the sensitivity analysis were based on the basic grid with the boundary element spacing reduced to 90% and 80% (rounded to the nearest even integer) for the 0.8 and 0.64 grid respectively. The density ($\rho = 1000$ kg m^{-3}) and kinematic viscosity ($\mu = 1 * 10^{-4}$ kg m^{-1} s^{-1}) were constant for these analyses and there was no upwinding.

As can be seen from Figures B.6–B.8 the solution approximated the theoretical solution best for higher grid densities. As the grid density increases the solution also becomes smoother as shown by the decreased waviness of the solution in Figures B.6 and B.9. This is a direct consequence of the decrease in element based Reynolds number with increased grid density.

To investigate the effect of dynamic viscosity the grid density was kept constant (the basic grid was used) and the kinematic viscosity was varied between $\mu = 1 * 10^{-2}$ kg m^{-1} s^{-1} and $\mu = 1 * 10^{-4}$ kg m^{-1} s^{-1}. The results are shown in Figures B.10–B.13. Increasing the viscosity results in a smoother or less wavy solution but this is at the expense of accuracy. This is not surprising as the higher viscosity results in a less ill-conditioned system of equations, but is not as good an approximation to inviscid flow.

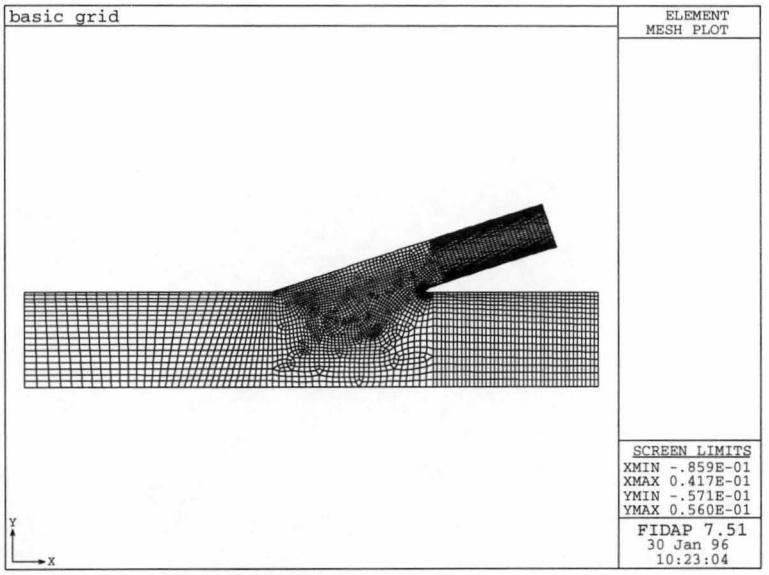

Figure B.4: FIDAP basic grid for sensitivity analysis (2-D).

Figures B.6–B.8 compare surface pressure distributions at various grid densities to the theoretical potential flow solution of Appendix A, while Figures B.10–B.12 provide the same comparison for varying fluid viscosity.

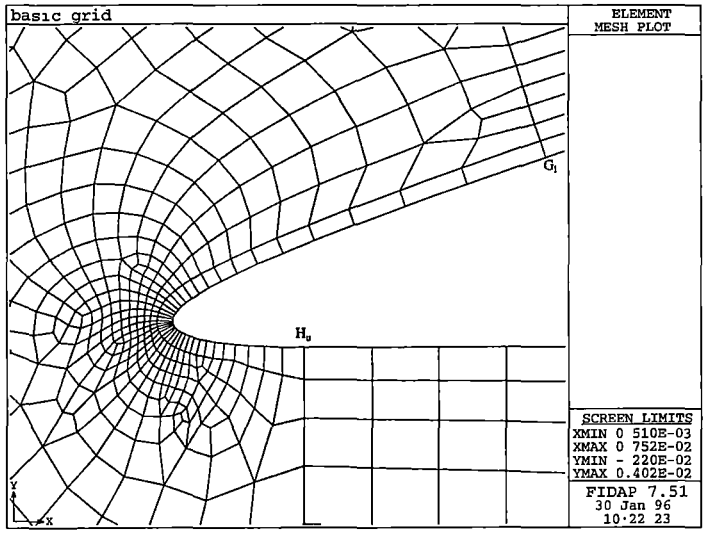

Figure B.5: Close up of basic grid density in region of cut-water.

Table B.1: Element spacing density for basic grid of two dimensional waterjet benchmarking case.

Boundary segment	No of Elements	Ratio 1	Ratio 2	Center
$A_u - E_u$	32	5	–	–
$E_u - G_u$	50	–	3	–
$G_u - D_u$	30	–	–	–
$D_u - D_l$	30	2	2	–
$D_l - G_l$	30	–	–	–
$G_l - H_u$	40	0.8	0.85	0.75
$H_u - B_u$	40	–	–	–
$B_u - B_l$	16	–	2	–
$B_l - H_l$	40	–	–	–
$H_l - E_l$	24	–	–	–
$E_l - A_l$	32	–	2	–
$A_l - A_u$	18	2	–	–
$E_u - E_l$	18	–	2	–
$H_u - H_l$	16	–	4	–
$G_u - G_l$	30	2	2	–

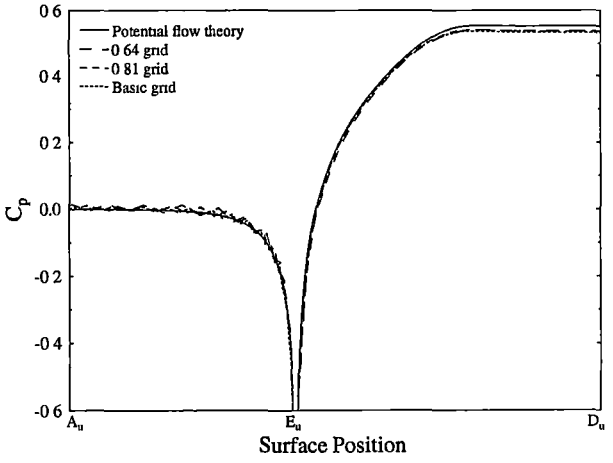

Figure B.6: Surface pressure along $A_u - E_u - D_u$ showing sensitivity to grid density

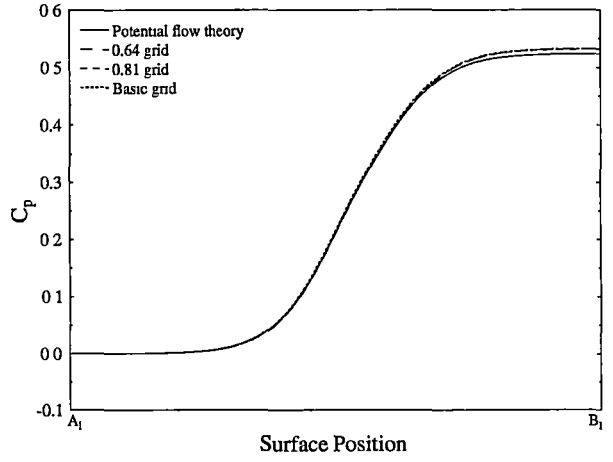

Figure B.7: Surface pressure along $A_l - B_l$ showing sensitivity to grid density

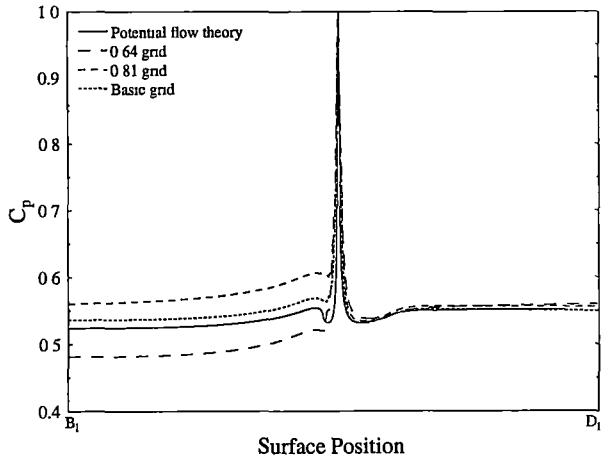

Figure B.8: Surface pressure along $B_u - D_l$ showing sensitivity to grid density

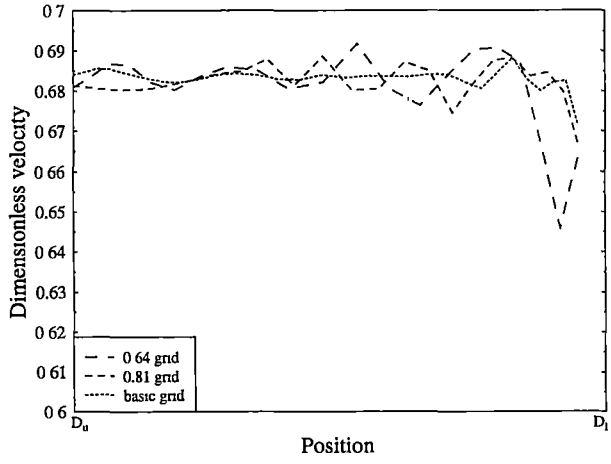

Figure B.9: Velocity distribution across intake showing sensitivity to grid density

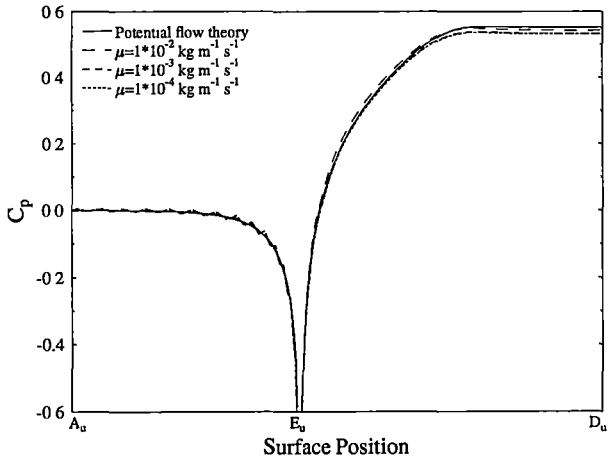

Figure B.10: Surface pressure along $A_u - E_u - D_u$ showing sensitivity to viscosity

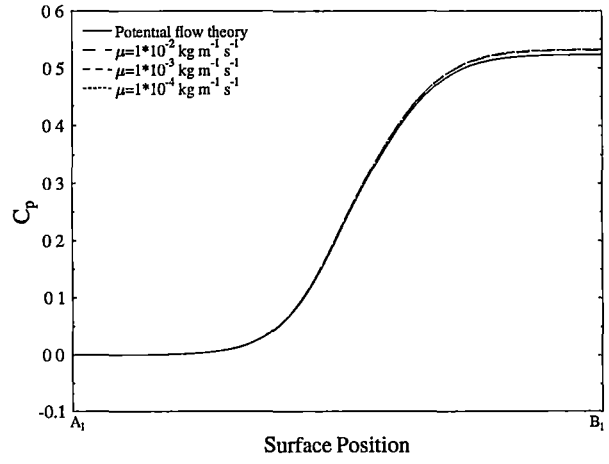

Figure B.11: Surface pressure along $A_l - B_l$ showing sensitivity to viscosity

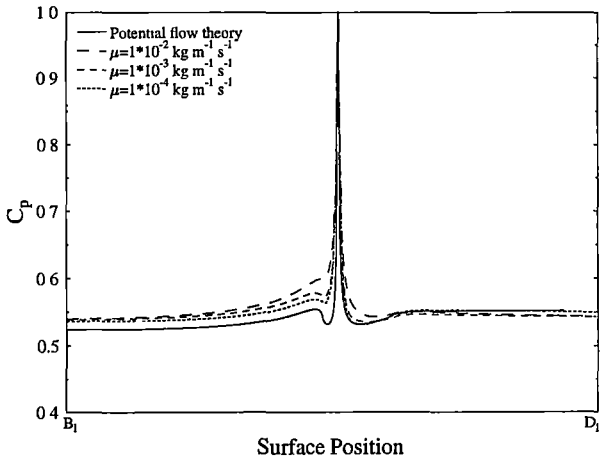

Figure B.12: Surface pressure along $B_u - D_l$ showing sensitivity to viscosity

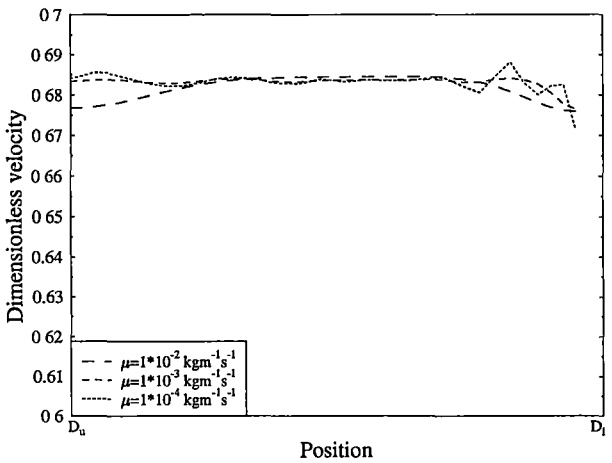

Figure B.13: Velocity distribution across showing sensitivity to viscosity

B.3 Tri-Star Intake

This test case was chosen because of its geometry being similar to the full three dimensional waterjet intake yet being very simple to mesh. The actual geometry chosen was case C2 from Bannsod and Bradshaw [13] which approximates the Lockheed Tri-Star aircraft dorsal intake, consisting of a 0.5D straight tube followed by a curved tube of R/D (R=centerline radius, D=tube diameter) of 2.25, a further 0.5D straight pipe and finally a R/D = 2.25 curved pipe.

Rowe [114] investigated the flow in a $45^o/45^o$ S-bend with the case of fully developed flow at the bend entrance, finding that tongues of high pressure fluid tend to surround the low pressure fluid at the exit of the S-bend. This effect is also present in Bannsod and Bradshaw [13]'s results. Rowe [114] also succinctly explains the mechanism of secondary flow formation in bends. A pressure gradient is set up which provides the necessary inward acceleration. However, this acceleration is more that sufficient for low energy (boundary layer) fluid, which is swept to the inside of the bend, the high energy fluid being displaced to the outside of the bend.

As solution of flow in a S-bend involves secondary flow an anisotropic eddy-viscosity model would be expected to produce more realistic results than an isotropic model. In addition to the standard Boussinesq eddy-viscosity model which makes the Reynolds stress a linear function of the stain rate tensor, FIDAP has available two anisotropic models: Speziale's model which gives the Reynolds stress as a quadratic function of the strain rate tensor and the Launder model which renders the Reynolds stress a cubic function of the strain rate tensor. The Launder eddy-viscosity model was the default used for this test case.

B.3.1 Boundary Conditions

The inflow boundary conditions as described in Bannsod and Bradshaw [13] were a free stream velocity of 45 m/s and a boundary layer momentum thickness Reynolds number of about 1500, corresponding to a boundary layer thickness (99% free stream) of 7.5 mm on a 150 mm diameter pipe. The boundary conditions for turbulent kinetic energy and dissipation were not directly known.

The boundary conditions in the boundary layer are most easily calculated in terms of dimensionless distances ($y^+ = \frac{y\sqrt{\tau_w \rho}}{\mu}$) and velocities ($u^+ = u\sqrt{\frac{\rho}{\tau_w}}$) which requires knowledge of the wall shear stress (τ_w). The boundary layer is relatively thin compared to the "potential core" of the flow. The boundary layer will also be turbulent, as it was artificially thickened by a 0.5 mm trip. The following equations from White [149] for a turbulent boundary layer on a flat plate should therefore be applicable:

$$C_f = 0.026 Re_x^{-1/7} \tag{B.1}$$

$$Re_\theta = 0.0142 Re_x^{6/7} \tag{B.2}$$

Using $Re_\theta = 1500$ gives $C_f = 3.78 * 10^{-3}$ and hence $\tau_w = 4.5$ Pa. This agrees well with data from Bannsod and Bradshaw [13] where $\tau_w = 4.56$ Pa.

The velocity at the first node from the wall was calculated using Reichardt's Law

$$u^+ = \frac{1}{\kappa}\ln(1+\kappa y^+) + 7.8\left[1 - \exp(\frac{-y^+}{11}) - \frac{y^+}{11}\exp(-0.33y^+)\right] \tag{B.3}$$

The velocity for the rest of the boundary layer was calculated assuming a power law distribution

$$\frac{u}{U} = \left(\frac{y}{\delta}\right)^{1/n} \tag{B.4}$$

where n was chosen to fit the velocity from Reichardt's Law at the first node from the wall.

FIDAP employs wall elements to resolve the rapid spatial variation of flow properties near the wall, and the formulation of the bias functions for these wall elements makes them very sensitive to the turbulent kinetic energy at the top of these elements (ie. the first node away from the wall). Using the results of Klebanoff [76] for the distribution of turbulence intensity in a flat plate boundary layer and converting this to turbulent kinetic energy using the relation

$$k = 1.5\,(IU)^2 \tag{B.5}$$

gave good results, where I is the conventional turbulence intensity.

The data of Klebanoff [76] was also used for the dissipation boundary condition, through the relation

$$\epsilon = w_2 \frac{U^3}{2.1\delta} \tag{B.6}$$

where the dimensionless dissipation $w_2 = \frac{\delta\nu}{U^3} \sum_i \sum_j \overline{\left(\frac{\partial u_i}{\partial x_j}\right)^2}$ is obtained from Klebanoff [76] and the factor 2.1 is introduced to account for the anisotropic nature of the turbulence the results for w_2 are based on.

The diffusion rates of Klebanoff [76] are calculated using measured dissipation rates. However, Bradshaw [16] questions these diffusion results, pointing out that diffusion does not integrate to zero, and hence the large diffusion loss in the inner boundary layer is likely to be spurious. As the diffusion data of Klebanoff [76] is calculated by difference using the measured dissipation data the accuracy of the dissipation data is also brought into question. Hence the dissipation boundary condition is calculated from the isotropic turbulence relation

$$\epsilon = \frac{15}{2}\nu \overline{\left(\frac{\partial u}{\partial y}\right)^2} \tag{B.7}$$

where

$$\frac{\partial u}{\partial y} = \frac{\tau_w}{\mu}\frac{\partial u^+}{\partial y^+} \tag{B.8}$$

and the partial derivative on the right hand side is found from differentiation of Reichardts law.

The boundary conditions for the free stream were calculated assuming a free stream turbulence level of 0.5% (as the s-bend is downstream of a blower and contraction), giving a free stream turbulent kinetic energy value of $k = 0.076$ J and a free stream dissipation rate of $\epsilon = \frac{k^{1.5}}{0.1\delta} = 27.90\ \mathrm{m^3/s^2}$. Overall this demonstrated the requirement for experimental determination of the dissipation rates for the waterjet CFD simulation.

Table B.2: Tristar intake test case grid data

Name	Information
g2	Basic Grid
g7	Based on g2 with 24 elements circumferentially on wall but core spacing unaltered
g8	Based on g2 with double number of elements in longitudinal direction
g9	Based on g2 with 1.4 times as many elements in longitudinal and circumferential directions
g10	Based on g2 with 1.4 time as many elements longitudinally and 24 circumferential elements

Table B.3: Tristar intake test case results

Source	$AVWPC$	D_c
Experimental	0.071	0.112
g2	0.1719	0.136
g7	0.1356	0.117
g8	0.1771	0.147
g9	0.1479	0.133
g10	0.1296	0.103

B.3.2 Results

The basic grid had an element distribution in cross section as shown in Figure B.14 and a longitudinal distribution as shown in Figure B.15 (the numbers prefixed with an S denote cross section numbers), the important parameter is the distance from the wall to the nearest node which was 1.365 mm or 0.182δ.

This basic grid was supplemented by four higher element density grids based of the parent basic grid. These grids are summarised in Table B.2.

For the highest density grid ($g10$) the y^+ value for the near wall elements was in the range 94–180 which is inside the recommended range of 30-300 for non-separated flow.

The two most significant single number comparisons of the numerical solutions for the various grids and the experimental results are the average velocity weighted pressure coefficient ($AVWPC$) and a distortion coefficient (D_c). The definition of which are

$$AVWPC = \frac{4}{\pi D^2} \int_0^{2\pi} \int_0^{D/2} \frac{\rho u}{\rho_{ref} u_{ref}} \frac{P_{ref} - P}{1/2 \rho_{ref} u_{ref}^2} r dr d\theta \tag{B.9}$$

where P is the total pressure, and D_c is the difference between the area weighted pressure coefficient (AVWPC without the $\frac{\rho u}{\rho_{ref} u_{ref}}$ factor) for any problem sector and any sub-sector within that problem sector. For the experimental results available the problem sector was taken to be the 60^o sector centered on $\theta = 180^o$. This is not the same as the DC_{60} values frequently used in British aero-engine compatibility research.

Table B.3 shows a summary of these quantities.

The numerical results show that both of these quantities are more sensitive to circumferential spacing than longitudinal spacing.

While the numerical results differ significantly from the experimental results (especially for $AVWPC$) it should be remembered that the inflow boundary conditions for turbulent quantities was not known. It is believed that this uncertainty accounts for the majority of the deviation.

Table B.4: Comparison of iso-tropic and anisotropic eddy viscosity modelling for grid $g7$

Source	$AVWPC$	D_c
anisotropic	0.1356	0.117
isotropic	0.2010	0.0236

Plots of total pressure loss coefficients at outlet (Figures B.16 and B.17) show several important features:

1. tongues of high energy fluid protruding into the low energy fluid at the bottom of the duct
2. the coarser circumferential grids shown evidence of corner flows at the vertices of the inscribed polygon defining the wall
3. a reduction in the extent of the low energy region with increasing grid density

The total pressure loss coefficient plots at outlet also show the significance of the use of an anisotropic eddy-viscosity model. For comparison the $g7$ grid was solved with identical boundary conditions but using an isotropic eddy-viscosity model (Boussinesq). The results for the isotropic and anisotropic cases are shown in Figures B.16 and B.17 respectively. For comparison the $AVWPC$ and DC are given in Table B.4, the most noticeable result being the obviously too low distortion coefficient.

Plots of wall shear stress distribution along the line $\theta = 180^o$ (Figure B.18) broadly follow the experimental results except at section four ($S4$). The experimental results show a very rapid increase from the results at $S3$ while the numerical results indicate a slow recovery from $S3$. Possible reasons for the disparity at $S4$ include

- the insertion of a small flat ring to take the experimental measurements, which would have resulted in a local discontinuity in curvature, and
- the effects of secondary flow on the Preston tube, which may have resulted in off calibration usage.

The numerical results can be manipulated to give a more rapid increase in wall shear stress by increasing the rate of turbulent mixing via suitable adjustment of the inflow turbulent boundary conditions. However, this unjustifiably requires the dissipation to be reduced by several orders of magnitude and produces very poor total pressure loss coefficients at outlet compared to the experimental data. In general, it is believed that the pressure loss coefficient plots are more reliable for comparison.

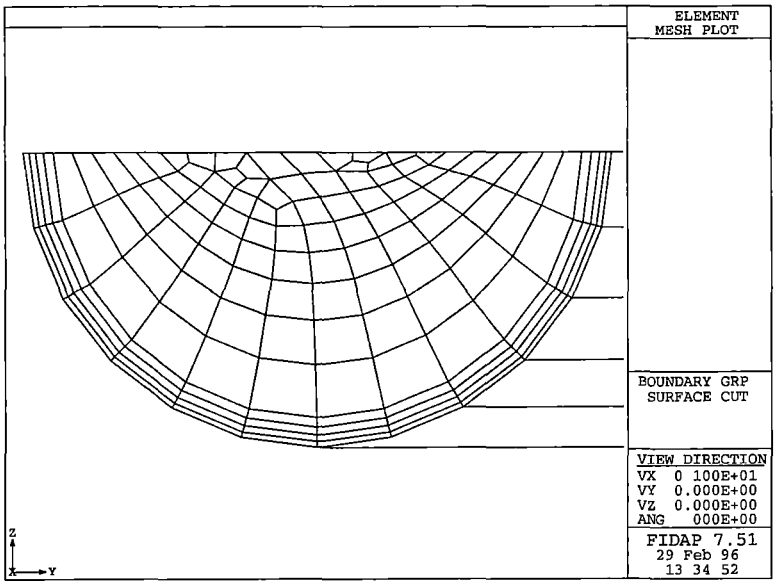

Figure B.14: Basic Grid cross sectional element distribution

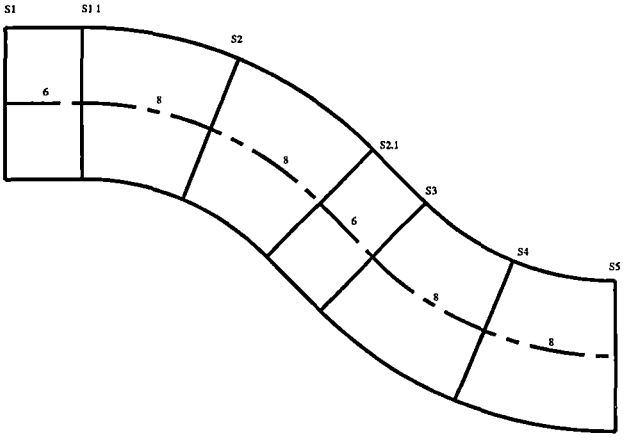

Figure B.15: Basic Grid longitudinal element distribution

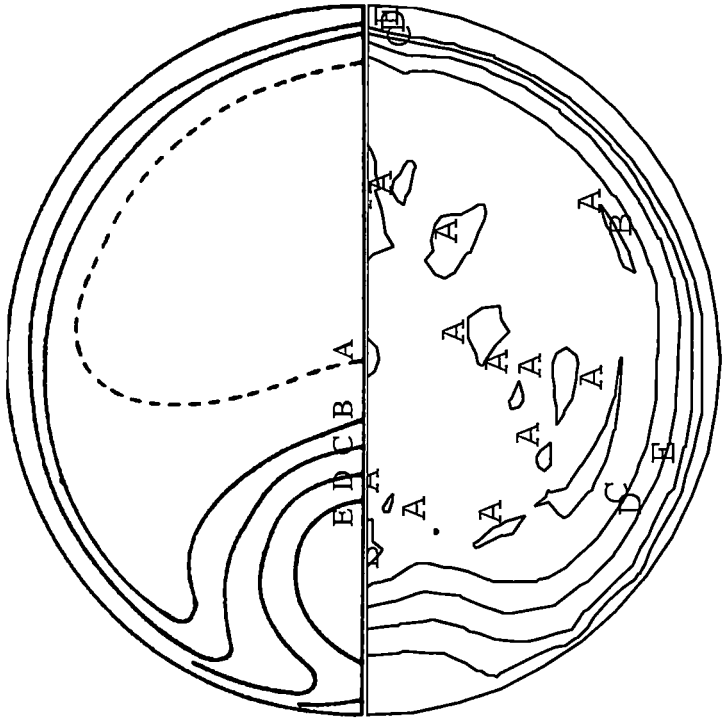

Figure B.16: Total pressure loss coefficient at outflow - experimental results on left, FIDAP isotropic eddy-viscosity model on right, contour levels A=0.01, B=0.1, C=0.2, D=0.3 and E=0.4

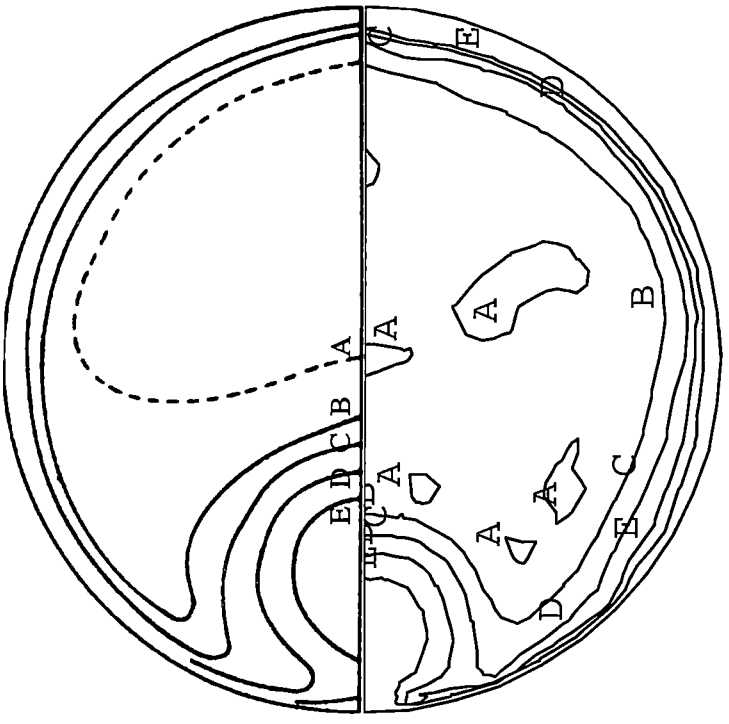

Figure B.17: Total pressure loss coefficient at outflow - experimental results on left, FIDAP anisotropic eddy-viscosity model on right, contour levels A=0.01, B=0.1, C=0.2, D=0.3 and E=0.4

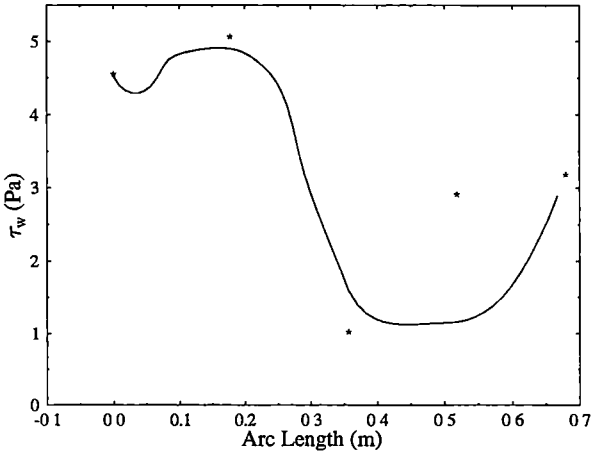

Figure B.18: Wall shear stress along duct bottom centre-line for grid g10

Appendix C

FIDAP Input File

Below is a typical FIDAP input file (input using the FIDAP readfile command) for a thin boundary layer simulation of cruise operation.

```
title
f2r050
/sp=grid density
$sp=2.0
/scl=scaling for correct evaluation of element jacobian
/    want element edge lengths of O(1)
$scl=10
/np=number of nodes per side 3 = 27 node brick 2 = 8 node brick
$np=2
/grad1=grading of elements toward waterjet wall
$grad1=4
/grad2=grading of elements toward hull
$grad2=5
/grad3=grading of elements at cutwater
$grad3=1.25
/grad4=grading of elements at tube-side/hull intersection
$grad4=2.00
fimesh(3-d,imax=(89*$sp),jmax=(88*$sp),kmax=(100*$sp),mxpoint=4000)
point
8  (41*$sp) (26*$sp) ( 13*$sp) (534.282386/$scl) ( -100/$scl) ( -35/$scl)
9  (41*$sp) (  26*$sp) ( 23*$sp) (534.282386/$scl) ( -100/$scl) ( 0/$scl)
10 (41*$sp) ( 32*$sp) ( 23*$sp) (540.4637381/$scl) ( 37.80413776/$scl) (0/$scl)
12 (41*$sp) (  30*$sp) ( 13*$sp) (534.282386/$scl) ( -25/$scl) ( -35/$scl)
14 (41*$sp) (  30*$sp) ( 23*$sp) (534.282386/$scl) ( 0/$scl) (0 )
28 (51*$sp) ( 26*$sp) ( 13*$sp) (681.2075521/$scl) ( -100/$scl) ( -70/$scl)
29 (51*$sp) ( 26*$sp) ( 23*$sp) (681.2075521/$scl) ( -100/$scl) ( 0/$scl)
30 (51*$sp) ( 32*$sp) ( 23*$sp) (681.2075521/$scl) ( -20/$scl) ( 0/$scl)
5  (41*$sp) (  30*$sp) (  7*$sp) (534.282386/$scl) ( 0/$scl) ( -80/$scl)
6  (41*$sp) (  16*$sp) (  7*$sp)  (534.282386/$scl) ( 0/$scl) ( -205/$scl)
7  (41*$sp) (  16*$sp) ( 13*$sp)  (534.282386/$scl) ( -100/$scl) ( -205/$scl)
25 (51*$sp) ( 30*$sp) (  7*$sp) (681.2075521/$scl) ( 0/$scl) ( -80/$scl)
26 (51*$sp) ( 16*$sp) (  7*$sp)  (681.2075521/$scl) ( 0/$scl) ( -205/$scl)
27 (51*$sp) ( 16*$sp) ( 13*$sp)  (681.2075521/$scl) ( -100/$scl) ( -205/$scl)
1  (41*$sp) (  38*$sp) ( 23*$sp) (554.039526/$scl) ( 75.4299/$scl) ( 0/$scl)
2  (41*$sp) (  38*$sp) ( 18*$sp) (554.039526/$scl) ( 75.4299/$scl) ( -70/$scl)
3  (41*$sp) (38*$sp) (17*$sp) (552.3425525/$scl) ( 70.72667972/$scl) (-75/$scl)
4  (41*$sp) (  38*$sp) ( 13*$sp) (534.282386/$scl) ( 5/$scl) ( -75/$scl)
17 (41*$sp) (  32*$sp) (  7*$sp) (534.282386/$scl) ( 5/$scl) ( -75/$scl)
11 (41*$sp) (  32*$sp) ( 13*$sp) (534.282386/$scl) ( 0/$scl) ( -35/$scl)
```

```
21 (51*$sp) ( 38*$sp) ( 23*$sp) (688.387326/$scl) ( 34.4080/$scl) ( 0/$scl)
22 (51*$sp) ( 38*$sp) ( 18*$sp) (688.387326/$scl) ( 34.4080/$scl) ( -70/$scl)
23 (51*$sp) (38*$sp) (17*$sp) (687.2014397/$scl) ( 29.55066806/$scl) (-75/$scl)
24 (51*$sp) ( 38*$sp) ( 13*$sp) (681.2075521/$scl) ( 5/$scl) ( -75/$scl)
37 (51*$sp) ( 32*$sp) (  7*$sp) (681.2075521/$scl) ( 5/$scl) ( -75/$scl)
31 (51*$sp) ( 32*$sp) ( 13*$sp) (681.2075521/$scl) ( -20/$scl) ( -40 /$scl)
18  0  0  0 (552.3425525/$scl) ( 70.72667972/$scl) ( -70/$scl)
19  0  0  0 (534.282386/$scl) ( 5/$scl) ( -80/$scl)
38  0  0  0 (687.2014397/$scl) ( 29.55066806/$scl) ( -70/$scl)
39  0  0  0 (681.2075521/$scl) ( 5/$scl) ( -80 /$scl)
45 (23*$sp) (30*$sp) (7*$sp) (305.343982/$scl) ( 0/$scl) ( 0/$scl)
46 (23*$sp) (16*$sp) (7*$sp) (150/$scl) 0 0
47 (23*$sp) (16*$sp) (13*$sp) (150/$scl) (-100/$scl) 0
48 (23*$sp) (26*$sp) (13*$sp) (400/$scl) ( -100/$scl) ( 0/$scl)
52 (23*$sp) (30*$sp) (13*$sp) (400/$scl) ( -30/$scl) ( 0/$scl)
53 (33*$sp) (30*$sp) (13*$sp) (450 /$scl) (-30/$scl) ( -35/$scl)
54 (33*$sp) (26*$sp) (13*$sp) (450/$scl) ( -100/$scl) ( -35/$scl)
55 (29*$sp) (16*$sp) (13*$sp) (150/$scl) (-100/$scl) (-205/$scl)
56 (29*$sp) (16*$sp) (7*$sp) (150/$scl) 0 (-205/$scl)
60 (33*$sp) (30*$sp) (23*$sp) (400/$scl) ( -30/$scl) ( 0/$scl)
61 (33*$sp) (26*$sp) (23*$sp) (400/$scl) ( -100/$scl) ( 0/$scl)
70 (51*$sp) (30*$sp) (37*$sp) (450/$scl) (7.85660622/$scl) (-35/$scl)
71 (51*$sp) (20*$sp) (37*$sp) (400/$scl) ( 9.475471/$scl) ( 0/$scl)
72 (51*$sp) (20*$sp) (31*$sp) (307.839747/$scl) ( 12.547061/$scl) ( 0/$scl)
73 0 0 0                      (305.343982/$scl) ( 6.521750/$scl) ( 0/$scl)
74 (31*$sp) (20*$sp) (31*$sp) (175.477322/$scl) ( 67.373373/$scl) ( 0/$scl)
75 (31*$sp) (20*$sp) (37*$sp) (188.8712897 /$scl) (99.7092722/$scl) ( 0/$scl)
76 (31*$sp) (30*$sp) (37*$sp) (194.6115412/$scl) (113.5674652/$scl) ( -35/$scl)
77 (31*$sp) (38*$sp) (37*$sp) (204.178627/$scl) ( 136.6644535/$scl) ( -35/$scl)
78 (31*$sp) (38*$sp) (31*$sp) (204.178627/$scl) ( 136.6644535/$scl) ( -75/$scl)
79 0 0 0                      (204.178627/$scl) ( 136.6644535/$scl) ( 0/$scl)
80 (41*$sp) (38*$sp) (37*$sp) (389.7869936/$scl) ( 59.78308606/$scl) (-35/$scl)
81 (41*$sp) (38*$sp) (31*$sp) (389.7869936/$scl) ( 59.78308606/$scl) (-75/$scl)
105 (53*$sp) (38*$sp) (31*$sp) (534.282386/$scl) ( 0/$scl) ( -80/$scl)
111 (51*$sp) (38*$sp) (37*$sp) (534.282386/$scl) ( 0/$scl) ( -35/$scl)
112 (53*$sp) (38*$sp) (37*$sp) (534.282386/$scl) ( -25/$scl) ( -35/$scl)
117 (51*$sp) (38*$sp) (31*$sp) (534.282386/$scl) ( 5/$scl) ( -75/$scl)
145 (53*$sp) (20*$sp) (31*$sp) (305.343982/$scl) ( 0/$scl) ( 0/$scl)
152 (53*$sp) (20*$sp) (37*$sp) (400/$scl) ( -30/$scl) ( 0/$scl)
153 (53*$sp) (30*$sp) (37*$sp) (450 /$scl) (-30/$scl) ( -35/$scl)
101 (51*$sp) (44*$sp) (47*$sp) (554.039526/$scl) ( 75.4299/$scl) ( 0/$scl)
102 (51*$sp) (44*$sp) (42*$sp) (554.039526/$scl) ( 75.4299/$scl) ( -70/$scl)
103 (51*$sp) (44*$sp) (41*$sp) (552.3425525/$scl) (70.72667972/$scl) (-75/$scl)
104 (51*$sp) (44*$sp) (37*$sp) (534.282386/$scl) ( 5/$scl) ( -75/$scl)
110 (51*$sp) (38*$sp) (47*$sp) (540.4637381/$scl) ( 37.80413776/$scl) (0/$scl)
111 (51*$sp) (38*$sp) (37*$sp) (534.282386/$scl) ( 0/$scl) ( -35/$scl)
82 (41*$sp) (38*$sp) (47*$sp) (403.1809137/$scl) ( 92.1188697/$scl) (0/$scl)
83 (41*$sp) (44*$sp) (47*$sp) (418.488251/$scl) ( 129.074051/$scl) ( 0/$scl)
84 (41*$sp) (44*$sp) (42*$sp) (418.488251/$scl) ( 129.074051/$scl) ( -70/$scl)
85 (41*$sp) (44*$sp) (41*$sp) (416.5748338/$scl) ( 124.4546533/$scl) (-75/$scl)
86 0 0 0                      (416.5748338/$scl) ( 124.4546533/$scl) (-70/$scl)
87 (41*$sp) (44*$sp) (37*$sp) (389.7869936/$scl) ( 59.78308606/$scl) (-75/$scl)
90 (49*$sp) (60*$sp) (60*$sp) (217.5725947/$scl) ( 169.0003527/$scl) ( 0/$scl)
210 (49*$sp) (40*$sp) (60*$sp) (540.4637381/$scl) ( 37.80413776/$scl) (0/$scl)
211 (49*$sp) (40*$sp) (50*$sp) (534.282386/$scl) ( 0/$scl) ( -35/$scl)
212 (49*$sp) (38*$sp) (50*$sp) (534.282386/$scl) ( -25/$scl) ( -35/$scl)
214 (49*$sp) (38*$sp) (60*$sp) (534.282386/$scl) ( 0/$scl) (0 )
```

```
252 (41*$sp) (38*$sp) (60*$sp) (400/$scl) ( -30/$scl) ( 0/$scl)
253 (41*$sp) (38*$sp) (50*$sp) (450 /$scl) (-30/$scl) ( -35/$scl)
270 (41*$sp) (40*$sp) (50*$sp) (450/$scl) (7.85660622/$scl) (-35/$scl)
271 (41*$sp) (40*$sp) (60*$sp) (400/$scl) ( 9.475471/$scl) ( 0/$scl)
275 (41*$sp) (60*$sp) (60*$sp) (188.8712897 /$scl) (99.7092722/$scl) ( 0/$scl)
276 (41*$sp) (60*$sp) (50*$sp) (194.6115412/$scl) (113.5674652/$scl) (-35/$scl)
277 (49*$sp) (60*$sp) (50*$sp) (204.178627/$scl) ( 136.6644535/$scl) (-35/$scl)
280 (49*$sp) (50*$sp) (50*$sp) (389.7869936/$scl) (59.78308606/$scl) (-35/$scl)
282 (49*$sp) (50*$sp) (60*$sp) (403.1809137/$scl) ( 92.1188697/$scl) (0/$scl)
301 (31*$sp) (44*$sp) (37*$sp) (204.178627/$scl) ( 136.6644535/$scl) (-75/$scl)
302 (31*$sp) (44*$sp) (47*$sp) (232.879932/$scl) ( 205.955534/$scl) (0/$scl)
303 (31*$sp) (38*$sp) (47*$sp) (217.5725947/$scl) ( 169.0003527/$scl) ( 0/$scl)
304 (31*$sp) (38*$sp) (37*$sp) (204.178627/$scl) ( 136.6644535/$scl) (-35/$scl)
305 0 0 0 (204.178627/$scl) ( 136.6644535/$scl) ( 0/$scl)
321 (61*$sp) (38*$sp) (23*$sp) (825.444751/$scl) ( 9.8897/$scl) ( 0/$scl)
323 (61*$sp) (38*$sp) (13*$sp) (824.8667712/$scl) ( 5/$scl) ( -75/$scl)
324 (61*$sp) (32*$sp) (7*$sp) (824.8667712/$scl) ( 5/$scl) ( -75/$scl)
325 (61*$sp) (30*$sp) (7*$sp) (824.8667712/$scl) ( 0/$scl) ( -80/$scl)
326 (61*$sp) (16*$sp) (7*$sp) (824.8667712/$scl) ( 0/$scl) ( -205/$scl)
327 (61*$sp) (16*$sp) (13*$sp) (824.8667712/$scl) (-100/$scl) ( -205/$scl)
328 (61*$sp) (26*$sp) (13*$sp) (824.8667712/$scl) ( -100/$scl) ( -70/$scl)
329 (61*$sp) (26*$sp) (23*$sp) (824.8667712/$scl) ( -100/$scl) ( 0/$scl)
330 (61*$sp) (32*$sp) (23*$sp) (824.8667712/$scl) ( -40/$scl) ( 0/$scl)
331 (61*$sp) (32*$sp) (13*$sp) (824.8667712/$scl) ( -40/$scl) ( -40/$scl)
339 0 0 0 (824.8667712/$scl) ( 5/$scl) ( -80/$scl)
341 (71*$sp) (38*$sp) (23*$sp) (1067.387326/$scl) ( 0/$scl) ( 0/$scl)
343 (71*$sp) (38*$sp) (13*$sp) (1067.387326/$scl) ( 0/$scl) ( -75/$scl)
344 (71*$sp) (32*$sp) (7*$sp) (1067.387326/$scl) ( 0/$scl) ( -75/$scl)
346 (71*$sp) (16*$sp) (7*$sp) (1067.387326/$scl) ( 0/$scl) ( -205/$scl)
347 (71*$sp) (16*$sp) (13*$sp) (1067.387326/$scl) (-100/$scl) ( -205/$scl)
348 (71*$sp) (26*$sp) (13*$sp) (1067.387326/$scl) ( -100/$scl) ( -90/$scl)
349 (71*$sp) (26*$sp) (23*$sp) (1067.387326/$scl) ( -100/$scl) ( 0/$scl)
350 (71*$sp) (32*$sp) (23*$sp) (1067.387326/$scl) ( -65/$scl) ( 0/$scl)
351 (71*$sp) (32*$sp) (13*$sp) (1067.387326/$scl) ( -65/$scl) ( -60/$scl)
361 (75*$sp) (38*$sp) (23*$sp) (1170/$scl) ( 0/$scl) ( 0/$scl)
363 (75*$sp) (38*$sp) (13*$sp) (1170/$scl) ( 0/$scl) ( -75/$scl)
364 (75*$sp) (32*$sp) (7*$sp) (1170/$scl) ( 0/$scl) ( -75/$scl)
366 (75*$sp) (16*$sp) (7*$sp)  (1170/$scl) ( 0/$scl) ( -205/$scl)
367 (75*$sp) (16*$sp) (13*$sp)  (1170/$scl)(-100/$scl) ( -205/$scl)
368 (75*$sp) (26*$sp) (13*$sp) (1170/$scl) ( -100/$scl) ( -90/$scl)
369 (75*$sp) (26*$sp) (23*$sp) (1170/$scl) ( -100/$scl) ( 0/$scl)
370 (75*$sp) (32*$sp) (23*$sp) (1170/$scl) ( -65/$scl) ( 0/$scl)
371 (75*$sp) (32*$sp) (13*$sp) (1170/$scl) ( -65/$scl) ( -60/$scl)
406 (23*$sp) (26*$sp) (40*$sp) (150/$scl) 0 0
407 (23*$sp) (26*$sp) (46*$sp) (150/$scl) (-100/$scl) 0
415 (29*$sp) (26*$sp) (46*$sp) (150/$scl) (-100/$scl) (-205/$scl)
416 (29*$sp) (26*$sp) (40*$sp) (150/$scl) 0 (-205/$scl)
446 (23*$sp) (12*$sp) (40*$sp) (-100/$scl) 0 0
447 (23*$sp) (12*$sp) (46*$sp) (-100/$scl) (-100/$scl) 0
455 (29*$sp) (12*$sp) (46*$sp) (-100/$scl) (-100/$scl) (-205/$scl)
456 (29*$sp) (12*$sp) (40*$sp) (-100/$scl) 0 (-205/$scl)
500 (29*$sp) (38*$sp) (37*$sp) (179.855679/$scl) ( 144.5674585/$scl) (-35/$scl)
501 (27*$sp) (38*$sp) (37*$sp) (155.0451795/$scl) (150.5239325/$scl) (-35/$scl)
502 (25*$sp) (38*$sp) (37*$sp) (129.843823/$scl) ( 154.5154355/$scl) (-35/$scl)
503 (23*$sp) (38*$sp) (37*$sp) (104.348/$scl) ( 156.672/$scl) ( -35/$scl)
504 (15*$sp) (38*$sp) (37*$sp) (0/$scl) ( 156.672/$scl) ( -35/$scl)
505 (3*$sp) (38*$sp) (37*$sp) (-300/$scl) ( 156.672/$scl) ( -35/$scl)
```

```
506 (15*$sp) (20*$sp) (31*$sp)
507 (15*$sp) (20*$sp) (37*$sp)
508 (15*$sp) (30*$sp) (37*$sp)
509 (15*$sp) (38*$sp) (31*$sp)
510 (3*$sp) (20*$sp) (31*$sp)
511 (3*$sp) (20*$sp) (37*$sp)
512 (3*$sp) (30*$sp) (37*$sp)
513 (3*$sp) (38*$sp) (31*$sp)
526 (15*$sp) (44*$sp) (37*$sp)
527 (15*$sp) (44*$sp) (47*$sp)
528 (15*$sp) (38*$sp) (47*$sp)
529 (3*$sp) (44*$sp) (37*$sp)
530 (3*$sp) (44*$sp) (47*$sp)
531 (3*$sp) (38*$sp) (47*$sp)
550 (49*$sp) (62*$sp) (50*$sp) (179.855679/$scl) ( 144.5674585/$scl) (-35/$scl)
551 (49*$sp) (64*$sp) (50*$sp) (155.0451795/$scl) (150.5239325/$scl) (-35/$scl)
552 (49*$sp) (66*$sp) (50*$sp) (129.843823/$scl) ( 154.5154355/$scl) (-35/$scl)
553 (49*$sp) (68*$sp) (50*$sp) (104.348/$scl) ( 156.672/$scl) ( -35/$scl)
554 (49*$sp) (76*$sp) (50*$sp) (0/$scl) ( 156.672/$scl) ( -35/$scl)
555 (49*$sp) (88*$sp) (50*$sp) (-300/$scl) ( 156.672/$scl) ( -35/$scl)
556 (41*$sp) (76*$sp) (50*$sp)
557 (41*$sp) (76*$sp) (60*$sp)
558 (49*$sp) (76*$sp) (60*$sp)
559 (41*$sp) (88*$sp) (50*$sp)
560 (41*$sp) (88*$sp) (60*$sp)
561 (49*$sp) (88*$sp) (60*$sp)
607 (41*$sp) (30*$sp) (72*$sp) (534.282386/$scl) ( -100/$scl) ( -205/$scl)
608 (41*$sp) (30*$sp) (82*$sp) (534.282386/$scl) ( -100/$scl) ( -35/$scl)
609 (41*$sp) (30*$sp) (92*$sp) (534.282386/$scl) ( -100/$scl) ( 0/$scl)
627 (51*$sp) (30*$sp) (72*$sp) (681.2075521/$scl) ( -100/$scl) ( -205/$scl)
628 (51*$sp) (30*$sp) (82*$sp) (681.2075521/$scl) ( -100/$scl) ( -70/$scl)
629 (51*$sp) (30*$sp) (92*$sp) (681.2075521/$scl) ( -100/$scl) ( 0/$scl)
701 (41*$sp) (24*$sp) (82*$sp) (534.282386/$scl) ( -200/$scl) ( -35/$scl)
702 (51*$sp) (24*$sp) (92*$sp)
703 (51*$sp) (24*$sp) (72*$sp)
704 (51*$sp) (36*$sp) (62*$sp) (681.2075521/$scl) ( -100/$scl) ( -305/$scl)
705 (51*$sp) (24*$sp) (62*$sp) (681.2075521/$scl) ( -200/$scl) ( -255/$scl)
777 (51*$sp) (30*$sp) (62*$sp) (681.2075521/$scl) (-130/$scl) (-255/$scl)
626 (51*$sp) (36*$sp) (72*$sp) (681.2075521/$scl) ( 0/$scl) ( -205/$scl)
606 (41*$sp) (36*$sp) (72*$sp)
706 (41*$sp) (24*$sp) (72*$sp)
707 (41*$sp) (24*$sp) (62*$sp)
709 (41*$sp) (24*$sp) (92*$sp)
867 (75*$sp) (30*$sp) (72*$sp) (1170/$scl)(-100/$scl) ( -205/$scl)
868 (75*$sp) (30*$sp) (82*$sp) (1170/$scl) ( -100/$scl) ( -90/$scl)
869 (75*$sp) (30*$sp) (92*$sp) (1170/$scl) ( -100/$scl) ( 0/$scl)
712 (75*$sp) (24*$sp) (82*$sp)
714 (75*$sp) (24*$sp) (72*$sp)
710 (75*$sp) (36*$sp) (62*$sp)
711 (75*$sp) (24*$sp) (62*$sp)
798 (41*$sp) (30*$sp) (62*$sp)
799 (75*$sp) (30*$sp) (62*$sp)
1899 (75*$sp) (14*$sp) (92*$sp) (1170/$scl) ( -545/$scl) ( 0/$scl)
866 (75*$sp) (36*$sp) (72*$sp) (1170/$scl) ( 0/$scl) ( -205/$scl)
828 (61*$sp) (30*$sp) (82*$sp) (824.8667712/$scl) ( -100/$scl) ( -70/$scl)
829 (61*$sp) (30*$sp) (92*$sp) (824.8667712/$scl) ( -100/$scl) ( 0/$scl)
848 (71*$sp) (30*$sp) (82*$sp) (1067.387326/$scl) ( -100/$scl) ( -90/$scl)
```

```
849 (71*$sp) (30*$sp) (92*$sp) (1067.387326/$scl) ( -100/$scl) ( 0/$scl)
827 (61*$sp) (30*$sp) (72*$sp) (824.8667712/$scl) (-100/$scl) ( -205/$scl)
847 (71*$sp) (30*$sp) (72*$sp) (1067.387326/$scl) (-100/$scl) ( -205/$scl)
846 (71*$sp) (36*$sp) (72*$sp) (1067.387326/$scl) ( 0/$scl) ( -205/$scl)
826 (61*$sp) (36*$sp) (72*$sp) (824.8667712/$scl) ( 0/$scl) ( -205/$scl)
907 (71*$sp) (16*$sp) (40*$sp) (534.282386/$scl) ( -100/$scl) ( -205/$scl)
908 (71*$sp) (26*$sp) (40*$sp) (534.282386/$scl) ( -100/$scl) ( -35/$scl)
947 (53*$sp) (16*$sp) (40*$sp) (150/$scl) (-100/$scl) 0
948 (53*$sp) (26*$sp) (40*$sp) (400/$scl) ( -100/$scl) ( 0/$scl)
954 (63*$sp) (26*$sp) (40*$sp) (450/$scl) ( -100/$scl) ( -35/$scl)
955 (59*$sp) (16*$sp) (40*$sp) (150/$scl) (-100/$scl) (-205/$scl)
1007 (71*$sp) (16*$sp) (46*$sp) (534.282386/$scl) ( -200/$scl) ( -205/$scl)
1008 (71*$sp) (26*$sp) (46*$sp)
1047 (53*$sp) (16*$sp) (46*$sp)
1048 (53*$sp) (26*$sp) (46*$sp)
1054 (63*$sp) (26*$sp) (46*$sp)
1055 (59*$sp) (16*$sp) (46*$sp)
1108 (61*$sp) (33*$sp) (40*$sp) (534.282386/$scl) ( -100/$scl) ( -35/$scl)
1109 (61*$sp) (33*$sp) (50*$sp) (534.282386/$scl) ( -100/$scl) ( 0/$scl)
1118 (61*$sp) (27*$sp) (40*$sp) (534.282386/$scl) ( -200/$scl) ( -35/$scl)
1154 (53*$sp) (33*$sp) (40*$sp) (450/$scl) ( -100/$scl) ( -35/$scl)
1161 (53*$sp) (33*$sp) (50*$sp) (400/$scl) ( -100/$scl) ( 0/$scl)
1171 (53*$sp) (27*$sp) (50*$sp)
1455 (63*$sp) (33*$sp) (40*$sp) (-100/$scl) (-100/$scl) (-205/$scl)
1407 (77*$sp) (33*$sp) (46*$sp) (150/$scl) (-100/$scl) 0
1415 (77*$sp) (33*$sp) (40*$sp) (150/$scl) (-100/$scl) (-205/$scl)
1447 (63*$sp) (33*$sp) (46*$sp) (-100/$scl) (-100/$scl) 0
1467 (63*$sp) (27*$sp) (40*$sp)
1417 (77*$sp) (27*$sp) (46*$sp) (150/$scl) (-200/$scl) 0
1425 (77*$sp) (27*$sp) (40*$sp)
1465 (63*$sp) (27*$sp) (46*$sp)
1500 (63*$sp) (34*$sp) (38*$sp) (-100/$scl) (-200/$scl) (-205/$scl)
1501 (63*$sp) (46*$sp) (38*$sp) (-100/$scl) 0 (-205/$scl)
1502 (63*$sp) (46*$sp) (28*$sp) (-100/$scl) (-100/$scl) (-305/$scl)
1503 (63*$sp) (34*$sp) (28*$sp) (-100/$scl) (-200/$scl) (-255/$scl)
1508 (63*$sp) (40*$sp) (38*$sp) (-100/$scl) (-100/$scl) (-205/$scl)
1507 (77*$sp) (34*$sp) (38*$sp) (150/$scl) (-200/$scl) (-205/$scl)
1504 (77*$sp) (46*$sp) (38*$sp) (150/$scl) ( 0/$scl) ( -205/$scl)
1505 (77*$sp) (46*$sp) (28*$sp) (150/$scl) ( -100/$scl) ( -305/$scl)
1506 (77*$sp) (34*$sp) (28*$sp) (150/$scl) ( -200/$scl) ( -255/$scl)
1509 (77*$sp) (40*$sp) (38*$sp) (150/$scl) ( -100/$scl) ( -205/$scl)
1557 (89*$sp) (34*$sp) (38*$sp) (534.282386/$scl) (-200/$scl) (-205/$scl)
1554 (89*$sp) (46*$sp) (38*$sp) (534.282386/$scl) ( 0/$scl) ( -205/$scl)
1555 (89*$sp) (46*$sp) (28*$sp) (534.282386/$scl) ( -100/$scl) ( -305/$scl)
1556 (89*$sp) (34*$sp) (28*$sp) (534.282386/$scl) ( -200/$scl) ( -255/$scl)
1559 (89*$sp) (40*$sp) (38*$sp) (534.282386/$scl) ( -100/$scl) ( -205/$scl)
1577 (89*$sp) (40*$sp) (28*$sp) (534.282386/$scl) (-130/$scl) (-255/$scl)
1578 (63*$sp) (40*$sp) (28*$sp) (-100/$scl) (-130/$scl) (-255/$scl)
1701 (41*$sp) (14*$sp) (82*$sp) (534.282386/$scl) ( -545/$scl) ( -35/$scl)
1706 (41*$sp) (14*$sp) (72*$sp) (534.282386/$scl) ( -545/$scl) ( -205/$scl)
1702 (51*$sp) (14*$sp) (92*$sp)
1703 (51*$sp) (14*$sp) (72*$sp)
1705 (51*$sp) (14*$sp) (62*$sp)
1707 (41*$sp) (14*$sp) (62*$sp)
1609 (41*$sp) (14*$sp) (92*$sp)
1711 (75*$sp) (14*$sp) (62*$sp)
1712 (75*$sp) (14*$sp) (82*$sp)
```

```
1869 (75*$sp) (14*$sp) (92*$sp)
2007 (38*$sp) (42*$sp) (70*$sp) (534.282386/$scl) ( -200/$scl) ( -205/$scl)
2008 (38*$sp) (42*$sp) (80*$sp) (534.282386/$scl) ( -200/$scl) ( -35/$scl)
2054 (30*$sp) (42*$sp) (80*$sp) (450/$scl) ( -200/$scl) ( -35/$scl)
2055 (26*$sp) (42*$sp) (70*$sp) (150/$scl) (-200/$scl) (-205/$scl)
2048 (20*$sp) (42*$sp) (80*$sp) (400/$scl) ( -200/$scl) ( 0/$scl)
2047 (20*$sp) (42*$sp) (70*$sp) (150/$scl) (-200/$scl) 0
2107 (38*$sp) (32*$sp) (70*$sp)
2108 (38*$sp) (32*$sp) (80*$sp) (534.282386/$scl) ( -545/$scl) ( -35/$scl)
2154 (30*$sp) (32*$sp) (80*$sp)
2155 (26*$sp) (32*$sp) (70*$sp)
2148 (20*$sp) (32*$sp) (80*$sp)
2147 (20*$sp) (32*$sp) (70*$sp)
2009 (38*$sp) (42*$sp) (90*$sp) (534.282386/$scl) ( -200/$scl) ( 0/$scl)
2200 (30*$sp) (42*$sp) (90*$sp) (400/$scl) ( -200/$scl) ( 0/$scl)
2109 (38*$sp) (32*$sp) (90*$sp)
2201 (30*$sp) (32*$sp) (90*$sp)
2300 (19*$sp) (42*$sp) (76*$sp) (150/$scl) (-200/$scl) 0
2301 (5*$sp) (42*$sp) (76*$sp) (-100/$scl) (-200/$scl) 0
2302 (5*$sp) (42*$sp) (70*$sp) (-100/$scl) (-200/$scl) (-205/$scl)
2303 (19*$sp) (42*$sp) (70*$sp) (150/$scl) (-200/$scl) (-205/$scl)
2304 (19*$sp) (32*$sp) (76*$sp) (150/$scl) (-545/$scl) 0
2305 (5*$sp) (32*$sp) (76*$sp)
2306 (5*$sp) (32*$sp) (70*$sp)
2307 (19*$sp) (32*$sp) (70*$sp)
2060 (38*$sp) (42*$sp) (60*$sp) (534.282386/$scl) ( -200/$scl) ( -255/$scl)
2160 (38*$sp) (32*$sp) (60*$sp) (534.282386/$scl) ( -545/$scl) ( -255/$scl)
2061 (26*$sp) (42*$sp) (60*$sp)
2161 (26*$sp) (32*$sp) (60*$sp)
2361 (19*$sp) (42*$sp) (60*$sp) (150/$scl) ( -200/$scl) ( -255/$scl)
2362 (19*$sp) (32*$sp) (60*$sp) (150/$scl) ( -545/$scl) ( -255/$scl)
2363 (5*$sp) (42*$sp) (60*$sp)
2364 (5*$sp) (32*$sp) (60*$sp)
2400 (61*$sp) (29*$sp) (94*$sp) (1170/$scl) ( -100/$scl) ( -305/$scl)
2401 (61*$sp) (29*$sp) (100*$sp) (1170/$scl) (-130/$scl) (-255/$scl)
2402 (61*$sp) (23*$sp) (100*$sp) (1170/$scl) ( -200/$scl) ( -255/$scl)
2404 (61*$sp) (23*$sp) (94*$sp) (1170/$scl) ( -200/$scl) ( -305/$scl)
2410 (27*$sp) (29*$sp) (94*$sp) (534.282386/$scl) ( -100/$scl) ( -305/$scl)
2411 (27*$sp) (29*$sp) (100*$sp)
2412 (27*$sp) (23*$sp) (100*$sp)
2413 (27*$sp) (13*$sp) (100*$sp)
2414 (27*$sp) (23*$sp) (94*$sp)
2420 (15*$sp) (29*$sp) (94*$sp) (150/$scl) ( -100/$scl) ( -305/$scl)
2421 (15*$sp) (29*$sp) (100*$sp)
2422 (15*$sp) (23*$sp) (100*$sp)
2423 (15*$sp) (13*$sp) (100*$sp)
2424 (15*$sp) (23*$sp) (94*$sp)
2430 (1*$sp) (29*$sp) (94*$sp) (-100/$scl) ( -100/$scl) ( -305/$scl)
2431 (1*$sp) (29*$sp) (100*$sp)
2432 (1*$sp) (23*$sp) (100*$sp)
2433 (1*$sp) (13*$sp) (100*$sp)
2434 (1*$sp) (23*$sp) (94*$sp)
2441 (57*$sp) (29*$sp) (94*$sp) (1067.387326/$scl) ( -100/$scl) ( -305/$scl)
2442 (47*$sp) (29*$sp) (94*$sp) (824.8667712/$scl) ( -100/$scl) ( -305/$scl)
2443 (37*$sp) (29*$sp) (94*$sp) (681.2075521/$scl) ( -100/$scl) ( -305/$scl)
2452 (37*$sp) (13*$sp) (94*$sp)
3000 (51*$sp) (8*$sp) (62*$sp) (681.2075521/$scl) ( -593.6/$scl) ( -305/$scl)
```

```
3001 (41*$sp) (8*$sp) (92*$sp) (534.282386/$scl) ( -593.6/$scl) ( 0/$scl)
3002 (51*$sp) (8*$sp) (92*$sp) (681.2075521/$scl) ( -593.6/$scl) ( 0/$scl)
3003 (41*$sp) (8*$sp) (62*$sp) (534.282386/$scl) ( -593.6/$scl) ( -305/$scl)
3020 (41*$sp) (8*$sp) (82*$sp) (534.282386/$scl) ( -593.6/$scl) ( -35/$scl)
3021 (41*$sp) (8*$sp) (72*$sp) (534.282386/$scl) ( -593.6/$scl) ( -205/$scl)
3010 (61*$sp) (8*$sp) (62*$sp) (824.8667712/$scl) ( -593.6/$scl) ( -305/$scl)
3014 (61*$sp) (8*$sp) (92*$sp) (824.8667712/$scl) ( -593.6/$scl) ( 0/$scl)
3011 (71*$sp) (8*$sp) (62*$sp) (1067.387326/$scl) ( -593.6/$scl) ( -305/$scl)
3015 (71*$sp) (8*$sp) (92*$sp) (1067.387326/$scl) ( -593.6/$scl) ( 0/$scl)
3012 (75*$sp) (8*$sp) (62*$sp) (1170/$scl) ( -593.6/$scl) ( -305/$scl)
3016 (75*$sp) (8*$sp) (92*$sp) (1170/$scl) ( -593.6/$scl) ( 0/$scl)
3100 (38*$sp) (26*$sp) (70*$sp)
3101 (20*$sp) (26*$sp) (80*$sp)
3102 (30*$sp) (26*$sp) (90*$sp)
3103 (38*$sp) (26*$sp) (80*$sp) (534.282386/$scl) ( -593.6/$scl) ( -35/$scl)
3104 (20*$sp) (26*$sp) (70*$sp)
3200 (19*$sp) (26*$sp) (76*$sp) (150/$scl) (-593.6/$scl) 0
3201 (19*$sp) (26*$sp) (70*$sp)
3202 (5*$sp) (26*$sp) (70*$sp)
3203 (5*$sp) (26*$sp) (76*$sp)
3301 (31*$sp) (66*$sp) (90*$sp) (534.282386/$scl) ( -545/$scl) ( -205/$scl)
3302 (31*$sp) (66*$sp) (80*$sp) (534.282386/$scl) ( -545/$scl) ( -255/$scl)
3303 (31*$sp) (60*$sp) (80*$sp) (534.282386/$scl) ( -593.6/$scl) ( -305/$scl)
3304 (31*$sp) (60*$sp) (90*$sp) (534.282386/$scl) ( -593.6/$scl) ( -205/$scl)
3305 (19*$sp) (66*$sp) (90*$sp) (150/$scl) ( -545/$scl) ( -205/$scl)
3306 (5*$sp) (66*$sp) (90*$sp) (-100/$scl) ( -545/$scl) ( -205/$scl)
3307 (5*$sp) (60*$sp) (80*$sp)
3308 (5*$sp) (66*$sp) (80*$sp)
3309 (5*$sp) (60*$sp) (90*$sp)
3310 (19*$sp) (66*$sp) (80*$sp)
line
8 9
9 14
14 10
10 11
11 12
12 14
12 5 $grad1 4
12 8
29 30
30 31
31 28
28 29
8 28
9 29
10 30
11 31
surface
8 10
28 30
9 30
9 28
11 30
11 28
3-d
8 30
line
```

```
8 7
7 6  $grad2 4
6 5
17 11 $grad4 3
28 27
27 26 $grad2 4
26 25
37 31 $grad1 3
arc
17 5 19
37 25 39
line
7 27
6 26
5 25
17 37
surface
27 8
27 6
37 6
37 11
6 11
26 31
3-d
11 26
line
11 4 $grad4 4
4 3
2 1
1 10 $grad1 3
31 24 $grad1 4
24 23
22 21
21 30 $grad1 3
arc
2 3 18
22 23 38
curve
1 21 5
(554.039526/$scl) ( 75.4299/$scl) ( 0/$scl)
(598.387326/$scl) ( 60.1718/$scl) ( 0/$scl)
(628.387326/$scl) ( 50.7657/$scl) ( 0/$scl)
(658.387326/$scl) ( 42.1652/$scl) ( 0/$scl)
(688.387326/$scl) ( 34.4080/$scl) ( 0/$scl)
2 22 5
(554.039526/$scl) ( 75.4299/$scl) ( -70/$scl)
(598.387326/$scl) ( 60.1718/$scl) ( -70/$scl)
(628.387326/$scl) ( 50.7657/$scl) ( -70/$scl)
(658.387326/$scl) ( 42.1652/$scl) ( -70/$scl)
(688.387326/$scl) ( 34.4080/$scl) ( -70/$scl)
line
2 22
3 23
4 24
surface
10 4
30 24
```

```
21 10
21 4
4 31
3-d
1 31
merge
4 31 17 31
line
12 53
53 52
8 54
54 48
53 54
7 55
55 47
6 56
56 46
52 45 $grad3 4
45 46
46 47
47 48
48 52
55 56 $grad2 4
curve
5 45 10
(534.282386 /$scl) (0 /$scl) (-80/$scl)
(514.282386 /$scl) (0 /$scl) (-79.69414635/$scl)
(484.282386 /$scl) (0 /$scl) (-78.06875826/$scl)
(444.282386 /$scl) (0 /$scl) (-73.55901367/$scl)
(404.282386 /$scl) (0 /$scl) (-65.85120857/$scl)
(374.282386 /$scl) (0 /$scl) (-57.21927653/$scl)
(344.282386/$scl) ( 0/$scl) ( -44.63088477/$scl)
(324.4568728/$scl) ( 0/$scl) ( -32/$scl)
(309.4042955/$scl) ( 0/$scl) ( -15/$scl)
(305.343982/$scl) ( 0/$scl) ( 0/$scl)
surface
46 52
52 7
7 46
46 5
5 52
3-d
6 52
line
14 60
9 61
60 53
61 54
60 61
surface
9 60
60 54
12 60
8 61
3-d
8 60
merge
```

```
60 54 54 52
line
112 111
111 80
80 77
arc
105 117 19
line
117 81
81 78
arc
145 72 73
line
72 74 $grad1 3
152 71
71 75 $grad1 3
153 70
70 76 $grad1 3
105 112 $grad1 3
112 153
153 152
152 145 $grad3 4
curve
105 145 10
(534.282386 /$scl) (0 /$scl) (-80/$scl)
(514.282386 /$scl) (0 /$scl) (-79.69414635/$scl)
(484.282386 /$scl) (0 /$scl) (-78.06875826/$scl)
(444.282386 /$scl) (0 /$scl) (-73.55901367/$scl)
(404.282386 /$scl) (0 /$scl) (-65.85120857/$scl)
(374.282386 /$scl) (0 /$scl) (-57.21927653/$scl)
(344.282386 /$scl) (0 /$scl) (-44.63088477/$scl)
(324.4568728 /$scl) (0 /$scl) (-32/$scl)
(309.4042955 /$scl) (0 /$scl) (-15/$scl)
(305.343982 /$scl) (0 /$scl) (0/$scl)
line
78 77 $grad1 3
77 76
76 75
75 74 $grad3 4
arc
74 78 79
line
117 111 $grad4 3
111 70
70 71
71 72 $grad3 4
80 81 $grad1 4
curve
72 117 10
(307.839747/$scl) ( 12.547061/$scl) ( 0/$scl)
(312.4148174/$scl) ( 12.3945794/$scl) ( -15/$scl)
(329.4856358/$scl) ( 11.82562954/$scl) (  -32/$scl)
(354.282386/$scl) ( 10.999183661/$scl) ( -45.50521094/$scl)
(384.282386/$scl) ( 9.999319717/$scl) ( -56.1849885/$scl)
(414.282386/$scl) ( 8.999455774/$scl) ( -63.60284488/$scl)
(454.282386/$scl) ( 7.666303849/$scl) ( -70.16352923/$scl)
(484.282386/$scl) ( 6.666439906/$scl) ( -73.14882313/$scl)
```

```
(514.282386/$scl) ( 5.666575962/$scl) ( -74.70689427/$scl)
(534.282386/$scl) ( 5/$scl) ( -75/$scl)
surface
145 112
74 77
145 75
145 78
112 75
112 78
3-d
145 77
merge
145 112 52 5
105 111 5 11
line
103 104
104 111 $grad4 3
111 110
110 101 $grad1 4
101 102
arc
102 103 18
line
85 87
87 80 $grad1 3
80 82
82 83 $grad1 4
83 84
arc
84 85 86
curve
101 83 6
(554.039526/$scl) ( 75.4299/$scl) ( 0/$scl)
(538.488251/$scl) ( 81.1608/$scl) ( 0/$scl)
(508.488251/$scl) ( 92.5760/$scl) ( 0/$scl)
(478.488251/$scl) ( 104.4601/$scl) ( 0/$scl)
(448.488251/$scl) ( 116.6783/$scl) ( 0/$scl)
(418.488251/$scl) ( 129.074051/$scl) ( 0/$scl)
102 84 6
(554.039526/$scl) ( 75.4299/$scl) ( -70/$scl)
(538.488251/$scl) ( 81.1608/$scl) ( -70/$scl)
(508.488251/$scl) ( 92.5760/$scl) ( -70/$scl)
(478.488251/$scl) ( 104.4601/$scl) ( -70/$scl)
(448.488251/$scl) ( 116.6783/$scl) ( -70/$scl)
(418.488251/$scl) ( 129.074051/$scl) ( -70/$scl)
line
110 82
104 87
surface
111 101
80 83
111 82
111 87
101 82
101 87
3-d
111 83
```

```
merge
111 87 111 81
111 101 11 1
line
212 214
214 210
210 282
282 90
90 277
277 280
280 211
211 212
210 211
282 280
253 252
252 271
271 275 $grad1 3
275 276
270 276 $grad1 3
270 253
211 270
270 271
212 253
214 252
90 275
277 276
surface
212 90
253 275
212 252
212 276
90 252
90 276
3-d
212 275
merge
212 210 12 10
211 282 111 82
212 276 112 76
276 252 76 152
212 252 12 60
line
302 303 $grad1 3
303 304
304 301 $grad1 4
arc
301 302 305
line
82 303
80 304
87 301
83 302
surface
304 302
304 87
304 82
302 82
```

```
302 87
3-d
80 302
merge
301 80 80 78
303 80 90 280
line
321 330 $grad1 3
330 329
329 328
328 327
327 326 $grad2 4
326 325
328 331
331 330
331 323 $grad1 4
331 324 $grad1 4
arc
325 324 339
line
30 330
29 329
28 328
27 327
26 326
25 325
37 324
24 323
31 331
curve
21 321 6
(688.387326 /$scl) (34.4080 /$scl) (0/$scl)
(718.488251/$scl) ( 27.5148/$scl) ( 0/$scl)
(748.488251/$scl) ( 21.4899/$scl) ( 0/$scl)
(778.488251/$scl) ( 16.3224/$scl) ( 0/$scl)
(808.488251/$scl) ( 11.9867/$scl) ( 0/$scl)
(825.444751/$scl) ( 9.8897/$scl) ( 0/$scl)
321 323 12
(825.444751 /$scl) (9.8897 /$scl) (0/$scl)
(825.444751 /$scl) (9.8897 /$scl) (-10/$scl)
(825.444751 /$scl) (9.8897 /$scl) (-20/$scl)
(825.444751 /$scl) (9.8897 /$scl) (-30/$scl)
(825.444751 /$scl) (9.8897 /$scl) (-40/$scl)
(825.444751 /$scl) (9.8897 /$scl) (-50/$scl)
(825.444751 /$scl) (9.8897 /$scl) (-60/$scl)
(825.444751 /$scl) (9.8897 /$scl) (-65/$scl)
(825.444751 /$scl) (9.8897 /$scl) (-70/$scl)
(825.3673164 /$scl) (9.224317634 /$scl) (-72.5/$scl)
(825.1557611 /$scl) (7.406459205 /$scl) (-74.330127019/$scl)
(824.8667712/$scl) ( 5 /$scl) (-75/$scl)
surface
326 331
328 321
37 326
26 327
27 328
28 329
```

```
29 321
21 323
24 331
31 324
28 331
31 330
3-d
326 31
328 30
331 21
merge
24 331 37 331
curve
321 341 10
(825.444751 /$scl) (9.8897 /$scl) (0/$scl)
(839.126426 /$scl) (8.4435 /$scl) (0/$scl)
(869.126426 /$scl) (5.6404 /$scl) (0/$scl)
(899.126426 /$scl) (3.5130 /$scl) (0/$scl)
(929.126426 /$scl) (1.9854 /$scl) (0/$scl)
(959.126426 /$scl) (0.9713 /$scl) (0/$scl)
(989.126426 /$scl) (0.3747 /$scl) (0/$scl)
(1019.126426 /$scl) (0.0903/$scl) (0/$scl)
(1049.126426 /$scl) (0.0052 /$scl) (0/$scl)
(1067.387326 /$scl) (0 /$scl) (0/$scl)
line
323 343
331 351
324 344
326 346
327 347
328 348
329 349
330 350
331 351
341 343
343 351 $grad1 3
351 344 $grad1 4
344 346
346 347 $grad2 3
347 348
348 349
349 350
350 341 $grad1 4
350 351
348 351
surface
346 351
348 341
321 343
323 347
331 344
324 346
326 347
328 349
329 341
3-d
346 331
```

```
348 321
merge
323 351 324 351
line
341 361
343 363
351 371
344 364
346 366
347 367
348 368
349 369
350 370
351 371
361 363
363 371 $grad1 3
371 364 $grad1 4
364 366
366 367 $grad2 3
367 368
368 369
369 370
370 361 $grad1 4
370 371
368 371
surface
366 371
368 361
341 363
343 367
351 364
344 366
346 367
348 369
349 361
3-d
366 351
368 341
merge
343 371 344 371
line
406 407
407 415
415 416 $grad2 4
416 406
446 447
447 455
455 456 $grad2 4
456 446
406 446 $grad2 3
407 447 $grad2 3
415 455 $grad2 3
416 456 $grad2 3
surface
406 415
446 455
406 447
```

```
406 456
415 447
415 456
3-d
415 446
merge
407 416 47 56
line
77 500
500 501
501 502
502 503
503 504
cdrive
75 78 77 504
line
504 505
cdrive
506 504 504 505
cdrive
301 303 77 504
504 527 504 505
merge
78 505 301 505
line
277 550
550 551
551 552
552 553
553 554
554 555
cdrive
277 275 277 554
554 557 554 555
merge
277 561 303 505
277 559 77 512
276 560 76 511
line
609 608
608 607
629 628
628 627
609 629
608 628
607 627
608 701
surface
609 628
607 628
cdrive
609 628 608 701
607 628 608 701
merge
609 628 9 28
608 627 8 27
line
```

```
627 626 $grad2 4
607 606 $grad2 4
626 704
704 777
777 705
705 703
surface
705 626
cdrive
705 626 627 607
merge
626 607 26 7
line
629 829
829 849
849 869
628 828
828 848
848 868
829 828
849 848
869 868
627 827
827 847
847 867
828 827
848 847
867 868
867 866 $grad2 4
847 846 $grad2 4
827 826 $grad2 4
surface
629 828
829 848
849 868
627 828
827 848
847 868
cdrive
627 869 629 702
merge
629 868 29 368
627 868 27 368
cdrive
626 705 627 867
merge
626 867 26 367
line
908 907
907 955
955 947
947 948
948 954
954 908
907 1007
surface
907 948
```

```
cdrive
907 948 907 1007
merge
908 947 8 47
908 1007 607 701
line
1108 1109
1109 1161
1161 1154
1154 1108
1108 1118
surface
1108 1161
cdrive
1108 1161 1108 1118
merge
1108 1161 8 61
1109 1118 609 701
1154 1118 1008 954
1154 1171 954 1048
line
1407 1415
1415 1455 $grad2 3
1447 1455
1447 1407 $grad2 4
1407 1417
surface
1415 1447
cdrive
1415 1447 1407 1417
merge
1407 1455 407 455
1407 1425 1055 947
line
1500 1508
1508 1501 $grad2 4
1501 1502
1502 1578
1578 1503
1503 1500
1500 1507 $grad2 4
surface
1500 1502
cdrive
1500 1502 1500 1507
merge
1501 1509 416 455
1508 1507 1447 1425
line
1507 1557
1559 1554 $grad2 4
1557 1559
1557 1556
1555 1577
1577 1556
1555 1554
1506 1556
```

```
1509 1559
1504 1554
1505 1555
surface
1556 1554
1506 1557
1506 1555
1504 1557
1504 1555
3-d
1504 1556
merge
1556 1554 606 707
1507 1559 907 1055
1559 1504 7 56
line
2402 2404
2404 2400
2400 2401
2401 2402
2400 2441
2441 2442
2442 2443
2443 2410
2410 2420
2420 2430 $grad2 3
surface
2400 2402
cdrive
2400 2402 2400 2410
2410 2412 2410 2420
2420 2422 2420 2430
merge
2400 2411 710 798
2410 2421 1505 1577
2420 2431 1505 1578
2401 2412 798 711
2411 2422 1577 1506
2421 2432 1578 1506
element(brick,nodes=($np^3),entity="fluid")
8 30
11 26
1 31
6 52
8 60
145 77
111 83
212 275
80 302
326 31
328 30
331 21
346 331
348 321
366 351
368 341
415 446
```

```
74 504
506 505
301 528
526 531
277 557
554 560
608 702
608 703
705 606
629 714
626 711
1007 948
1118 1161
1425 1447
1500 1505
1506 1554
2404 2411
2414 2431
element(boundary,quad,nodes=($np^2),entity="wall")
17 26
1 24
5 46
145 78
101 87
87 302
21 323
37 326
321 343
324 346
341 363
344 366
406 456
78 506
509 510
301 530
element(boundary,quad,nodes=($np^2),entity="sym")
1 29
52 46
14 61
145 75
101 82
214 275
82 302
329 21
321 349
341 369
406 447
75 506
507 510
302 531
275 561
609 702
869 702
1048 947
1109 1171
1417 1447
element(boundary,quad,nodes=($np^2),entity="inflow")
```

```
366 371
368 361
869 712
867 712
866 711
2400 2402
element(boundary,quad,nodes=($np^2),entity="outflow")
446 455
1447 1467
1500 1502
2430 2433
element(boundary,quad,nodes=($np^2),entity="impeller")
504 506
526 528
557 554
element(boundary,quad,nodes=($np^2),entity="jet_eflux")
505 510
529 531
560 555
element(boundary,quad,nodes=($np^2),entity="entrain")
2402 2434
702 711
702 707
1007 1048
1118 1171
1425 1465
1506 1557
1506 1500
element(boundary,quad,nodes=($np^2),entity="wind_wall")
704 606
626 710
1501 1505
1504 1555
2404 2430
end
fiprep
entity(name="fluid",fluid)
entity(name="wall",wall)
entity(name="sym",plot)
entity(name="entrain",plot)
entity(name="inflow",plot)
entity(name="outflow",plot)
entity(name="impeller",plot)
entity(name="jet_eflux",plot)
entity(name="wind_wall",wall)
bcnode(ux,entity="entrain",subroutine=6)
0.01434 17.74 0.825 1.177 1.846e-5 $scl
bcnode(uy,entity="entrain",subroutine=6)
0.01434 17.74 0.825 1.177 1.846e-5 $scl
bcnode(uz,entity="entrain",subroutine=6)
0.01434 17.74 0.825 1.177 1.846e-5 $scl
bcnode(pressure,entity="entrain",subroutine=6)
0.01434 17.74 0.825 1.177 1.846e-5 $scl
bcnode(kinetic,entity="entrain",subroutine=6)
0.01434 17.74 0.825 1.177 1.846e-5 $scl
bcnode(dissipation,entity="entrain",subroutine=6)
0.01434 17.74 0.825 1.177 1.846e-5 $scl
```

```
bcnode(uy,entity="inflow",zero)
bcnode(uz,entity="inflow",zero)
bcnode(ux,entity="inflow",subroutine=9)
0.01434 17.74 0.825 1.177 1.846e-5 $scl 0.01434 0.825 8.38809
bcnode(dissipation,entity="inflow",subroutine=39)
0.01434 17.74 0.825 1.177 1.846e-5 $scl 0.01434 0.825 8.38809,
27.66 1959.,
55.30  1994.,
82.94 1923.,
110.59  1425.,
165.88  1028.,
221.16  943.,
276.44  705.,
387.03  384.,
497.56  174.,
663.41  41.,
829.22  4.76,
1105.18  0.782,
1381.40  0.536,
1933.75  0.215,
2486.11  0.05
bcnode(kinetic,entity="inflow",subroutine=39)
0.01434 17.74 0.825 1.177 1.846e-5 $scl 0.01434 0.825 8.38809,
27.66 0.0855,
55.30  0.0861,
82.94 0.0834,
110.59  0.0790,
165.88  0.0750,
221.16  0.0725,
276.44  0.0649,
387.03  0.0578,
497.56  0.0486,
663.41  0.0228,
829.22  0.0102,
1105.18  0.0064,
1381.40  0.0055,
1933.75  0.0031,
2486.11  0.0016
bcnode(uy,entity="outflow",zero)
bcnode(uz,entity="outflow",zero)
bcnode(uy,entity="jet_eflux",zero)
bcnode(uz,entity="jet_eflux",zero)
bcnode(uz,entity="sym",zero)
bcnode(velocity,entity="wall",zero)
bcnode(velocity,entity="wind_wall",zero)
bcflux(x,entity="inflow",constant=0)
bcflux(x,entity="jet_eflux",constant=91.83)
icnode(velocity,read,entity="fluid")
icnode(dissipation,read,entity="fluid")
icnode(kinetic,read,entity="fluid")
density(set=1,constant=1.177)
viscosity(set=1,constant=1.846e-5,K.E.)
turboptions(RNG,consistent,delay=1,revised)
execution(newjob)
problem(3-d,nonlinear,turbulent)
scale(value=(1e-3*$scl))
solution(segregated=100,cgs=0,cr=0,precondition=21,pprojection)
```

```
pressure(mixed,continuous)
relaxation
0.3 0.3 0.3 0.3 0.3 0.3 0.3 0.3
options(upwinding)
upwinding(streamline)
1.0 1.0 1.0 0 0 5.0 5.0 5.0
renumber(bandwidth)
extrapolate(off)
printout(none)
dataprint(none)
end
create(fisolv)
end
```

Appendix D

Static Pressure Tapping Locations

D.1 Cross-sections

Cross section 1 was located at static pressure tappings 1–11.
Cross section 2 was located at static pressure tappings 18–24.
Cross section 3 was located at static pressure tappings 28–36.
Cross section 4 was located at static pressure tappings 68–73.
Cross section 4a was located 38 mm upstream of cross section 4.

Figure D.1 shows the location of these cross sections (and the pressure tappings).

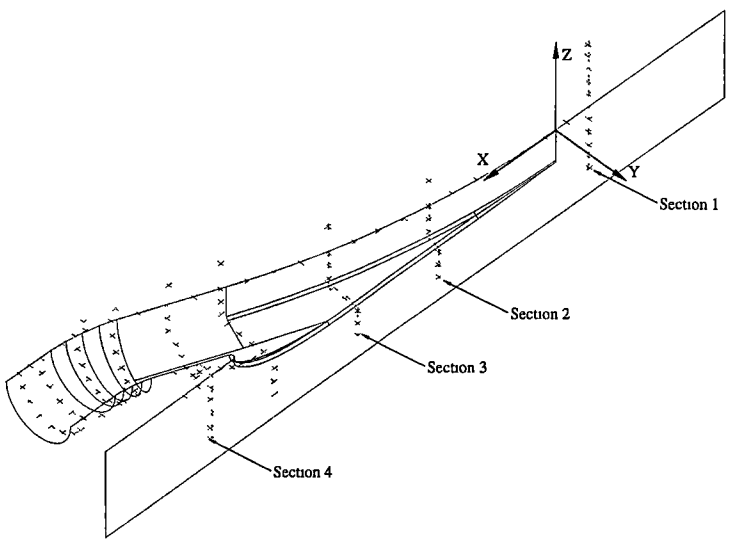

Figure D.1: Location of pressure tappings and measurement cross-sections, half model shown for reference.

D.2 Static Pressure Tappings

This data was provided by Dr R. Coleman and Mr. H. Clement from the Spatial Information Science, Department of Geography and Environmental Studies, University of Tasmania, who optically surveyed the model.

tapping	x(mm)	y (mm)	z(mm)
1	-74.64577	2.1104701E-02	146.6774
2	-74.70692	-6.5543219E-02	119.4613
3	-75.22482	0.4210752	90.56161
4	-75.28597	0.4387409	60.15048
5	-75.34711	0.4503028	29.92999
6	-75.92616	-4.7204085E-03	-4.0255525E-04
7	-76.96196	3.1856354E-02	-29.11322
8	-76.53578	-4.0372834E-04	-58.93056
9	-77.08426	7.4028037E-02	-90.14136
10	-78.60737	0.1542959	-119.6573
11	-79.15585	2.0101201E-02	-144.4781
12	-24.99996	0.7202612	-0.1752094
13	25.86508	0.4417295	0.5179950
14	74.90314	2.263031	0.3789846
15	125.9211	4.449407	0.2442623
16	175.1120	8.705990	0.1847651
17	225.8566	14.32886	0.2691043
18	275.7794	20.46110	61.30038
19	275.2004	21.01437	0.4873904
20	275.6266	20.96244	-28.72762
21	274.0729	20.57856	-58.96099
22	274.6158	-0.9338250	-90.77735
23	274.5546	-0.9813225	-119.1906
24	273.5188	-0.9119031	-149.3100
25	323.6918	29.71239	0.6721249
26	375.2295	40.20152	0.1138708
27	422.3813	50.96246	-0.3363805
28	471.2702	63.98549	61.52295
29	470.6911	64.55524	0.2067179
30	470.6300	64.54713	-29.41146
31	470.0815	64.62797	-60.82050
32	468.7992	52.42882	-74.52394
33	468.3962	22.61333	-75.10040
34	466.3801	-1.190486	-91.78573
35	466.3190	-1.185599	-121.8003
36	465.8011	-0.6959359	-150.7991
37	519.5494	79.10785	0.2849028
38	567.5555	95.66669	0.5202386
39	613.6428	112.8576	8.1476346E-02
40	659.9134	130.9639	61.20595

41	659.8217	131.4802	0.5902340
42	659.2733	131.5060	-29.12598
43	658.2374	131.5586	-58.73452
44	656.8940	118.4409	-74.17016
45	658.9276	88.47581	-74.85081
46	660.4433	58.04422	-75.24136
47	660.9536	27.07598	-72.25253
48	662.6222	-0.3620265	-89.65948
49	664.0231	-0.4292210	-120.2795
50	662.9872	-0.3697956	-150.0938
51	706.0313	150.5899	1.114924
52	756.6555	160.2315	58.26086
53	752.7281	169.6854	1.143026
54	752.6365	169.1901	-28.49108
55	753.7010	163.5890	-53.88731
56	756.3460	143.9133	-71.04089
57	766.5742	119.9085	-75.12224
58	779.1779	94.64655	-75.25240
59	788.4620	70.84399	-68.72437
60	800.4272	50.42941	-51.17743
61	806.9116	35.89366	-23.24020
62	810.7491	33.90829	0.2060908
63	688.7616	25.65165	-67.10064
64	717.5444	24.06494	-58.84725
65	740.5708	24.29620	-50.22915
66	765.5773	24.73911	-36.90952
67	795.2751	29.67310	-20.23723
68	815.4926	0.3307937	1.0568874E-02
69	816.4060	0.2059229	-27.90915
70	816.8322	6.2751584E-02	-54.32555
71	816.7711	0.1980462	-88.33591
72	817.1971	0.2638139	-121.1576
73	815.7047	0.7785820	-149.0488
74	848.7528	0.2695676	-2.090725
75	880.0637	0.2588252	-1.991881
76	853.9736	52.29580	-1.392147
77	798.9377	188.8409	0.2645530
78	852.9101	189.6636	51.21433
79	844.7211	208.9424	1.218606
80	846.8215	204.3944	-28.44092
81	852.2394	190.1750	-53.11856
82	860.2144	169.6469	-69.39913
83	871.2644	143.2208	-75.86499
84	881.4009	117.4872	-71.80441
85	896.1373	94.52591	-56.54677
88	889.6198	222.7524	1.669494
89	914.4694	203.8594	52.78468

90	910.8804	226.3710	-0.1131984
91	911.0620	222.3280	-26.55772
92	914.9568	207.2555	-52.16398
93	917.5407	186.5567	-67.84714
94	921.2503	160.1574	-76.01426
95	926.3300	131.8366	-72.93894
96	928.7000	106.7656	-59.24634
97	935.0007	89.50968	-37.59631
98	936.4916	80.99158	-4.455094
99	939.0246	230.4740	2.0892762E-02
100	986.5397	231.4487	-1.245094
101	989.0355	225.4157	-31.15913
102	986.5646	210.1782	-54.46537
103	986.5284	186.7197	-70.54412
104	985.7603	159.0690	-76.75213
105	985.9669	130.9947	-71.85966
107	984.9829	90.71427	-35.65630
108	983.5802	82.77193	0.4044550
109	1012.003	231.8046	-1.134174
110	1037.466	232.2030	-2.319762
111	1034.601	226.4735	-31.22390
112	1032.618	211.2056	-54.53882
113	1033.038	187.2458	-71.12996
114	1032.819	160.5417	-77.39856
115	1033.086	133.4743	-73.48097
116	1033.446	107.4898	-57.92501
117	1033.929	91.11376	-37.04773
118	1036.456	83.41732	-1.078376

Bibliography

[1] R. Aartojärvi. Review of test methods adopted for water jets at the KaMeWa marine laboratory. Technical Report R-504, KaMeWa Marine Laboratory, 1994.

[2] A. M. Abdel-Fattah and S. A. Fisher. An auxiliary intake system for an unmanned aircraft. In *Proc. Tenth International Symposium on Air Breathing Engines*, pages 1199–1208, 1991.

[3] M. Abramowitz and I. Stegun, editors. *Handbook of Mathematical Functions: with formulas, graphs and mathematical tables.* Dover Publications, 1965.

[4] K. Alexander. Two stage water-jets for high-speed commercial craft. In *IMAS 91*, pages 141–146, 1991.

[5] K. Alexander, H. Coop, and T. van Terwisga. Waterjet-hull interaction: Recent experimental results. *SNAME Transations*, 102:87–105, 1994.

[6] J. Allison. Marine waterjet propulsion. *SNAME Transations*, 101:275–335, 1993.

[7] J. L. Allison. Using CFD to design water-jet inlets. *Mechanical Engineering*, pages 82–83, 1997.

[8] J. L. Allison and C. Dai. Steering and reversing gear for very large waterjets. In *RINA Proc. International Symposium on Waterjet Propulsion Latest Developments*, 1994.

[9] J. L. Allison and P. Goubault. Waterjet propulsion for fast craft–optimized integration of hull and propulsor. In *Proc. FAST'95*, volume II, pages 1117–1130, 1995.

[10] F. E. Ames. The influence of large-scale high-intensity turbulence of vane heat transfer. *Trans. ASME, Journal of Turbomachinery*, 119:23–30, 1997.

[11] L. Arcand. The performance of two axial flow waterjet pumps. In *Symposium on Pumping Machinery for Marine Propulsion*, pages 103–120, 1968.

[12] L. Arcand and C. R. Comolli. Optimization of waterjet propulsion for high-speed ships. *Journal of Hydronautics*, 2(1):2–8, 1968.

[13] P. Bannsod and P. Bradshaw. The flow in S-shaped ducts. *The Aeronautical Quarterly*, XXIII:131–140, 1972.

[14] R. A. Barr. Supercavitating and superventilated propellers. *SNAME Transactions*, 78:417–450, 1970.

[15] A. Betz. *Introduction to the theory of flow machines.* Pergamon Press, 1966.

[16] P. Bradshaw. The turbulence structure of equilibrium boundary layers. *Journal of Fluid Mechanics*, 29(4):625–645, 1967.

[17] P. Bradshaw, editor. *Turbulence*, volume 12 of *Topics in Applied Physics.* Springer-Verlag, 1978.

[18] P. Bradshaw and F. Y. F. Wong. The reattachment and relaxation of a turbulent shear layer. *Journal of Fluid Mechanics*, 52(1):113–135, 1972.

[19] J. H. Brandau. Performance of waterjet propulsion systems-a review of the state-of-the-art. *Journal of Hydronautics*, 2(2):61–73, 1968.

[20] E. P. Bruce, W. S. Gearhard, J. R. Ross, and A. L. Treaster. The design of pump-jets for hydrodynamic propulsion. In *Fluid Mechanics, Acoustics and Design of Turbomachinery, Part II*, pages 795–893, 1971.

[21] E. Brundrett and W. D. Baines. The production and diffusion of vorticity in duct flow. *Journal of Fluid Mechanics*, 19:375–394, 1964.

[22] R. Burton. *Vibration and Impact.* Addison-Wesley Publishing Company, Inc., 1958.

[23] J. L. Campbell and S. H. Ellis. Engine/inlet compatibility analysis procedure. *Journal of Aircraft*, 8(5):301–307, 1971.

[24] D. J. Cockrell and B. E. Lee. Production of shear profiles in a wind tunnel by cylindrical rods placed normal of the stream. *Journal of the Royal Aeronautical Society*, 70:724–725, 1966.

[25] D. C. Collis and M. J. Williams. Two-dimensional convection from heated wires at low Reynolds numbers. *Journal of Fluid Mechanics*, 6:357–384, 1959.

[26] D. S. Conte and C. de Boor. *Elementary Numerical Analysis: an algorithmic approach.* McGraw-Hill, 1972.

[27] N. J. Cook. Simulation techniques for short test-section wind tunnels: Roughness, barrier and mixing device methods. In *Wind tunnel modeling for civil engineering applications*, pages 126–136. Cambridge University Press, 1982.

[28] H. G. Coop, A. J. Bowen, and K. V. Alexander. Waterjet propulsion - recent applications and current research at the University of Canterbury. In *IPENZ Annual Conference*, 1992.

[29] J. P. Crowder. Add fluorescent minitufts to the aerodynamicist's bag of tricks. *AIAA, Astronautics & Aeronautics*, 18(11):54–56, 1980.

[30] C. Dai, C. Kerr, P. Nguyen, and H. Wang. A novel flush inlet design methodology for waterjet propulsion. In *Proc. FAST'95*, volume II, pages 1367–1378, 1995.

[31] O. L. Davies and P. L. Goldsmith, editors. *Statistical Methods in Research and Production.* Oliver and Boyd, 1972.

[32] G. H. Davison. The case for engine-speed water jets in high speed craft. In *Proc. High-speed Surface Craft Conference*, pages 218–232, 1990.

[33] G. de Vahl Davis. The flow of air through wire screens. In *Proc. 1st Australiasian Confernce on Hydraulics and Fluid Mechanics*, pages 191–212, 1962.

[34] M. Delao. Some experimental results of tests of a low-speed, waterjet propulsion system. *Journal of Hydronautics*, 1(2):97–101, 1967.

[35] G. Dyne and P. Lindell. Waterjet testing in the SSPA towing tank. In *RINA Proc. International Symposium on Waterjet Propulsion Latest Developments*, 1994.

[36] E. A. Eichelbrenner. Three-dimensional boundary layers. *Annual Review of Fluid Mechanics*, 5:339–360, 1973.

[37] J. W. English. Practical considerations on waterjets with flush intakes. In *RINA Proc. International Symposium on Waterjet Propulsion Latest Developments*, 1994.

[38] A. P. Farr and G. A. Schumacher. System for evaluation of F-15 inlet dynamic distortion. In *Instrumentation for Airbreathing Propulsion*, pages 59–76, 1972.

[39] E. H. Fisher and N. Rhodes. Uncertainty in computational fluid dynamcs. *Journal of Mechanical Engineering Science*, 210:91–94, 1996.

[40] Fluid Dynamics International. *FIDAP Theory Manual*, 1993.

[41] Fluid Dynamics International. *FIDAP Tutorial Manual*, 1993.

[42] Fluid Dynamics International. *FIDAP Users Manual*, 1993.

[43] M. Førde, E. Ørbekk, and N. Kubberud. Computational fluid dynamics applied to high speed craft with special attention to water intake for water jets. In *Proc. FAST'91*, pages 69–89, 1991.

[44] C. J. Freitas. Perspective: Selected benchmarks from commercial CFD codes. *Trans. ASME, Journal of Fluids Engineering*, 117:208–218, 1995.

[45] D. A. Frith. Water-jet propulsion system design studies using a computer. Technical Report 74-GT-114, ASME, 1974.

[46] N. Fujisawa and Y. Ogawa. Model and prototype performances of waterjet propulsion systems for small-scale high-speed hydoplane boat. In *Fourth International Symposium on Transport Phenomena and Dynamics of Rotating Machinery*, volume B, pages 256–268, 1992.

[47] S. J. Gallimore and N. A. Cumpsty. Spanwise mixing in multistage axial flow compressors: Part 1–experimental investigation. *Trans ASME, Journal of Turbomachinery*, 108:2–9, 1986.

[48] F. B. Gessner and J. B. Jones. On some aspects of fully-developed turbulent flow in rectangular channels. *Journal of Fluid Mechanics*, 23(4):689–713, 1965.

[49] Golden Software Inc. *Surfer Reference Manual*, 1987.

[50] E. L. Goldsmith and J. Seddon, editors. *Practical Intake Aerodynamic Design.* Blackwell Scientific Publications, Oxford, 1993.

[51] S. Goldstein, editor. *Modern Developments in Fluid Dynamics*, volume I. Dover Publications Inc., 1965.

[52] C. A. Gongwer. The influence of duct losses on jet propulsion devices. *Jet Propulsion*, pages 385–386, 1954.

[53] M. C. Good and P. N. Joubert. The form drag of two-dimensional bluff-plates immersed in turbulent boundary layers. *Journal of Fluid Mechanics*, 31(3):547–582, 1968.

[54] A. D. Gosman and C. W. Rapley. A prediction method for fully-developed flow through non-circular passages. In *Proceedings of the First International Conference on Numerical Methods in Laminar and Turbulent Flow*, pages 271–285. Pentech Press, 1978.

[55] G. Griffith-Jones and A. J. Bowen. Modelling of the flow through a 3D curved intake of a waterjet propulsion unit in a planing hull. In *Proc. 11th Australasian Fluid Mechanics Conference*, pages 1205–1208, 1992.

[56] G. J. Griffith-Jones. *Investigation of Incompressible Flow Through an Intake Duct with Applications to Waterjet Propulsion.* PhD thesis, University of Canterbury, 1994.

[57] F. E. Grubbs. Sample criteria for testing outlying observations. *The Annals of Mathematical Statistics*, XXI:27–58, 1950.

[58] K. Haglund, R. Svensson, and O. Björheden. Design and testing of a high-performance water jet propulsion unit. In *Symposium on Small Fast Warships and Security Vessels*, pages 223–236, 1982.

[59] M. R. Hale and D. H. Vorrie. Hydro-jet propulsion reduces vibration. *Engineering*, 198:118–119, 1964.

[60] V. Haroutunian and M. S. Engelman. On modeling wall-bound turbulent flows using specialized near-wall finite elements and the standard $k - \epsilon$ turbulence model. In *Advances in Numerical Simulation of Turbulent Flows*, pages 97–105, 1991.

[61] V. Haroutunian and M. S. Engelman. Two-equation simulations of turbulent flows: A commentary on physical and numerical aspects. In *Advances in Finite Element Analysis in Fluid Dynamics*, pages 95–105, 1993.

[62] R. Hatte and H. J. Davis. Selection of hydrofoil waterjet propulsion systems. *Journal of Hydronautics*, 1(1):12–22, 1967.

[63] P. Henrici. *Applied and Computational Complex Analysis*, volume 1. Power series-integration-conformal mapping-location of zeros. John Wiley & Sons, 1974.

[64] J. O. Hinze. *Turbulence.* McGraw-Hill, second edition, 1975.

[65] T. Hoshino and E. Baba. Determination of propulsive performance of waterjet in model and full scales. In *21st Intennational Towing Tank Conference, Supplement to the report of the water-jets group*, 1996.

[66] L. Iannone and R. Rocchi. A new proposal of performance evaluation and analysis for flush-inlet waterjet crafts. *Hydrocarbons*, pages 159–179, 1993.

[67] I. E. Idel'chik. *Handbook of Hydraulic Resistance.* CRC Press Inc., 1994.

[68] F. P. Incropera and D. P. DeWitt. *Fundamentals of Heat and Mass Transfer.* John Wiley & Sons, 1990.

[69] ITTC. Report of the high speed marine vehicles committee. In *Proc. 18th International Towing Tank Conference*, volume 1, pages 304–313, 1987.

[70] R. C. Jenkins and A. L. Loeffler Jr. Modeling of subsonic flow through a compact offset inlet diffuser. *AIAA Journal*, 29(3):401–408, 1991.

[71] S. Johnson. Intake design - hull boundary layer simulation, 1995. University of Tasmania, Honours Thesis CM95/23.

[72] V. E. Johnson Jr. Water-jet propulsion for high-speed hydrofoil craft. *Journal of Aircraft*, 3(2):174–179, 1966.

[73] H. Joubert and M. Goutines. Use of CFD methods to design engine nacelles. Technical Report 93-GT-117, ASME, 1993.

[74] T. Kashiwadani. On the design method of waterjet inlet for the SES 'Meguro 2'. In *Proc. FAST'97*, pages 677–684, 1997.

[75] H. C. Kim. Hydrodynamic aspects of internal pump-jet propulsion. *Marine Technology*, pages 80–98, 1966.

[76] P. S. Klebanoff. Characteristics of turbulence in a boundary layer with zero pressure gradient. Technical Report 1247, National Advisory Committee for Aeronautics, 1955.

[77] C. Kruppa, H. Brandt, and C. Östergaard. Water jet propulsion for high-speed vehicles. Technical Report T6239, Mintech Translation, 1969. Translation of *Wasserstrahlantriebe fur Hochgeschwindigkeitsfahrzeuge.*

[78] C. F. L. Kruppa. Propulsion systems for high-speed marine vehicles. In *Proc. 2nd Conference on High-Speed Marine Craft*, 1990.

[79] C. F. L. Kruppa. On pump installation efficiency. In *21st Intennational Towing Tank Conference, Supplement to the report of the water-jets group*, 1996.

[80] B. E. Larock and D. R. Schamber. Approaches to the finite element solution of two-dimensional turbulent flows. In *Computational techniques in transient and turbulent flow*, volume 2, chapter 9, pages 253–282. Pineridge Press Limited, 1981.

[81] E. Laws and J. Livesey. Flow through screens. *Annual Review of Fluid Mechanics*, 10:247–266, 1978.

[82] D. C. Leslie. *Developments in the theory of turbulence.* Clarendon Press, 1973.

[83] J. Levy. The design of water-jet propulsion systems for hydrofoil craft. *Marine Technology*, pages 15–25 and 41, 1965.

[84] P. C. Manins. A study of hydraulic jet propulsion in a destroyer. Technical Report Mechanical Engineering Note 316, Aeronautical Research Laboratories, 1970.

[85] N. N. Mansour, J. Kim, and P. Moin. Reynolds-stress and dissipation-rate budgets in a turbulent channel flow. *Journal of Fluid Mechanics*, 194:15–44, 1988.

[86] N. Matherson. Wind tunnel studies of a ship model using vortex generators to improve wake velocities. Technical Report Aerodynamics note 347, Aeronautical Research Laboratories, 1974.

[87] K. M. McCreath and A. J. W. Smith. Boundary layer influence of the performance of submerged intakes. *Journal of the Royal Aeronautical Society*, 71:581–583, 1967.

[88] L. M. Milne-Thomson. *Theoretical Hydrodynamics.* MacMillan & Co Ltd, 1968.

[89] J. Moore and B. L. Smith. Flow in a turbine cascade: Part 2–measurement of flow trajectories by ethylene detection. *Trans ASME, J Engineering for Gas Turbines and Power*, 106:409–413, 1984.

[90] F. T. F. Morgado and L. M. C. Gato. An integral calculation method for incompressible three-dimensional boundary layers in axisymmetric diffusers. *International Journal of Heat and Fluid Flow*, 12(2):150–157, 1991.

[91] H. K. Myong and N. Kasagi. Prediction of anisotropy of the near-wall turbulence with an anisotropic low-Reynolds-number $k-\epsilon$ turbulence model. *Trans. ASME, Journal of Fluids Engineering*, 112:521–524, 1990.

[92] H. K. Myong and T. Kobayashi. Prediction of three-dimensional developing turbulent flow in a square duct with an anisotropy low-Reynolds-number $k-\epsilon$ model. *Trans. ASME, Journal of Fluids Engineering*, 113:608–615, 1991.

[93] M. Namia and F. B. Gessner. A calculation method for developing turbulent flow in rectangular ducts of arbitrary aspect ratio. *Journal of Fluids Engineering*, 117: 249–258, 1995.

[94] J. F. Nash and A. G. J. Macdonald. A turbulent skin friction law for use at subsonic and transonic speeds. Technical Report 1206, U.K. National Physical Laboratory, 1966.

[95] B. Nereng, K. Holden, and C. V. Svendsen. Development and experience of water-jet propulsion systems. In *Second International Congess, Marintime Association of the East Mediterrean*, pages 1147–1179, Trieste, 1981.

[96] S. Ostrach. An analysis of laminar free convection flow and heat transfer about a flat plate parrallel to the direction of the generating body force. Technical Report 1111, National Advisory Committee for Aeronautics, 1953.

[97] B. R. Pai and J. H. Whitelaw. Simplification of the razor blade technique and its application to the measurement of wall-shear stress in wall-jet flows. *The Aeronautical Quartely*, XX:355–364, 1969.

[98] R. G. Parker. Water jet drive - aspects of design and use and its place among propulsion systems. In *proc. Propulsion for Small Craft - Propellers, Sterngear, Engines and Installation*, pages 10/1–10/11, 1982.

[99] D. J. Parsons and P. G. Hill. Effects of curvature on two-dimensional diffuser flow. *Trans. ASME, Journal of Fluids Engineering*, 95:349–360, 1973.

[100] V. C. Patel, W. Rodi, and G. Scheuerer. Turbulence models for near-wall and low Reynolds number flows: A review. *AIAA Journal*, 23(9):1308–1319, 1985.

[101] A. E. Perry, K. L. Lim, and S. M. Henbest. An experimental study of the turbulence structure in smooth- and rough-wall boundary layers. *Journal of Fluid Mechanics*, 177:437–466, 1987.

[102] D. Pike. Hydraulic propulsion. *Marine Propulsion*, pages 20–22, 1987.

[103] J. Pingzhong and W. Lixiang. The application of waterjet propulsion in high-performance vehicles in china. In *Proc. International High-Performance Vehicle Conference*, 1988.

[104] V. S. Pratap and D. B. Spalding. Numerical computations of the flow in curved ducts. *Aeronautical Quarterly*, 26:219–228, 1975.

[105] B. D. Pratte and W. D. Baines. Profiles of the round turbulent jet in a cross flow. *Journal of the Hydraulics Division, Procedings of the ASCE*, 93:53–64, 1967.

[106] W. H. Press, B. P. Flannery, S. A. Teukolsky, and W. T. Vetterling. *Numerical recipes in Pascal.* Cambridge University Press, 1989.

[107] J. V. Pylkkänen. A test case of the application of a CFD code for predicting waterjet inlet flow. In *21st Intennational Towing Tank Conference, Supplement to the report of the water-jets group*, 1996.

[108] K. G. Ranga Raju, J. Loeser, and E. J. Plate. Velocity profiles and fence drag for a turbulent boundary layer along smooth and rough plates. *Journal of Fluid Mechanics*, 76(2):383–399, 1976.

[109] V. Rivoire and Y. Vigneron. CFD environment for aerodynamic design at Aerospace Avions. *Cray Channels*, 15(2):5–9, 1993.

[110] J. L. Roberts and G. J. Walker. Performance of water jet propulsion systems with boundary layer ingestion. In *Proc. Twelfth Australasian Fluid Mechanics Conference*, pages 271–274, 1995.

[111] J. L. Roberts and G. J. Walker. Bounding ingestion stream-tube determination via a CO tracer. *Experiments in Fluids*, In Press.

[112] J. L. Roberts, G. J. Walker, and M. R. Davis. Flow distribution at waterjet intakes. In *Proc. FAST '97*, pages 669–675, 1997.

[113] J. C. Rotta. Turbulent boundary layers in incompressible flow. *Progress in Aeronautical Sciences*, 2:1–219, 1962.

[114] M. Rowe. Measurements and computations of flow in pipe bends. *Journal of Fluid Mechanics*, 43(4):771–783, 1970.

[115] S. M. Roy. The evolution of the modern waterjet marine propulsion unit. In *RINA Proc. International Symposium on Waterjet Propulsion Latest Developments*, 1994.

[116] C. L. Rumsey and V. N. Vatsa. A comparison of the predictive capabilities of several turbulence models using upwind and central-difference computer codes. Technical Report 93-0192, AIAA, 1993.

[117] Sadtler Research Laboratories. *The Interpretation of Vapor-Phase Infrared Spectra.* Sadtler Research Laboratories, 1984.

[118] H. I. H. Saravanamuttoo, editor. *Recommended Practices for Measurement of Gas Path Pressures and Temperatures for Performance Assessment of Aircraft Turbine Engines and Components.* AGARD, 1990. Advisory Report No.245.

[119] T. Sasajima and Y. Mishima. Air drawing criteria for semi-scoop type waterjet inlet for SES. In *21st Intennational Towing Tank Conference, Supplement to the report of the water-jets group*, 1996.

[120] G. J. Seil, C. A. J. Fletcher, and L. J. Doctors. Optimisation of waterjet inlets using computational fluid dynamics. In *Proc. FAST'97*, pages 59–64, 1997.

[121] L. Smith Jr. Wake ingestion propulsion benefit. *AIAA Journal of Propulsion and Power*, 9(1):74–82, 1993.

[122] C. G. Speziale. On nonlinear $k - l$ and $k - \epsilon$ models of turbulence. *Journal of Fluid Mechanics*, 178:459–475, 1987.

[123] S. Steen and K. J. Minsaas. Experiences from design and testing of waterjet inlets for high speed craft. In *Proc. Fast'95*, pages 1255–1270, 1995.

[124] P. R. Sterland and M. A. Hollingsworth. An experimental study of multiple jets directed normally to a cross-flow. *Journal of Mechanical Engineering Science*, 17 (3):117–124, 1975.

[125] B. S. Stratford. The prediction of separation of the turbulent boundary layer. *Journal of Fluid Mechanics*, 5:1–16, 1959.

[126] A. J. Strazisar. The changing roles of experimental and computational fluid mechanics. *Global Gas Turbine News*, pages 16–18, 1994.

[127] R. Svensson. A description of the water jets selected for 'Destriero'. In *Proc. Fast'91*, pages 1169–1184, 1991.

[128] R. Svensson. Water-jet propulsion of high-speed craft. In *IMAS 91*, pages 147–157, 1991.

[129] R. Svensson. Water jets: When do they make sense? In *Ferries 93*, 1993.

[130] R. Svensson. The role of hydrodynamic research in water jet propulsion. *International Cruise & Ferry Review*, pages 137–141, 1996.

[131] J. Szantyr and T. Bugalski. Numerical analysis of flow inside a waterjet. *Polish Maritime Research*, 1996.

[132] C. Taylor, C. E. Thomas, and K. Morgan. Analysis of turbulent flow with separation using the finite element method. In *Computational techniques in transient and turbulent flow*, volume 2, chapter 10, pages 283–325. Pineridge Press Limited, 1981.

[133] S. Thurston and R. C. Amsler. Review of marine propellers and ducted propeller propulsion devices. *Journal of Aircraft*, 3:255–261, 1966.

[134] R. H. Tindell. Highly compact inlet diffuser technology. *AIAA Journal of Propulsion and Power*, 4:557–563, 1988.

[135] R. H. Tindell. Computational fluid dynamic applications for jet propulsion system integration. *Trans. ASME, Journal of Engineering for Gas Turbines and Power*, 113:40–50, 1991.

[136] R. H. Tindell, C. A. Hoelzer, and D. Alexander. F-14 inlet development experience. *Trans. ASME, Journal of Engineering for Power*, 104:751–759, 1982.

[137] G. Törneman. The importance of high manoeuvrability for efficient operation. In *RINA Proc. International Symposium on Waterjet Propulsion Latest Developments*, 1994.

[138] A. A. Townsend. *The structure of turbulent shear flow.* Cambridge monographs on mechanics and appled mathematics. Cambridge university press, second edition, 1976.

[139] S. R. Turnock, A. W. Hughes, R. Moss, and A. F. Molland. Investigation of hull-waterjet flow interaction. In *Proc. FAST'97*, pages 51–58, 1997.

[140] H. J. A. van de Vorst, R. Verbeek, and A. J. A. M. Hendriks. Design considerations of waterjet propulsion systems. In *Proc. 13th Fast Ferry International Conference*, page 34, 1997.

[141] T. van Terwisga. The effect of waterjet-hull interaction on thrust and propulsive efficiency. In *Proc. FAST'91*, volume 2, pages 1149–1167, 1991.

[142] T. van Terwisga. On the prediction of the powering characteristics of hull-waterjet systems. Technical Report S410837, MARIN, 1992.

[143] T. van Terwisga. A theoretical model for the powering characteristics of waterjet-hull systems. In *Proc. FAST'93*, pages 975–991, 1993.

[144] T. J. C. van Terwisga. *Waterjet-hull interaction.* PhD thesis, Delft University, 1996.

[145] W. S. Viall. The engine inlet on the 747. Technical Report 69-GT-41, ASME, 1969.

[146] J. H. Wagner, R. P. Dring, and H. D. Joslyn. Inlet boundary layer effects in an axial compressor rotor: Part II–throughflow effects. *Trans ASME, Journal of Engineering for Gas Turbines and Power*, 107:381–386, 1985.

[147] G. J. Walker. *An investigation of the boundary layer behaviour on the blading of a single-stage axial-flow compressors.* PhD thesis, University of Tasmania, 1971.

[148] R. E. Walraevens and N. A. Cumpsty. Leading edge separation bubbles on turbomachine blades. Technical Report 93-GT-91, ASME, 1993.

[149] F. M. White. *Viscous Fluid Flow.* McGraw-Hill, 1974.

[150] D. C. Wilcox. *Turbulence Modeling for CFD.* DCW Industries, 1993.

[151] K. G. Winter. An outline of the techniques available for the measurement of skin friction in turbulent boundary layers. *Progress in Aerospace Sciences*, 18:1–57, 1977.

[152] D. C. Wisler, R. C. Bauer, and T. H. Okiishi. Secondary flow, turbulent diffusion, and mixing in axial flow compressors. *Trans ASME, Journal of Turbomachinery*, 109:455–482, 1987.

[153] W. Yang, editor. *Handbook of Flow Visualization.* Hemisphere Publishing Corporation, 1989.

[154] O. C. Zienkiewicz and R. L. Taylor. *The Finite Element Method*, volume 2. Solid and Fluid Mechanics Dynamics and Non-Linearity. McGraw-Hill Book Company, fourth edition, 1991.